UNIVERSITA' DEGLI STUDI DI TRIESTE

XXVII CICLO DEL DOTTORATO DI RICERCA IN GEOSCIENZE

NEO-DETERMINISTIC SEISMIC HAZARD ASSESSMENT
(NDSHA) FOR SUMATRA:
APPLICATION AT REGIONAL AND LOCAL SCALES

Settore scientifico disciplinare: GEO/10

DOTTORANDO
IRWANDI IRWANDI

COORDINATORE
GIOVANNI COSTA

SUPERVISORE DI TESI
GIULIANO PANZA

ANNO ACCADEMICO 2014-2015

In memory of the Acehnese people who lost their lives
in the earthquake and tsunami of 26 Desember 2004.

We will keep and share their experience for the next generation
in the spirit of seismic hazard mitigation in order to save the humanity.

Abstract

The Standard Probabilistic Seismic Hazard Assessment (PSHA) method cannot fill in the knowledge gap in the physical processes behind an earthquake. It can supply only generic guidelines based on attenuation relationships. A more adequate definition of the seismic ground motion can be given by the Neo-Deterministic Seismic Hazard Analysis (NDSHA), which is based on the possibility of efficiently computing realistic synthetic seismograms, by taking into account the physics of seismic waves generation and propagation. NDSHA has been applied in many countries (Panza et al., 2013), and has not yet been contradicted by observation. Earthquake hazard assessment studies in Sumatra were based on PSHA, therefore we decided to apply NDSHA. However, due to the complexity of fault systems and of tectonic setting, with high seismicity and significant destructive earthquakes in that region, some modifications are required.

Sumatra Island is almost completely surrounded by several types of faults, from Sunda subduction, strike-slip and branching Sumatra fault, Ninety East Ridge and Investigator Ridge. For the application of NDSHA, the faults have been classified into 15 different seismogenic zones, based on tectonic setting and clustering of focal mechanisms. Due to the size, shape and complexity of the seismogenic zones, an enhanced source definition procedure has been successfully developed starting from the standard version NDSHA. Several new features and options have been implemented in the magnitude smoothing procedure, so that it is now possible to request ellipsoidal smoothing with azimuthal decay and enhanced source depth definitions.

The structural model for density, Vp, Vs, Qp, and Qs has been compiled from regional data for deep layers and using the global model (Crust 2.0 and Litho 1.0) for the upper ones. The model consists of 49 layered structures, each associated with a polygon belonging to a 1°x1° grid, rotated 54° to be mostly aligned with the coastline.

An updated procedure for the quick generation of ground shaking scenarios based on the computation of synthetic seismograms by the modal summation technique allowed the rapid execution of parametric tests successfully used to validate the structural model for the case study of the Takengon earthquake scenario July 2, 2013 M6.1. The results have been compared, for frequencies up to 10 Hz, with the ShakeMap produced by USGS, and with the accelerograms recorded by BMKG. A satisfactory agreement has been obtained for both comparisons, except for the stations located on thick sedimentary layers that induce strong site effects, neglected in the quick parametric modelling.

NDSHA has been used on the regional scale, i.e. the whole Sumatra and adjacent islands, by calculating synthetics seismogram from all the sources obtained applying the modified smoothing procedure to the events available in the historical seismicity catalogues. 2,612 sources have been defined, and 953 receiver sites. An updated algorithm for path definition has been defined in order to reduce the number of synthetic seismograms required to obtain the hazard maps. For each receiver site the most significant sources have been sorted out, speeding up the computations by a factor of 4.5 without compromising the quality of the final hazard map.

NDSHA has been applied also to the local scale using high resolution data describing the lateral heterogeneities along selected profiles, for microzonation purposes. A hybrid method that combines the 1D modal summation technique with the 2D finite differences technique has been used to generate the synthetic seismograms, and to identify the amplification pattern along the profile. We investigated the local site effects observed for the sedimentary basin at Banda Aceh City. The basin is located between two bedrock structures, characterized by the Lhoknga limestone and the Ulee Batee volcanic rock. We considered two scenarios, from the subduction zone and from the strike slip zone. The simulation results evidenced the correlation between amplifications and the thickness of the sedimentary layers.

The enhanced NDSHA was successfully applied in Sumatra taking into consideration complex seismogenic zones, both on a regional and local scale. Future studies should improve the definition of the structural model, mostly for its upper part, by performing regional surface wave tomography instead of using global data. Detailed investigations should be also dedicated to the definition and characterization of proper extended source models for mega earthquakes.

Keywords: Sumatra, NDSHA, Source Definition Procedure, Microzonation.

Riassunto

Il metodo probabilistico standard per la stima della pericolosità sismica (PSHA) non può riempire adeguatamente il vuoto di conoscenza sui processi fisici che scatenano un terremoto. Può solo fornire delle linee guida generiche basate sull'utilizzo di relazioni di attenuazione. Una descrizione più adeguata del moto del suolo si può ottenere mediante la metodologia neodeterministica (NDSHA), basata sul calcolo efficiente di sismogrammi sintetici mediante la tecnica della somma dei modi, eventualmente accoppiata con le differenze finite nel caso di modellazioni a scala locale.

NDSHA è già stato applicato in molte nazioni (Panza et al., 2013), e i suoi risultati non sono stati ancora contradetti dalle osservazioni. Per quanto riguarda Sumatra, le stime di pericolosità sismica disponibili finora erano tutte basate su PSHA, e si è pertanto deciso di applicare NDSHA anche a questa regione. A causa della complessità tettonica dell'isola, dell'elevata sismicità e della presenza di terremoti distruttivi di magnitudo molto elevata, si è ritenuto opportuno implementare alcune modifiche agli algoritmi solitamente utilizzati per definire le sorgenti sismiche e i percorsi sorgente-sito.

L'isola di Sumatra è quasi completamente circondata da faglie di stile diverso: dalla subduzione di Sunda ai sistemi di faglie ramificate strike-slip di Sumatra, per finire con i Ninety East Ridge e l'Investigator Ridge. Per l'applicazione di NDSHA le faglie sono state raggruppate in 15 zone sismogenetiche, definite in base allo stile tettonico, all'ubicazione delle faglie attive e alla distribuzione spaziale dei terremoti finora osservati. A causa delle dimensioni delle zone sismogenetiche, della loro forma e della loro complessità, si è ritenuto opportuno estendere le capacità dell'algoritmo che porta alla definizione delle sorgenti sismiche in NDSHA, soprattutto per quel che riguarda la procedura di lisciamento delle magnitudo riportate nei cataloghi storici della sismicità. È quindi ora possibile, in aggiunta alle opzioni finora disponibili, definire il lisciamento su forma ellittica con la possibilità di un decadimento azimutale del valore di magnitudo, nonché agire con più parametri sulla profondità delle sorgenti.

Il modello strutturale di densità, Vp, Vs, Qp e Qs è stato compilato a partire da modelli a scala regionale uniti a modelli globali (Crust 2.0 e Litho 1.0) per gli strati superiori. Il modello è costituito da 49 strutture stratificate, ciascuna associata a un poligono che appartiene a una griglia di 1°x1°, ruotata di 54° per essere grossomodo allineata con la linea di costa.

È stata parimenti aggiornata la procedura per la rapida generazione di scenari di scuotimento del suolo, così da poter effettuare rapidamente dei test parametrici, usati con successo per la validazione del modello strutturale fatta utilizzando le registrazioni del terremoto M=6.1 di Takengon del 2 luglio 2013. Il risultato della modellazione è stato confrontato con le ShakeMaps prodotte dall'USGS e con gli accelerogrammi registrati da BMKG. Un accordo soddisfacente è stato ottenuto per entrambi i confronti, se si escludono le stazioni ubicate su una spessa coltre sedimentaria generatrice di forti effetti di sito, trascurati in queste rapide modellazioni parametriche.

NDSHA è stato applicato a scala regionale, cioè all'intera isola di Sumatra e alle isole minori immediatamente adiacenti, generando i sismogrammi sintetici a partire dalle sorgenti ottenute con la procedura di lisciamento applicata ai cataloghi storici disponibili. Sono state definite 2612 sorgenti e 953 siti di osservazione dello scuotimento del suolo. L'algoritmo per la selezione

dei percorsi significativi da utilizzare nella generazione dei sismogrammi è stato adattato alle dimensioni e alle caratteristiche dell'area in esame, così da poter ridurre il numero di sismogrammi sintetici necessari per la definizione delle mappe di pericolosità sismica. Per ciascun sito di osservazione vengono così selezionate le sorgenti più significative, senza compromettere la qualità dei risultati ottenuti ma riducendo di un fattore 4.5 i tempi di calcolo.

NDSHA è stato successivamente applicato anche a scala locale usando dati ad alta risoluzione descrittivi delle eterogeneità laterali del modello strutturale in corrispondenza di alcuni profili selezionati a scopo di microzonazione. Un metodo ibrido che combina la tecnica modale con le differenze finite è stato usato per la generazione dei sismogrammi sintetici e per identificare i pattern di amplificazione lungo i profili. Sono stati studiati gli effetti di sito per il bacino sedimentario di Banda Aceh, localizzato fra le strutture calcarea di Lhoknga e le rocce vulcaniche di Ulee Batee. Sono stati considerati gli scenari di scuotimento associati sia a terremoti avvenuti nella zona di subduzione che nel sistema di faglie trascorrenti. I risultati delle simulazioni mostrano una buona correlazione fra le amplificazioni ottenute rispetto a una condizione di bedrock e lo spessore della coltre sedimentaria.

La versione estesa e migliorata di NDSHA è stata in questo lavoro applicata a Sumatra tenendo in considerazione il complesso sistema di zone sismogenetiche sia a scala regionale che a scala locale. In una continuazione delle ricerche sarebbe opportuno migliorare la definizione del modello strutturale, soprattutto nella sua parte più superficiale, mediante analisi tomografica delle onde di superficie. Studi dettagliati dovrebbero anche essere dedicati alla caratterizzazione delle faglie responsabili dei terremoti di magnitudo più elevata e alla modellazione del rilascio dell'energia sismica.

Parole chiave: Sumatra, NDSHA, Definizione delle sorgenti sismiche, Microzonazione

Abstrak

Metode *Probabilistic Seismic Hazard Assessment* (PSHA) memiliki keterbatasan dalam memahami perhitungan secara fisis proses terjadinya suatu gempa bumi. Semua perhitungan hanya didasarkan pada persamaan attenuasi. Perhitungan yang lebih teliti tentang tingkat bahaya gempa bumi dapat dilakukan dengan metode *Neo-deterministik Seismik Hazard Assessment* (NDSHA) yang menggunakan proses komputasi yang efesien untuk melakukan perhitungan fisis dari sumber gempa saat gelombang seismik dibangkitkan hingga proses perambatannya hingga mencapai penerima. Metode NDSHA telah diterapkan di banyak negara (Panza et al., 2013) dan sejauh ini menunjukkan kecocokkan dengan hasil pengamatan lapangan. Kebanyakan kajian bahaya gempa di Sumatera didasarkan pada metode PSHA, sehingga dirasa perlu untuk menerapkan metode NDSHA. Namun karena Sumatera memiliki sistem sesar dan kondisi tektonik yang rumit, intensitas gempa yang tinggi, serta banyaknya gempa bumi besar yang merusak, sehingga perlu dilakukan modifikasi metode yang selama ini telah digunakan.

Pulau Sumatera dikelilingi oleh berbagai tipe patahan, dari subduksi Sunda, patahan geser serta pencabangannya, *Ninety East Ridge*, dan *Investigator Ridge*. Untuk menerapkan metode NDSHA, zona sumber gempa dibagi kedalam 15 bagian yang didasarkan pada kondisi tektonik dan mekanisme gempanya.Pengayaan versi standar NDSHA telah berhasil dilakukan untuk menagani besarnya variasi kekuatan gempa, distribusinya, dan komplektisitas sumber zona gempa. Disamping itu telah ditambahakan fasilitas baru diantaranya proses *smoothing* magnitudo gempa,*ellipsoid smoothing* serta penentuan kedalaman sumber gempa.

Model struktur kerapatan massa, Vp, Vs, Qp, dan Qs diperoleh dari hasil kompilasi data regional dan khusus untuk lapisan atas digunakan model global (Crust 2.0 dan Litho 1.0). Model tersebut terdiri dari 49 struktur dan setiap poligon meliputi area 1°x1° grid yang diputar 54° sehingga sejajar dengan garis pantai.

Prosedur untuk membuat skenario goncangan tanah berdasarkan perhitungan seismogram sintetik dengan teknik *modal summation* yang dapat dihitung secara cepat dengan bantuan program tes parametrik. Program tersebut telah berhasil diperbaharui serta dilakukan validasi pada model struktural untuk studi kasus gempa Takengon 2 Juli 2013 M6.1. Perbandingan tersebut berhasil dilakukan dengan membandingkan hasil simulasi pada frekuensi maksimum 10 Hz, dengan *ShakeMap* (peta goncangan tanah) yang dihasilkan oleh USGS dengan akselerogram yang direkam oleh BMKG. Perbandingan tersebut menunjukan hasil yang akurat kecuali pada beberapa stasiun yang terletak di lapisan sedimen tebal yang mengalami efek tapak yang kuat dan faktor tersebut diabaikan pada test parametrik.

NDSHA telah digunakan dalam skala regional, yaitu di Sumatera dan di pulau terdekat lainnya, dengan menggunakan data sintetis seismogram dari sumber gempa yang didefinisika dari prosedur *smoothing* yang telah diperkaya dalam penelitian ini. Setelah memasukan data dari katalog sejarah kegempaan maka terdefinisikan 2.612 sumber gempa dan 953 lokasi penerima. Selain itu, algoritma jalur sumber-penerima telah berhasil diperbaharui dan yang digunakan untuk menentukan seismogram sintetik yang kemudian akan digunakan untuk menghasilkan peta bahaya gempa. Dengan memilih jalur sumber-penerima yang relatif signifikan, maka proses komputasi dapat dipercepat hingga 4.5 kali tanpa mengurangi kualitas hasil akhir dari perhitungan peta bahaya gempa.

NDSHA telah diaplikasikan juga untuk skala lokal dengan menggunakan data resolusi tinggi yang mampu menggambarkan heterogenitas lateral pada profil tertentu untuk tujuan mikrozonasi. Metode hybrid, yang merupakan gabungan teknik *modal summation* 1D dengan teknik *finite differences* 2D, telah digunakan untuk menghasilkan seismogram sintetik serta mampu mengidentifikasi pola amplifikasi pada suatu profil. Pada penelitian ini telah diteliti efek tapak lokal untuk cekungan sedimen di Kota Banda Aceh. Cekungan ini terletak di antara dua struktur batuan dasar, ditandai dengan batuan kapur Lhoknga dan batuan vulkanik Ulee Batee. Pada penelitian ini digunakan dua skenario, dari zona subduksi dan dari zona sesar. Hasil simulasi membuktikan adanya korelasi antara amplifikasi dan ketebalan lapisan sedimen.

Metode NDSHA yang diperkaya telah berhasil diterapkan di Sumatera dengan kemampuan menangani zona sumber gempa yang kompleks baik dalam skala regional maupun lokal. Pengembangan lebih lanjut dimasa yang akan datang diharapkan dapat menggunakan model struktur lapisan bagian atas yang lebih akurat dengan menggunakan data tomografi regional bukan dari data global. Khusus untuk gempa-gempa besar harus dilakukan penyelidikan yang lebih rinci dengan menggunakan model sumber gempa *extended*.

Kata kunci: *Sumatera, NDSHA, Definisi Sumber Gempa, Mikrozonasi.*

Table of Contents

1. Introduction

Located in the western part of Indonesia, Sumatra is the second biggest island in the country. Measured at about 1,790 km in length and 435 km in width, the island crosses the equator near the center. The interior of Sumatra is dominated by two geographical regions: the Barisan Mountains in the west and the swampy plains in the east. The volcanic activity mostly occurs along the Barisan Mountains chain, where the active volcano Mount Kerinci resides at about the midpoint of the chain. The volcanic activity endows the region with fertile land and beautiful sceneries, for instance those around Lake Toba. Furthermore, the volcanic activity also enriches the region with deposits of coal and gold. And because Sumatra is located on the Pacific Ring of Fire, it also experiences some of the most powerful earthquakes ever recorded, such as those in 1797, 1833, 1861, 2004, 2005, 2007, 2012.

The Great Sumatran fault (a strike-slip fault) and the Sunda megathrust (a subduction zone) dominate the entire length of the island along its west coast. On 26 December 2004, the western coast and islands of Sumatra, especially the Aceh province, were struck by a tsunami following the Indian Ocean M9.0 earthquake. More than 170,000 Indonesians were killed, mostly in Aceh. Other more recent earthquakes that struck Sumatra include the March 2005 and the October 2010 Sumatra earthquakes.

1.1 Previous Seismic Hazard Maps for Sumatra

The first available seismic hazard assessment study of Indonesia, which includes Sumatra island, and used in the seismic building code in Indonesia dates back to 1983, and it is based on Beca and Ferner (1978) work (Figure 1.1, left). In 2002, the Minister for Public Work, *Pekerjaan Umum* (PU), released a new seismic hazard map based on probabilistic method (PSHA) under Standard National Indonesia (SNI 03-1726-2002) (Figure 1.1, right).

Since the seismic hazard map was published in SNI 03-1726-2002, many updates needed to be incorporated in the next seismic hazard map in order to get a more accurate and more reliable estimation of peak ground acceleration. These updates include the recent seismic activities, the latest research works regarding fault characteristics around Java and Sumatra, the improvements of the method in seismic hazard assessment, and the latest provisions in International Building Code 2000 (IBC 2000) (Irsyam, 2008). Those updates from 2002 to 2010 should have improved the

estimation of PGA in the hazard map. However, according to the score of GSHAP, they had done little in improving the estimation. The result showed that PSHA alone has a poor predicting capability, which had been confirmed in the studies by Kossobokov & Nekrasova (2012) and Nekrasova & Kossobokov (2012).
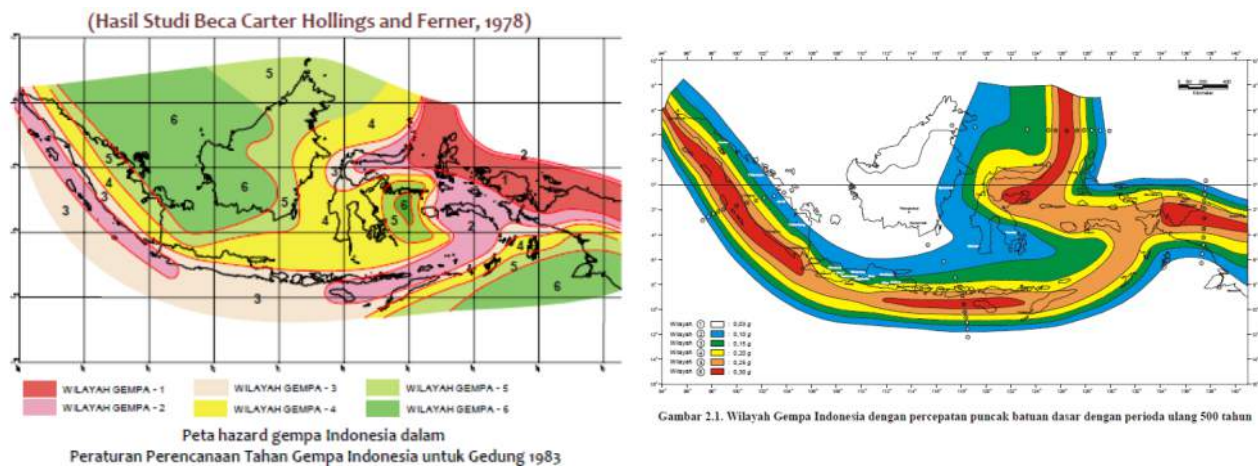

Figure 1.1 The early hazard map used for building code from 1983 to 2000 (SNI, 2002) (left). The seismic hazard map, approved by SNI, was used from 2002 to 2010. (right).

1.2 Current Seismic Hazard Map

In 2009, PU established a team to revise and update the SNI 03-1726-2002 seismic hazard map by using not only a probabilistic method (PSHA) but also a deterministic method (DSHA). The outcome was the current seismic hazard map standardized at a national scale. This hazard map is known as the building code of SNI 1726-2012.

The team's assessment used three seismic source models: fault zone, subduction zone, and gridded seismicity. The earthquake source models were derived by taking into account all available information from earthquake catalogs, tectonic settings, geographical and geological data, and focal mechanisms. The fault source was treated as a plane in a three-dimensional space, where the calculation of a distance from a site takes place on a certain point along the plane. The fault parameters used to develop the seismotectonic sources were fault traces, focal mechanism, slip-rate, dip, length and width of the fault.

Because the ground motion records needed to develop an attenuation relationship (GMPE) in the Indonesian region were insufficient, the relationships from the regions were used instead. The selection of the other regions was based upon the similarity on the source characteristic, geologic and tectonic conditions where the attenuation functions had already been developed. Most of the attenuation relationships in the assessment were those from the Next Generation Attenuation

(NGA), which was derived using the worldwide observed earthquake data.

The new Indonesian building code, SNI 1726-2012, follows the concept of MCEG, used by ASCE 7-10 for the purpose of geotechnical calculation. The calculation combines both the results from PSHA within 2% probability of exceedance in 50 years (2,500 years earthquake) and from DSHA within the area located near the active fault. Both approaches are utilized according to the procedure proposed by Leyendecker et al. (2000).

The map shows the PGA estimation involved in the recent Indonesian Earthquake Resistant Building Code SNI 1726-2012 (Figure 1.2). SNI 1726-2002 partially adopts the concept of Unified Building Code (UBC) 1997, for better preparedness for any potential disaster caused by a strong earthquake. The occurrence of many strong earthquakes in Indonesia (e.g 2004, 2005 and 2009 earthquakes) motivated the release of this map. Some of these major earthquakes were the 2004 Aceh Earthquake (Mw 9.0–9.3), which was followed by a tsunami, and the 2005 Nias Earthquake (Mw 8.7). These earthquakes underline an urgent need to consider a new conceptual approach and technological shift shown in the transition of UBC 1997 to IBC 2000, which later evolved further into the current IBC 2006.
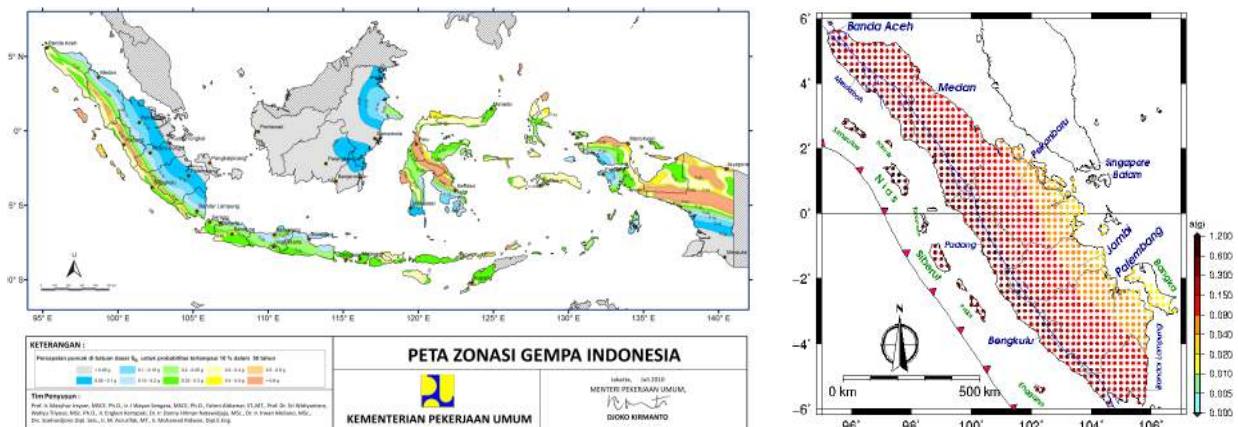

Figure 1.2, (left) Seismic Hazard Map of Indonesia (SNI 1726-2012): 10% probability of exceedance in 50 years (URL: http://loketpeta.pu.go.id/peta/zonasi-gempa-indonesia-4). (right) The same data plotting scale we used in this study.

The probabilistic and deterministic maps for estimation of seismic hazard in Indonesia have been developed based upon updated available seism tectonic data, implementing new fault models, incorporating new GMPE as NGA, and dividing seismic sources into the fault, subduction, and background zones. Due to the absence of GMPE developed using data observed from the Indonesia, as well as to the disruption of the tensor nature of the earthquake ground motion, predicted by continuum mechanics, in the computed strong motion, caused by the adoption of these relationships, there is a need for a reliable and rigorous definition and characterization of seismic hazard parameters.

1.3 Early Effort to Produce Deterministic SHA for Sumatra

As an active fault, Sumatra Fault can cause a significant hazard because of its shallow hypocenters and its proximity to the highly populated areas. However, the proximity from the active faults does not always mean a uniform level of hazard. Although the slip rate is high in some portions along the active faults, they may not accumulate a significant strain to produce a large earthquake. That is the case as shown by Natawidjaja & Triyoso (2007). Their study investigated the Sumatra Fault and attempted to produce the DSHA map. By taking into account the fault segmentation and the source parameters, the map hypothesized to show the expected PGA within the maximum credible earthquake (MCE) as shown in Figure 1.3 (left).
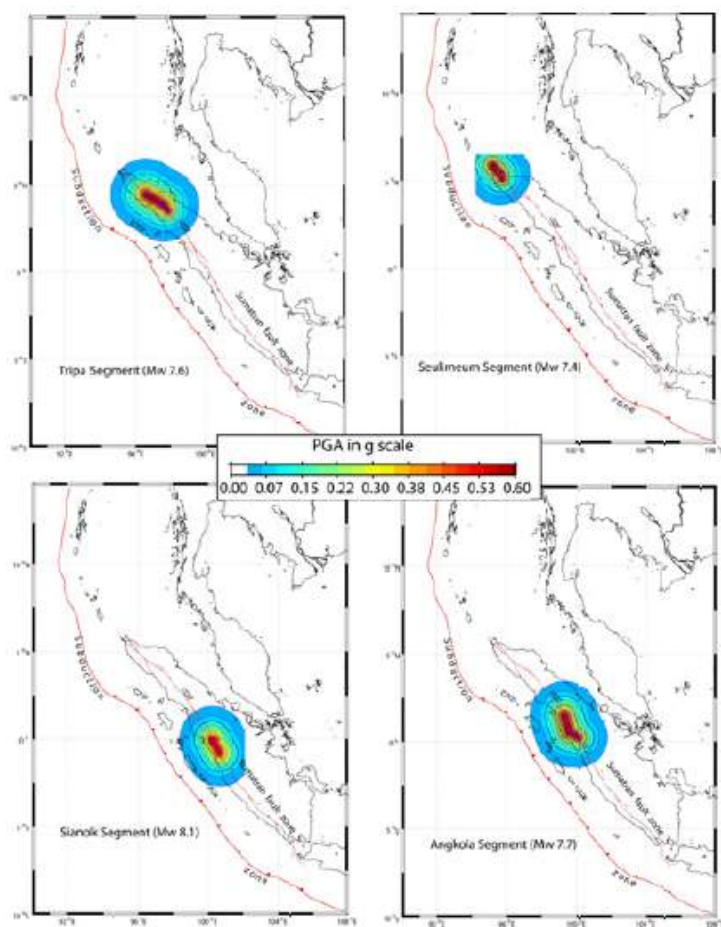

Fig. 7. Deterministic Seismic Hazard Assesments (DSHA). Maps of expected peak ground accelerations (PGA) of the maximum credible earthquake (MCE) on several fault section of SFZ using empirical relation equations of Fukushima and Tanaka [1990].
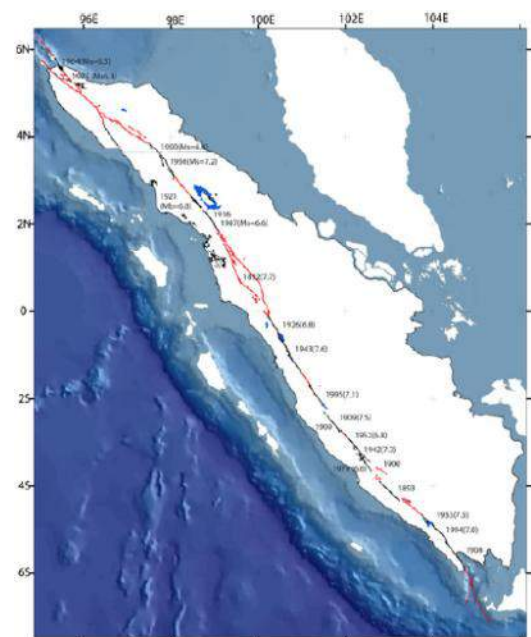
Fig. 6. Map showing the unbroken fault segments in the last century denoted by dark gray color code segments.

Figure 1.3 Exercise to produce DSHA based on attenuation relationship (left) with source they define from several study (top), after Natawidjaja & Triyoso (2007)

In addition, they also used the attenuation relationship developed by Fukushima & Tanaka (1990). The examples of the results are shown in Figure 1.3. In general, the results indicate that the earthquakes with a magnitude of 7 give out PGA > 0.3g and PGA > 0.5g for the distance of the source site less than 45km and 10km, respectively. Based on those physical characteristics of an earthquake source, Fukushima & Tanaka (1990) consider the saturation of acceleration amplitude in a near-source region, whose extent depends on the size of the earthquake. The attenuation

relationships that Fukushima & Tanaka (1992) proposed are also used by GSHAP (1999) for Indonesia and Malaysia. Petersen et al. (2004) found that these attenuation relationships are reliable to have been applied for the sites up to 500 km away from the seismic sources of the subduction-zone type, whereas the attenuation relationships proposed by Young et al. (1997) give inconsistent values for the sites more than 200 km away.

The deterministic seismic hazard map strongly depends on the attenuation equations being applied to the whole area. This assumption does not take care of the characteristics of the structural models, which differ from place to place. A study to evaluate an earthquake-hazard potential requires a set of appropriate data on the fault segmentations that determine the maximum credible earthquake (MCE) from the fault slip rates and the geometry fault ruptures. Therefore, this study uses this source of information to reliably define and characterize the MCE using the available modern instrument. Natawidjaja & Triyoso (2007) have studied the Sumatra strike slip fault to define the MCE based on the field geology and the historical seismicity. The defined values from their study are also used in this study.

1.4 The Neo-Deterministic Seismic Hazard Assessment

Recent advances in the physical knowledge of seismic waves generation and propagation processes, along with the improving computational tools, make possible the realistic modeling of the ground shaking caused by an earthquake, taking into consideration the complexities of the source, and of the propagation path. A neo-deterministic scenario-based approach to seismic hazard assessment (NDSHA) has been developed for naturally supplying the realistic time series of ground shaking, including reliable estimates of ground displacement readily applicable to the seismic isolation techniques. The NDSHA procedure, which represents a drastic enhancement of DSHA, permits incorporating, as they become available, new geophysical and geological data, as well as the information from the different Morph structural Zonation (MZ) developed for the space-time identification of strong earthquakes. All this leads to the natural definition of a set of scenarios of expected ground shaking at the bedrock. On the local scale, further investigations can be performed taking into account the local soil conditions, in order to compute the seismic input (realistic synthetic seismograms) for engineering analysis of relevant structures, such as historical and strategic buildings (Panza et al., 2013).

The NDSHA approach has already been applied in several regions worldwide, including a number of local scale studies accounting for two-dimensional and three-dimensional lateral heterogeneities in inelastic media. A pilot application of the approach, including the detailed evaluation of the expected ground motion accounting for site effects and seismic engineering analysis, has been carried out at a site located in the Friuli Venezia Giulia Region (NE Italy).

Furthermore, some applications using a highly efficient analytical methodology developed for modeling the propagation of the seismic wavefields in three-dimensional inelastic media are presented. This procedure, based on the computer code developed from a detailed knowledge of the seismic processes and the propagation of seismic waves in heterogeneous media, allows not only the detailed study of instrumental and macroseismic data but also the realistic estimate of the seismic hazard, in those areas for which scarce (or no) historical or instrumental information is available, and the relevant parametric analysis: different source and structural models can be taken into account to create a wide range of possible ground shaking scenarios from which to extract essential information, including uncertainty ranges, for decision making (Panza et al., 2013).

NDSHA is an innovative, but already well consolidated, procedure that supplies realistic time histories, with very solid physics roots, from which it is natural to retrieve peak values for ground displacement, velocity, and design acceleration in correspondence of earthquake scenarios (e.g. Parvez et al., 2010; Paskaleva et al., 2010). The synthetic seismograms can be efficiently constructed with the modal summation technique (e.g. Panza et al., 2001; La Mura et al. 2011) to model ground motion at sites of interest, using the available knowledge of the physical process of the earthquake generation and wave propagation in realistic media, and this makes it possible to easily perform detailed parametric analysis that permits to account for the uncertainty in input information.

In addition, the proposed methodology for seismic microzoning has been successfully applied to several urban areas worldwide in the framework of the UNESCO/IUGS/IGCP projects "Realistic Modeling of Seismic Input for Megacities and Large Urban Areas" (e.g. Panza et al., 2001, 2001b, 2002), as well as in the framework of various scientific networks like "Seismic Hazard and Risk Assessment in North Africa", "Seismic microzoning of Latin America cities" and "Seismic Hazard in Asia". The methodology has been applied to assess the importance of non-synchronous seismic excitation of long structures, like dams and bridges, as well.

1.5 The Advantages of using NDSHA for Sumatra

NDSHA addresses some issues largely neglected in a traditional hazard analysis, namely how crustal properties affect attenuation: ground motion parameters are not derived from overly simplified attenuation relations, but rather from the synthetic time histories. Starting from the available information on the Earth's structure (mechanical properties), seismic sources, and the level of seismicity of the investigated area, it is possible to estimate PGA, PGV, and PGD or any other parameter relevant to seismic engineering, which can be extracted from the computed theoretical signal.

The evidenced limits of PSHA estimates, which are due not only to scarcity of data, but also to the not valid physical model and the mathematical formulation employed (Castanos H. e Lomnitz C., (2002), PSHA: is it Science? Wang, 2011; Paskaleva et al., 2007, 2010;), become unacceptable when considering the number of casualties and injured people (Wyss et al., 2012). The evolving situation makes it compulsory for any national or international regulation to be open to accommodate the most important new results, as they are produced and validated by the scientific community.

Table 1.1 List of the deadliest earthquakes occurred during the period 2000-2011, and the corresponding intensity differences, $\Delta I_0 = I_0 M - I_0(mPGA)$, among the observed values and predicted by GSHAP. $I_0(M)$ and $I_0(mPGA)$ are computed from the observed magnitude M and the maximum GSHAP PGA around the observed epicenter, see (Panza et al., 2013, Kossobokov and Nekrasova, 2010).

Region	Date	M	Fatalities	Intensity difference ΔI_0
Sumatra-Andaman "Indian Ocean Disaster"	26.12.2004	9.0	227898	4.0
Nias (Sumatra, Indonesia)	28.03.2005	8.6	1313	3.3
Padang (Southern Sumatra, Indonesia)	30.09.2009	7.5	1117	1.8

The lessons learnt from the largest earthquakes, occurred in Sumatra during the last decade (table 1.1), show that the performances of the standard probabilistic approach to a seismic hazard assessment (PSHA) as implemented by GSHAP are very unsatisfactory (e.g. Kossobokov and Nekrasova, 2010). This is due not only to scarcity of data (epistemic uncertainty) but also to the not valid physical model and mathematical formulation employed (Wang, 2011; Paskaleva et al., 2007; Castanos and Lomnitz, 2002). Moreover, it is nowadays recognized by the engineering community that PGA estimates alone are not sufficient for the adequate design, in particular for special buildings and infrastructures, since not only the velocities but also the displacements may play a critical role, and the dynamical analysis of the construction response requires a complete time series of ground motion. Therefore, the need for an appropriate estimate of the seismic hazard, aimed not only at the seismic classification of the national territory, but also at the capability of properly accounting for the local amplifications of ground shaking (with respect to bedrock), as well as for the fault properties (e.g. directivity) and the near-fault effects, is a pressing concern for seismic engineers.

The implementation of NDSHA is challenging due to the complex tectonic setting, high seismicity, and the not-well-known but complex structural model of Sumatra. An earthquake with a magnitude of 9 can generate a global disaster. In turn, such a disaster will attract many scientist to investigate the area and also help to increase the awareness of natural disaster in Indonesia and

worldwide. Compared to other regions, Sumatra has no well recorded history of earthquakes. Ambiguity in determining the historical earthquakes also gives some difficulties especially those occurred inland. Other significant difficulties come from the limited information available about the crust structure model in the uppermost 20 km, which may significantly influence the result of synthetic seismogram from which the pickup PGA to be put in a hazard map. The complexity of the tectonic setting in Sumatra can create its own challenge when applying the NDSHA method. Therefore, a detailed evaluation and improvement in the smoothing procedure adopted in NDSHA is also needed to treat each seismogenic zone individually depending on its tectonic setting complexity, more details is available in Chapter 5. For a practical requirement, especially for the capital city of Banda Aceh, which is located in an alluvium sediment zone, this study also investigates the amplification effect using such a hybrid method (Fah et al., 1994 and Panza et al, 2009). This study will be used to mitigate an earthquake disaster in Banda Aceh and to help to create a plan to deal with any seismic hazard in the future.

1.6 Area and Scope of Study

Indonesia is the world's 15th largest country in terms of land area, and world's 7th-largest country in terms of combined sea and land area. There are 17,508 islands between 11°S and 6°N latitudes, and 95°E and 141°E longitudes. During the last decades, many seismic hazard studies concerning Sumatra have been carried out, e.g. Petersen et al. (2004) (PSHA) and Natawijaya et al. (2007) (DSHA). Sumatra is the most active tectonic zone in Indonesia because of the presence of the oblique subduction process that produced the Sumatra Fault, along which several destructive earthquakes have occurred. Consequently, the application of NDSHA in Sumatra is challenging.

The Sumatra region is affected by complex tectonic settings and seismicity; therefore, this study emphasizes on the effort to construct appropriate seismogenic zones for NDSHA. In Chapter 2, we introduce 15 seismogenic zones to accommodate this complexity, and each zone has been treated individually according to its tectonic setting and seismic activity, and this cannot be done with the existing version of NDSHA. Therefore, we focus on the procedure enhancement for the source smoothing by updating the NDSHA original version as discussed in Chapter 3. Using the physical simulation based on NDSHA, we construct the structural model for Sumatra. We combine the tomography data from the global and regional data to construct the structural model for V_P, Vs, density, and attenuation as further discussed in Chapter 4. In order to test the structural model, we produce and update the parametric test of the modal summation program for the investigation of the sensitivity of SH according to different input parameters. The updated parametric test routine is used to verify the Takengon earthquake with a magnitude of 6.1 that occurred on 2 July 2013 as

shown in Chapter 5. The application of the source definition produced by the enhanced smoothing procedure completes the NDSHA calculation at a regional scale. In order to decrease the time needed for the seismic hazard computation, we develop a new procedure to explore the efficient source-receiver paths. The efficiency of the NDSHA calculation at a regional scale is shown in Chapter 6. In order to estimate the effect of the seismic performance on some existed buildings, NDSHA can operate at a local scale. In Chapter 7, the result of the site characterization illustrates the city of Banda Aceh according to its sedimentary layers.
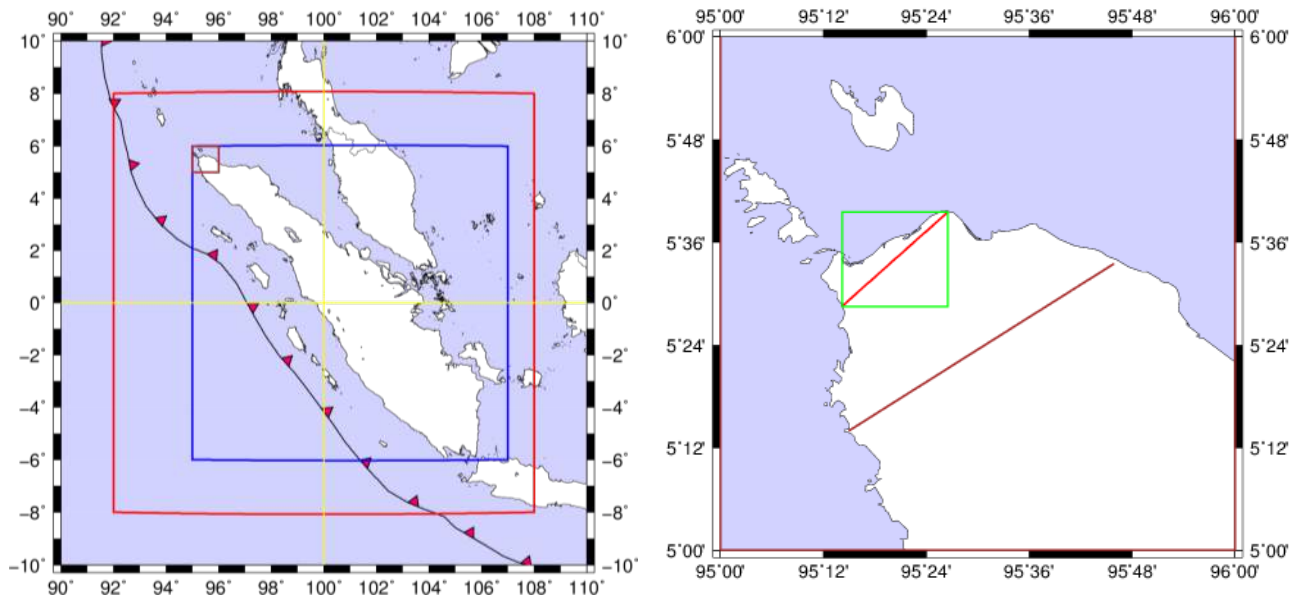

Figure 1.4 (left) Regional scale study in Sumatra: the red box delimits the seismogenic zones and the blue box the seismic zones. (right) Local scale study for microzonation of the city of Banda Aceh.

2. Seismogenic Zones of Sumatra

2.1 Tectonic Setting

Prior to the 2004 devastating earthquake, the Sumatra subduction zone received relatively little attention compared to other zones either those in Japan or the United States. This strong earthquake and the associated large seismic sea waves were like a lesson for the communities living around active seismogenic zones where the earthquake and tsunami hazards can be severe. Since the work done by Fitch (1972), Sumatra was often cited as a classic example of slip partitioning, which occurs when the relative motion between two obliquely converging plates is taken up on multiple, parallel faults.
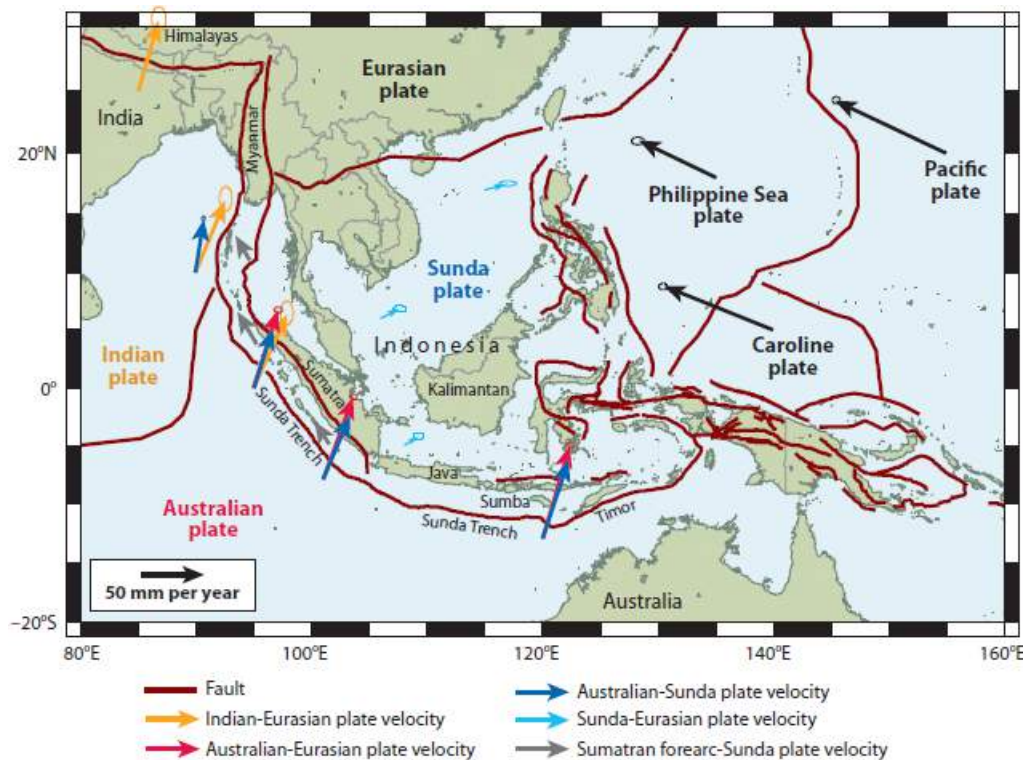

Figure 2.1 Plate tectonic setting of Sumatra. Vectors show relative velocities of plate pairs as labeled (McCaffrey, 2009).

Sumatra is part of a long convergent belt that extends from the Himalayan front southward through Myanmar and continues south past the Andaman and Nicobar Islands and Sumatra, south of Java and the Sunda Islands (Sumba, Timor), and then wraps around towards the north, see Figure 2.1. This trench accommodates the northward motion of the Australian plate into Eurasia. Additionally, the trench is known with several local names but here is called the Sunda subduction zone, in general, and sometimes the Sumatran subduction zone, when referring to the stretch

offshore Sumatra. West of Sumba, the dense lithosphere of the Indian Ocean seafloor subducts beneath the continental Sunda shelf, whereas to the east, the lighter continental Australian lithosphere thrusts beneath the oceanic lithosphere. The along-strike change in the average density of lithosphere being subducted coincides with changes in the character of the tectonics.

Sumatra is situated on the Sunda continental margin and exposes granitic rocks as old as 240 Ma (Hamilton 1979). Generally, from northeast to southwest, the island's geology is characterized by oil-bearing sedimentary basins in the northeast, the Barisan mountains (Figure 2.2), which include the volcanic arc and Sumatran fault, running along the length of the island near the southwest coast, the offshore forearc basins, the forearc high (islands of the Simeulue-Enggano ridge), the deep trench, and the subducting oceanic plate. Sumatra was rifted from the northern edge of Australia (north of New Guinea) during the Triassic to early Jurassic (~200–250 Ma). Sumatra would have been a stable continental margin from then until the subduction began to occur in the Cretaceous (possibly ~100 Ma).

2.2 Active faults in and around Sumatra

The rate and direction of the subduction of the lithosphere under the Sunda forearc, however, are further modified by the independent motion of the forearc. Fitch (1972) explained the presence of the Sumatran fault and other similar faults inboard subduction zones by the process now known as slip partitioning. That is, in some cases of oblique subduction where the two plates do not converge at the right angle to the strike of the trench, it requires smaller overall shear force to share the shearing (trench-parallel) component of the relative motion between two separate faults (Figure 2.3a) instead of on one fault. In the case of partitioning, one fault is the subduction thrust, which takes up all of the trench-normal slip (the dip-slip component) and some fraction of the trench-parallel slip (the strike-slip component). A second fault, within the overriding plate and commonly strike-slip in nature, takes up a portion of the trench-parallel motion. The subduction thrust and strike-slip fault isolate a wedge of forearc called the sliver plate (Figure 2.2a right). The slip rates on the separate faults can be inferred from their geometries and knowledge of the overall convergence (Figure 2.2b right).

The Sumatran fault, unlike other great transcurrent faults, is highly segmented (Katili, 1974, Bellier et al., 1997, Sieh & Natawidjaja, 2000). Most segments are less than 100 km long, and only 2 of the 19 segments identified by Sieh & Natawidjaja (2000) are longer than 200 km. The segments are separated by step-overs of a few kilometers or more. The importance of the short segments and wide step-overs is that they limit the area that can slip in a single event, and magnitudes tend to be limited to Mw ~7.5 or smaller throughout (see figure 2.2-left).
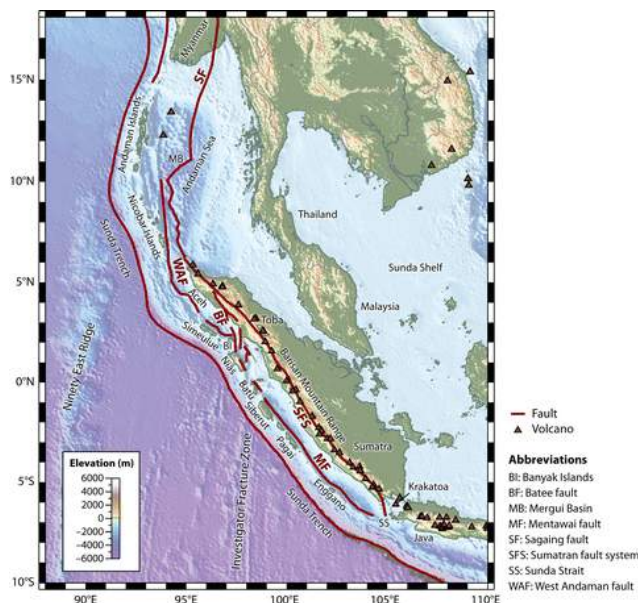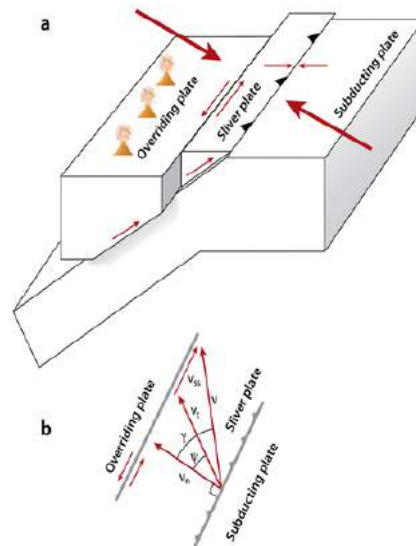
Figure 2.2 (left) Physiographic map of the Sumatran region. The triangles indicate the locations of active volcanoes. The thick red lines are faults. (right) (a) Block diagram showing the geometry of the sliver plate and its motion under conditions of oblique subduction. (b) The vector geometry of such a system. (McCaffrey 2009)
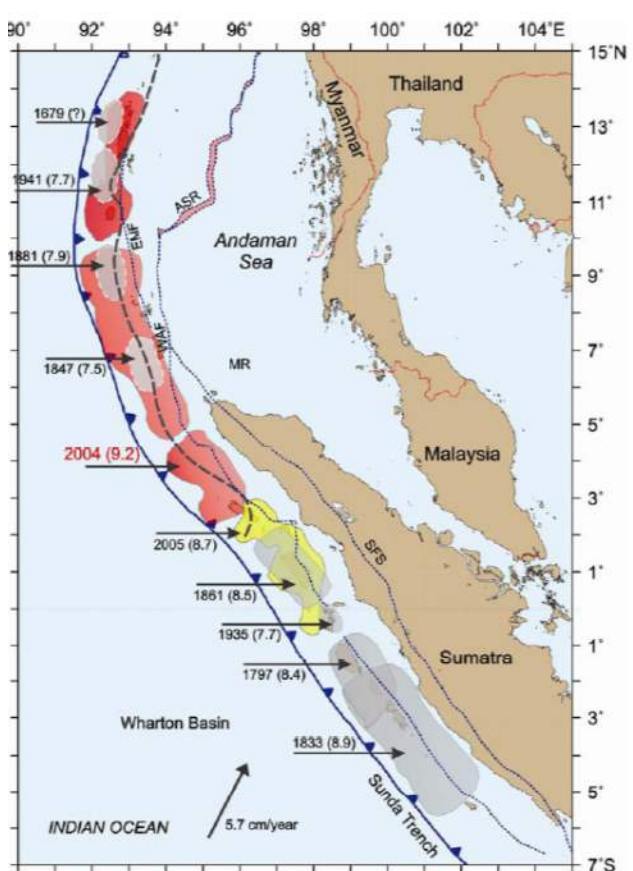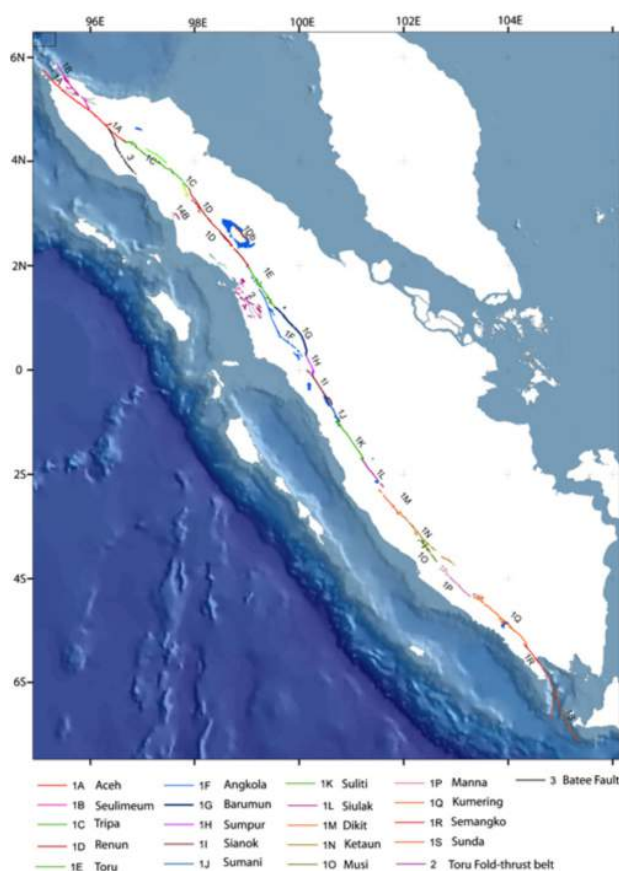

Figure 2.3 (left) Map of the principal active traces of the Sumatran fault zone (SFZ). TheSFZ can be divided into 20 fault segments. Ends of segments are mostly major fault step-overs of 4 km-width or more of separations, (Sieh & Natawidjaja, 2000). (right) Sunda subduction zone or Sumatra subduction zone (McCaffrey, 2009).

12

2.3 Seismicity of Sumatra

An incidental feature of the Sunda subduction zone is the non-volcanic forearc ridge that pops up above sea level forming many islands between the trench and the mainland. The islands allow near-trench, land-based observations that are not possible at most other subduction zones. The forearc ridge is the top of a thick sequence of sediments and sections of sea floor, known as the accreted wedge, which are folded, faulted, and plastered onto the upper plate, see Figure 2.4.
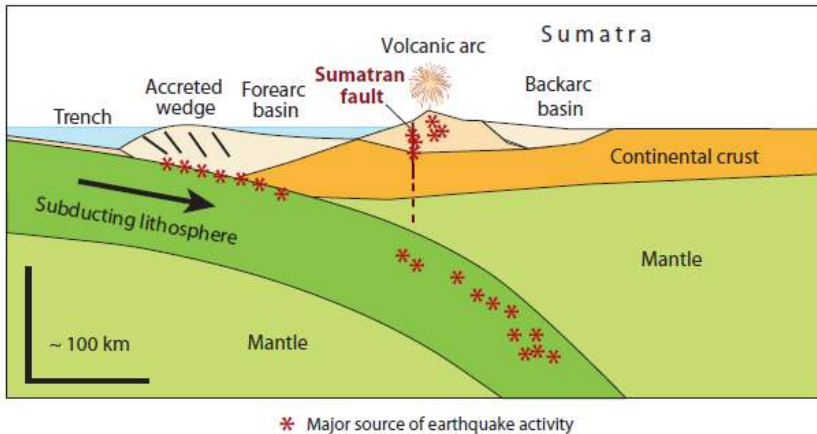

Figure 2.4. Schematic cross-section of the Sumatran plate boundary, where * marks major source of earthquake activity.
http://www.virtualuppermantle.info/Merapi.htm

Sumatra is among the most active regions on Earth in terms of earthquakes, owing to the confluence of multiple plates moving at very high relative speeds. The earthquake activity around Sumatra has multiple sources: thrust earthquakes on the subduction fault, strike-slip earthquakes on the Sumatran fault, deeper earthquakes within the subducting lithosphere, and volcanic earthquakes, see Figure 2.4.

The earthquake size is now defined by the moment magnitude $Mw = 2/3 (\log Mo - 9.1)$ (Hanks & Kanamori 1978), where the seismic moment Mo is given b $\mu \times d \times L \times W$. The rigidity μ is an elastic constant that varies from ~2 to ~7×10^{10} N m^{-2} within the region of a shallow earthquake activity. The factor L is the length of the fault, which can reach hundreds of kilometers for thrusts or strike-slip earthquakes, and W is the dimension of the fault surface in the direction of dip into the Earth. The amount of slip in the earthquake, d, in general scales with L by a factor of 10^{-5} (Wells & Coppersmith 1994) so that magnitudes are largely determined by the slip area LW.

The largest of these earthquakes are associated with subduction thrust faults, where the slip on the boundary between the subducting and overriding plate can occur over a very wide area. The maximum depth to which a slip occurs during crustal earthquakes may be temperature limited, and thus, under normal conditions, crustal earthquakes are shallow. Hence, for a near-vertical strike-slip fault like the Sumatran fault, will at most be ~20 km, and the earthquake magnitude Mw is typically less than ~8.0. In fact, Mw for earthquakes on the Sumatran fault appears to be limited at ~7.6, possibly also due to the high degree of segmentation (i.e., limiting L) as noted earlier. Earthquakes on the Sumatran fault are shallow strike-slip events and reveal right lateral motion (Figure 2.4); that

is, the southwest side of the fault moves northwest relative to the northeast side. In the past two centuries, the Sumatran fault has produced more than a dozen notable and damaging earthquakes.

Because subduction thrust faults dip at relatively low angles (< 30º) into the earth and because the sliding of the cold upper portions of the oceanic lithosphere deep into the earth cools the fault to greater depths, the width in subduction thrust earthquakes can reach hundreds of kilometers, thus allowing much larger earthquakes to take place. For this reason, most earthquakes around the world that reach magnitudes in excess of 8.0 are at the subduction zones.
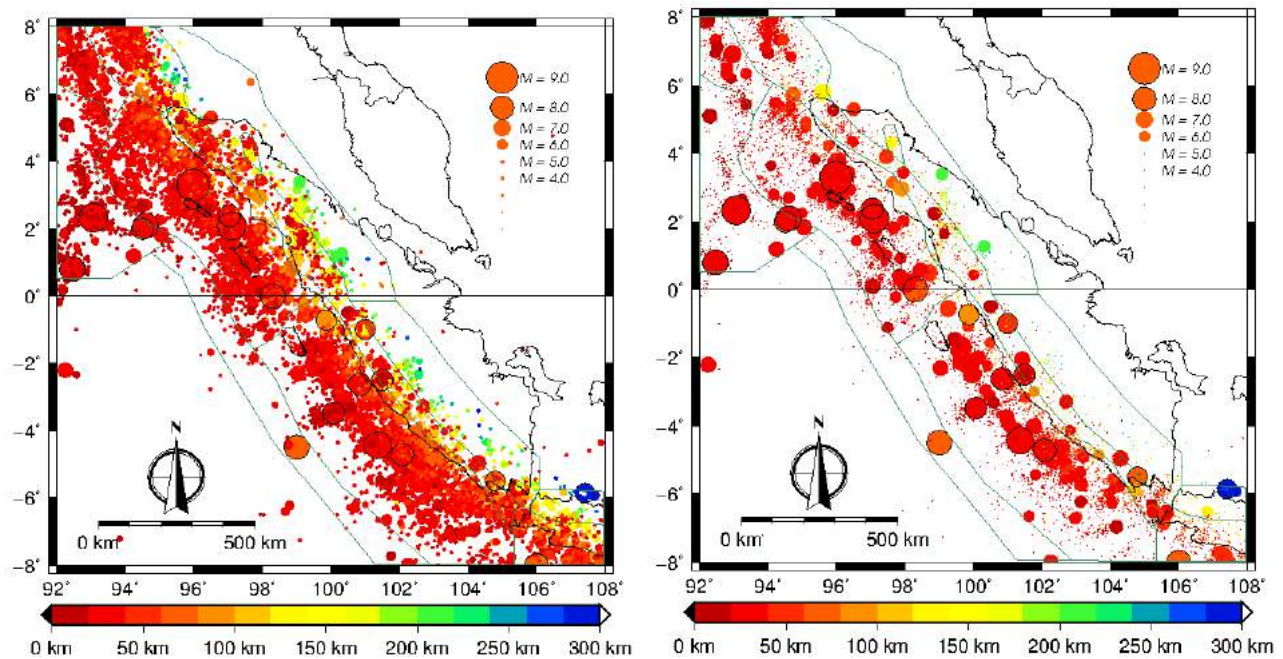

Figure 2.5. Seismicity of Sumatra from USGS earthquake catalog (left) for all magnitude ranges. (right) plot only above 6 with filled circle and dots for lower magnitudes.

2.4 Earthquake Catalogs

The first step of any seismic hazard assessment is identification of seismic sources that can affect the area of study, this step needs as can as possible complete, long and accurate earthquake catalog. One of the important advantages of NDSHA is that it is not necessary to involve the earthquake recurrences nor the "return period", which are subject to large uncertainties, the former, and physics rootless, the latter. The needed parameters are earthquakes location and magnitude Maximum Historical Earthquake (MHE) or MCE. In this study we make use of the available earthquake catalogs to establish homogeneous and completed one as show in table 2.1.

In this study, the USGS catalogs are used for the time span from 1907 to 2015 to define the location, configuration, and the potential seismic sources in and around the Sumatra region. The data freely available can be downloaded from http://earthquake.usgs.gov/earthquakes/search/. This catalog is the most complete catalog used in this study in terms of the number of data and time

duration. A historical earthquake catalog is also accessible from the USGS website since 2014, and it goes back to 1797. The USGS catalog shows the increasing earthquake depth corresponding to the increasing distance from the Sunda Trench.

Tabel 2.1: list of earthquake catalog for Sumatra limited to the interest region

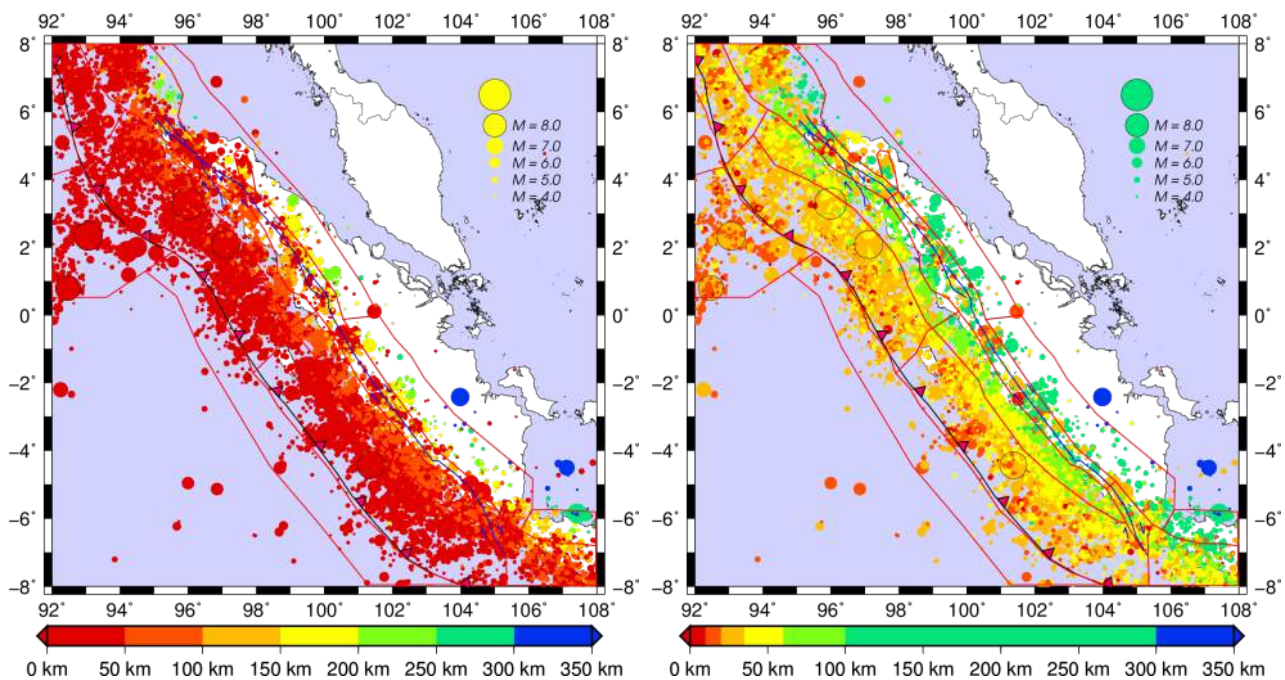| catalog	depth (km)		magnitude		time		Number of data
	min	max	Min	max	begin	end	
USGS	0.3	631.4	3.7	9	1907-01-04	current	14132
USGS history	20	564	6.6	8.8	1797-11-24	1971-02-04	21
Engdahl	4.4	601.7	5.5	9	1907-1- 4	2007-9-29	327
ISC	10	596.3	5.22	9	2007-08-08	1914-06-25	727
BMKG	1	650	1.8	8.3	2008-11-27	2012-11-01	5195
Pesicek	0.424	630.2	3.6	7.1	1960-1-7	2009-12-25	5514

Figure 2.6: Plot of the USGS catalogs with different depth color bar scale. This important to take care the depth of earthquake

The USGS catalog, in this study is combined with the catalogs from Engdahl et al. (1998), ISC (International Seismological Center), BMKG (Badan Meteorologi, Klimatologi, dan Geofisika) and Pesicek et al., (2010). The Engdahl catalog is a global catalog of locations and magnitudes of instrumentally recorded earthquakes from 1900 to 2008 (Engdahl et al., 1998). ISC provides several earthquake parameters such as an event location, an origin time, and focal mechanisms. The ISC event catalog has two categories the reviewed ISC Bulletin and ISC Bulletin. The reviewed ISC Bulletin is a subset of the ISC Bulletin that has been manually reviewed by the ISC analysts. This

includes all events that have been relocated by the ISC, (Engdahl et al., 1966, ISC, 2013). The Indonesia government under the BMKG, who has the responsibility for the operation of several seismometers and accelerometers, produces an earthquake catalog for Indonesia and is used in this study to cover the lower magnitude earthquakes, where the seismicity is low. Pesicek et al. (2010) makes their relocated earthquake available from their study for the body wave tomography in Sumatra. The relocated earthquakes are important to determine the depth of an earthquake source for the strike-slip earthquake along the Sumatra fault. Figure 2.7 shows the relatively uniform distribution in the catalog by Pesicek et al. (2010) compared to the other catalogs. The catalog discussed here is based on the 3 centuries of observation. However, the earthquake is a geological phenomenon, which needs a long record to adequately characterize the fault. This is particularly important for the Sumatra fault as the near seismic zone along with any less recorded seismic activity more than the subduction zone. In order to improve the poor earthquake catalog for the Sumatra fault, the earthquake information geological investigations (Natawidjaja and Triyoso 2007) is used after applying some updates in the estimated earthquake magnitude based on the detailed evaluation of the geologic and historical records.
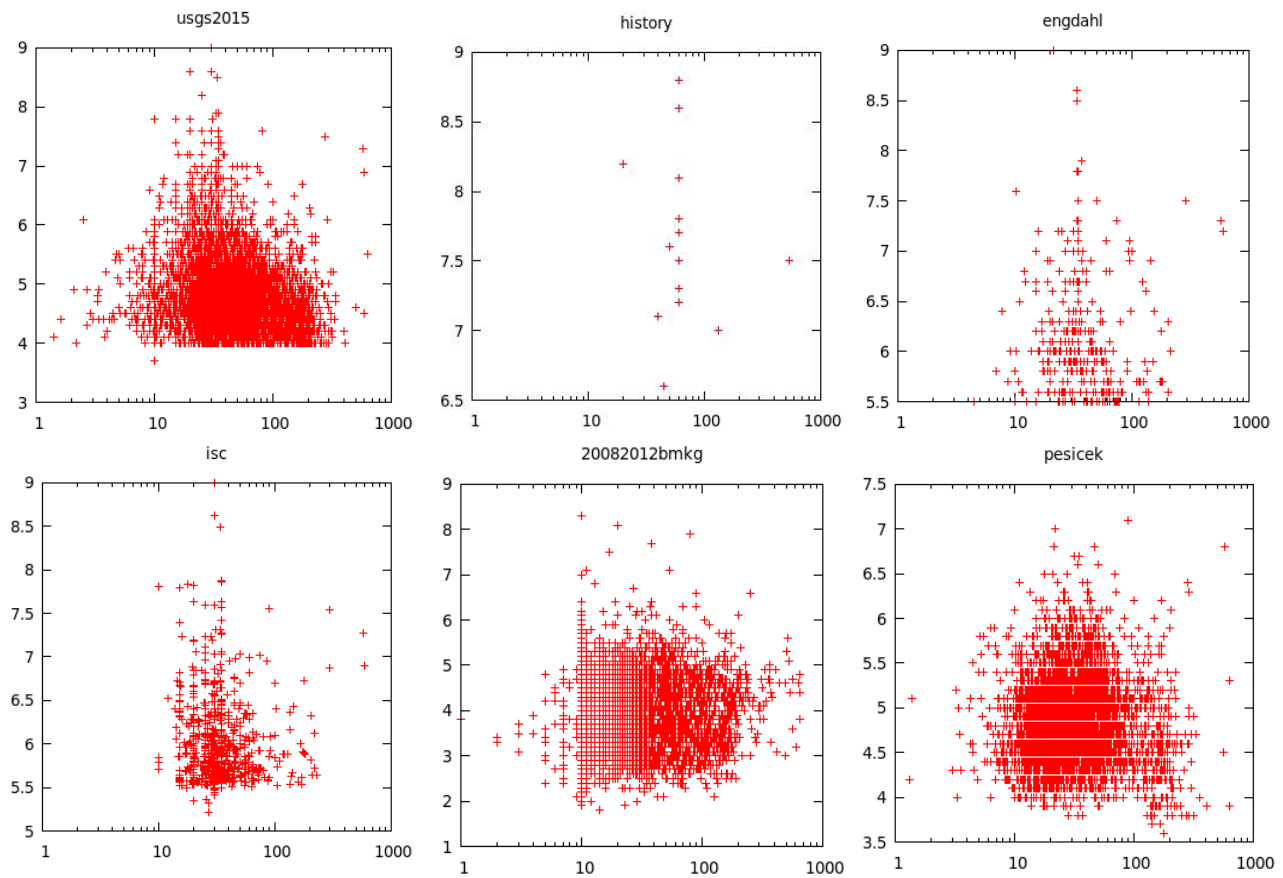

Figure 2.7 : Distribution of magnitude versus depth, in km, for several catalogs

In order to combine several earthquake catalogs compiled by different authors with different details and completeness, we use an advanced selection procedure, namely eqc4select.exe (in original version handled by the beginning part of `ecells.out`). The program combines several catalogs by applying basic selection criteria to single catalogs, namely `default.eqc`. The catalogs list can be put in the file default.cat, or put in the passing parameter, e.g.:

```
eqc4select.exe sumfull.cat
```

This selection procedure is very useful when dealing with huge data sets with different format, and it also is useful to remove any errors in the data if they are not in the proper range. This selection procedure reduces the number of the recorded events significantly and will be useful for the subsequent calculation (smoothing process). Finally, an analysis is needed to define the selection criteria for this procedure based upon the experience, knowledge, and needs, e.g.

```
#      file                   depth       magnitude       year
#polygon    catalog           min    max    min    max    min    max
sumg.poc   usgs2015.eqc       8     200     4      9      2010   2016
sumg.poc   usgs2015.eqc       8     200     4      9
sumg.poc   usgs2015.eqc       8     200
sumg.poc   usgs2015.eqc
```

The polygon is the first selection criteria, and for this study we use the same polygon because we are using the global earthquake catalog. The BMKG is a national catalog that covers the whole Indonesian territory, and in the following study it is used by extracting the seismicity for the Sumatra region (95E- 108E, 8S-8N). This selection will work for the original standard format (`.eqc`) and comma-separated values (`.csv`). The csv format is easy to edit because it does not depend on characters but is separated by commas and is also easy to edit using a spreadsheet program like libreoffce-cal or excel, which can even be loaded to QGIS directly for visualization.

Table 2.2: Configuration file to be passed to `eqc4select.exe` for selecting earthquake for as input for next step smoothing process.

polygon	catalog	dmin	dmax	Mmin	Mmax	ymin	ymax	col
sumg.poc	history.eqc	10	200	4	9	1000	1990	0
sumg.poc	usgs2015.eqc	15	200	4	9	1900	1961	0
sumg.poc	pesicek.eqc	2	200	3.5	8	1960	2010	0
sumg.poc	usgs2015.eqc	8	200	4	9	2010	2016	0
sumg.poc	bmkg.eqc	10	100	3	9	2008	2013	0
sumg.poc	engdahl.eqc	2	300	3	9	1907	2008	0
sumg.poc	isc.eqc	10	300	5	9	1914	2008	0
sumg.poc	danny7.csv	10	200	4	9	1000	2100	0

First optional selection criteria for minimum and maximum depth (*dmin* and *dmax*) could be used to remove the deep earthquakes, which are not significant contributors to hazard. Second optional criteria for minimum and maximum magnitude could be used if we do not really trust the

lower and upper limit of the magnitude given by the earthquake catalogs. So, the smoothing procedure could be applied individually for each seismotectonic zone. The third optional selection criteria is the range of time of observation in the unit of year, this option could be used with the highly trusted period of a specific catalog. For instance, during the period 1960-2010, we prefer to use the relocated earthquake catalog Pesicek et al. (2010) to that of by USGS. Meaning that the USGS catalog is used from 1960-1961 and from 2010-2016, as shown in Table 2.2. The initial combination of all catalogs contains 25910 records, and after preforming the selection produce the number of records reduces significantly to 13317 records. Figure 2.8 shows the seismicity before and after applying the selection procedure.
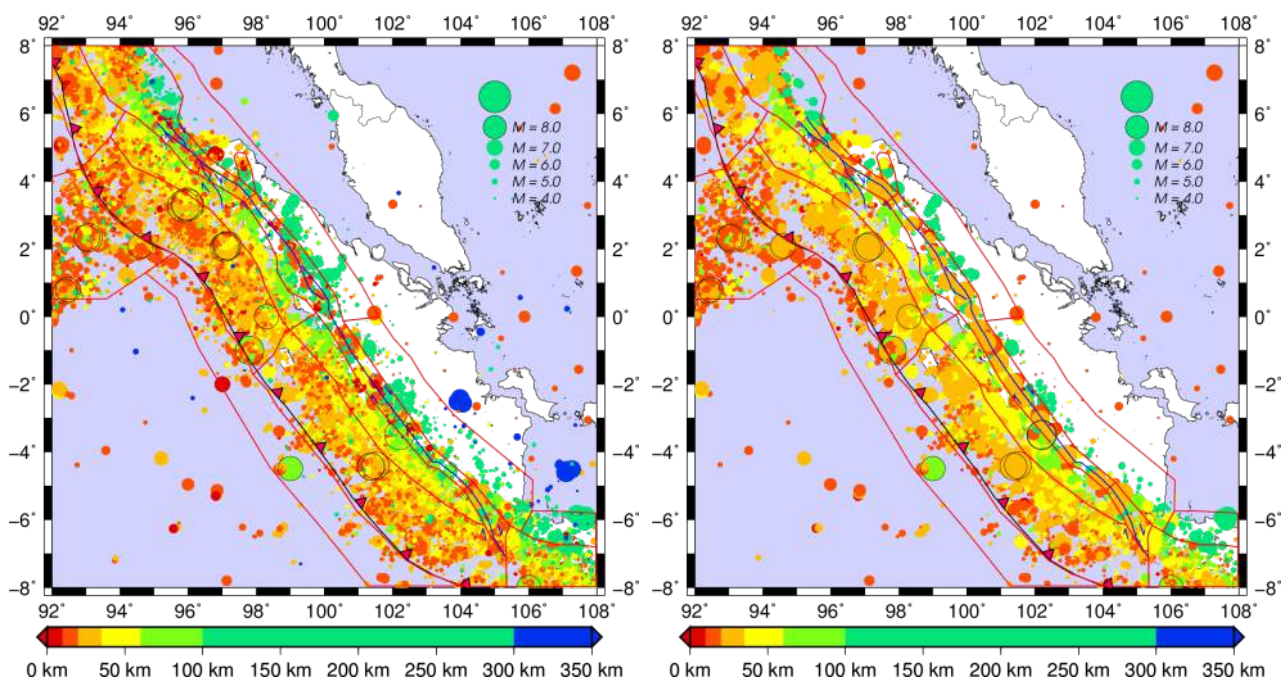

Figure 2.8 (left) Combination of all catalogs. (right) Plot after performing the selecting procedure of the events from different catalogs.

2.5. Seismogenic Zones

In an anthropized area, it is now technically possible to identify zones in which the heaviest damage can be predicted. A first-order zoning can be carried out at the regional scale, based on the knowledge of the average properties of seismic sources and on the structural models. Microzonations are possible as well, provided that detailed information about the source, path, and local site conditions are available. A drastic change is required in the goal of zoning that must be a pre-disaster activity performed to mitigate the effects of the next earthquake, using all available technologies. Seismic zoning can use the scientific data banks, integrated in an expert system, by means of which it is possible not only to identify the safest and most suitable areas for urban

development, but also to define the seismic input that is going to affect a given building.

Starting from the available information on the Earth's structure, seismic sources, and the level of seismicity of the investigated area, it is possible to estimate the peak ground acceleration, velocity, and displacement (PGA, PGV, and PGD, respectively) or any other parameter relevant to seismic engineering, which can be extracted from the computed theoretical signals. This procedure allows us to obtain a realistic estimate of the seismic hazard in those areas for which scarce (or no) historical or instrumental information is available and to perform the relevant parametric analyses (Panza et al., 2001).
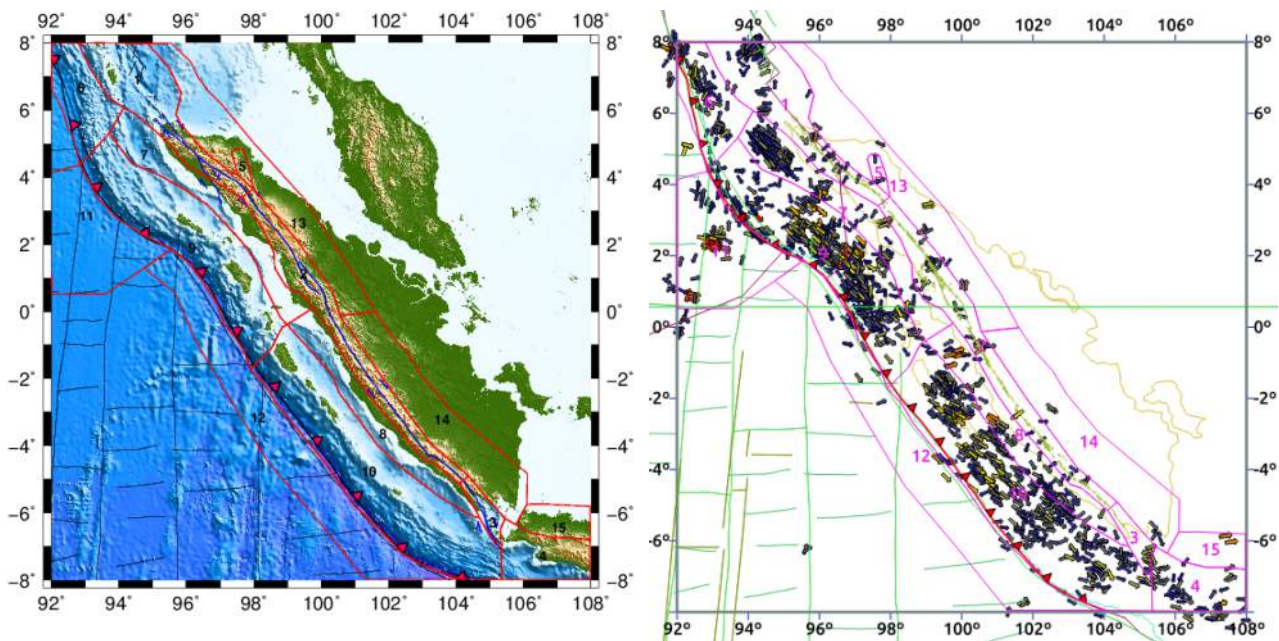

Figure 2.9. (left) Faults related to seismogenic zones. (right) Selected focal mechanics from QGIS by magnitude and strike direction pattern.

Sumatra is surrounded by several kinds of faults, from subduction, strike slip, spreading, inter-plate from Ninety East Ridge and Investigator Ridge as show in Figure 2.9. There are several simple seimogenic zones already introduced after (Petersen et al., 2004) for use with PSHA. But the available seismogenic zones (e.g. Petersen et al. 2004) are too simple to fulfill the NDSHA requirement, complexity of earthquake rupture process and recent tectonics affecting Sumatra. So there is a need for updating the seismogenic model to accommodate the new data and studies.

Based on Figures 2.9 and 2.8 and on the spatial distribution of focal mechanisms from International Seismological Centre (ISC 2013) Bulletin, we define 15 seismogenic zones (see Table 2.3).

1. The Aceh zone is characterized by a relatively high seismic activity with a relatively shallower depth and the maximum recorded magnitude is about 6.7. There are several earthquakes, which

have occurred in this zone e.g. 21 January 2013 M6.1 that causes some damage in Tangse, and 2 July 2013 M 6.1 that caused 39 fatalities, 420 injured in Takengon. The last earthquake namely the Takengon earthquake will be discussed extensively in the next chapter for the verification of the computed data. The dominant focal mechanism in this zone is the strike slip mechanism. The Sumatra fault starts to divide at its northern tip into two branches: western branch (the Banda Aceh zone) and eastern branch (the Lokop zone). The Western branch starts to branch out again in the north of Zone 1 into the Aceh fault and the Selimum fault. The Western branch is intensively monitored by AGNeSS network (Ito et al. 2008, 2012, Gunawan et al. 2014, Tabei et al. 2015) and AGOGO network (Irwandi et al., 2010). Recently, geological investigations are carried out to assess the activity of the Aceh fault, and the result showed it is now inactive and completely vanishing in the Andaman Sea. On the other hand, the Selimum fault becomes an active fault and continues toward Weh Island. Accordingly to the nomenclature by Natawijaya et.al 2007 (Figure 2.3), there are 4 segments in this seismogenic zone: Aceh fault, Seulimeum fault, Tripa fault, and Batee fault.

2. The Semangko zone which is aligned along the Great Sumatra fault, is characterized by a narrow zone of seismic activity, and it is strongly segmented with a specific MCE for each segment as explained by Natawijaya et al. (2007). There are debates among geologists about whether the middle part of the Sumatra fault is splitting into two faults (i.e. Angkola and Barumun segments) or is due to the presence of the pull-apart basin: the most accepted hypothesis is the presence of the pull-apart basin. This seismogenic zone is the main contributor to hazard in Sumatra due to the earthquake shallow focal depth and to its proximity to the populated areas. Several recent destructive earthquakes occurred with a high frequency ground motion caused a relevant damage to the low buildings, like that of on 6 March 2007 with M6.3 at depth 19 km that caused 68 fatalities and more than 460 injured.

3. The Krakatau zone, the head of the Sumatra fault, also contains the southern part of the Sumatra fault. In this zone, the islands of Krakatoa are located in the Sunda Strait between Java and Sumatra. The fault plane solution for earthquakes inside this zone is relatively not uniform; there are also strike slip, oblique subduction mechanisms and volcanic origin earthquakes in this zone. A destructive earthquake occurred on the 15 February 1994 with M6.9 at 23km focal depth and caused 196 fatalities, 2.000 injured. Almost all buildings in Liwa town collapsed.

4. The Jawa Sea zone or the Java Subduction zone is the Java Sea part of the Sunda Subduction zone where the dominant focal mechanism is relatively a pure thrust (strike=270°, dip=29°, and rake=89°) because the Australian plate is moving perpendicular to the Sunda plate. This seismogenic zone represents low hazard to Sumatra, but it will be significant for several important cities in Indonesia like Bandung or Jakarta. On 2 September 2009, a large earthquake M ~7.0

caused 46 fatalities on Java without any significant effects on Sumatra. In spite of the low expected hazard from the Java zone, conservatively, this study considered the zone as a potential source of hazard and provided a wide view about the other possible sources.

5. The Lokop zone: the Sumatra fault is at the first-order divided into the Lokop fault on the northern part, and it is not considered in the existed PSHA map (SNI 1726-2012). On 20 November 1994, the earthquake with magnitude 6.1 occured but was not well documented. This branching will become clearer if we look at a large scale where the Andaman zone is diverging and forming the Mergui Basin (Curray 2005).
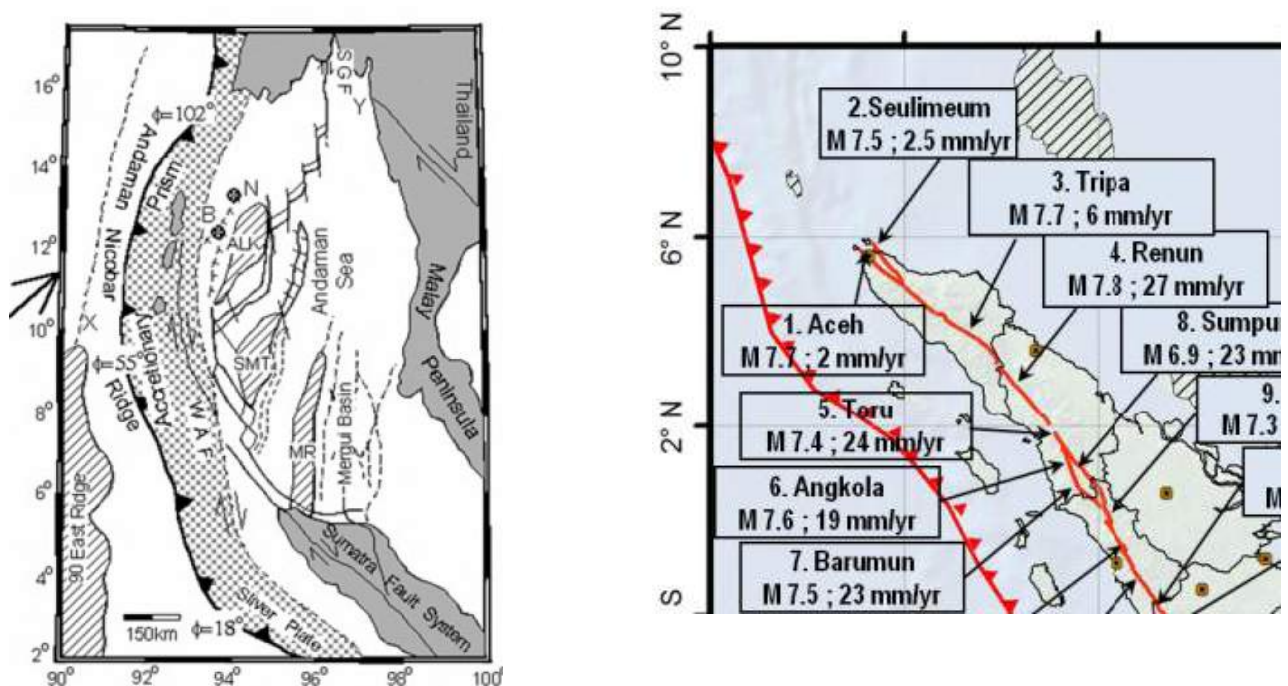

Figure 2.10. (left) the Mergui basin shows the existing active faults in seismogenic zone of Lokop (Curray & Munasinghe 1991; Curray 2005; Chakraborty 2008, which is not discussed in the current standard PSHA (right) Maximum magnitude and slip rate of influenced seismic source (clipped from: Irsyam et al., 2010 and Irsyam et al., 2013)

6. The NSR (North Sumatra Ridge) zone is named after Curray (2005). This zone is too far from Sumatra as it is from the Java Sea zone, and it has no historical impacts on the studied region. However, we considered this zone to be conservative. The recent large earthquake M 7.2 in this zone was on 26 December 2004 as an aftershock of the 2004 Sumatra-Andaman earthquake.

7. The Meulaboh zone, which is the northern part of the Sunda subduction zone, is classified as an intermediate depth earthquake (range ~45-90km) zone even though this definition does not follow the standard classification of earthquakes based on the focal depth. A big earthquake happened on 0 May 2010 with magnitude 7.2 at depth 61.4 km with no relevant damage (in a long period) and generated 50cm tsunami that caused some panic among people living along the coastline because

they experienced the 2004 tsunami earlier.

8. The Padang zone is the southern intermediate depth subduction zone (with the earthquake depth range ~30-80km). A big earthquake, known as the Bengkulu earthquake, happened on 12 September 2007 with magnitude 7.6 and depth 35km caused 21 fatalities. Another large earthquake happened on 30 September 2009 (the Padang earthquake) with M 7.6 at depth 80 km and caused 1117 fatalities, 1214 serious injured, and 1688 minor injured. In reference to the USGS (2009) poster, on the basis of the currently available fault mechanism information, and the earthquake depth of 80 km, it is likely that this earthquake occurred within the subducting Australian Plate rather than on the plate interface itself. The recent earthquake was deeper than the typical subduction thrust earthquakes that generally occur at depths less than 50 km.

9. The Nias zone, which is the northern shallow depth subduction zone, generates mega earthquakes and tsunami such as the Sumatra Andaman earthquake on 26 December 2004 M 9.1 and the Nias earthquake on 28 March 2005 magnitude 8.6 at depth 30 km. This subduction zone is classified as the swallow depth earthquakes zone (range ~10-30 km) with strike 325º dip 7º and rake 100º.

10. The Mentawai zone, which is the southern shallow depth subduction zone, generated the earthquake on 12 September 2007 with magnitude 8.5 at depth 34 km. Another large earthquake occurred on 4 June 2000 with magnitude 7.9 at depth 33 km, strike 328º, dip 9º, and rake 114º near Pagai Island.

11. The Interplate zone or Inter-plate strike slip ridge is far from Sumatra and the adjacent island. The zone produced an unexpected earthquake on 11 April 2012 with magnitude 8.6 and depth 20 km as a result of strike-slip fault within the oceanic lithosphere of the Indo-Australia plate and was reactivated from the Ninety East Ridge as far as east 97°E. This earthquake is also known as the Indian Ocean earthquake with strike 199º, dip 80º, and rake 3º.

12. The Sunda Trench zone, with relatively small magnitude earthquakes, is well known as a low hazard zone to Sumatra in comparison to the subduction zone. We introduced this seismic zone because it is located before the contact between the oceanic crust (Australia plate) and the continental crust (Sunda plate), and it has a mechanism with strike 321º, dip 64º, and rake 7º, which is different from the characteristic of the subduction zone,.

13. The Medan zone takes its name from the biggest city in Sumatra as the northern deep subduction zone. Most of the earthquakes here are deep (150-215km) earthquakes, and the zone is considered a minor contributor of hazard. The biggest earthquake in this zone occurred on 1 December 2006 with magnitude 6.3 at depth 204 km.

14. The Palembang zone gets its name from the location of the second largest city in Sumatra, and

the zone is located in the polygon of the outhern deep subduction zone. Most of the earthquakes are at the 100-150km depth and contributing low hazard to Sumatra. The largest earthquake here occurred on 15 May 2015 with magnitude 6.0 with depth 150 km.

15. The Jakarta zone gets its name from the capital city of Indonesia. Most of the earthquakes here are at ~300 km depth. The largest earthquake occurred in this zone was on 8 August 2007 with magnitude 7.5 at depth 280 km.

Generally speaking, we can classify the seismogenic zones based on their contribution to hazard in Sumatra into three types: high, moderate and low. The zones contributing to high hazard are Aceh, Semangko, Krakatau, Meulaboh, Padang, Nias, Mentawai; the zones contributing moderate hazard are Lokop, Inter-plate, Medan, Palembang; the zones contributing low hazard are Java Sea, NSR, Sunda Trench, Jakarta.

The definition and characterization of the seismogenic zones are complicated and not an easy process to study them and furthermore need to incorporate all available information for accurate and precise demarcation. The details of focal mechanisms used for the definition of the seismogenic zones in this chapter are presented in Table 2.3 and the corresponding beach ball is shown in Figure 2.11. Accordingly, we need a comprehensive study to define an optimized seismogenic zonation by integrating all information from different disciplines.
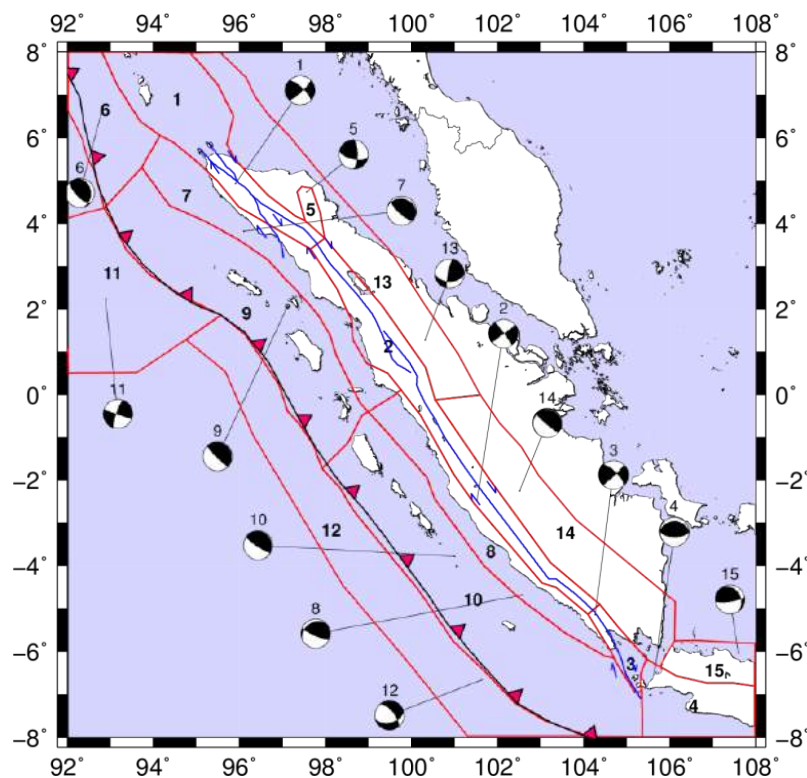

Figure 2.11. Selected focal mechanisms for each seismogenic zone.

Table 2.3. Focal mechanisms definition for the seismogenic zones for each seismogenic zones

Poly. index	Strike (º)	Dip (º)	Rake (º)	Depth (km)	Related event date	M max	Description	name
1	313	72	168	12	2013-01-21	6.1	Spreading strike slip fault from Aceh to Andaman Tail Sumatra Sumatra Fault	Aceh zone
2	324	87	179	9	2009-10-01	6.5	Long Great Sumatra Fault	Semangko zone
3	315	71	176	16.2	1994-02-15	6.8	Head Sumatra Sumatra Fault	Krakatau zone
4	270	29	89	38	2000-10-25	6.7	Java Subduction	Jawa Sea Zone
5	1	68	150	15	2003-09-13	5.2	Branching Sumatra Fault to Lokop	Lokop Zone
6	351	27	121	13.6	2004-12-26	7.2	North Sumatra Ridge zone	NSR zone
7	284	21	63	45	2010-05-09	7.2	Northern intermediate subduction zone	Meulaboh Zone
8	236	23	34	36	2001-02-13	7	Southern intermediate subduction zone	Padang zone
9	325	7	100	30	2005-03-28	8.2	Northern shallow subduction zone	Nias zone
10	328	9	114	24.4	2007-09-12	8.5	Southern shallow subduction zone	Mentawai zone
11	199	80	3	25	2012-04-11	8.6	Inter-plate strike slip ridge	Inter-plate zone
12	321	64	313	7	1982-11-11	6.2	Sunda Trench	Sunda Trench zone
13	191	80	46	211	1999-11-11	6.1	Northern deep subduction zone	Medan zone
14	291	7	71	217.1	2002-06-16	5.7	Southern deep subduction zone	Palembang zone
15	330	30	155	304.8	2007-08-08	7.5	Deep java subduction zone	Jakarta zone

3. Enhanced Source Definition

3.1 Original Version of Source Definition Algorithm

NDSHA can provide strong ground motion synthetic seismograms based on a realistic physical simulation by elaborating the available seismogenic zones and structural models taken from the geological and geophysical data. Surely we have to play with the varied computational time for the calculation. For instance, after the compilation and selection of the seismic catalogs in previous chapter, we consider 13317 events. In the seismicity plot, there are several events within the same cell area (grid). Thus, we need to decide the source definition (only a single source event) of which event is representative for the given grid cell. The first part in definition of seismic sources is the handling of the seismicity data as shown in Figure 3.1. Basically, what is needed is an evenly spaced distribution of the maximum magnitude over the territory, but the data available from the earthquake catalogs are widely scattered. Furthermore, the earthquake catalogs are both incomplete and contaminated with errors, so a smoothed distribution is preferable (Panza et al., 1990).
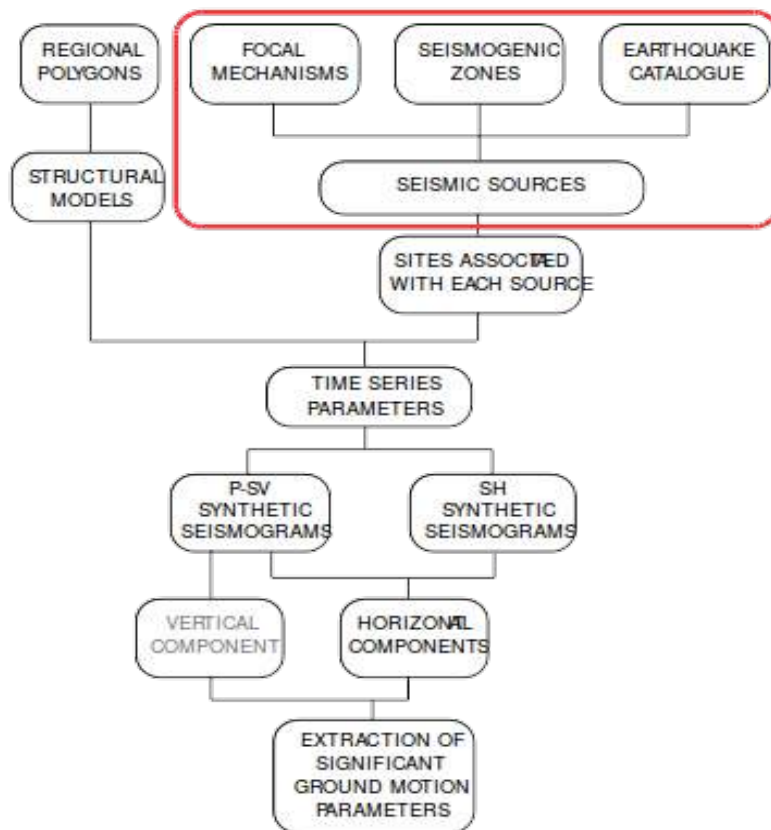

Figure 3.1. Red box is source definition procedure from full flow-chart of the deterministic procedure for seismic hazard assessment at regional scale (Panza et al., 1990).

The smoothing procedure is shown in Figure 3.2. The punctual distribution of the epicenters given in Figure 3.2a is discretized into cells (Figure 3.2b), and the maximum magnitude of the events pertinent to each cell is retained. In the case where the earthquake catalog contains different estimates of magnitudes (e.g., M_b, M_s, or M from the macroseismic epicentral intensity, I_0), the maximum among them is considered. It is then convenient to represent the data graphically, and the symbols are associated with the magnitude ranges (Figure 3.2c). In most cases, the smoothing obtained by considering just the discretized cells is not enough. A centered smoothing window is then considered so that the earthquake magnitudes are analyzed not only in the central cell but also in the neighboring ones. The idea of a constant magnitude within each seismogenic area (choosing the maximum available value) has been shown to be a poor choice, since for the larger seismogenic areas, it leads to an overestimation of the seismicity. Three possible smoothing windows are shown in Figure 3.2d.
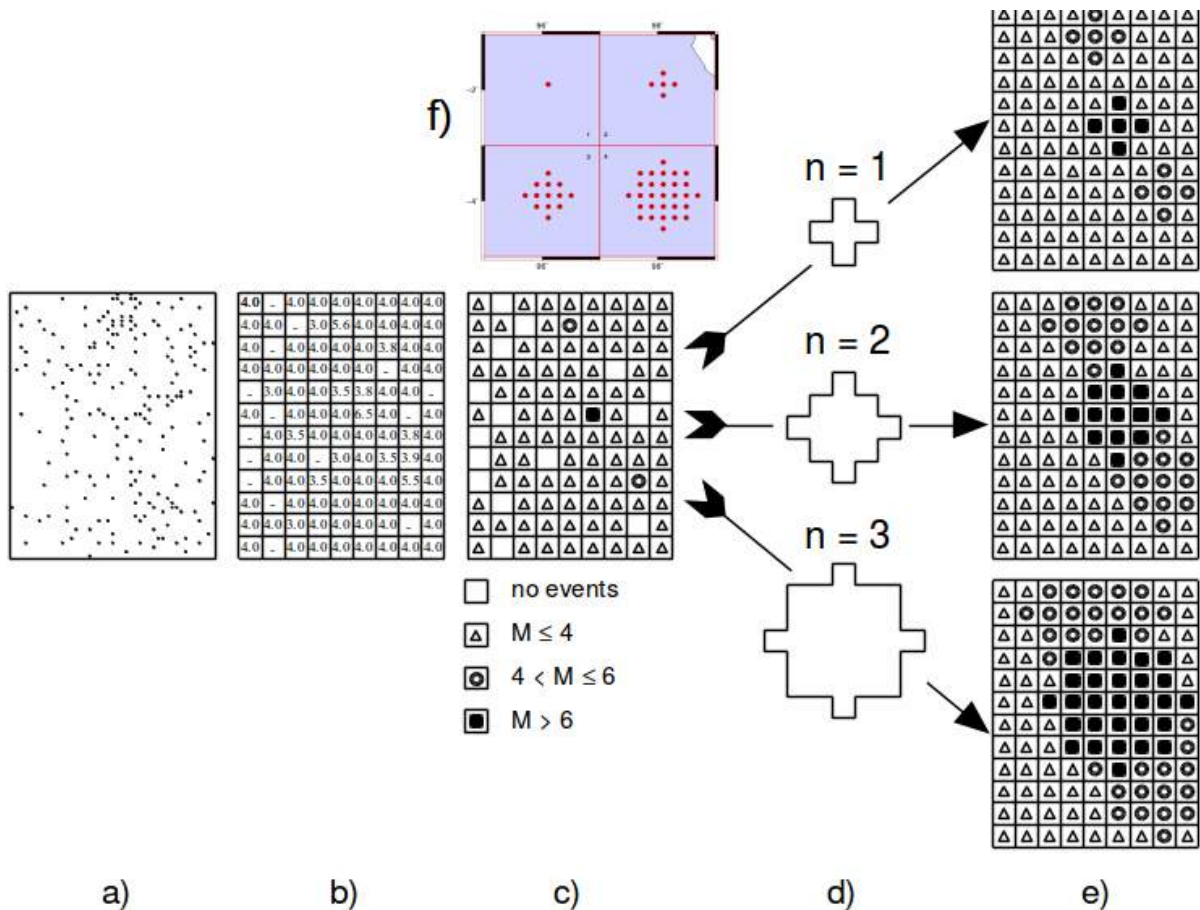

Figure 3.2. Discretization and smoothing of seismicity. (a) Distribution of epicenters; (b) definition of cells and choice of the maximum magnitude; (c) graphic representation; (d) smoothing windows of radius n=1, n=2, n=3; (e) smoothed distribution of magnitude.(Panza et al., 1990) and (f) updated smoothing version result.

Their radius is expressed in terms of the number of cells n. In the example, the values n=1, n=2 and n=3 are considered. By applying those windows to the distribution in Figure 3.2c, the results of Figure 3.2e are obtained. At a first glance, it appears that the distribution of the maximum magnitude given by the window with n=3 is quite exaggerated with respect to the starting data of Figure 3.2c. Its intersection with a hypothetic seismogenic area (shown in Figure 3.2a) gives quite a reasonable distribution (Figure 3.2b), which allows us to account for errors in the location of the source and for its extension in space. The smoothing corresponding to radius n=3 (smoothing 1) is chosen to produce the deterministic maps of hazard.

The proposed smoothing procedure is applied to the compiled earthquake catalog and the seismogenic zone (see Chapter 2: Figure 2.7-right and Figure 2.9), where the whole territory is discretized with a grid size (0.2°X 0.2°). The map shown in Figure 3.3 is the result of the application of the original version of the source definition procedure. The result also shows some limitations of the original procedure, which is not adequate for the Sumatra seismogenic zone, and the proposed improvement will be discussed in this chapter.
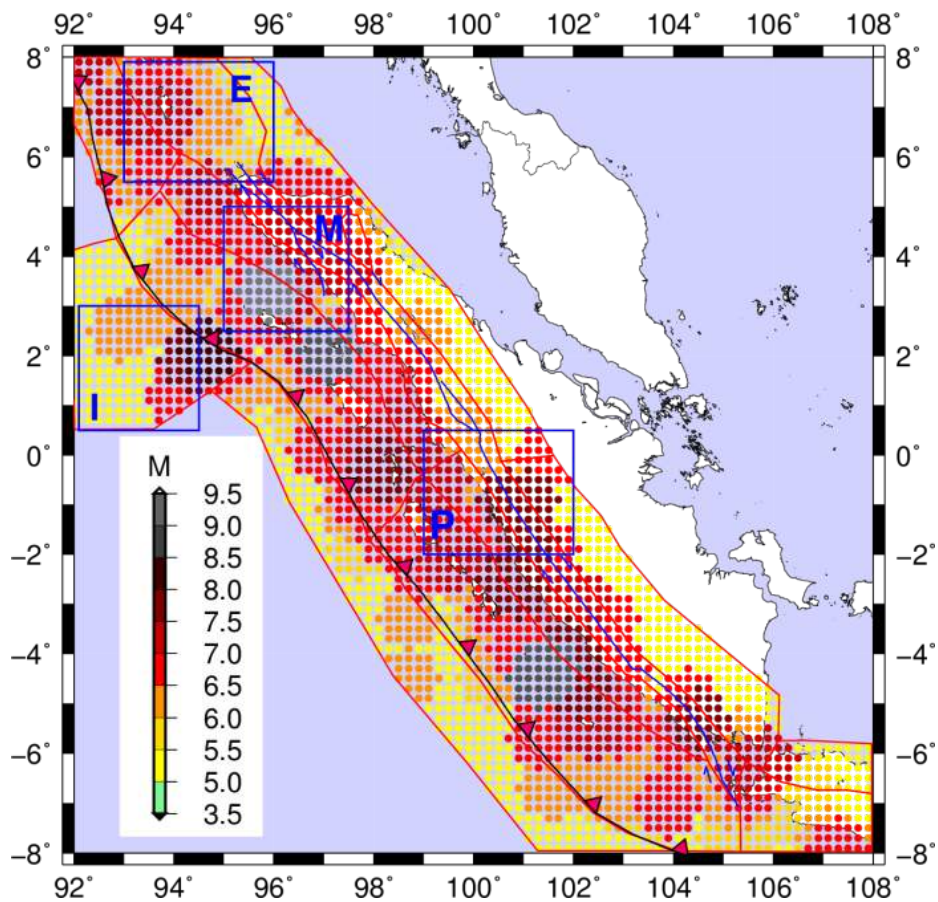

Figure 3.3. Source definition generated by the original version.

3.2 Enhanced Magnitude Smoothing Algorithm

Due to the complexity and variety of the seismogenic zones in Sumatra, there is a need for an advanced smoothing procedure, which has been developed from the original version. In the original version, it is only possible to set the characteristic of smoothing globally "entire zones" in `makehaz.par,` the main configuration file.

```
Parameters for program makehaz                          (v0004)
. . . . .
-------------------------------------------------------------
SOURCE DEFINITION
-------------------------------------------------------------
5.0                Min magnitude associated with the run
0  99              Min and maximum magnitude taken from catalogues
1000 2009          First and last year in catalogue    (years)
  .2               Cell size                            (degrees)
  3                Smoothing radius                     (cells)
  0                Min. events for smooth               (count)
  0  50            Min and max depth                    (km)
0                  Source depth (sdepth)     (0=sut,999=auto,x=km)
-------------------------------------------------------------
```

Listing 3.1. The part of lines of `makehaz.par` for settings the smoothing procedure for entire territory

The parameters should be put strictly in order; this means it is not acceptable to insert additional comment lines, unless after adding numbers of spaces of value in some line as show in listing 3.1. In order to make the setting of the seismogenic zone more flexible, we can no longer use a rigid format for the machine-oriented interface (machine friendly). Then, we have to start using a flexible format for the human-oriented interface (user friendly) instead of a fixed and rigid format read only by a computer program. The new format should have high flexibility to adding new lines or command lines, but should not follow a strict order; also it is possible to insert updated parameters and to update the version of software without introducing any new standard format for a new version.

In order to make a user friendly configuration file format, we also should tell the computer how to distinguish and understand each line in the file. Therefore, we use three techniques of recognition: in order, tag notation, and extension of the file. This technique could be integrated without affecting the core computer program. We use a familiar symbol for making commands (in this case, we use symbol # or !, as a familiar symbol in Bash and Fortran).

For the handling of the earthquake catalogs, the original version uses the configuration file `cells.par,` and the updated version also uses a single configuration file namely `eqc4select.par` as discussed in the previous chapter. On the other hand, for the handling of the smoothing procedure, the original version needs only one configuration `makehaz.par` but the

updated version needs two configuration files: `eqc4smooth.par` and `namejob.pas` as show in Listing 3.2.

```
File eqc4smooth.par
#collection of file and parameter needed for smoothing
test
dummy.pos
dummy.fps
dummy.pas
dummy.eqc
dummy.dph
frame 95 99 -5 -1


File dummy.pas


#tag zone radius  divsel  slope group minRun minCare maxCap   sstrike   sdip sdepth dcare

SUZ   0   3       0.1     0     0      0       5       9        0         0   20     50
SMO   1   4
SMO   2   2
CES   3           0.2
CES   4   4       0.2


File : dummy.eqc.csv
year,mm,dd, second  , lat  ,  long  , mag, depth, note
2000,01,01,     0.00, -2.00,    96.0, 7.0,   5.0, 001
2000,01,01,     0.00, -2.00,    98.0, 7.0,   5.0, 001
2000,01,01,     0.00, -4.00,    96.0, 7.0,   5.0, 001
2000,01,01,     0.00, -4.00,    98.0, 7.0,   5.0, 001
```

Listing 3.2. The configuration file for updated version smoothing procedure file `eqc4smooth.par`, individual control for each seismogenic zones file `dummy.pas`, and the earthquake catalog file `dummy.eqc.csv` to produce dummy test map figure 3.3.

In: *.eqc *.poc makehaz.par	in: *.eqc *.poc default.cat
ecell.out	**eqc4select.exe** → selected.eqc

ecell.out   → *.cel
in:makehaz.par
  esmooth.out → *.gri
in: *.pos
  einscat.out → *.mag
in: *.pos *.fps
  eselmec.out → *.mec
  emecmed.out → *.sut (final)
	in: *.pos *.fps *.pas
	in: eqc4smooth.par
	  eqc4smooth.exe → ***.sut** (final)

Listing 3.3: List of programs to produce source file *.sut: (left) the original version with 5 program (right) the updated version with two programs.

29

There are several steps to get the final source definition as shown in Figure 3.2. The original version uses 5 separated programs for each step as shown in Listing 3.3 (left), but the updated version reduces these steps into a compact single program namely `eqc4smooth.exe,` see Figure 3.4.
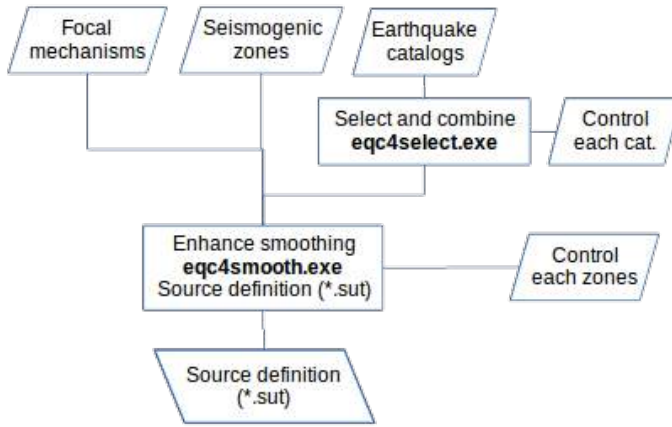

Figure 3.4. Updated version of enhancement source definition procedure and the location of two programs `eqc4select.exe` and `eqc4smooth.exe`.

There are two ways for executing this program: without or with the passing parameter. Without the passing parameter will read the default configuration file `eqc4smooth.par`, and with the passing parameter, there is the possibility to read the other file names, e.g.:

```
eqc4smooth.exe
eqc4smooth.exe dummy_par.par
```

The final output of the program is the generation of the source definition file `test.sut.` This file becomes the input in the next stage of the NDSHA [sites associated with each source] as shown in Figure 3.1. However, the updated version remains to produce the intermediate files (`*.cel,` `*.ung, *.unm, *.zs.uni`) to keep it compatible with the original version.
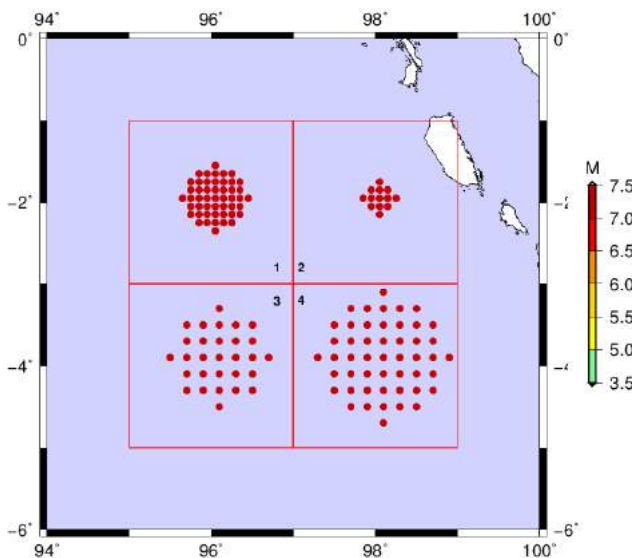
Figure 3.5. Source definition (`test.sut`) described in the configuration file (listing 3.2).
zone 1 with setting *radius*=4,*divsel*=0.1º
zone 2 with setting *radius*=2,*divsel*=0.1º
zone 3 with setting *radius*=3,*divsel*=0.2º
zone 4 with setting *radius*=4,*divsel*=0.2º

In Listing 3.2, the configuration file `eqc4smooth.par` declares the project name `test` and read the parameter of smoothing (`*.pas`) from the file `dummy.pas`. The first line is used as a comment line; this is a good way to always keep the first line for a comment line which can be used to recognize the file (type or version) and is also important for QGIS as a column definition. After the comment line, the program gives the possibility for setting the default parameters by putting the SUZ tag with polygon number 0. Without this line, the default parameters value will be provided by the software.

#tag	zone	radius	divsel	slope	group	minRun	minCare	maxCap	sstrike	sdip	sdepth	dcare
SUZ	0	3	0.1	0	0	0	5	9	0	0	20	50

The third line (`SMO 1 4`) and the fourth line (`SMO 2 2`) with tag SMO will set the radius smoothing 4, and 2 cells for zone 1 and 2 sequentially. In addition, the size of the source cell *divsel*=0.1º is taken from the default value 3, which is defined in the second line as shown above. Moreover, the fifth line (`CES 3 0.2`) with the CES tag will set the cell size 0.2º but the smoothing radius value is the default one. The last line (`CES 4 4 0.2`) gives the possibility to set the parameters, i.e. the smoothing radius, 4 cells, and the size of cell 0.2º in a single line. This flexibility of adopting the individual smoothing parameters for each zone could help in appropriately addressing the uncertainty for each zone based upon the amount of available knowledge about the earthquake parameters and the other zone definition-based characters. The Figure 3.5 shows that by adopting those different parameters will lead to a different source definition (each polygon contains single event). The detailed description of the proposed format for reading the smoothing parameters is showed in Table 3.1. Each line begins by a tag name column (e.g. SUZ, CES, SMO, MIG, ELP, SDP) and the second column is the given number of each zone (polygon). The separator of the field in the configuration file is made using the space bar character only as using a tab character is not allowed.

The smoothing parameters can be categorized into: magnitude smoothing, magnitude limitation, ellipticity, and depth enhancement, see Table 3.1. The first parameter for the magnitude smoothing is the radius. The choice of the smoothing radius and its units being used (cell or degree) is based upon the evaluation of the analyst. Using a smoothing radius unit in degree could be more compatible with a real map and could maintain the real size of the smoothing area even when the cell size is changing. The program will recognize the distance in degrees; the negative value means that the unit is in degrees (e.g. -0.6 mean 0.6º). For example, the zones 1, 2, 3, 4 have radius = 3, 3, -0.6, -0.6 sequentially. Therefore, Zone 1 and 2 have a radius 3 cell, whereas Zone 3 and 4 have radius 0.6º geographically. When applying a different cell size, *divsel* = 0.1, 0.2, 0.1, 0.2 for zones no 1, 2, 3, 4 respectively, the zones with radius defined in degrees unit (3 and 4) will keep the same

31

geographical radius even for a different cell size, as shown in Figure 3.7 (left). The advantages of using the proposed smoothing parameters for each zone will reduce the source resolution for the far source zones and increase the source resolution for the near source zones relative to the site of interest. This feature should solve the problem in Figure 3.3 area box I, where the inter-plate zone is a far source zone.

Table 3.1. Tags rule for controlling parameters of smoothing process for each seismogenic zone.

tag	zone	Magnitude Smoothing	Magnitude Limitation	Ellipticity	Depth
SUZ	N	Radius Divsel slope group	minRun minCare maxCap	sstrike sdip	sdepth dcare
CES	N	Radius Divsel			
CES	N	Divsel			
SMO	N	Radius Divsel slope group			
SMO	N	Radius slope group			
SMO	N	Radius slope			
SMO	N	Radius			
MIG	N		minRun minCare maxCap		
MIG	N		minRun minCare		
MIG	N		minRun		
ELP	N			sstrike sdip	
SDP	N				sdepth dcare
SDP	N				sdepth

One of the steps in the original smoothing version, from Figure 3.2c to 3.2e, does not consider the polygon zones. The seismogenic zones only take into account the focal mechanism and are used to remove the source definition outside the seismogenic zones. In the updated version, this step considers the polygon zones information. There are several features that can be enhanced by considering the polygon zones during this step. One of the enhanced features in the updated version is the zone grouping, where the smoothed cells cannot penetrate into a different group number, see Figure 3.7 (right) between zone 1 and 2. The special group (number 0) will be affected from all the groups as shown in Figure 3.8. The grouping feature will create a partitioning effect for each different group and transparent effect for the same group. This effect is important to solve the problem shown in the box (P) (Figure 3.3) in which the events from the zones in the strike slip Sumatra fault system do not reach the subduction zones as shown in Figure 3.6c and 3.6d.

The smoothing algorithm from the original version provides the same magnitude value for the whole smoothing radius as showed in Figure 3.3 box P. Applying this algorithm to Sumatra will produce the overestimation of the ground motion parameters because the magnitude 9 smoothing earthquake is very close to the land as shown in Figure 3.9 (left). Therefore, there is a need to enhance the smoothing algorithm by decreasing the magnitude with the distance by adopting a slope parameter value based upon the assigned magnitude as show in Figure 3.9 (right).

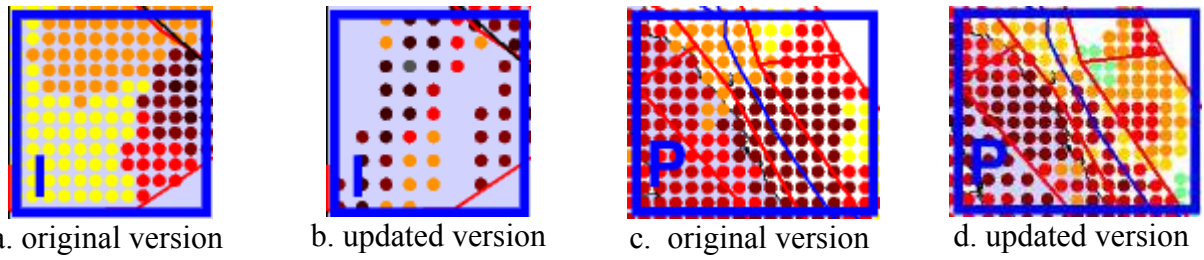| a. original version | b. updated version | c. original version | d. updated version |

Figure 3.6. The comparison between original version (problem taken from Figure 3.3) and updated version. a. and b. for resolution issue. c. and d. for partitioning issue.
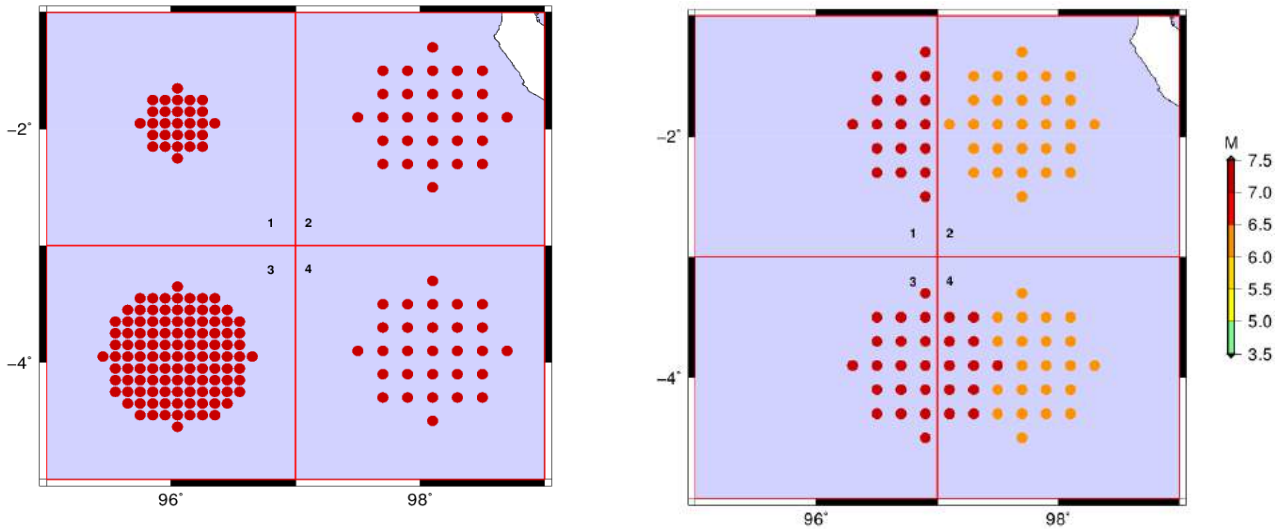

Figure 3.7 (left) The smoothing radius in degree will preserve the geographical size of smoothing area where as radius in cells cannot keep it. {radius =3, 3, -0.6, -0.6, *divsel*=0.1, 0.2, 0.1, 0.2} (right) the zones can be grouping where the smoothing effect will be transfer if the same group. {group = 0, 1, 0, 0}
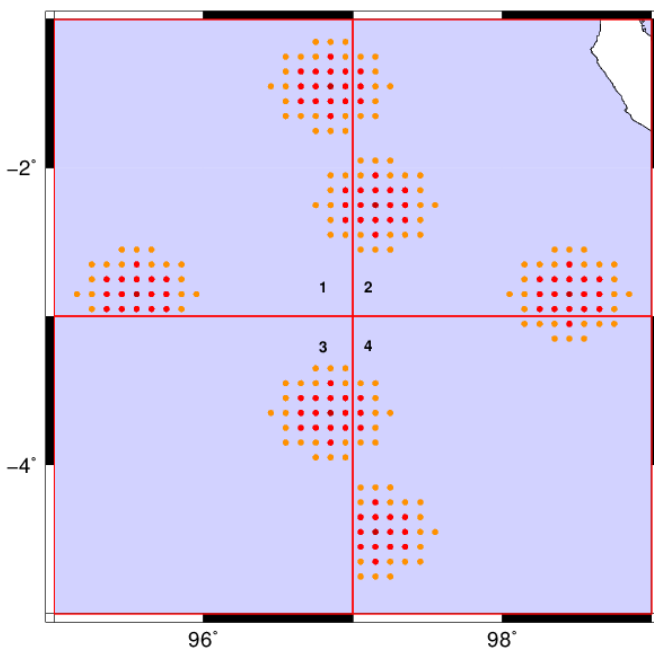
Figure 3.8 Dummy zone for detailed explanation the grouping effect (portioning and transparent). The zone 1, 2, 3, 4 has group number = 1, 1, 4, 0 sequentially.

Same group number (polygon 1 and 2 with number 1) will affected each other (transparent).

Different group number (polygon 1 and 3 with number 1 and 4) will not affected each other (partitioning).

Special group (number 0) will affected from all groups number as shown in polygon 4.
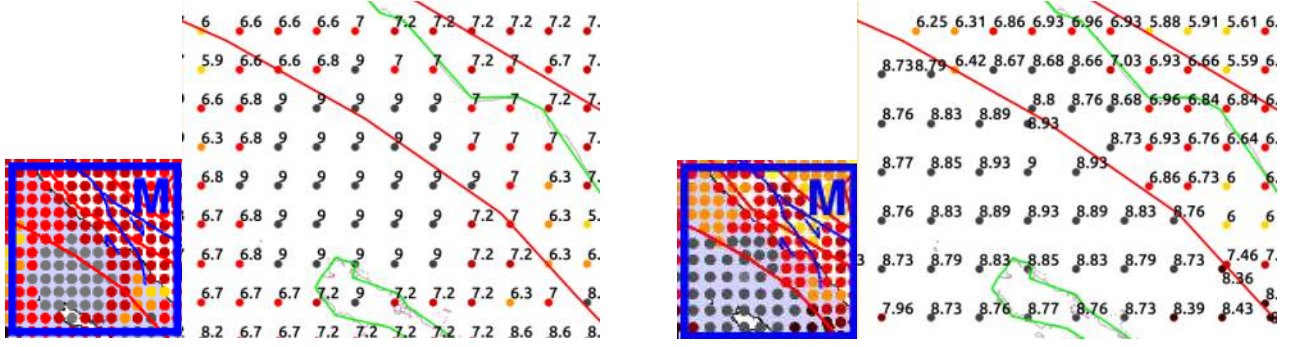
Figure 3.9. Magnitude of source definition from original version (right) and (left) updated version.

The magnitude smoothing algorithm requires the introduction of the slope parameter. The slope value will determine how rapidly the magnitude decreases with respect to the distance from the epicenter of the event. If the slope parameter is 0, it will be similar to the original version. Figure 3.10 shows the smoothing algorithm that uses a simple linear approximation to determine the smoothing magnitude:

$$M_{smoothing} = M_{max} - distance * slope \qquad (3.2)$$

This enhanced magnitude smoothing process is implemented successfully in the updated version as shown in Figure 3.11 for a dummy test.
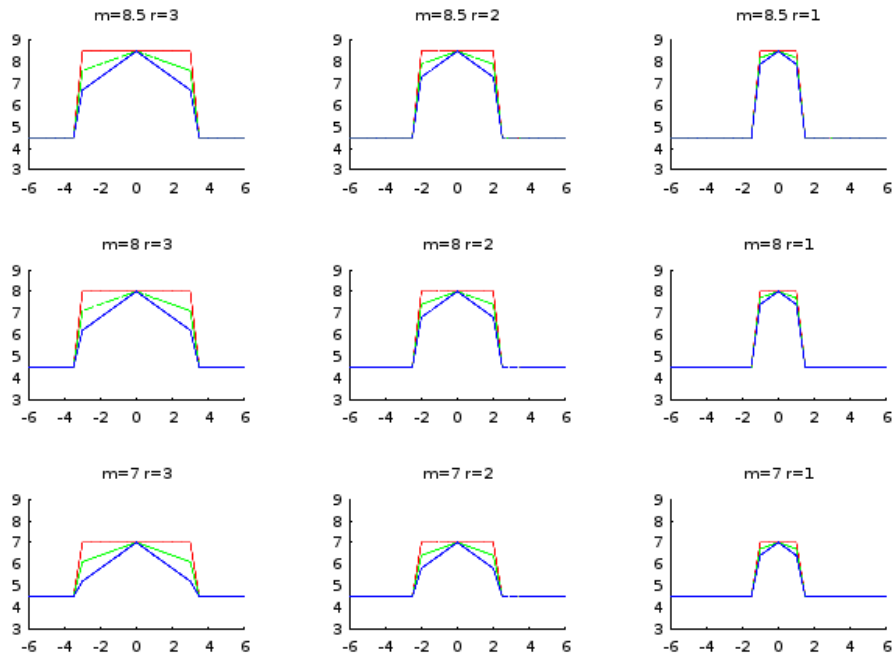
Figure 3.10. Different slope parameters, red line slope=0, green=0.3, blue=0.6. Slope with 0 slope parameter is mean original version. (Vertical axis magnitude and horizontal axis distance from center event). Minimum run magnitude *minRun*=4.5.
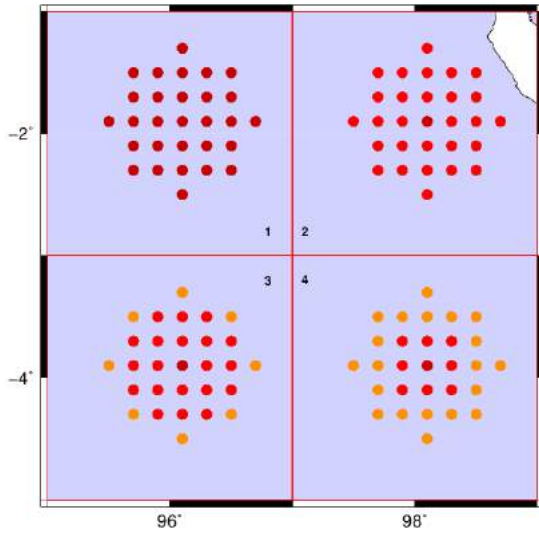
Figure 3.11. Effect of different slope values (slope=0, 0.5, 1, 1.5) for zones 1, 2, 3, 4 with fixes radius of 3 cells. The zone 1 has slope=0 the magnitude for all smoothing point same magnitude 7.5 similar with original version. In zone 2, 3, 4 the magnitude 7.5 only in the center other point will decrease according distance and slope parameter.

In reality the smoothing process is not dealing with several earthquakes like the dummy test. In the case of Sumatra, we deal with a big number of the selected earthquakes (13317 in this study). Therefore, we need to control the limitation of the data involved in the smoothing process and to set the lower and upper limit for each zone. For information, the program `eqc4select.exe` also performs the limitation procedure (minimum and maximum magnitude criteria) for each catalog as mentioned in Chapter 2. Three parameters, *minRun, minCare, maxCap* are introduced, which are the minimum magnitude to be adopted for each cell, the minimum magnitude will be adopted from the catalog, and the maximum magnitude will be defined for each cell, respectively (see Figure 3.12).

The parameter *maxCap* is the maximum magnitude and will be defined for each zone. If the magnitude of the events inside the seismic zones is above the maxCap, it will be terminated to maxCap. There are two main reasons to introduce this parameter. The first reason is that we are less confident about the MCE value from the geological study in a specific zone. Other limitations come from the point source consideration for the big magnitude sources for which the extended source representation should be considered. In the case of Sumatra, the MCE for the Semangko zone is obtained by Natawijaya (2009) with magnitude about 7.8 based on the surface geology and historical studies, but if it was based on the instrumental record, it is more accurate to put *maxCap*=7.5. On the other hand, the Sunda subduction zone can generate the mega earthquake (Sumatra-Andaman 2004) with M~8.9-9.3. Because of the limitation of the point source approximation for the big magnitude events, we terminate the maximum earthquake magnitude to 9.0 even if it was more in the catalog by setting *maxCap*=9.
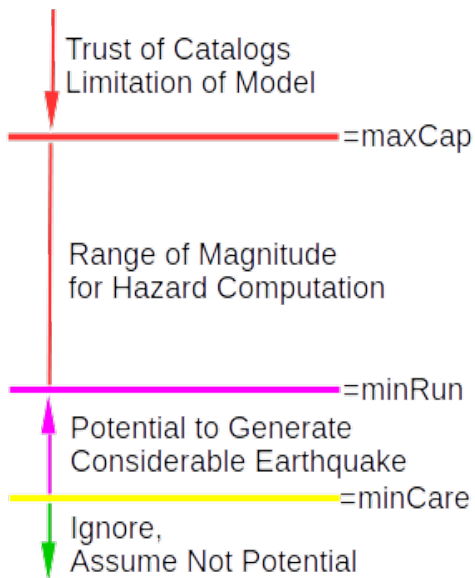
Figure 3.12. Diagrammatic explanation of the parameters for magnitude limitation in the source smoothing algorithm for each seismogenic zones.

maxCap= maximum cap (terminated) magnitude will define for cells

minRun= minimum magnitude will run (set) for cells

minCare= minimum magnitude will care (take) from the catalogs

Parameter *minRun* is the minimum magnitude that will be adopted for the cells. This value is based on our knowledge about the minimum magnitude for the specific seismogenic zone based on the statistical analysis of seismicity, seismotectonic, and geodynamic of the zone. Adopting *minRun*=0 will be useful for the rare earthquake, and those that look like a small cluster, for example, the deep Sumatra subduction zone (polygon no 13 and 14). Adopting *minRun*=0 is useful for the seismogenic zones that have the strike-dip mechanism where there are no additional details about the exact location of the faults or their makeup, but we just decide to increase the area of the seismogenic zones, such as the Aceh zone and the inter-plate zone. For the areas that we trust have a certain minimum magnitude, we can set the value, for example, for the Sumatra fault (Semangko and Krakatau zone) we set *minRun*=5.5. The Sunda subduction zone has a greater minimum magnitude value; thus, we set *minRun*=6 for the intermediate depth zones (Meulaboh and Padang) and *minRun*=6.8 for the shallow depth subduction zones (Nias and Mentawai).

As mentioned at the beginning paragraph of this chapter, the purpose of the smoothing process is to deal with the uncertainties associated with the parameters in the earthquake catalogs. Using smoothing regardless the azimuthal distribution (circular smoothing) is a good option, if there is no information about the preferred orientations. However in some cases, we know the Sumatra strike-slip fault generates an earthquake along a narrow zone. Therefore, we enhanced the geometrical smoothing algorithm by introducing the ellipsoid factor parameters *sstrike* and *sdip*, see Figure 3.13. The choice of the name *sstrike* (smooth strike) and *sdip* (smooth dip) is due to the fact that the value is mostly similar to those of the geological strike and dip and use the same convention as Aki and Richards (1980). The major axis is following the strike line, and the minor axis is parallel to the dip direction, see Figure 3.13.
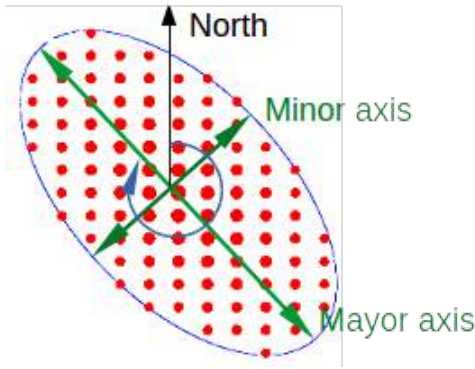
Figure 3.13. Enhanced geometrical smoothing procedure. The picture shows the example with parameter radius=8 cells; slopes=1; *sdips*=60; *sstrikes*=328. The length of the mayor axis is equal to the radius and the minor axis is given by the formula

$$tan(sdips) = \frac{mayorAxis}{minorAxis}$$

The implementation of the ellipsoid smoothing feature is not trivial, after some effort we successfully developed this algorithm, and Figure 3.14 shows the dummy test for several variations of *sstrike* and *sdip*. Figure 3.14 (left) shows that a different *sdip* with a constant *sstrike*=0 will produce an ellipsoid easily, but when the *sstrike* is not zero for a different *sdip,* an advanced algorithm is needed. Nevertheless, the updated version is successfully doing this job as shown in Figure 3.14 (right).
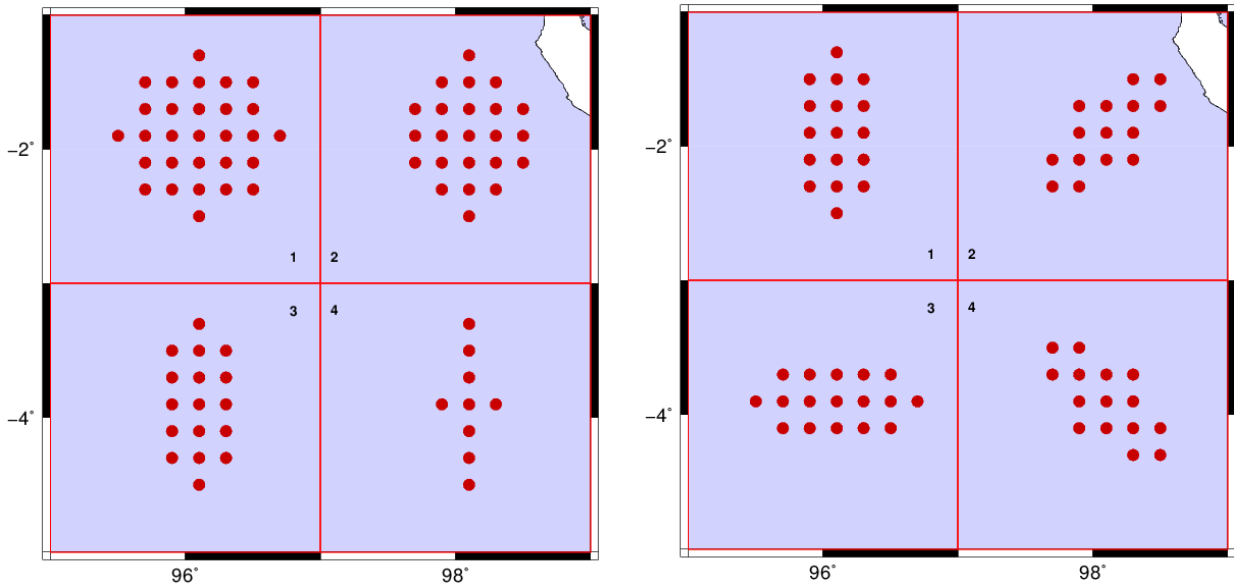
Figure 3.14. Ellipsoid smoothing effect at radius=3 for (left) *sstrike*=0 with various *sdip*= 0 , 30, 60, 70. (right) At *sdip*=60 with various *sstrike*=0, 45, 90,315.

For the subduction zones where the dip value is smaller than 60°, the ellipsoid smoothing is not really necessary because the smoothing geometry remains close to the circular geometry. But for the strike slip with the dip greater than 60°, the ellipsoid smoothing should be considered because the smoothing geometry is changing significantly, see Figure 3.14. Therefore, the application of this procedure is important for the Aceh zone and the inter-plate zone, where the strike slip fault could generate earthquakes in a narrow zone area. The updated smoothing version can carry out this job successfully, and the comparison with the original version is shown in Figure 3.15.
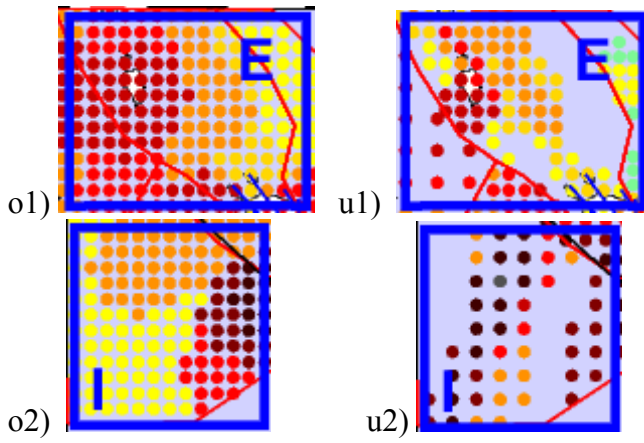
o1) u1)

o2) u2)

Figure 3.15. o1, o2) Original version creates circular smoothing effect. u1, u2) Updated version produce create geometrical feature.

3.3. Enhanced Source Depth Definition

Beside the earthquake magnitude, the focal depth can greatly affect the estimated earthquake ground motion and peak ground motion parameters. In the original smoothing algorithm, the depth of the earthquake source is computed as a function of magnitude (10 km for M<7, 15 km for M≥7) (see Equation 3.1), but it is also possible to assign to each source an average depth determined from the analysis of the available catalogs. Keeping the focal depth fixed (for classes of magnitude) and shallow is important due to the large errors generally affecting the focal depth reported in the earthquake catalogs, and due to the fact that the strong ground motion is mainly controlled by shallow sources (Vaccari et al., 1990).

$$h = \begin{cases} 10km & , M < 7 \\ 15km & , 7 \leq M < 8 \\ 20km & , M \leq 8 \end{cases} \tag{3.1}$$

The original smoothing algorithm provides four options for determining the depth. The first option sets a fixed value of depth for all the polygons, but for the depths lower than 10km, the depth is set to 10. The second option, by putting 999, will determine the depth according to the magnitude following the tabulation (3.1). The third option makes it possible to read the depth from the focal mechanics file (`.fps`). With the fourth option, by putting 0, the program will read the source information including the focal depth from the given `*.sut` file. The last option will be used, if the original NDSHA version at the regional scale needs to read the source definition file generated by the updated smoothing program.

The option provided by the original smoothing version cannot be sufficient to handle the complexity of the Sumatra seismogenic zones. One of them, the focal depth of the subduction zone, increases from the trench zone through the forearc zone until the backarc zone as shown in Figure 3.16. The change in the focal depth depends on the location; therefore, we add a new feature in the

updated version to have the possibility to take the depth from the depth distribution file (`.dph`). The focal depth will be interpolated from the scattered depth distribution in format 3 column x(long) y(lat) d(km). With the updated smoothing program, it is possible to pick up the depth from the maximum earthquake in each cell in the region, see Table 3.2. We successfully implemented this features as show in Figure 3.17.

Table 3.2. Option for *sdepth* parameter and how to get depth information for each zone

Option	Explanation
0	set depth fix 10km (if lower than 10 will bring to 10km).
27	set depth to a given value 27km.
999 or c	depth as function of magnitude, see equation 3.1.
fps	depth is taken from .fps file (per polygon)
file.dph	depth is interpolate from depth distribution file.dph
d	take from depth of maximum magnitude in the cell
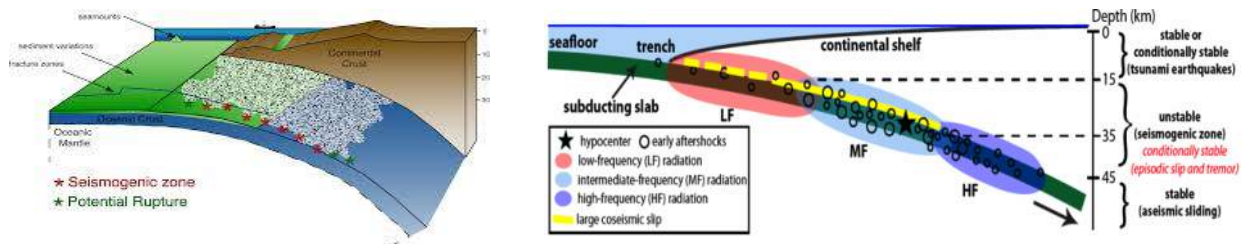
Figure 3.16. The depth of hypocenter is changing gradually following the slab plate interface at the subdution zone. http://faculty.smu.edu/hdeshon/research.html,
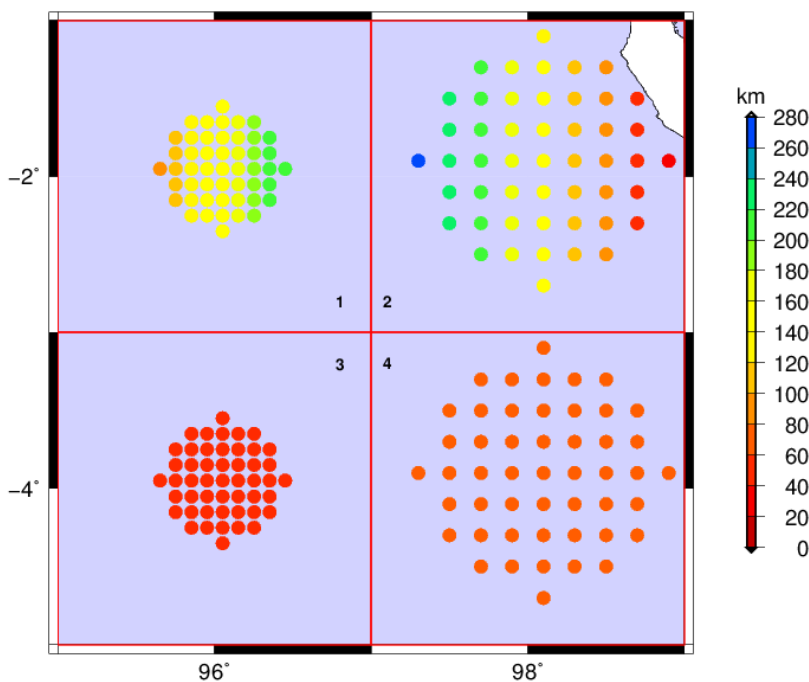Yao et al., 2013, http://staff.ustc.edu.cn/~hjyao/research.htm

Figure 3.17. Plot of the depth of the source, after smoothing process with parameter in each zone sequentially:
sdepth=dph, dph, fps, 60
divsel=0.1, 0.2, 0.1, 0.2
and radius=4 for all zones.

39

3.4 Application to the Sumatra Seismogenic Zones

The new features and control on the individual seismotectonic zone give us more pros and the flexibility in using the analyst's knowledge to set the parameters. The challenge does not only come from the increase of the number of the parameters for each zone but also from the very large number of the parameters in case many zones are used. In the case of the Sumatra seismogenic zones, there is a need to control 15 zones. Compared with the original version, that is extremely simple, we are able to control a few variables, such as radius, *divsel*, *minRun, minCare, maxCap, sdepth* for all of the zones. Therefore, we should have a good knowledge about the seismogenic zones before using the enhanced features from the updated smoothing procedure; otherwise, we can work with the original version by only adopting the default parameters being used in the original version, and this choice will certainly lead to very conservative results that can be considered as the upper bounds indicators.

The choice of these values is based upon the analyst's knowledge, which in turn is based on the available data. For example, from the instrumental catalog after 1960, the maximum magnitude is M7.0 in the Sumatra strike-slip, as show in Figure 3.18. Therefore, we do not really trust the MCE in the Sumatra fault that can be M7.8. In our opinion, the magnitude of 1943 earthquake ~7.8 is overestimated by geologists. The only point of weakness of using the analyst's expertise is the short time span of the existing catalogs, which is relatively to the geological time scale. We choose the value of *maxCup* to be equal to M7.5 to be conservative but without exaggerating the controlling magnitude. For the Sumatra subduction zone we freely set the value to the maximum *maxCup*=9.0.
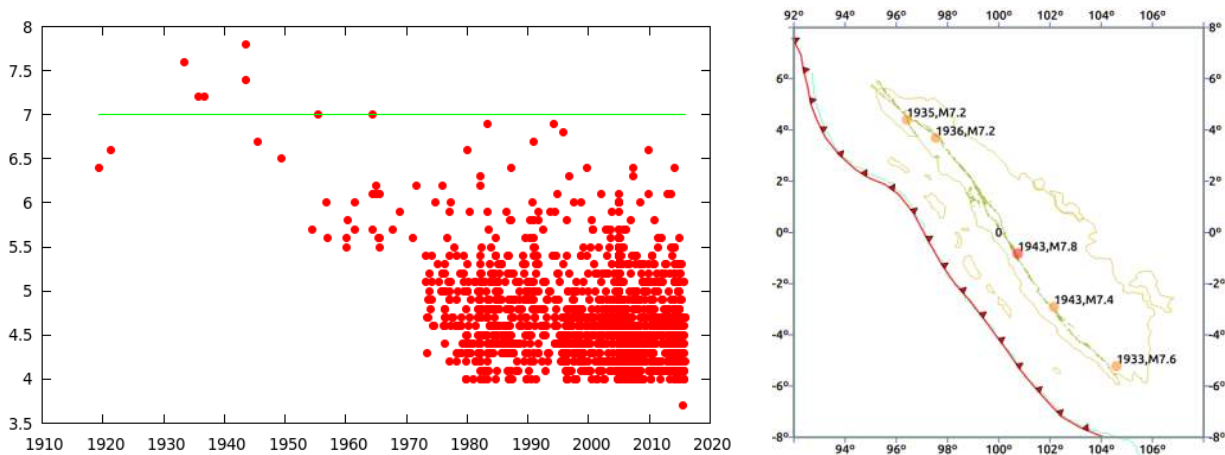

Figure 3.18. (left) the time domain distribution of earthquake along Sumatran fault zone. (right) the location of big earthquake along the fault.

The Sumatra fault is segmented into several relatively small segments as show in Figure 3.3 (left); each zone has its individual MCE; therefore, we prefer a small smoothing radius parameter (radius=2-3) for the Sumatra fault zones. On the other hand, the Sunda subduction zone is

characterized by the large segments as shown in Figure 3.3 (right) and the wide zone of an earthquake occurrence. Therefore, we prefer bigger smoothing radius parameter (radius=3 - 4) for the Sunda subduction zones.

The determination of the cell size (*divsel*) parameter is based on how sensitive the estimated hazard is to the adopted grid spaces. Generally, the near source zones are relatively more sensitive to the epicenter location than the far source ones. Therefore, we adopted a high grid resolution (*divsel*=0.15º - 0.2º) for the inland zones, e.g. Aceh, Semangko, and Lokop zones. We adopted a low grid resolution (*divsel*=0.3º - 0.4º) for the far source zones, e.g. the Java Sea zone, the inter-plate zone, and the NSR zone. The default value given by the program for the general case is *divsel*=0.2º.

The default value of the slope is 0.3, and for the subduction zones, intermediate zones (Meulaboh Zone and Padang zone), and deep zones (Medan and Palembang zone), we use the slope value equal to 0.6. For the intermediate zone, care should be taken by making the smoothing value not diffused into the land area. For the deep zones, we want to make the event dominant only in a small spot region. Actually, we need a lot of parametric studies to understand what the appropriate value of the slope feature is for our estimation.

The main motivation for developing the updated smoothing procedure is that because we find more problems in the Sumatra seismogenic zone which need the adoption of the partitioning effect, which prevents it from the penetration of the smoothing effect into the neighboring zones. There are two group zones that have the smoothing number not equal to zero. The first is the Sumatra fault zone system (Aceh, Semangko, Krakatau, and Lokop zone) because the faults generate earthquakes in narrow zones namely group=1. The Second is the deep subduction zones system (Medan zone and Palembang zone); these zones are not affected by the Sumatra subduction zones as group=2. Others groups of the zones we set to group=0.

The last new feature in the updated magnitude smoothing procedure is the ellipsoid smoothing which has two parameters *sstrike* and *sdip*. This feature adopted only for the Sumatra strike slip and interplate strike slip, both have a geological dip greater than 60º. The selected parameter values for each seismogenic zone are shown in Table 3.3.

Because of the Sumatra strike slip zone overlay in the Sunda subduction zone, we have to extract the strike-slip shallow earthquake from the deep Sunda subduction zone earthquake. The contribution of the shallow depth earthquakes to the hazard is relatively small. After plotting the depth with respect to the magnitude for each zone, we can recognize a clear separation in depth between more and less than about 50 km (except zone 1, see also Figure 3.23 polygon=1 for clear separation).

Table 3.3 gives information about the controlling parameters for the updated magnitude

smoothing process by `eqc4select.exe` program to pick up the maximum magnitude for each cell and the result is shown in Figure 3.20 (right). After picking up the maximum magnitude, the `eqc4select.exe` file makes smoothing with the neighbored cells by taking into account the seismogenic zones parameters for the final source definition, as shown in Figure 3.21 (right).

Tabel 3.3 Configurations file for updated smoothing algorithm process for Sumatra seismogenic zones

| tag	Zone	radius	divsel	slope	Group	minRun	minCare	maxCap	sstrike	sdip	sdepth	dcare	note
SUZ	0	2	0.2	0.3	0	5	5	9	0	0	fps	300	default
SUZ	1	2	0.2	0.3	1	0	5	7.5	313	67	20	50	Aceh zone
SUZ	2	3	0.2	0.3	1	5.5	5	7.5	324	67	20	50	Semangko zone
SUZ	3	2	0.2	0.3	1	5.5	5	7.5	0	0	d	50	Krakatau zone
SUZ	4	3	0.3	0.3	0	0	5	9	0	0	dph	300	Jawa Sea Zone
SUZ	5	2	0.15	0.3	1	5.2	5	7.5	0	0	d	50	Lokop Zone
SUZ	6	3	0.4	0.3	0	0	5	9	0	0	dph	300	NSR zone
SUZ	7	3	0.2	0.6	0	6	5	9	0	0	dph	150	Meulaboh Zone
SUZ	8	3	0.2	0.6	0	6	5	9	0	0	dph	150	Padang zone
SUZ	9	4	0.25	0.3	0	6.8	6	9	0	0	dph	100	Nias zone
SUZ	10	4	0.25	0.3	0	6.8	6	9	0	0	dph	100	Mentawai zone
SUZ	11	-1	0.3	0.3	0	0	6	9	199	72	fps	300	Inter-plate zone
SUZ	12	-1	0.3	0.3	0	0	6	9	0	0	fps	100	Sunda Trench zone
SUZ	13	3	0.18	0.6	2	0	4	9	0	0	d	300	Medan zone
SUZ	14	3	0.18	0.6	2	0	4	9	0	0	d	300	Palembang zone
SUZ	15	2	0.2	0.3	0	0	5	9	0	0	c	300	Jakarta zone
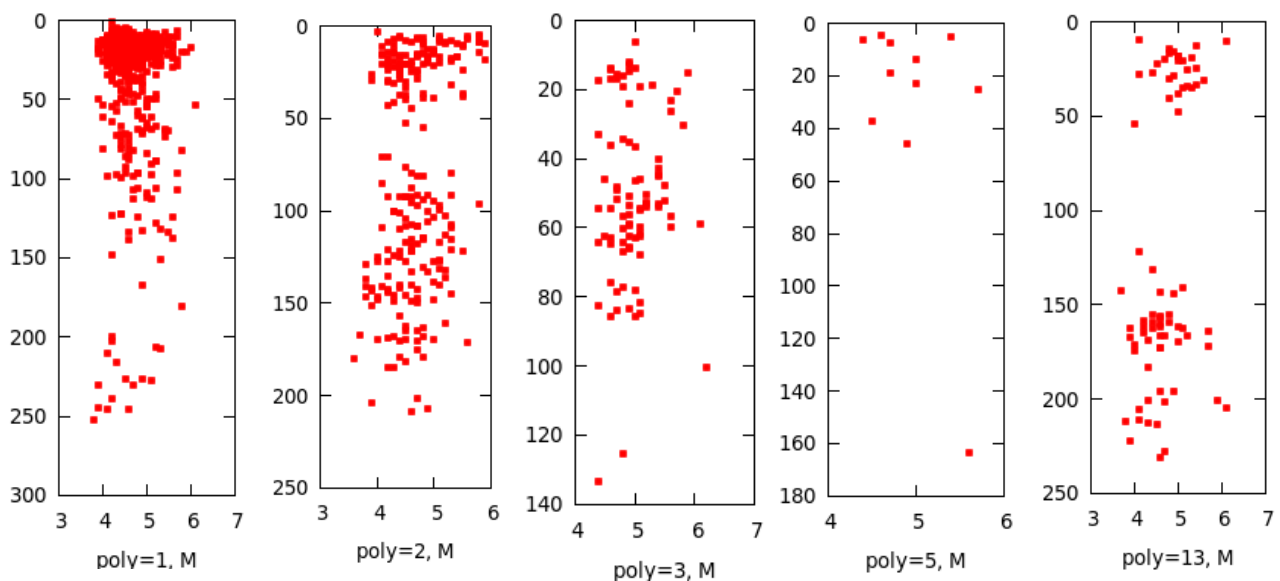
Figure 3.19. Depth distribution with respect to magnitude of earthquake for Sumatra strike slip seismogenic zones. Relocated hypocenters from Pesicek et al. (2010).
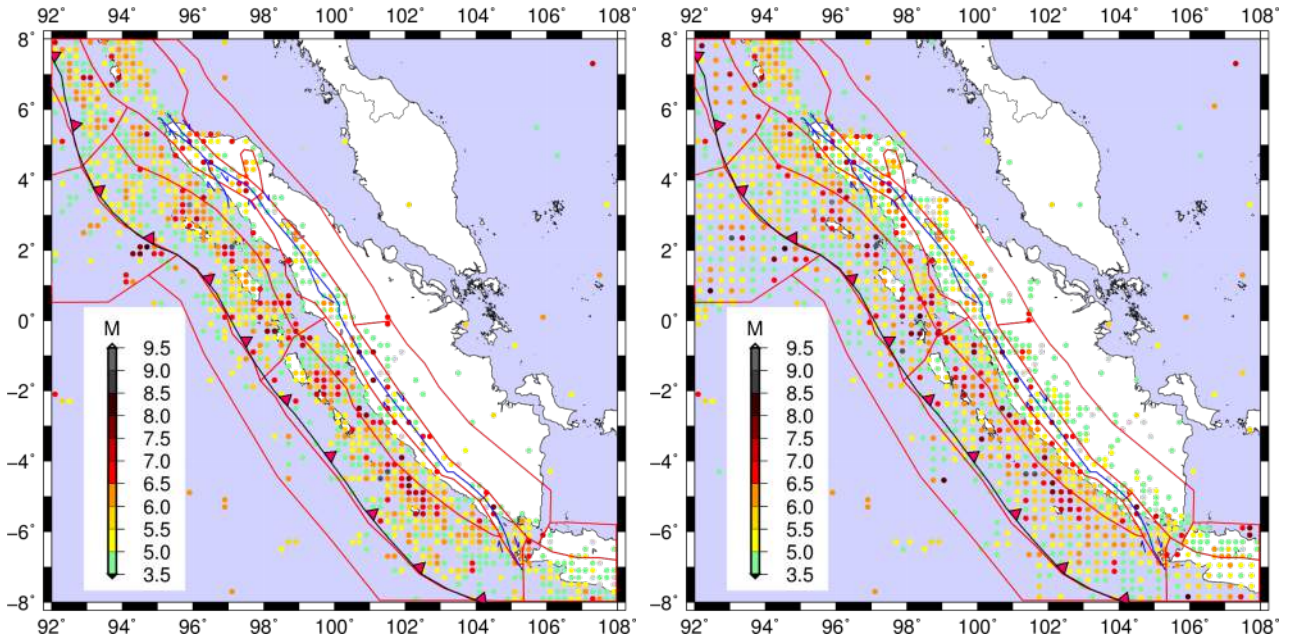
Figure 3.20. Picking up the max magnitude in each cell (before smoothing process) : (left) original algorithm (right) updated algorithm
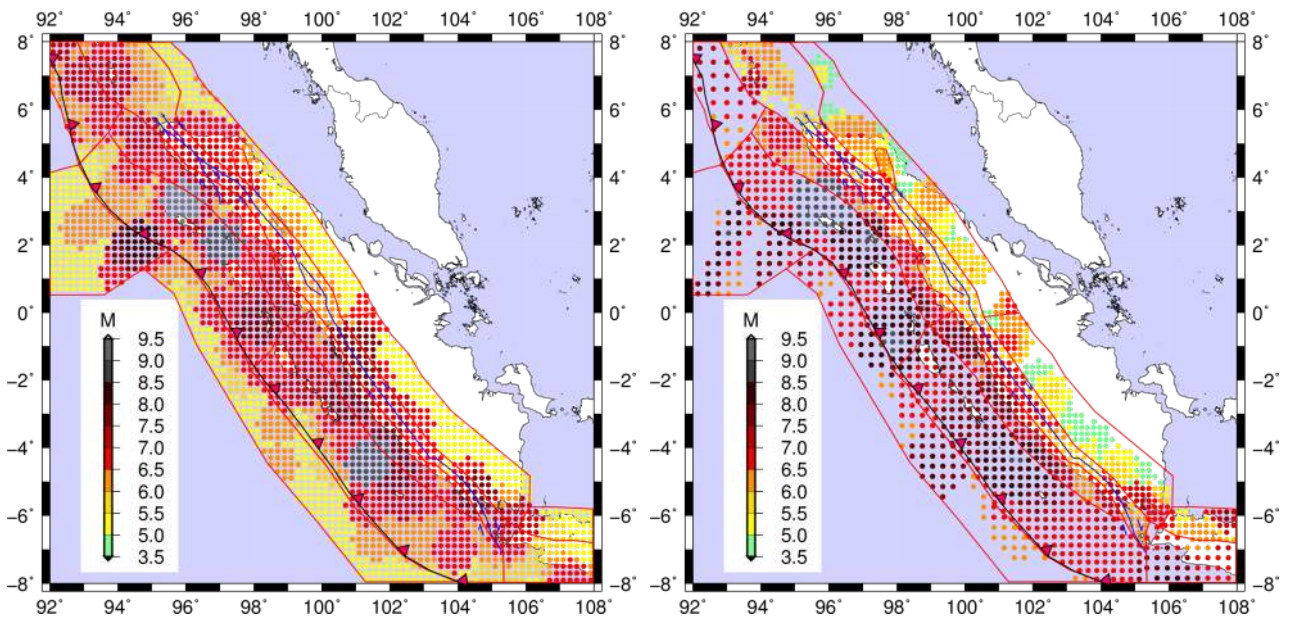

Figure 3.21. Magnitude after smoothing process: (left) original version (right) updated version.

The definition of the source magnitude (The figure 3.21 right) is one of the final results of the source definition. Another parameter is the focal mechanism, which is taken from the focal mechanism file (`.fps`) for the associated zones. All values for the source definition are already completed except those for the source depth definition. Therefore, we have to understand the characteristic focal depth in each zone before adopting the *sdepth* parameter. The subduction process plays the main role in determining the focal depth as shown in Figure 3.22.
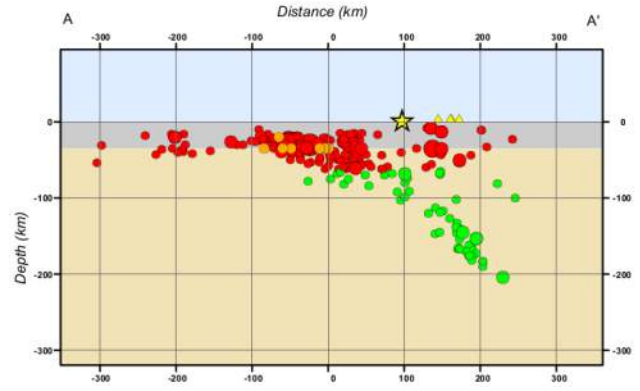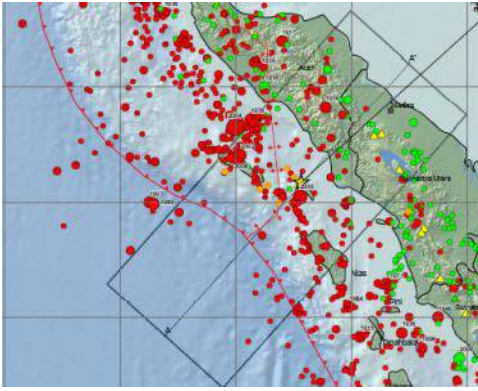
Figure 3.22. (left) The depth distribution (right) The cross section of the hypocenter USGS (2010)
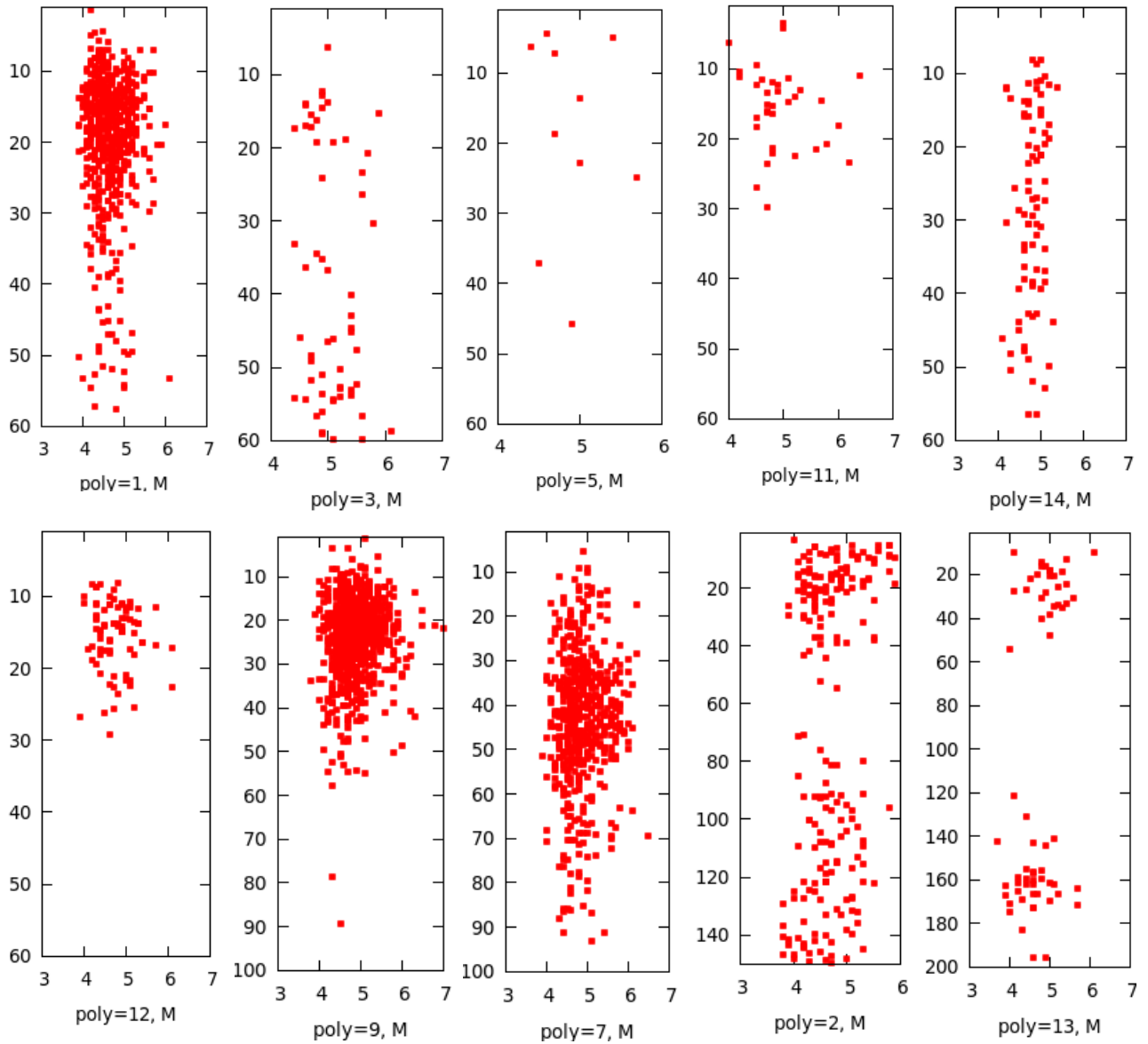
Figure 3.23: plots of earthquakes depth (km) versus magnitude (data from Pesicek et al. 2010). The lower part is arranged based on the location from swallow (left) to deep (right) earthquakes for zones, following box in figure 3.21(left).

44

In order to determine the *sdepth* parameter, we tried to find the depth versus the magnitude relationship as shown in Figure 3.23. The Seismogenic zone in Aceh, as polygon 1, shows the median distribution about 20 km, thus we choose *sdepth*=20. It is also almost similar to the other strike slip zones. For the deep subduction zones, it is relatively difficult to decide the source depth because the seismicity does not have a preferred depth, as shown in Figure 3.20. Therefore, we use the option *sdepth*=d, where the depth is taken from the maximum magnitude in the cells. The condition of the interplate zone can be represented by the earthquake on 11 April 2012 M8.6, and we put the value in the focal mechanism file, thus we set *sdepth*=fps.

The focal depth for the subduction zones obviously starts from shallow (zone 12) to deep (zone 13), as shown in the lower part of Figure 3.22. This gives us a strong motivation to use a slab distribution for the subduction zones 4,6,7,8,9,10. Fortunately, the slab information for a major subduction in the world has been publish by USGS as slab 1.0, see Figure 3.24. Thus, we can adopt the *sdepth*=dph, where the depth distribution is provided by the file `sum_slabcut.dph` (we crop and reduce the resolution from the original slab file to reduce the number of points).

The final result of the source depth definition is shown in Figure 3.25 (right), in which the result from the updated version is compared with the result from the original one Figure 3.25 (left). The information about the event depth in the original version is taken from their source definition file (`.sut`), and the actual value does not enter the computation because at the path definition algorithm in hazard estimation, the depth is defined by the function of magnitude, see Equation 3.1 The enhanced smoothing algorithm has successfully provided more realistic depth definition regarding the Sumatra subduction zone.
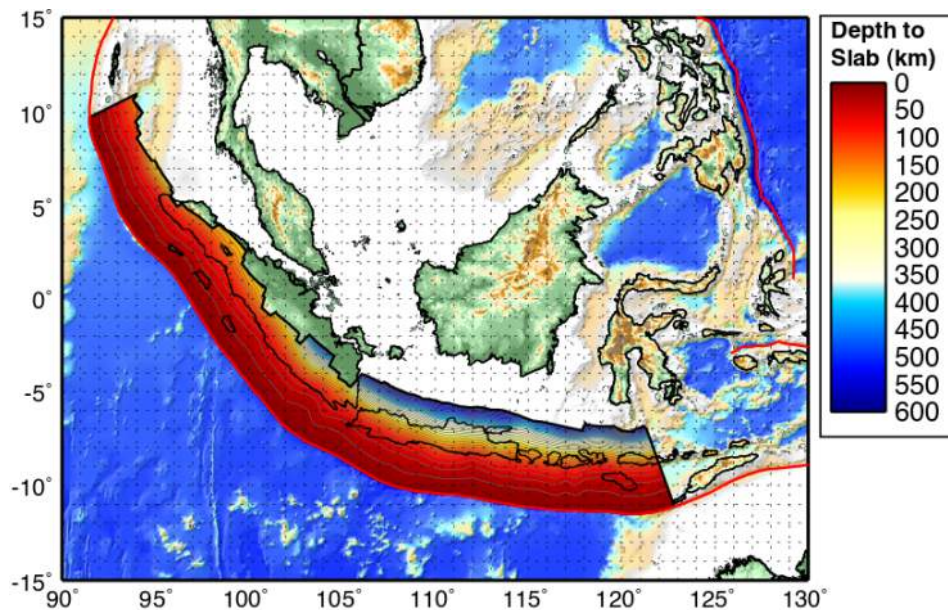
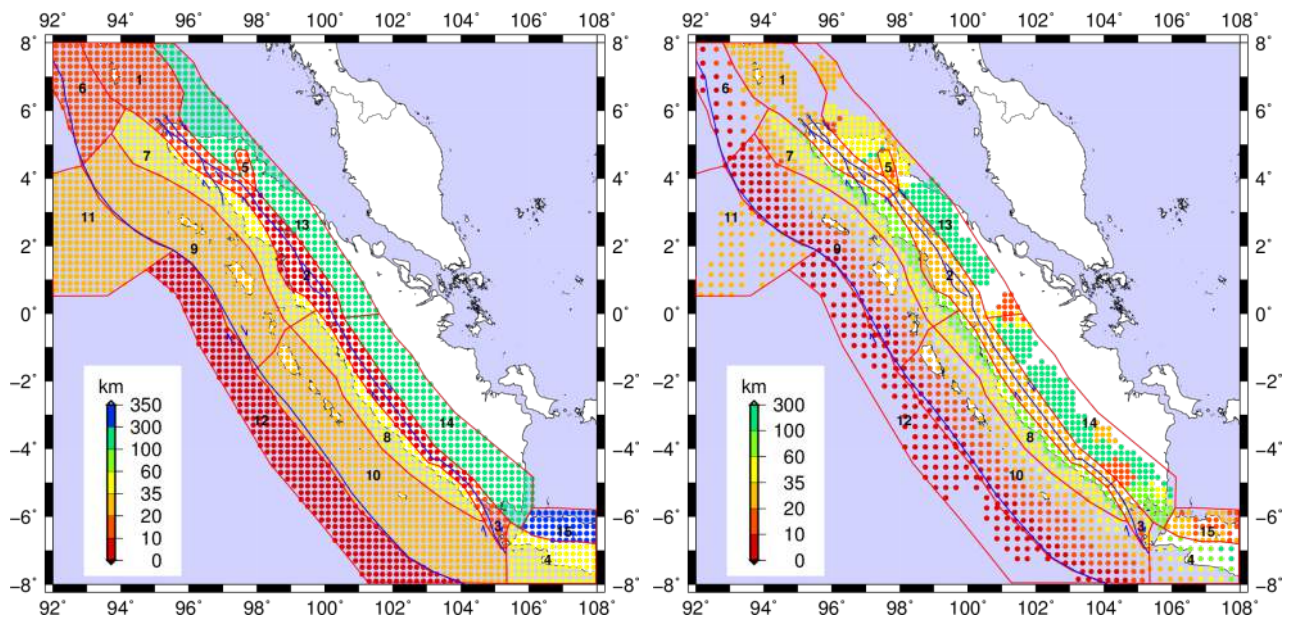Figure 3.24. Slab 1.0 distribution for Sunda subduction zone (Hayes, 2012).

Figure 3.25. Depth after smoothing source from original version (left) and updated version (right).

4. Geology and Structural Model of Sumatra

4.1. Geology of Sumatra

Geologically, Sumatra forms the southwestern margin of the Sunda Craton, which extends eastwards into Malaysia Peninsular and the western part of Borneo (Figure 4.1). The backbone of the main island is formed by the Barisan Mountains, which extend the whole length of Sumatra in a narrow belt, parallel to, and generally only a few tens of kilometres, from the SW coast. A Pre-Tertiary basement is exposed extensively in the Barisan Mountains and in the Tin Islands of Bangka and Billiton. The oldest rocks which have been reliably dated are the sediments of the Carboniferous-Permian age, although the Devonian rocks have been reported from a borehole in the Malacca Strait, and the undated gneissic rocks in the Barisan Mountains may represent a Pre-Carboniferous continental basement. All the older rocks, which lie mainly to the NE of the Sumatra fault system, show some degree of metamorphism, mainly to low-grade slates and phyllites, but the younger Permo-Triassic sediments and volcanics are less metamorphosed.

The area to the SW of the Sumatra fault is composed largely of variably metamorphosed Jurassic-Cretaceous rocks. The Pre-Tertiary basement is cut by the granite intrusion that ranges in age from Permian to Late Cretaceous. Locally within the Barisans, the basement is intruded by the Tertiary igneous rocks and is overlain to the NE and SW by the volcaniclastic and siliciclastic sediments in the hydrocarbon- (oil and gas) and coal-bearing Tertiary sedimentary basins. These basins have backarc, forearc, and interarc relationships to the Quaternary to Recent volcanic arc. The lavas and tufts from these young volcanoes overlie the older rocks throughout the Barisans and, in particular, cover an extensive area in North Sumatra around Lake Toba. The recent alluvial sediments occupy small grabens within the Barisan Mountains, developed along the line of the Sumatra fault and cover the lower ground throughout Sumatra. These alluvial sediments are of the fluvial origin immediately adjacent to the Barisans, but pass into the swamp, lacustrine and coastal deposits towards the northeastern and southwestern margins of the island (Barber et al., 2005).

In terms of the Holocene epoch tectonics, Sumatra forms the active southwestern margin of the Sunda Craton (Sundaland), the southeastern promontory of the Eurasian Plate. The Indian Ocean plate moves with a velocity of about 7.7 cm/year in the north-northeast (NNE) direction, which become oblique to be subducted at the Sunda Trench. The profiles across the landward side of the Sunda Trench imaged the removal of the packages of the sediment from the downgoing plate to build a forearc ridge accretionary complex (Hamilton 1979; Karig et al. 1980). The oblique

subduction results in the northwestward movement of a 'sliver' plate (Curray 1989) decoupled both from the downgoing Indian Ocean plate and the Sunda Land plate, along the Wadati-Benioff zone, which dips northeastwards at 30º and along the vertical Sumatran Fault System. This fault system has a low dipping angle, a characteristics common to E- or NE-directed subduction zones (Doglioni and Panza 2015). The Wadati-Benioff zone intersects the fault at a depth of some 200 km. The active Sumatran Fault System runs the whole length of Sumatra through the Barisan Mountains, from Banda Aceh to the Sunda Strait, and it is paralleled by a line of the Quaternary volcanoes, mostly quiet, but some currently active. Sumatra is separated by a linear ridge, with the emergent islands in the marine basins more than 1000 m deep, extending from Simeulue in the north to Enggano in the south. The Malacca Strait and the Java Sea form the southern parts of the Sunda Shelf. Across the shelf, the seafloor is shallow with a depth of less than 200 m and remarkably flat.
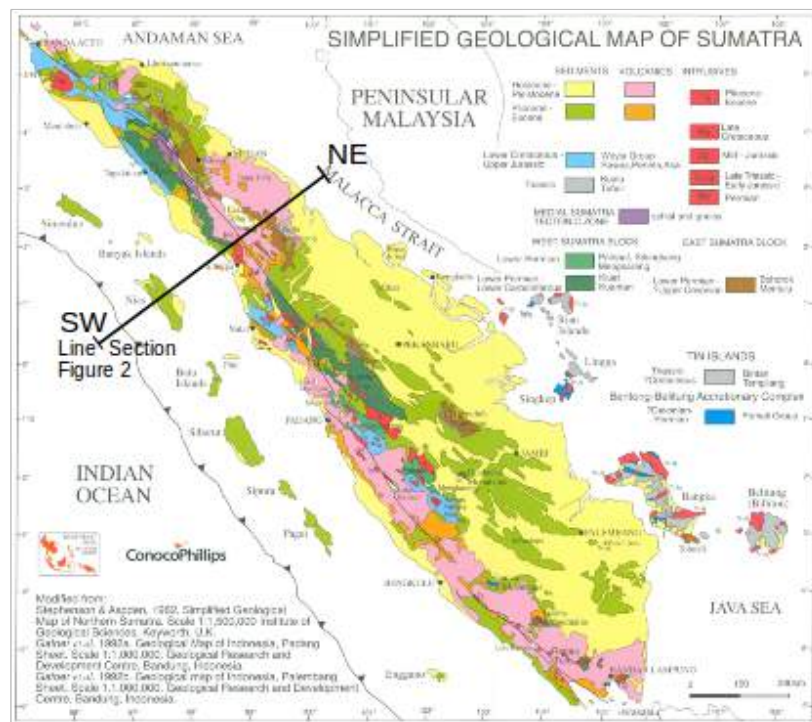
Figure 4.1. Simplified geological map of Sumatra (Barber et al, 2005), the cross-section along the (NE-SW) line is shown in figure 4.2.
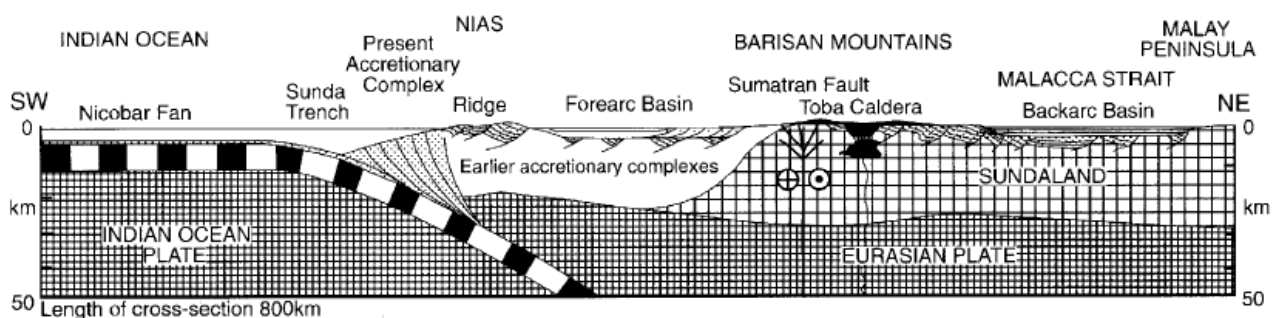

Figure 4.2. Diagrammatic section across the Sumatran Subduction System from the floor of the Indian Ocean to the Malay Peninsula, drawn to scale (Barber, 2005).

4.2 Compilation of the Available Tomography Data

The realistic seismic hazard estimation needs an as possible accurate source model and a structural model. NDSHA can provide the strong ground motion parameters based on the realistic physical simulation of the seismic wave propagation within the structural model. The NDSHA relies on the modal summation technique, which is able to involve the physical parameters of the soil/rock for the simulating seismic wave propagation, i.e. density, V_p, V_s, Q_p, and Q_s, not only in the laterally homogeneous medium, as discussed Panza et al. (2013) entitled: Seismic hazard and strong ground motion: an operational neo-deterministic approach from national to local scale. Providing the accurate structural models is a challenging work because there is a need to conduct a 3D tomography in order to obtain the physical (mechanical properties) parameters needed for modeling the seismic wave propagation. Constructing a structural model with new data is not one of the scopes of this study, and we make use of the available tomography studies to get a suitable structural model.

The 26 December 2004 Mw 9.1 and the 28 March 2005 Mw 8.7 Sumatra-Andaman earthquakes are among the largest ever recorded in the instrumental era and provide a unique opportunity to investigate the subduction megathrust and seismogenic zone processes using modern techniques. Several recent studies have taken advantage of the satellite-derived gravity data obtained by NASA's Gravity Recovery and Climate Experiment (GRACE) to successfully measure the time-dependent gravity response of the 2004 earthquake. For instance, Pesicek (2009) has constructed a 3D density model, whose calculated gravity effects agree well with those in a recent model of the observed mean gravity determined from the GRACE measurements. The gravity model is used for the GRACE derived model GGM02c (Tapley et al., 2005). The gravity modeling of the region surrounding the rupture area of the 2004 Sumatra-Andaman great earthquake has been conducted to better constrain the regional three-dimensional (3D) density structure from Finite Element Modeling (FEM) of deformation due to this event. Adjustments to the original FEM design for these features, which include the thinned crust associated with the Andaman backarc-spreading center, low-density sediments of the Bengal fan, and the thickened crustal roots below Burma and the Malay Peninsula. Pesicek (2009) has not yet published the model; however, the gravity model is from the initial model (Masterlark & Hughes, 2008) in the Tomoeye package (Gorbatov et. al 2004). The model has a resolution 0.5º, a space domain longitude from 90º to 109º, and a latitude - 5º to 21º, and the 7-layer vertical resolution (50, 100, 150, 200, 250, 300, and 350 km) as shown in Figure 4.3. The slab subduction is well defined by the density. For the value of the layers lower than 350 km is taken from the reference model AK135 (Kennett, 1995). The density of the subducting slab is less than that of the surrounding mantle, as also observed in the other subduction zones in the Mediterranean (Brandmayr et al. 2011, ElGabry et al. 2013). This fact is in full agreement with the

concept of the polarized plate tectonics (Doglioni and Panza, 2015) and disproves one of the basic concepts of the standard plate tectonics: the slap pull progress.
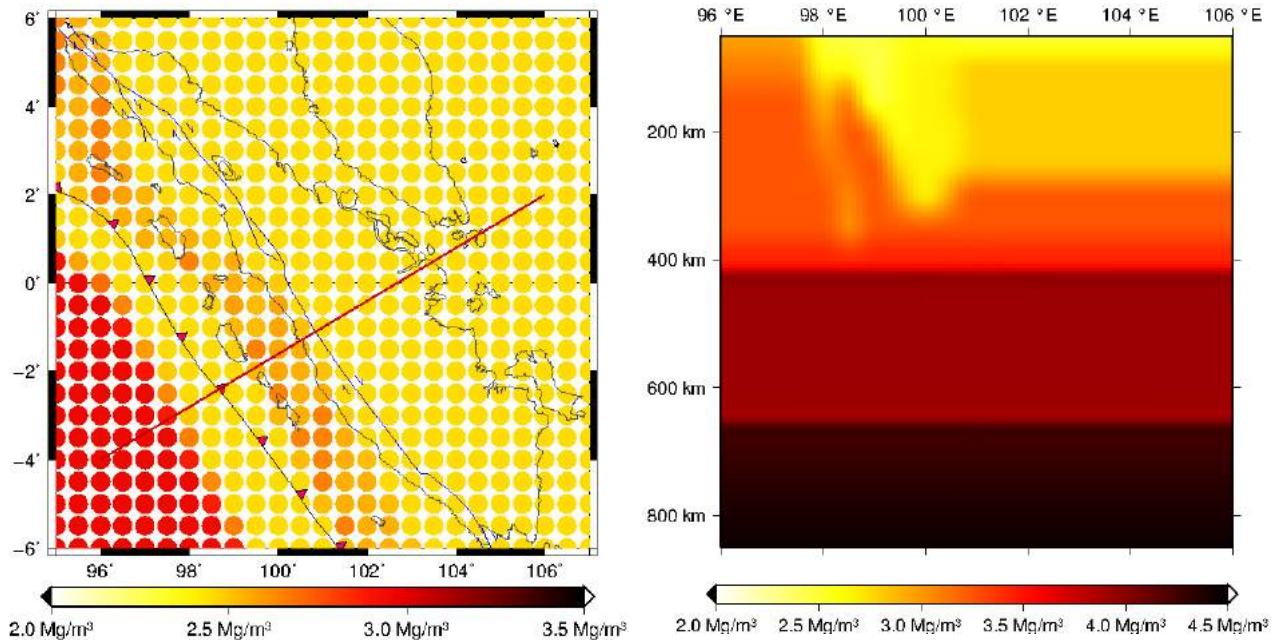

Figure 4.3. (left) Density model distribution at depth 50km (Persicek et al., 2009).
(right) Vertical smoothed cross section extended with ak135 for z deeper than 350km

Pesicek et al. (2010) also takes the advantage of the increased ray coverage due to seismicity following the 2004 December and 2005 March great earthquakes, an improved iterative regional-global tomographic method (travel time P-wave tomography) was applied to the Sumatra–Andaman and adjacent regions which the propose for better constrain the 3-D mantle velocity heterogeneity in the region. Velocity and hypocentral parameters were iteratively perturbed to sharpen the image of the subducted slab. These tests show significant increases in amplitude and decreased smearing of synthetic slab features. Thus, when applied to the real data, similar enhancements are inferred in the resulting model, which better illustrates the complex slab geometry in the upper-mantle and transition zone regions along the Sumatra, Andaman and Burma subduction zones. The regional P-wave tomography study is covering the whole Sumatra Island as shown in figure 4.4.

The S-wave tomography data, in Figure 4.5, is from courtesy Sriwidiyantor (2008), which is derived by using an updated version of the reprocessed S arrival time data of Engdahl et al. (1998). The information from the S-wave data helps to characterize the inferred velocity variations, but previous studies have not produced any good constraints on the slab structure. This is likely due to the relatively high noise level of the International Seismological Centre (ISC) S-wave data. However, the refinement of the travel time data, particularly the reprocessing of the multiple data sets to extract the improved S-wave information conducted by Engdahl et al. (1998) has greatly benefited the current study. Engdahl et al. (1998) used the S phases in the initial source location and

50

an appropriate S-wave reference velocity model (ak135; Kennett et al. 1995). Most aspects of the S-wave tomographic imaging technique employed here are similar to those of the P-wave data, except that for a ray to be included in the inversion, the travel-time residual for S relative to the ak135 reference model has to lie in the range +/-15.0 s, in contrast to the dynamic reweighting of the P-wave residuals (Pesicek et al. 2010) and (Widiyantor 2011).
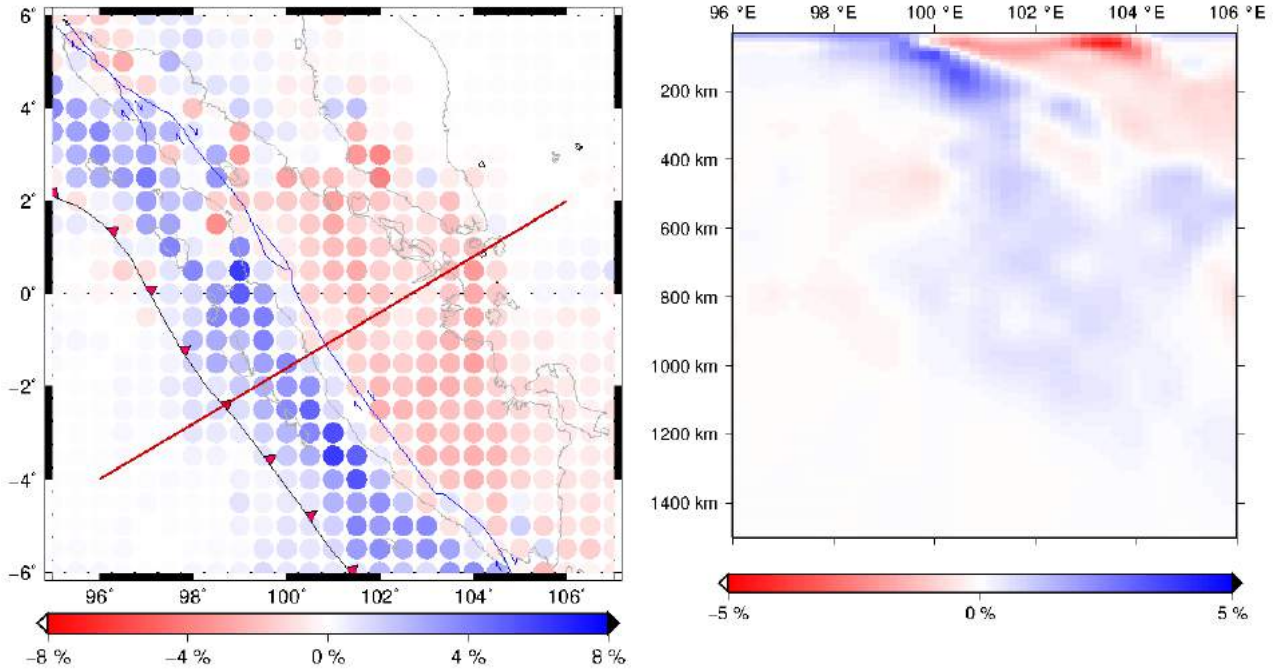

Figure 4.4. (left) P-wave tomography (Pesicek, et al. 2010) within the 3th layer at z=90km. (right) Vertical cross section along the red line profile (left) (ref. AK135).
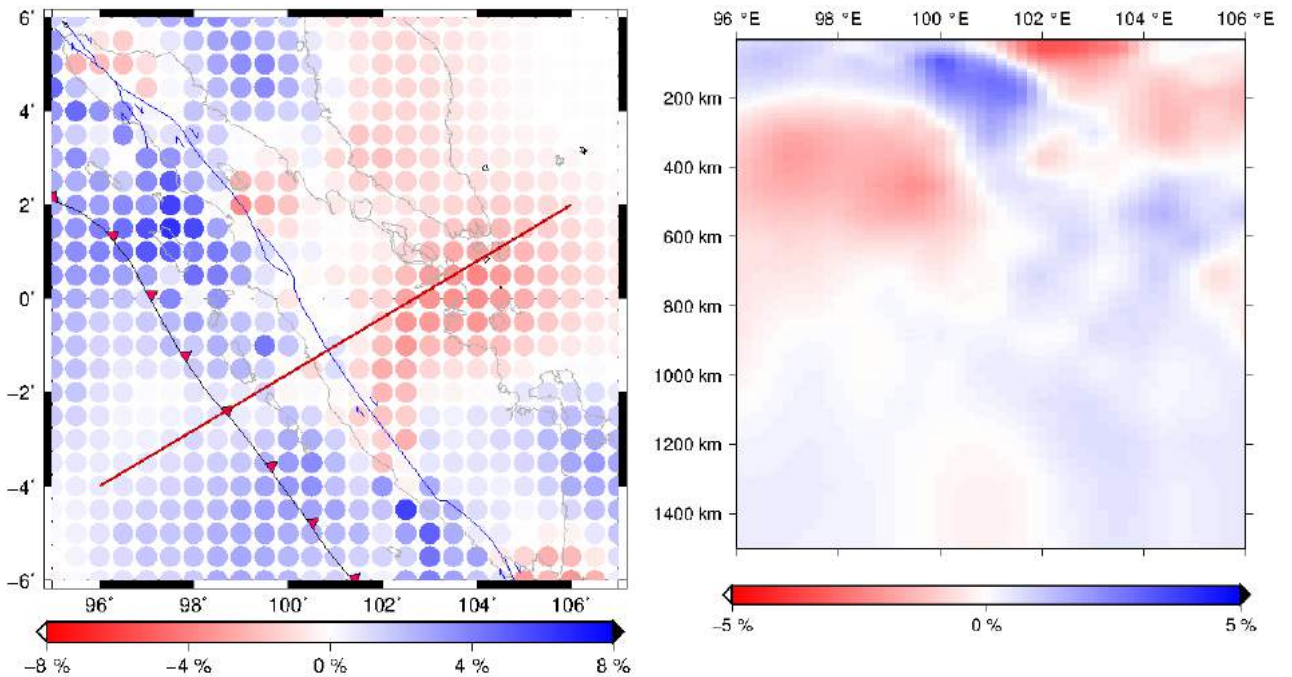
Figure 4.5. (left) S-wave tomography for the 3th layer at z= 90km (ref. AK135). (right) Vertical cross section along the red line profile (left), data from (Widiyantor 2008)

The tomography images for P-wave (Figure 4.4-left) and S-wave (Figure 4.5-left) show the boundary between the two plates, the positive perturbation value related to the cool oceanic crust and the negative value related to the hot continental crust. Both tomography data also show the slab under the subduction from the Sunda Trench and the vertical sections across the convergent margin in the middle Sumatra from SW to NE (red line) in Figure 4.4 (right) and 4.5 (right). By summing up the main properties of the velocity and density tomography models, it is possible to note that in the study region: (a) the density of the subducting slab is less than that of the surrounding mantle material, (b) the Vp and Vs velocities in the subducting slab are larger than those in the surrounding mantle. This fact contradicts the popular beliefs that the subducting slabs are at the same time faster and denser than the surrounding mantle, which is in perfect agreement with the fact that both V_P and V_S are inversely proportional to the density. For a more detailed discussion see (Doglioni and Panza, 2015).

The slow (relative to models of the wave speed) progress in the development of the attenuation model is not surprising since the wave amplitude, which is typically used to measure attenuation, requires a more complex interpretation than that of the wave travel time or the phase delay. The three-dimensional attenuation model in this study from Dalton et al. (2008) is derived from the observations of the fundamental mode Rayleigh wave amplitude anomaly in the period range $50 - 250$ s, namely the QRFSI12 model. The data are measured from the vertical-component seismograms derived from the earthquakes with $M_W > 6.0$ that were recorded by the global and regional stations, and the algorithm is described by Ekstrom et al. (1997) for making the measurements. The data are ratios of the observed to the synthetic wave amplitude, where the reference seismogram is calculated using the appropriate moment tensor and the centroid location from the Harvard CMT catalog (Dziewonski et al., 1981). The QRFSI12 has a poor resolution for Sumatra as shown in Figure 4.6. For a future study, we have to find a more detailed and higher resolution attenuation model for Sumatra, but the present day knowledge is acceptable for our purposes.

The attenuation information from the QRFSI12 model is only the shear-wave attenuation Q_s, but the modal summation also needs a compressional wave attenuation Q_p. There is a very well known relationship to get the bulk attenuation from the shear attenuation $Q_p = (9/4)Q_s$ as explained in many text books such as (Anderson 1989) and (Stein and Wysession 2003). The attenuation model from the QRFSI12 is really poor in terms of the complexity of the geology of Sumatra. Because we have V_p and V_s (VPS) for a resolution 0.5 degree for Sumatra, we try to apply some weight as the weighting factor VPS data. We use the simple relation proposed by Richard and Stewart (2006) with the relationship $Q_p = 1.0/(0.0241*(V_p/V_s)-0.0357)$. We put the weight for Q_p from this relationship about 0.2 and 0.8 from the QRFSI12.
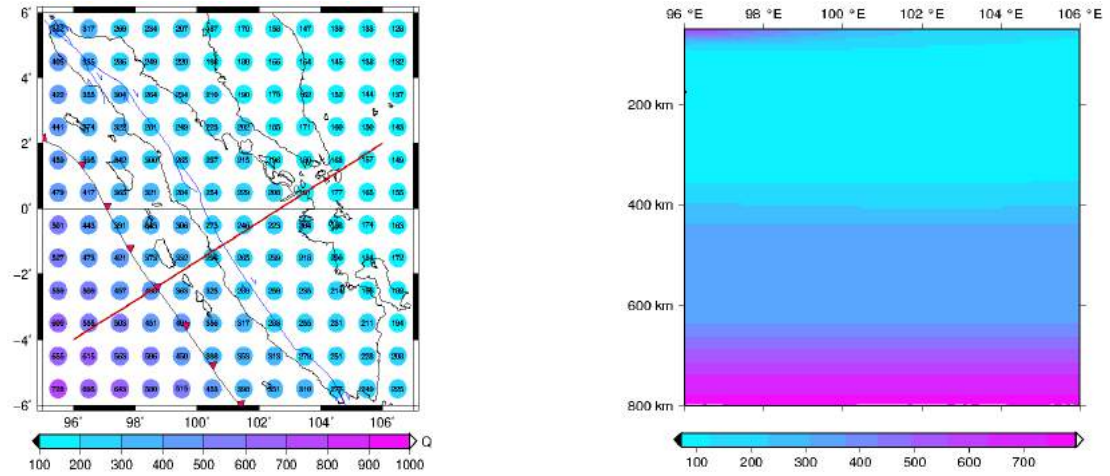
Figure 4.6. (left) shear-wave attenuation model QRFSI12 (from Dalton et al., 2008). (right) Vertical cross section for profile red line

The discussed models above have a good resolution in a deeper part until the depth of 1500 km, and the other models give a high resolution until the depth of 350 km; also they have a limited resolution in the upper layers. The reliability of the simulation depends on how reliable the detail is in the structure model being used. Therefore, critically combining all available information could provide a high vertical resolution in the uppermost layers. The adopted structural models are obtained from the surface wave tomography studies, e.g. model CRUST2.0 (Bassin et al. 2000) and LITHO1.0 (Pasyanos et al., 2014). The global models of the Sumatra region are shown in Figure 4.7 and 4.8, respectively.
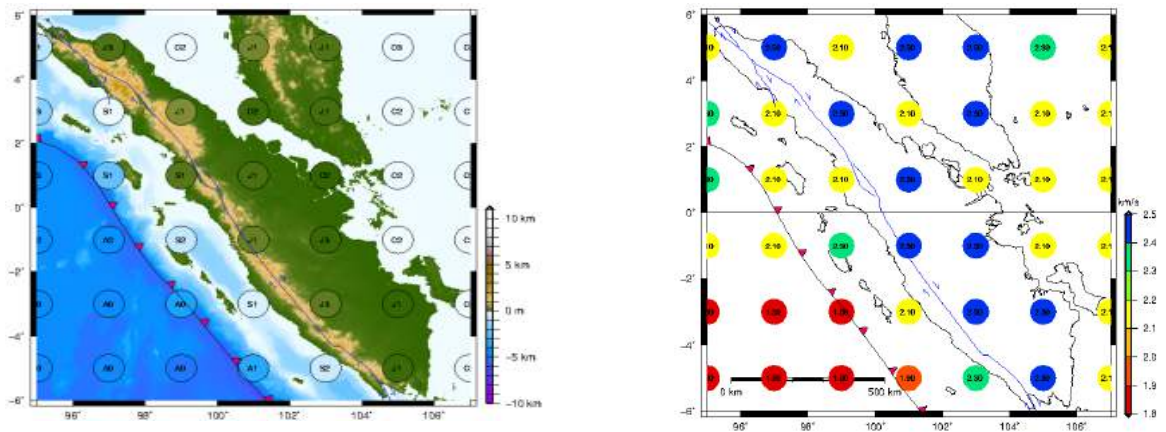
Figure 4.7 (left) Matching depth from Crust 2.0 (resolution 2º) with SRTM data. (right) the V_p model at the upper crust layer (5th layer)

The global crustal model CRUST2.0 uses the keys to assign the various types of the crustal structure (such as Archean, early Proterozoic, rifts, etc.) in each cell. CRUST2.0 was adjusted in type to better reflect the edges of the shelves and the coastline. The thickness of the sediments in each adopted cell is about 1.0 km meanwhile the average crustal thickness about 5 km. The 2x2

degree model is composed of 360 1D-profiles, where one of these profiles is assigned to each 2 x 2 degree cell. Each individual profile is a 7-layer 1D-model with i.e. 1) Ice 2) water 3) soft sediments 4) hard sediments 5) upper crust 6) middle crust 7) lower crust. The parameters VP, VS and rho are given explicitly for these 7 layers as well as the mantle below the Moho (Bassin et al. 2000). The upper crust layer for Sumatra has been plotted in Figure 4.7.
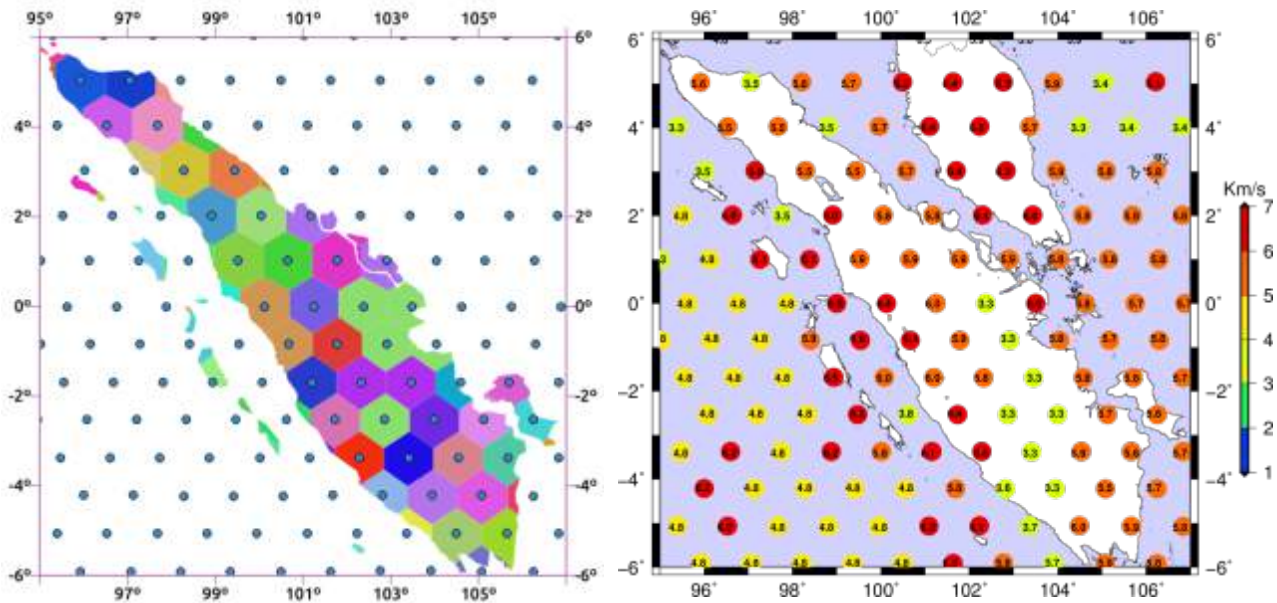

Figure 4.8 (left) The icosahedron tessellation distribution of point Litho1.0 (resolution 1º) and overlay with future alternative polygon. (right) the V_P model at lower sediment layer (5th layer).

The compilation of the crustal model initially follows the philosophy of the widely used crustal model CRUST2.0 that assigns the elastic properties in the crystalline crust according to the basement age or the tectonic setting. CRUST1.0, introduced in 2013, serves as a starting model in a comprehensive effort to compile a global model of the Earth's crust and lithosphere. The Moho depth in CRUST1.0 (Laske et al. 2013) is based on 1ºx1º, which are the averages of a recently updated database of the crustal thickness data from the active source seismic studies as well as from the receiver function studies. In each 1-degree cell, boundary depth, compressional, and shear velocity as well as the density is given for 8 layers: water, ice, 3 sediment layers, and upper, middle and lower crystalline crust. The topography, bathymetry and ice cover are taken from ETOPO1, and the sediment cover is based on their sediment model (Laske and Masters, 1997). For the cells with no local seismic or gravity constraints, the statistical averages of the crustal properties, including the crustal thickness, were extrapolated. However, in places with the constraints for the depth to basement and the mantle are given explicitly and no longer assigned by the crustal type. This allows for much smaller errors in both.

The CRUST2.0 has a complete set of data for the Sumatra region for all depth and well tested but low in the lateral resolution 2ºx2º. We tried to use the updated version with a higher

lateral resolution, CRUST1.0, but there is a missing part for the velocity V_p at layer 4. Therefore, we skip the CRUST1.0 and step toward using LITHO1.0; the model is then validated against the new global surface wave dispersion maps and adjusted in the areas of extreme misfit.

It appears that LITHO1.0 (Pasyanos et al., 2014) represents a reasonable starting model of the Earth's shallow structure (crust and uppermost mantle) for the purposes in which these models are used, such as the travel time tomography or in the efforts to create a 3D reference earth model. The model matches the surface wave dispersion over a frequency band wider than the band used in the inversion. There are several avenues for improving the model in the future by including the attenuation and anisotropy, as well as by making use of the surface waves at higher frequency. Each of the nodes has a unique profile where the layering is more detailed than in CRUST2.0, since the sedimentary layer is divided into upper, middle, and lower sediments. The lower sediment layer for Sumatra is presented in Figure 4.8. Other additional layers under the crust for LITHO1.0 are one layer for the lithospheric mantle (lid), and one for the asthenospheric mantle. The parameters of the layer thickness, V_P, V_S, rho, and Q (placeholder values) are given explicitly for all layers. The parameters below the asthenosphere blend into the ak135 model (Kennett et al., 1995).

4.3 Observational Sites and Rotated Cellular Polygons

NDSHA produces realistic strong ground motion estimation through the incorporation of the detailed crustal structure and the source information. This is an advantage using the NDSHA method that has to be paid with a high computational cost. Therefore, the optimum spacing between sites where the structural models are specified is required to decrease the computational time. In this study, we adopted a grid space of 0.2º as shown in Figure 4.9 (right). Beside using 0.2º grid interval, we also put directly the observation point in the center of an Island if not filled, when applying 0.2 degree interval.

There are 954 receiver sites (locations where the synthetic seismograms are computed) as shown in Figure 4.9 (right). Because of the modal summation method needs to calculate the spectral modes for each structure, it is better to group similar structural models at the close receiver sites within a polygon. In this study, we rotated the cellular polygons by 54º. The rotation of the structural zones will contribute in the enhancement of the hazard computation as show in Figure 4.9 (left). As the first advantage, the rotation reduces the number of the polygons because we can avoid producing the small polygons at Conner near the coastline. The total number of the polygons is 49, which 14 polygons for the small Islands and 35 polygons for the Sumatra island. The second advantage is that the polygons will be aligned along the orientation of the geological layer near west, and the polygon near east will orient in the same direction as the thick sedimentary cover orientation. Finally, with the 3D heterogeneous modal summation, we can construct the ray part

from the subduction zone perpendicular to the polygon side, and this will be a matter for a future study (La Mura et al., 2011, Panza et al., 2013).

The observation points can be defined as a regular grid for estimating the seismic-hazard map at different scales as shown in Figure 4.9 (left) or from the actual observation points such as seismometer, accelerometer, and observed intensity data. Figure 4.10 (left and right) shows the accelerometer, and the seismometer network run by the Indonesia Meteorological and Geophysical Agency (BMKG).
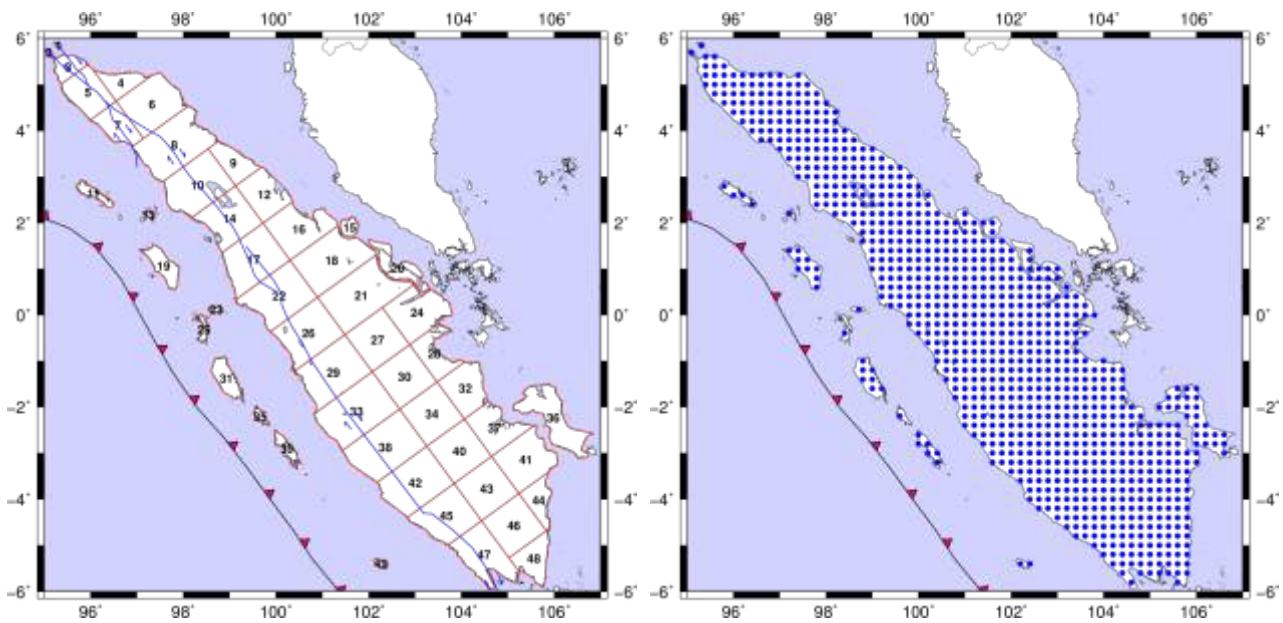
Figure 4.9 (left) Rotated by 54º cellular polygons used to define the structural model in this study. (right) Distribution of computation points in this study inside the polygons
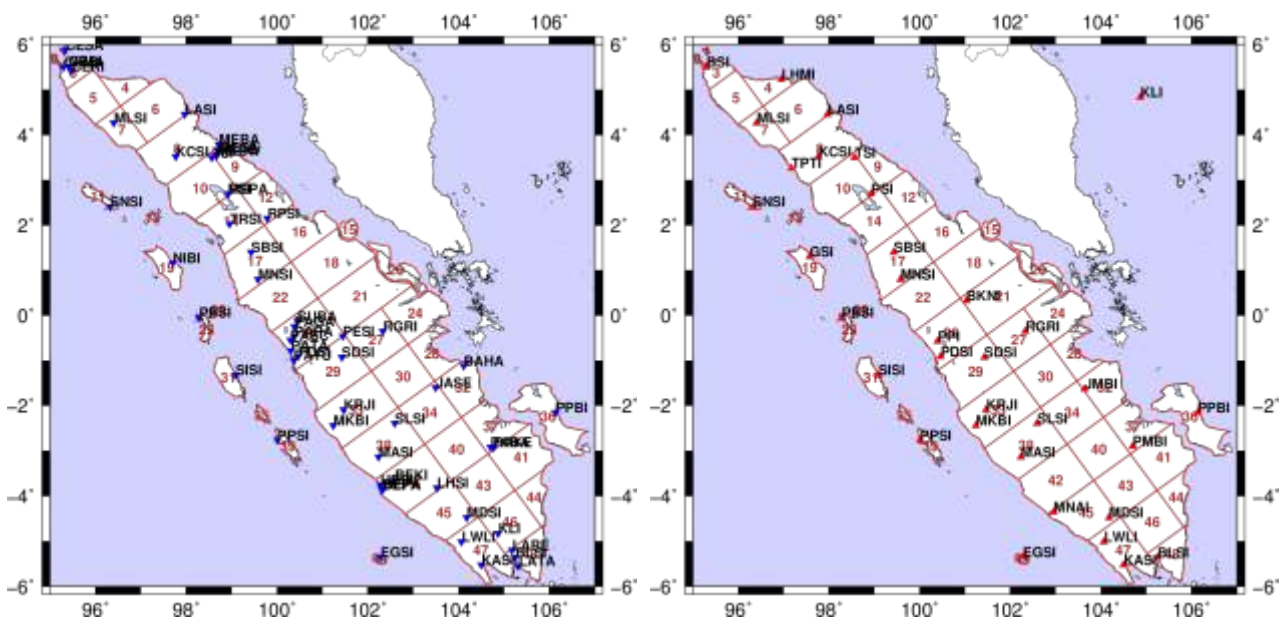
Figure 4.10 (left) Distribution of BMKG accelerometers for Sumatra (right) Distribution of BMKG seismometers for Sumatra and associated structural polygon.

56

We make a simple program `por4obs.exe` to assign the observation points with the associated structural polygons. For example, the observation point from the accelerometer accsum1.obs, our structural polygon `sumg.por,` and the new observation file has been associated with the structural polygon by following the command in Figure 4.11.
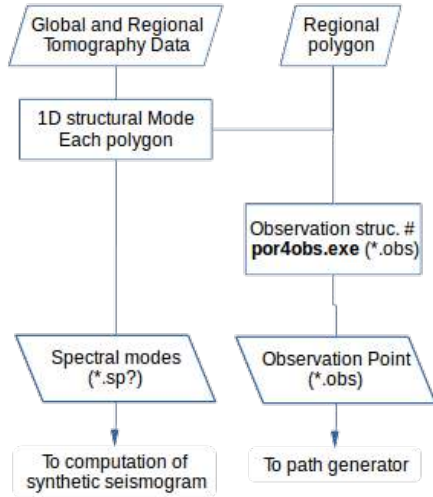

Figure 4.11. Diagram procedure for production the spectral modes and observation point by following command

```
por4obs.exe sumg.por accsum1.obs > acc.obs
por4obs.exe sumg.por dx 0.5 > sum2.obs
```

The *.obs file will send to paths generator program, where as the spectral modes (see figure 4.13) send to modal summation computation for generating synthetic seismogram

4.4 Structural Model of Sumatra

The structural model for each polygon is represented by the 1D structural model that defines the physical properties of the propagation path i.e. density, V_P, V_S, Q_P, and Q_S, which affects the resultant strong ground motion at the target site. We extracted the values by interpolation from the available studies, at the centroid area of each polygon, from the available 3D models, as discused in Section 4.2. After performing the interpolation and the compilation using several tomography studies, we obtained the requested 1D structural model. Listing 4.1 shows the 1D structural model under the Banda Aceh city related to the polygon number 3 in Figure 4.9-left. The plot of the structural model for the whole depth (until 1500 km) is shown in Figure 4.12 (left), and the upper layer resolution is shown in Figure 4.12 (right).

After adopting the appropriate structural models for each area, there is a need to compute the spectrum file for each model being used for a specific frequency (Panza et al, 1983). The computation of the modes for a given structural model is the prerequisite for the computation of the synthetic seismograms. The algorithm for the computation of the eigenvalues for Rayleigh wave for the solution of the elastic wave propagation in the multilayered media as the quotient of product of the matrices is given by Knopoff (1964) and Panza (1985). The structure should reach at least 80 km in depth for 10 Hz computations (100 km would be even better), and about 1100 km for 1 Hz

computations (the detailed description of this procedure is shown in the manual developed by Vaccari (2015m). Figure 4.12-left shows the Rayleigh-wave and Love-wave dispersion curves for the structure under the Banda Aceh city.

```
%thk(km)   rho    Vp(km/s)    Vs(km/s)    Qp        Qs        depth(km)   layer, 95.5165,  5.3823
1.1787     1.97   2.169145    0.708092    1350.13   600.00    1.17866     1           SEDS1-BOTTOM
6.8135     2.47   5.147437    2.904619    1350.13   600.00    7.99216     2           CRUST1-BOTTOM
8.4092     2.67   6.113295    3.495663    1350.13   600.00    16.40134    3           CRUST2-BOTTOM
15.1265    2.85   6.686211    3.815870    1350.13   600.00    31.52783    4           CRUST3-BOTTOM
92.8497    3.30   8.123616    4.628840    450.04    200.00    124.37752   5           LID-BOTTOM
100.0000   3.30   7.961142    4.326709    157.52    70.00     224.37752   6           ASTHENO-BOTTOM
55.62248   2.65   8.572799    4.639019    208.83    92.72     280.00000   7           M65
60.0000    2.78   8.753242    4.750742    201.59    89.51     340.00000   8           M62
70.0000    3.47   8.939481    4.861714    156.31    69.40     410.00000   9           M69
80.0000    3.93   9.550887    5.220524    416.59    184.97    490.00000   10          M55
80.0000    3.92   9.810226    5.370601    420.98    186.92    570.00000   11          M51
90.0000    3.92   10.119212   5.566250    425.83    189.07    660.00000   12          M48
90.0000    4.29   10.932946   6.094822    1315.11   583.91    750.00000   13          M44
90.0000    4.40   11.122142   6.236225    1271.93   564.74    840.00000   14          M43
90.0000    4.49   11.280877   6.265922    1255.96   557.65    930.00000   15          M41
90.0000    4.57   11.451852   6.338050    1240.11   550.61    1020.00000  16          M39
110.0000   4.63   11.602945   6.432203    1223.39   543.18    1130.00000  17          M37
120.0000   4.69   11.771735   6.541500    1204.54   534.82    1250.00000  18          M36
150.0000   4.76   11.950846   6.629762    1182.80   525.16    1400.00000  19          M33
```

Listing 4.1. File `sumh0003.stp` is the structural model under Banda Aceh city
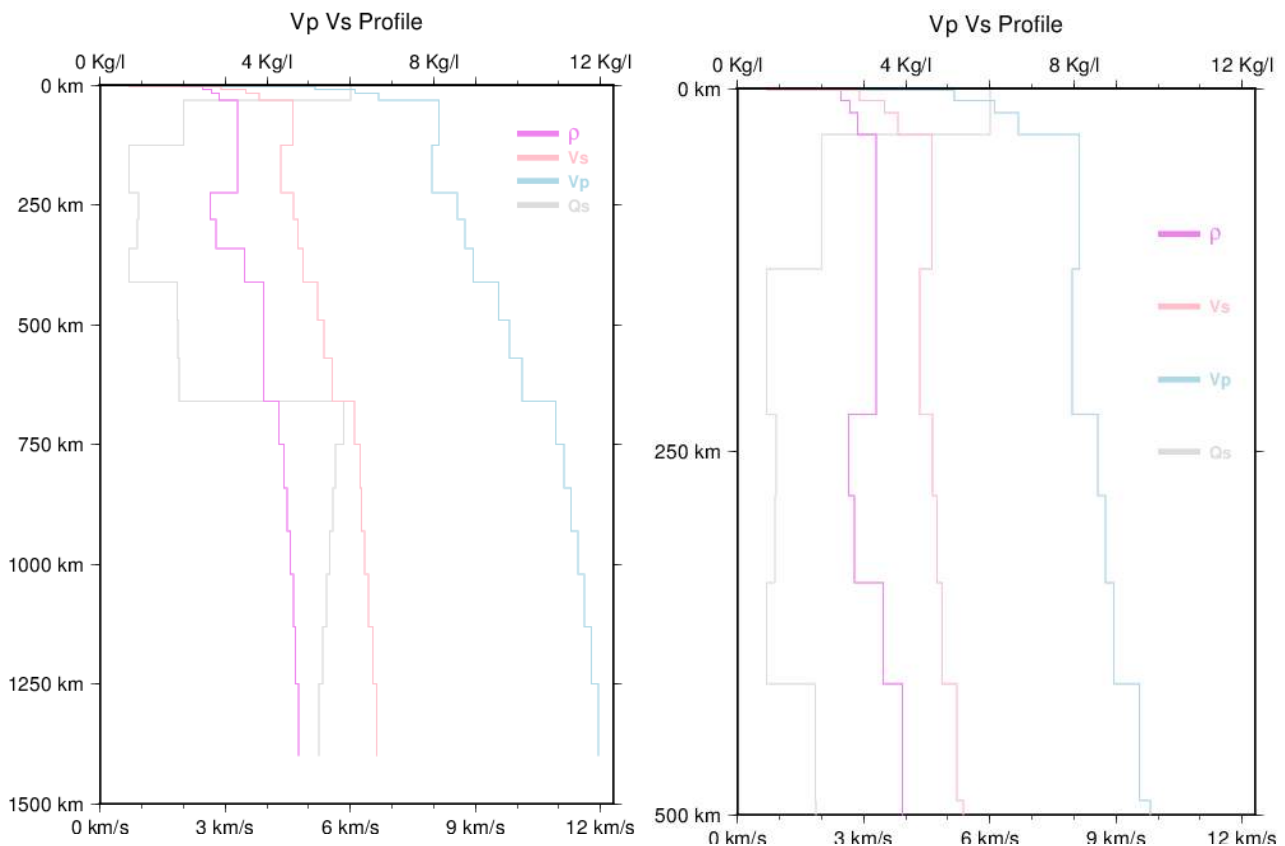

Figure 4.12: Structural model under Banda Aceh city related polygon 3 (file sumh0003.stp)
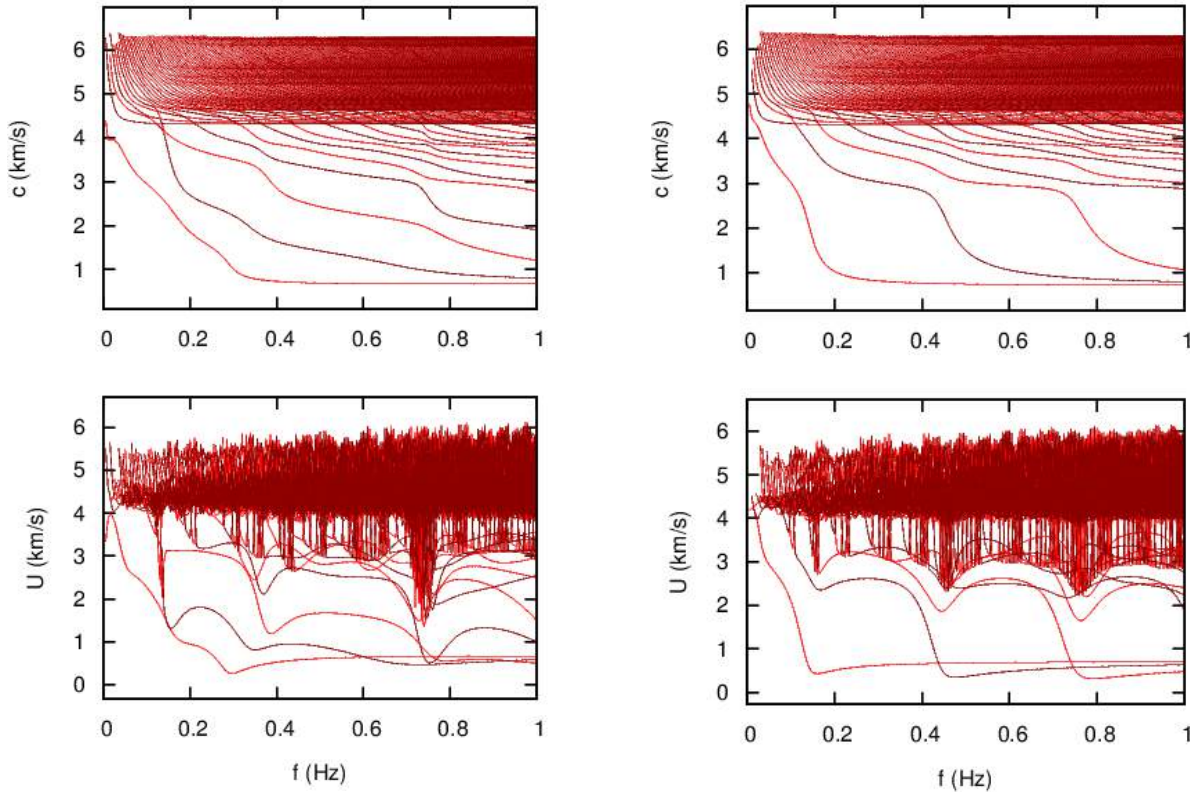
Figure 4.13. Dispersion curve for (left) Rayleigh wave (right) Love wave for Banda Aceh structural model as shown in figure 4.11. Upper is phase velocity and lower is group velocity

The adopted structural model is validated by comparison with the other result (Kenneth et al. 2012) from the receiver function as shown in Figure 4.13 (left). The comparison is carried out for ρ, V_S, and V_P in the structural model of the polygon 4 and 19, where the LMHI and GSI seismometer stations are located as shown in Figure 4.14 (right). The comparison for ρ, V_S, and V_P computed using the receiver function from LITHO1.0 and CRUST2.0 carried out by Kenneth et al. (2012) for both figures that show that they are relatively similar, and the LITHO1.0 model (solid line) more closely approaches the receiver function, and we prefer to use the LITHO1.0 for the upper part of the structural model. In order to improve the quality of the upper parts of the structural model, the surface wave tomography could be performed in a future study. Figure 4.15 shows the entire structural models used in this study as an overlay.

59
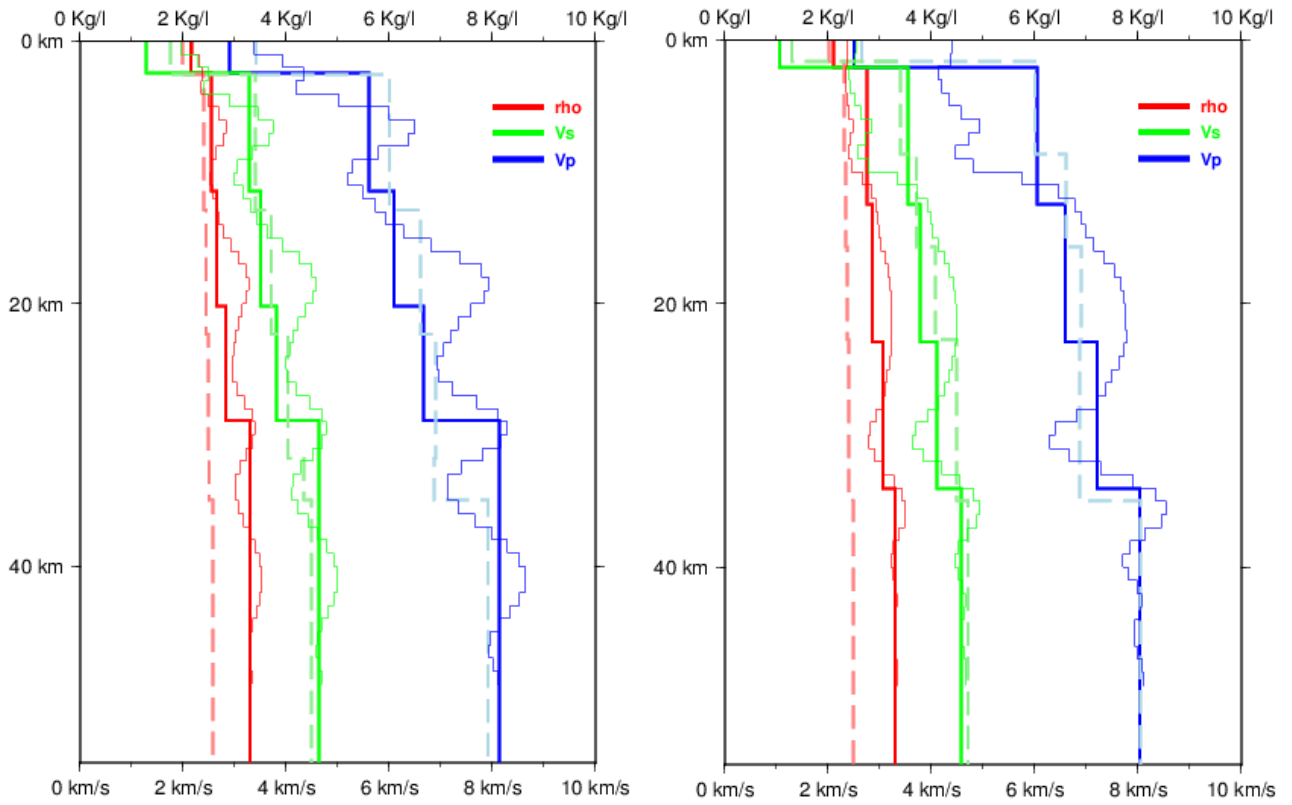
Figure 4.14: The LITHO1.0 model (solid line) more closely approach the receiver function inversion model (thin line, Kenneth et al., 2012) compare to CRUST2.0 (dash line) especially the density model. (left) Station LHMI at structural polygon 4 and (right) station GSI at structural polygon 19.
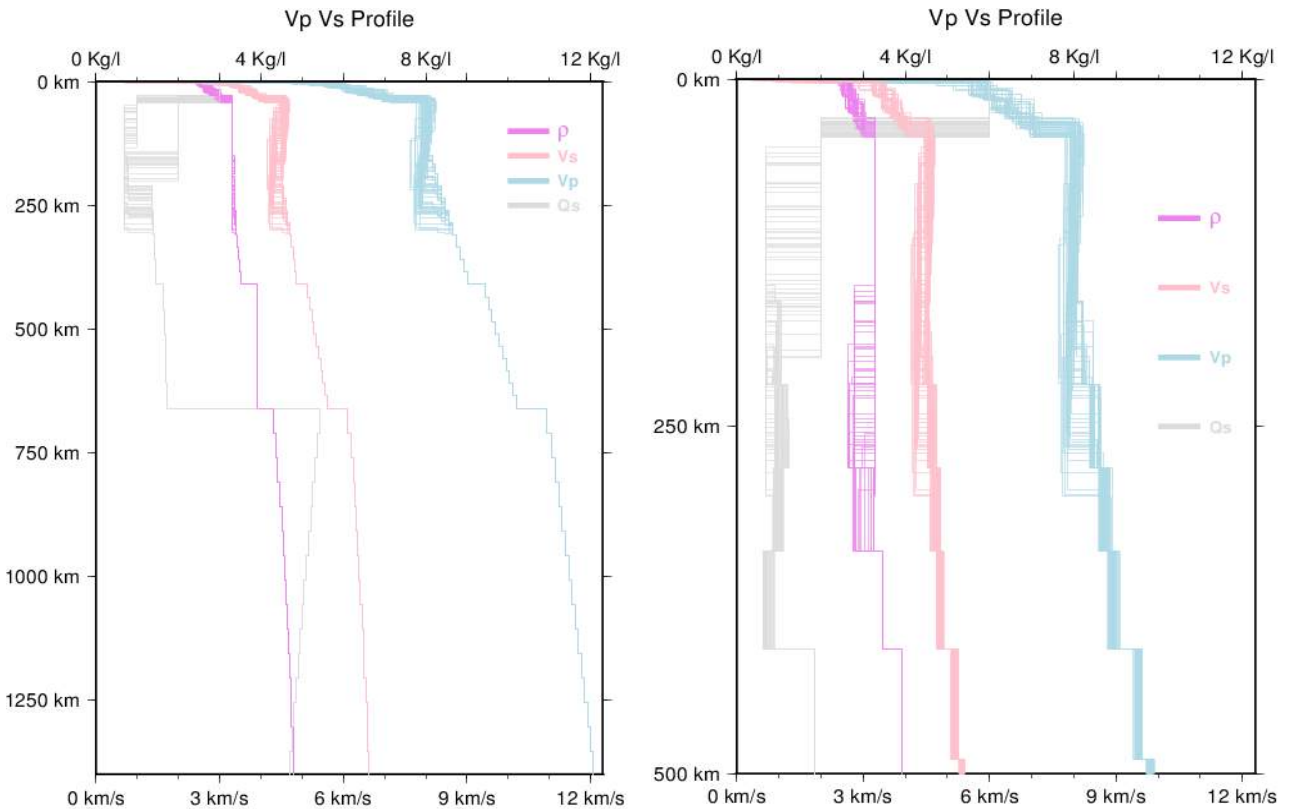

Figure 4.15: The overlay all of the structural models used in the simulation

5.Modal Summation Technique and Validation

5.1 Seismic Wavefield and Modal Summation

Seismic waves can be represented as elastic perturbations propagating within a medium, originated by a transient disequilibrium in the stress field. In the study of elastic bodies, to take into account macroscopic phenomena, it is assumed that the medium is a continuum, i.e., that the matter is distributed continuously in space. Therefore, it is possible to define the mathematical functions that describe the fields associated with the displacement, stress and deformation.

Considering the balance of the forces such as inertia, body forces, and surface forces acting on a cubic element within the continuum, and applying the Newton's laws of motion, we obtain the system of equations of motion.

$$\rho \frac{\partial^2 u_x}{\partial t^2} = \rho X + \frac{\partial \sigma_{xx}}{\partial x} + \frac{\partial \sigma_{yx}}{\partial y} + \frac{\partial \sigma_{zx}}{\partial z}$$

$$\rho \frac{\partial^2 u_y}{\partial t^2} = \rho Y + \frac{\partial \sigma_{xy}}{\partial x} + \frac{\partial \sigma_{yy}}{\partial y} + \frac{\partial \sigma_{zy}}{\partial z} \tag{5.1}$$

$$\rho \frac{\partial^2 u_z}{\partial t^2} = \rho Z + \frac{\partial \sigma_{xz}}{\partial x} + \frac{\partial \sigma_{yz}}{\partial y} + \frac{\partial \sigma_{zz}}{\partial z}$$

where a Cartesian coordinate system (x, y, z) is adopted. $s_{ij}(\mathbf{x},t)$ (i=x, y, z; j=x, y, z) indicates the second-order stress tensor, ρ is the density of the material, and X, Y, Z are the components of body forces for a unit mass.

In general, the relation between the stress and deformation can take a very complex form since they have to consider the effects of the parameters like pressure, temperature, and the amount of the variability of the stress. Nevertheless, by assuming that the deformations and stresses in short duration (the conditions mostly satisfy the problems in the ground motion estimation) are small, we can then think of that the solid behaves linearly, and the constitutive relation linking the stresses and the deformation becomes the Hooke's laws of stress tensor. After applying some symmetry and assuming the locally isotropic stress, we get the equation

$$\sigma_{ij} = \lambda e_{kk} \delta_{ij} + 2\mu e_{ij} \tag{5.2}$$

and the quantities λ and μ are called *Lamè parameters*.

Using Equation 5.2, Equation 5.1 becomes a linear system of three differential equations with three unknowns: the three components of the displacement vectors, whose coefficients depend on the elastic parameters of the material. It is not possible to find the analytic solution for this system of equations; therefore, it is necessary to add further approximations, chosen according to the adopted resolving method. Two ways can be followed. In the first way, an exact definition of the medium is given, and a direct numerical integration technique is used to solve the set of those differential equations. The second way implies that the exact analytical techniques are applied to an approximated model of the medium that may have the elastic parameters varying along one or more directions of heterogeneity. In the following, we introduce the analytical solution valid for a flat layered halfspace that constitutes the base of knowledge for the treatment we will develop for the models with the lateral discontinuities.

Let us consider a halfspace in a system where the Cartesian coordinates are the vertical z-axis positive downward and the free surface, where the vertical stresses are null and thus defined by the plane z=0 (Figure 5.1).
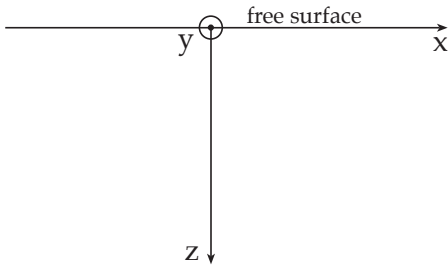
Figure 5.1. Adopted reference system for a vertically heterogeneous halfspace.

Let us assume that l, m, and r are piecewise the continuous functions of z, and that the body wave velocities, $\alpha = \sqrt{\frac{\lambda + 2\mu}{\rho}}$ and $\beta = \sqrt{\frac{\mu}{\rho}}$, assuming their largest value, a_H and b_H, when $z > H$, remain constant for the greater depths. If the elastic parameters depend only upon the vertical coordinate, using Equation 5.1, Equation 5.2 becomes:

$$\rho \frac{\partial^2 u_x}{\partial t^2} = \rho X + (\lambda + 2\mu)\frac{\partial^2 u_x}{\partial x^2} + (\lambda + \mu)\frac{\partial^2 u_y}{\partial x \partial y} + (\lambda + \mu)\frac{\partial^2 u_z}{\partial x \partial z}$$

$$+ \mu \frac{\partial^2 u_x}{\partial y^2} + \mu \frac{\partial^2 u_x}{\partial z^2} + \frac{\partial \mu}{\partial z}\frac{\partial u_x}{\partial z} + \frac{\partial \mu}{\partial z}\frac{\partial u_z}{\partial x}$$

$$\rho \frac{\partial^2 u_y}{\partial t^2} = \rho Y + (\lambda + 2\mu)\frac{\partial^2 u_y}{\partial y^2} + (\lambda + \mu)\frac{\partial^2 u_x}{\partial x \partial y} + (\lambda + \mu)\frac{\partial^2 u_z}{\partial x \partial z}$$

$$+ \mu \frac{\partial^2 u_y}{\partial x^2} + \mu \frac{\partial^2 u_y}{\partial z^2} + \frac{\partial \mu}{\partial z}\frac{\partial u_y}{\partial z} + \frac{\partial \mu}{\partial z}\frac{\partial u_z}{\partial y}$$

$$\rho \frac{\partial^2 u_z}{\partial t^2} = \rho Z + (\lambda + 2\mu)\frac{\partial^2 u_z}{\partial z^2} + (\lambda + \mu)\frac{\partial^2 u_x}{\partial x \partial z} + (\lambda + \mu)\frac{\partial^2 u_y}{\partial x \partial z}$$

$$+ \mu \frac{\partial^2 u_z}{\partial x^2} + \mu \frac{\partial^2 u_z}{\partial z^2} + \frac{\partial \lambda}{\partial z}\left(\frac{\partial u_x}{\partial x} + \frac{\partial u_y}{\partial y} + \frac{\partial u_z}{\partial z}\right) + 2\frac{\partial \mu}{\partial z}\frac{\partial u_z}{\partial z}$$

(5.3)

The boundary conditions that must be satisfied when solving Equation 5.3 are the free surface condition at z=0. The complete solution of Equation 5.3 can be represented in an integral form. At large distances from the source, compared with the wavelength, the main part of the solution is given by Rayleigh and Love modes (see e.g., Levshin (1973) and Aki and Richards (1980)).

By neglecting the body forces, we can consider solutions of Equation 5.3 having the form of the plane harmonic waves propagating along the positive x axis:

$$\mathbf{u}(\mathbf{x}, t) = \mathbf{F}(z)e^{i(\omega t - kx)} \tag{5.4}$$

The source is introduced in the medium representing the fault, which itself is supposed to be a planar, as a discontinuity in the displacement and shear stresses fields, with respect to the fault plane. On the contrary, the normal stresses are supposed to be continuous across the fault plane. Maruyama (1963) and Burridge and Knopoff (1964) demonstrated with the representation theorem the rigorous equivalence of the effects between a faulted medium with a discontinuity in the displacements and shear stress fields, and an unfaulted medium where the proper body forces are applied.

Following the procedure proposed by Kausel and Schwab (1973), we assume that the periods and wavelengths, which we are interested in, are large compared with the rise time and the dimensions of the source. Therefore, the source function, describing the discontinuity of the displacement across the fault, can be approximated by a step function in time and a point source in space. Furthermore, if the normal stress is continuous across the fault, then for the representation theorem the equivalent body force in an unfaulted medium is a double-couple with a null total moment. With this assumption, the eigenvalues and eigenfunctions of the problem are already determined; we can write the expression for the displacement with varying time, i.e., the synthetic seismogram, for the three components of motion. The asymptotic expression of the Fourier transforms of the displacement $\mathbf{U} = (U_x, U_y, U_z)$, at a distance r from the source, can be written as $U = \sum_{m=1}^{\infty} {}^m U$, where m is the mode index and:

$$^m U_x(r, z, \omega) = \frac{e^{-\frac{3}{4}i\pi}}{\sqrt{2\pi}} \left[\chi_R(h_s, \varphi)S(\omega)\frac{\sqrt{k_R}e^{-ik_R r - \omega r C_{2R}}}{\sqrt{r}}\frac{\epsilon_0 u_x(z, \omega)}{2c_R v_{gR} I_{1R}} \right]_m$$

$$^m U_y(r, z, \omega) = \frac{e^{-\frac{3}{4}i\pi}}{\sqrt{2\pi}} \left[\chi_L(h_s, \varphi)S(\omega)\frac{\sqrt{k_L}e^{-ik_L r - \omega r C_{2L}}}{\sqrt{r}}\frac{u_x(z, \omega)}{2c_L v_{gL} I_{1L}} \right]_m \tag{5.5}$$

$$^m U_z(r, z, \omega) = {}^m U_x(r, z, \omega)\frac{e^{-\frac{i\pi}{2}}}{\epsilon_0}$$

The suffixes R and L refer to the quantities associated with Rayleigh and Love modes, respectively.

In Equation 5.5, $S(\omega) = |S(\omega)| \exp[i \cdot \arg(S(\omega))]$ is the FT of the source time function while $\chi(h_S, \varphi)$ represents the azimuthal dependence of the excitation factor (Ben-Menhaem and Harkrider, 1964)

$$\chi_R(h_s, \varphi) = d_0 + i(d_{1R} \sin \varphi + d_{2R} \cos \varphi) + d_{3R} \sin 2\varphi + d_{4R} \cos 2\varphi$$

$$\chi_L(h_s, \varphi) = \qquad i(d_{1L} \sin \varphi + d_{2L} \cos \varphi) + d_{3L} \sin 2\varphi + d_{4L} \cos 2\varphi$$

(5.6)

with:

$$d_0 = \frac{1}{2} B(h_s) \sin \lambda \sin 2\delta$$
$$d_{1R} = -C(h_s) \sin \lambda \cos 2\delta \qquad\qquad d_{1L} = G(h_s) \cos \lambda \sin \delta$$
$$d_{2R} = -C(h_s) \cos \lambda \cos \delta \qquad\qquad d_{2L} = -G(h_s) \sin \lambda \cos 2\delta$$
$$d_{3R} = A(h_s) \cos \lambda \sin \delta \qquad\qquad d_{3L} = \frac{1}{2} V(h_s) \sin \lambda \sin 2\delta$$
$$d_{4R} = -\frac{1}{2} A(h_s) \sin \lambda \sin 2\delta \qquad\qquad d_{4L} = V(h_s) \cos \lambda \sin \delta$$

(5.7)

where φ is the angle between the strike of the fault and the direction obtained connecting the epicenter with the station, measured anticlockwise; h_s is the focal depth; δ is the dip angle and λ is the rake angle (see Figure 5.2). The functions of h_S that appear in Equation 5.7 depend on the values assumed by the eigen functions at the hypocenter

$$A(h_s) = -\frac{u_x^*(h_s)}{u_z(0)}$$

$$B(h_s) = -\left(3 - 4\frac{\beta^2(h_s)}{\alpha^2(h_s)}\right) \frac{u_x^*(h_s)}{u_z(0)} - \frac{2}{\rho(h_s)\alpha^2(h_s)} \frac{\sigma_{zz}^*(h_s)}{\dot{u}_z(0)/c}$$

$$C(h_s) = -\frac{1}{\mu(h_s)} \frac{\sigma_{zx}(h_s)}{\dot{u}_z(0)/c}$$

(5.8)

$$G(h_s) = -\frac{1}{\mu(h_s)} \frac{\sigma_{zy}^*(h_s)}{\dot{u}_y(0)/c}$$

$$V(h_s) = -\frac{\dot{u}_y(h_s)}{\dot{u}_y(0)} = \frac{u_y(h_s)}{u_y(0)}$$

where the asterisk, *, indicates the imaginary part of a complex quantity, i.e., u_x*, σ_{zz}*, and σ_{zy}* are real quantities. The details in proving the above equation was done by Panza et.al (2001).

The synthetic seismogram can be obtained with the three significant digits as long as the condition kr>10 is satisfied (Panza et. al., 1973), and a realistic kinematic model of a finite fault can easily be adopted (e.g., Panza and Suhadolc, 1987; Sarah et. al., 1998) in conjunction with the modal summation technique. The seismogram is computed by summing the time series radiated by the single point-sources with the appropriate time-shifts that are defined by the rupture process. The resultant time series show the great influence on the directivity, and the distribution of energy released in time may have influence on the synthesized ground motion (Panza et.al 2001).

At each site, the horizontal components (P–SV radial and SH transverse) synthetic seismograms are first computed for a seismic moment of 10^{-7} N m and then scaled to the magnitude of the earthquake using the moment–magnitude relation from Kanamori (1977). The finiteness of the source is accounted by scaling the spectrum using the spectral scaling law proposed by Gusev (1983) as reported by Aki (1987). For the period between 1 and 2 s, the Gusev spectral fall-off produces higher spectral values than the ω^{-2} spectral fall-off, and thus guarantees a conservative hazard computation (Vaccari 1995).

For the acceleration, the deterministic modeling can be extended to frequencies greater than 1 Hz by using the existing standard design response spectra (Panza et al., 1996). The design ground acceleration values are obtained by scaling the chosen normalized design response spectrum (normalized elastic acceleration spectra of the ground motion for 5 % critical damping) with the response spectrum computed at frequencies below 1 Hz. The design ground acceleration (DGA) is obtained through extrapolation using standard code response spectra following the procedure described by Panza et al. (1996).
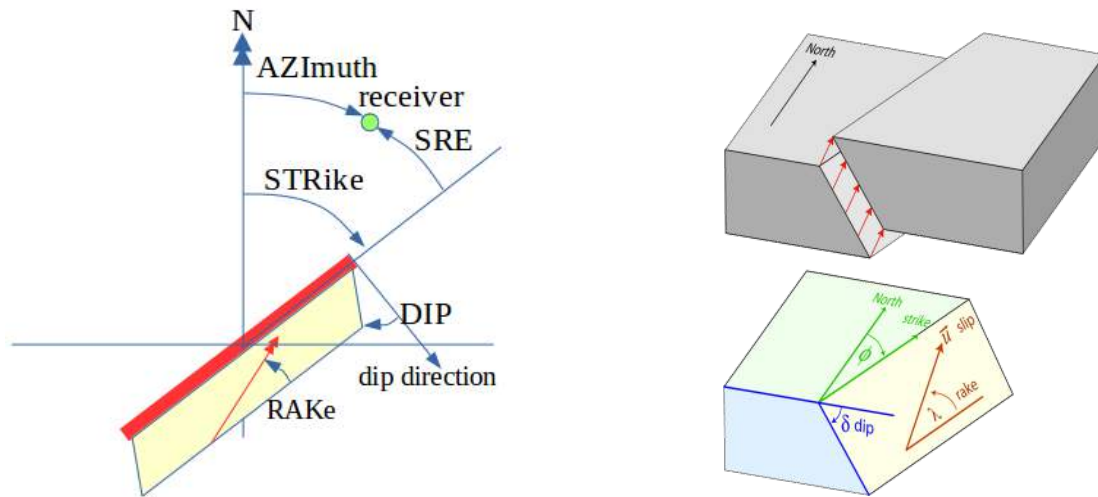
Figure 5.2. Angle conventions used for the source system.

5.2 Parametric Test for Modal Summation Technique

There are several approximations adopted to use the modal summation to generate a synthetic seismogram. In order to understand the synthetic seismogram and to define the effect of different input parameters in the resultant ground motion, the parametric test program can be carried out by running `eparatest.out`. The input parameters are described in detail in the filename `eparatest.par` with a fixed format, (e.g. SRE, DIP), see Listing 5.1. A quick reference manual for this original version of 1D Modal Summation Technique parametric test is supplied by Vaccari (2015m).

```
Parameter file for program eparatest
--------------------------------------------------------------------------------
svalp                   Test label (root for output filenames - 13 chars max)
0                       Ref. box for values not listed below (0=no, 13 chars max)
svalp.spl               Love spectrum file
svalp.spr               Rayleigh spectrum file
2                       Motion (1=displ, 2=vel, 3=acc)
50                      Time length for plot seismograms (s)
1 13.0 45.0 80          Source (1=point, 2=extended), lon, lat, strike (Nord)
SRE 1   0 360 15        Strike (loop 0=no,1=yes, start, stop, step) (Degrees)
DIP 0  30  90 10        Dip (loop 0=no,1=yes, start, stop, step) (Degrees)
RAK 0  10  40 10        Rake (loop 0=no,1=yes, start, stop, step) (Degrees)
SDE 0   7   9  1        Source Depth (loop 0=no/1=yes, start, stop, step) (km)
EDI 0  15 200 15        Epic. Distance (loop 0=no/1=yes, start, stop, step) (km)
RDE 0   0   3  1        Receiver Depth (loop 0=no/1=yes, start, stop, step) (km)
MOD 0   0   0  1        Modes (loop 0=no/1=yes, start, stop (step must be 1) )
INT 0   1  30  1        Interpolation (0-9) (flag 0=no,1=yes, start, stop, step)
MAG 0 6.5 7.0 .1        Magnitude (flag 0=no,1=yes, start, stop, step)
```

Listing 5.1 Original version parametric test (file name: `eparatest.par`)

```
Parameter file for program readpar2.out
--------------------------------------------------------------------------------
tak1                    Test label (root for output filenames - 13 chars max) (*)
0                       Ref. box for values not listed below (0=no, 13 chars max)
sumg.por                Polygon file
2                       Motion (1=displ, 2=vel, 3=acc) (*)
50                      Time length for plot seismograms (s)(*)
1                       Source (1=point, 2=fix dir,   3=auto dir, 4=ext true)
96.665  4.645           Epicentral coordinates (Lon, Lat, Degrees)(*)
--------------------------------------------------------------------------------
0./Gusev/               Path to scaling curves (0=call pulsyn)(*)
gbilpx                  Name of file(s) for scaling (for source type 2)
../ita001.src           Reference .src file (0=auto) (not used for pre-computed scaling curves)
--------------------------------------------------------------------------------
SPX "s/shof"
#SPX "s/shtf"
#s/shtf0006.spx         #this for uniform structural spectral
#2013-07-02T07:37:02.61 6.1 Mw 4.645 96.665 13.0 Northern Sumatra, Indonesia # 315 80 170
SUT 96.665    4.645     13.0         315 80 170    6.1       Takengon
STR 0  315 100  5       Fault strike (Degrees)(*)
#     96.4040   4.2668  0007    0.000   MLSI
#OBS 96.4040   4.2668   MLSI
#EDI 50.958, SRE 100.471 MLSI
#CEL 0.1
#AZI 0  30 60  10
#DIP 0  80  90 10       Dip (loop 0=no,1=yes, start, stop, step) (Degrees)(*)
#DIP 1 30   80 50       Dip (loop 0=no,1=yes, start, stop, step) (Degrees)(*)
RAK 0  170  40 10       Rake (loop 0=no,1=yes, start, stop, step) (Degrees)(*)
SDE 0  13.0  15  2      Source Depth (loop 0=no/1=yes, start, stop, step) (km)(*)
EDI 1  2 70 2      Epic. Distance (loop 0=no/1=yes, start, stop, step) (km)(*)
#EDI 50
SRE 0  100  110 10    Strike-Receiver (loop 0=no,1=yes, start, stop, step) (Degrees)
#SRE 2  0  360  5     Strike-Receiver (loop 0=no,1=yes, start, stop, step) (Degrees)
RDE 0  0   3  1       Receiver Depth (loop 0=no/1=yes, start, stop, step) (km)(*)
MOD 0  0  9  1        Modes (loop 0=no/1=yes, start, stop (step must be 1) )(*)
INT 0  1  10  1       Interpolation (0-9) (flag 0=no,1=yes, start, stop, step)(*)
MAG 0  6.1 7.0 .3     Magnitude (flag 0=no,1=yes, start, stop, step)(*)
#DIR 0 180 180 0
#XST 0 -0.5 0.5 0.5   X-coord nucleation point (-0.5 - 0.5) (along strike)
#YST 0 -0.5 0.5 0.5   Y-coord nucleation point (-0.5 - 0.5) (along dip)
#XSZ 0  5 10 1        X-Size (km along strike) (flag -1=auto)
#YSZ 0  3 10 1        Y-Size (km along dip)    (flag -1=auto)
#MAC 0  0.7 0.9 0.1      Mach number for rupture velocity computation
#RND 0  1  120 1      Random seed for source time function gen. (0=Fix, 1=Variate)
#RRR 010           # if 1 set to initial and also for loop (000=Slip,Rup.Vel,Time Hist) I71,I72,I73
frame 95 100 2 6
COM  rad tra rzz sns sew res
ALL d v a dga
```

Listing 5.2 Updated version parametric test, rich of high flexibility features for user

We developed a new updated version of the parametric test routine which involves the new features and advantages e.g. the flexible configuration file and the polar plot, integrated with an

extended source. The new proposed routine is more flexible (user-friendly) in editing and adding some notes relative to a relatively rigid format now in use (see Listing 5.2). The main motivation for updating the existing parametric test routine is to easily handle the spectral structural information from the regional polygon (i.e. `sumg.por`). Moreover, it is capable of addressing the extended source, but it will not be discussed in this thesis because it needs a better understanding of the extended source mechanism and the related parameters, those of which could be developed in a future study.

There are two ways for executing this updated parametric test routine: without and/or with a passing parameter. Without a passing parameter, the test routine will read the default configuration file `eparatest.par`, and with a passing parameter, there is a possibility the test routine reads another filename, e.g.:

```
readpar2.exe
readpar2.exe paratest2.par
```

Executing the command will generate several configuration files needed by the modal summation procedure, plotting procedure, and script `par2job.sh` to run all the commands sequentially. There are possible 3 categories input styles for each line:

(1) sequential header input style: the number or text given in order per line sequentially.

```
tak1                    Test label (root for output filenames - 13 chars max) (*)
0                       Ref. box for values not listed below (0=no, 13 chars max)
2                       Motion (1=displ, 2=vel, 3=acc) (*)
50                      Time length for plot seismograms (s)(*)
1                       Source (1=point, 2=fix dir,   3=auto dir, 4=ext true)
96.665  4.645            Epicentral coordinates (Lon, Lat, Degrees)(*)
----------------------------------------------------------------
0./Gusev/               Path to scaling curves (0=call pulsyn)(*)
gbilpx                  Name of file(s) for scaling (for source type 2)
../ita001.src           Reference .src file (0=auto) (not used for pre-computed scaling curves)
```

the line ------- or beginning with # will be ignored .

(2) tag identification input style: in which a number or text can be used to set some variables or features depending on our choice. For example, to apply a loop in an epicenter distance `EDI 1 2 70 2`, also it is possible to set a constant distance `EDI 50`. The example with the text input is `ALL d v a dga` and `SPX "s/shtf"`.

(3) extension filename input style: in which we need only to insert the filename, and the parameters will be defined by their extension (not depending on a line). The filename should follow the convention, for example, `sumg.por`.

The existing parametric test has maximum two loops per run to systematically change the variables being used. The null loop will only generate a synthetic seismogram, the single loop will

produce result with a single arbitrary variable, for example, that of in Figure 5.6, in which the looping is applied for the epicenter distance EDI. The double loop will produce the results for 2 arbitrary variables such as those shown in Figure 5.3 EDI and STR. Additionally, the figure shows the advantages of the modal summation for calculating the strong ground motion, which could take into account the angular radiation pattern. Figure 5.5 shows the capability of using a regional structural polygon, which could produce PGA with a more realistic pattern based on the structural condition being in use. Figure 5.4 (right) and (left) show that the adoption of different cutoff frequencies is not affecting the radiation pattern but is affecting the maximum value of PGA.
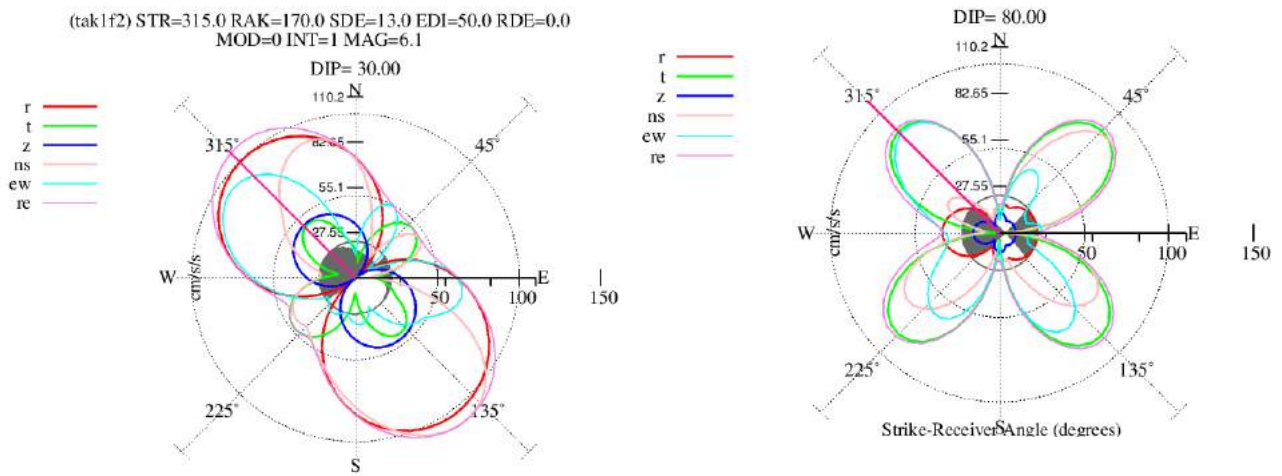
Figure 5.3 Angular radiation pattern generated with change of variable SRE and EDI with uniform structural model s/shtf0006.sp?
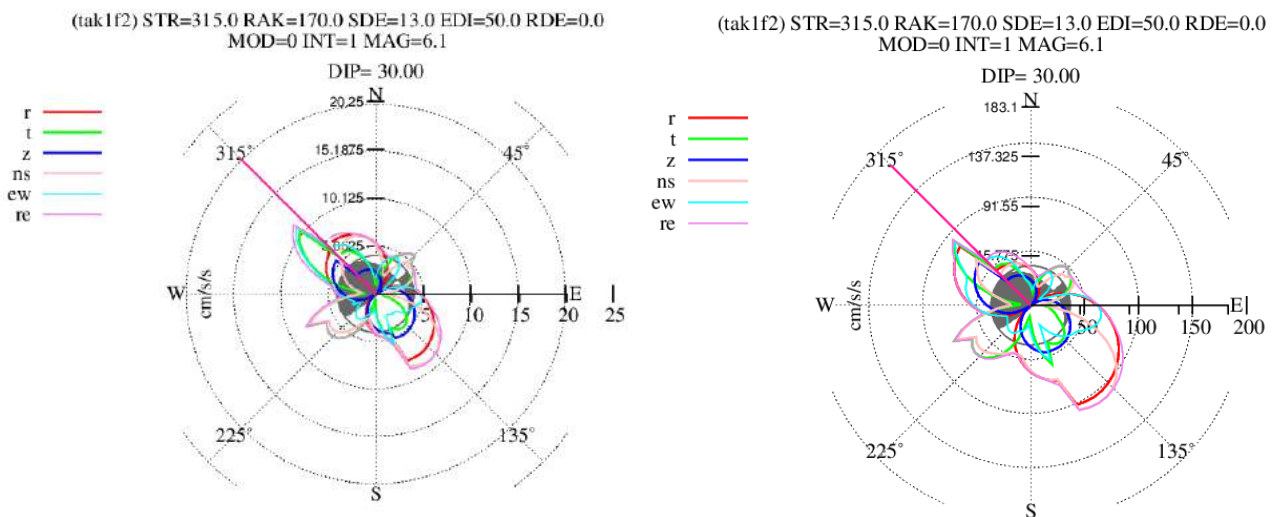
Figure 5.4 Angular distribution pattern for PGA at 1hz cutoff reaches values above 10. cm/s^2 (left) and at 10hz cutoff the PGA reaches values above 90. cm/ s^2 (right)

Figure 5.5 shows the parametric test for a single loop in EDI (an epicenter distance). There is no difference in PGD estimated with a different cutoff frequency i.e. 1Hz and 10Hz , as it is natural since, as a rule, the displacement peaks at periods larger than 1s (i.e. frequency below 1hz). The PGV is different (about by a factor of 2) when using 1Hz and 10Hz max frequency. In contrast, the PGA shows a significant difference between 1Hz and 10Hz based run, about a factor of 5. As a consequence, there is a clear limitation in the use of modal summation technique for earthquakes with the epicentral distance (EDI) less than the source depth (SDE) especially for estimating the PGA. Therefore, for the future development, the modal summation method should be combined with another method, such as DWN (Discrete Wave Number) (Pavlov 2002, 2009, Magrin, 2013).
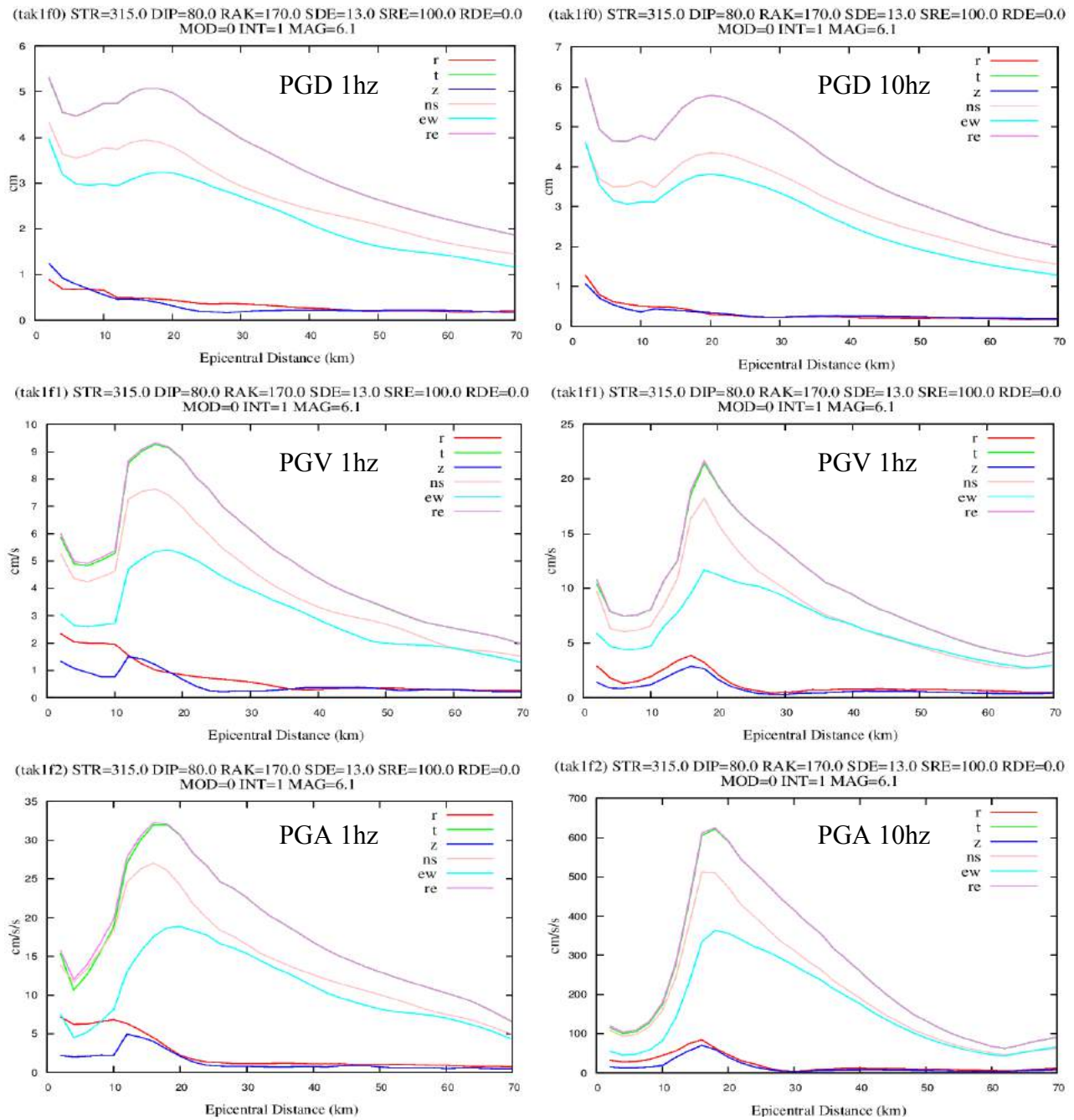
Figure 5.5 Radial distributions of PGD (top), PGV (middle), PGD (bottom) with maximum frequencies 1Hz (left) and 10Hz (right) for several components differentiated by color line.

5.3 Validation to the Takengon Earthquake 2013 M6.1

One of the recent destructive earthquakes originated at the Sumatra fault system was on 2 July 2013, where the earthquake was with magnitude 6.1 and geodynamical investigate by AGNeSS network (Ito et al. 2016). The earthquake struck near Takengon, the capital city of the Central Aceh Regency in North Sumatra. This event caused significant casualties and damage of the property. At least 42 people were killed, 2,500 injured, 6 missing, 53,339 displaced, and 20,401 buildings destroyed in the Bener Meriah-Central Aceh area. One person was killed by a landslide in Bener Meriah. Several landslides damaged roads, cutting off an access to 9 villages. The earthquake was felt with the Intensity Modified Mercalli Intensity Scale (MMI IV) in Banda Aceh, Lhokseumawe, and Takengon,, with (MMI III) in Medan, with (MMI III) in Georgetown and Gelugor (Malaysia) including Ayer Itam, Balakong, Butterworth, Petaling Jaya, Sungai Ara, and Tanjong Bunga, and in Phuket (Thailand) as reported by USGS (USGS 2013).
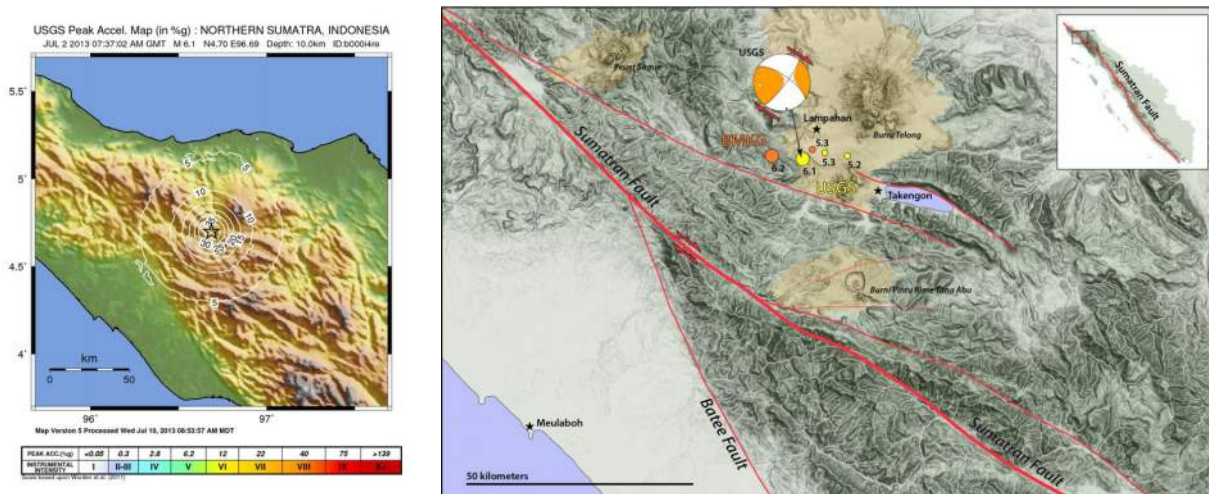
Figure 5.6 (left) Shaking map from USGS; (right) First-order interpretation of the tectonic settings around the epicenter of the Mw 6.1 earthquake of July 2, 2013.
http://www.earthobservatory.sg/news/magnitude-61-earthquake-hits-northern-sumatra

Table 5.1 Information from USGS about Takengon Earthquake

Origin

Catalog	Mag	Time	Depth	Status	Location
✔ US	6.1 mww	07:37:02	13.0	REVIEWED	4.645 °N 96.665 °E

Focal Mechanism

Catalog	Mechanism	Nodal Plane 1 Strike,Dip,Rake	Nodal Plane 2 Strike,Dip,Rake	Source
✔ US		(315°,80°,170°)	(47°,80°,10°)	US[3]

The following earthquake parameters obtained by USGS will be used to carry out the parametric test

```
#2013-07-02T07:37:02.61 6.1 Mw 4.645 96.665 13.0 Northern Sumatra, Indonesia
SUT 96.665   4.645    13.0        315 80 170   6.1       Takengon
```

The resulted map is computed using 0.1x0.1 degree grid space

```
CEL 0.1   # for generate PGV and PGA map
```

USGS provides detailed information about the Takengon of 2 July 2013 M=6.1 earthquake, and the shake map is available as well and can be obtained from the USGS website at http://earthquake.usgs.gov/earthquakes/shakemap/global/shake/b000i4re. The shake map provides information about the PGV and PGA (Figure 5.7-top-left) in a numeric digital format which allows for comparison with the obtained results from the updated version of the parametric test.
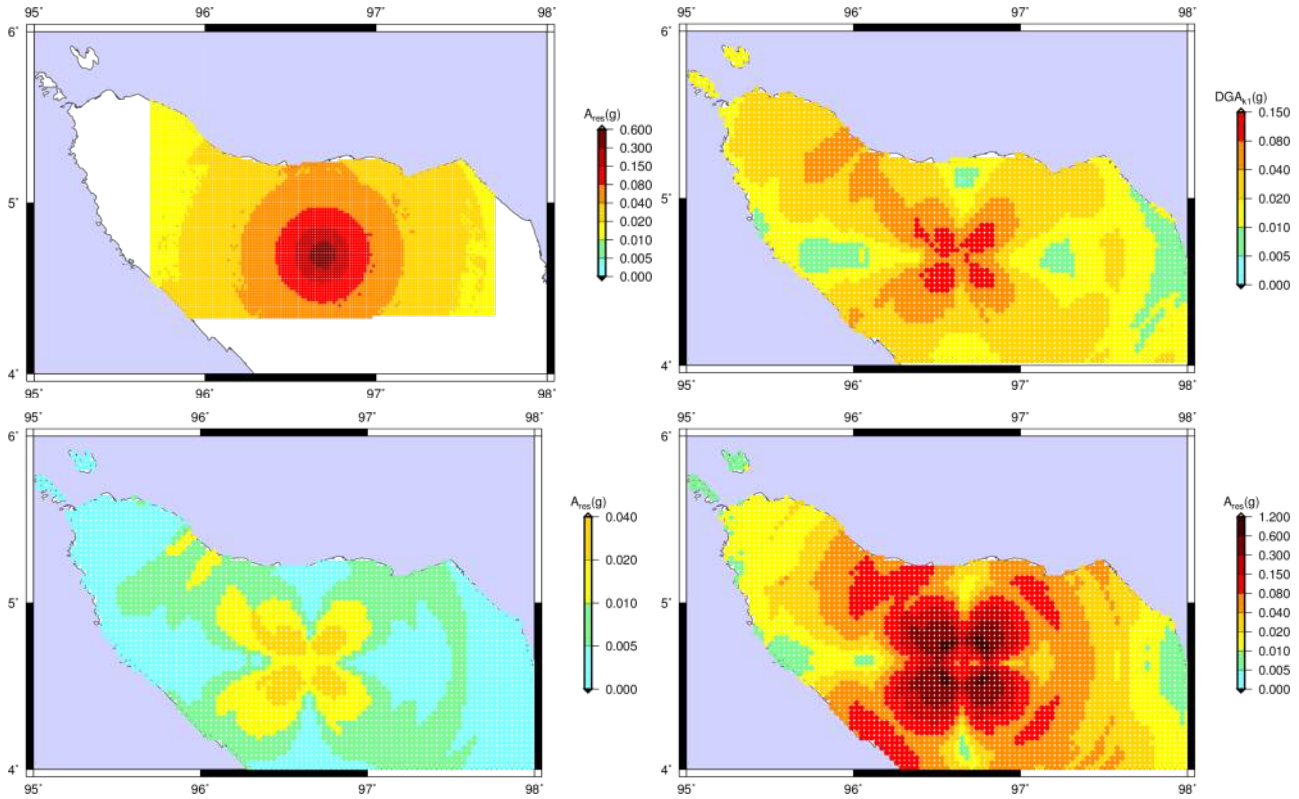
Figure 5.7. (top-left) PGA from USGA shake map (top-right) DGA at 1hz cutoff calculation
(bottom-left) PGA at 1hz cutoff calculation (top-right) PGA at 10hz cutoff calculation
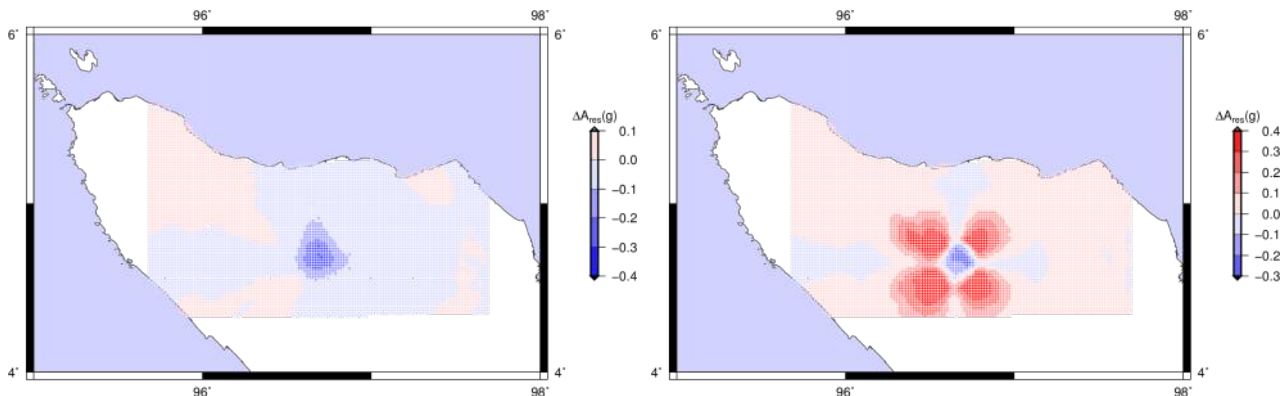
Figure 5.8. (left) Difference: DGA 1hz cutoff – USGS PGA (g);
(right) Difference: PGA 10hz cutoff – USGS PGA (g)

The values given in the shake map from USGS have a quite uniform angular distribution, that cancels any source mechanism effect, whereas the modal summation has the advantage to

produce an angular distribution of the radiation pattern that preserves the signature of the focal mechanism. The DGA at 1hz and the PGA at 10hz is similar to the PGA in the shake map, and Figure 5.8 shows the difference. The PGA computed at 10Hz cutoff frequency reaches a value larger than the one from the shake map and shows a well defined radiation pattern.

The PGV from the USGS shake map is shown in Figure 5.9 (top-left) and also has no specific angular distribution regarding the focal mechanism. The PGV produced by 10Hz and 1Hz computations are shown in Figure 5.9 (top-right) and figure 5.9 (bottom-left). The difference between the PGV estimated by the modal summation technique and the PGV obtained by the USGS shake map is shown in Figure 5.10. The PGV at 1Hz computation is lower than the PGV from the shake map, whereas the estimated PGV based on 10 Hz computation shows a greater value.

Figure 5.9 PGV for Takengon earthquake M6.1
(top-left) PGV from USGA shake map
(top-right) PGA at 10hz calculation
(bottom-left) PGA at 1hz calculation

Figure 5.10 (left) Difference: PGV 1hz – USGS PGV (cm/s)
(right) Difference: PGV 10hz – USGS PGV

72

(a)

(b)

(c)
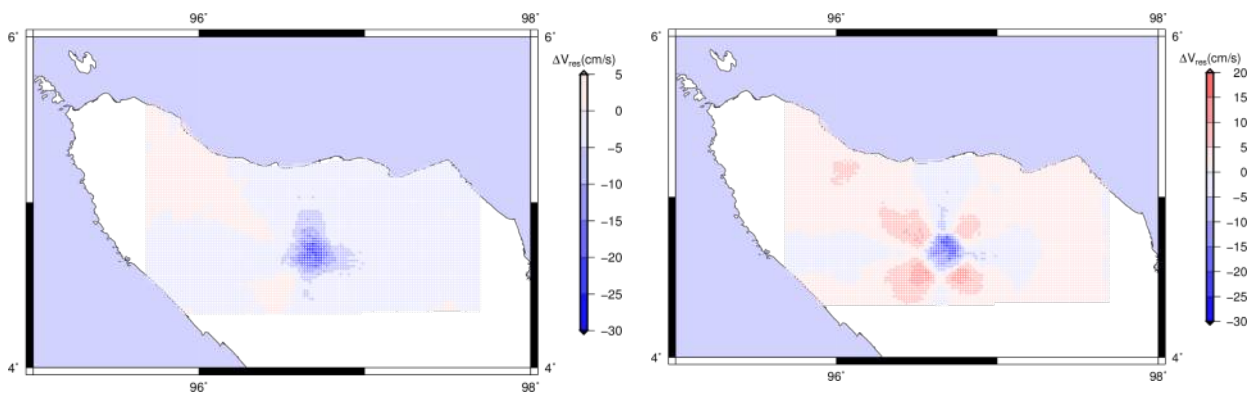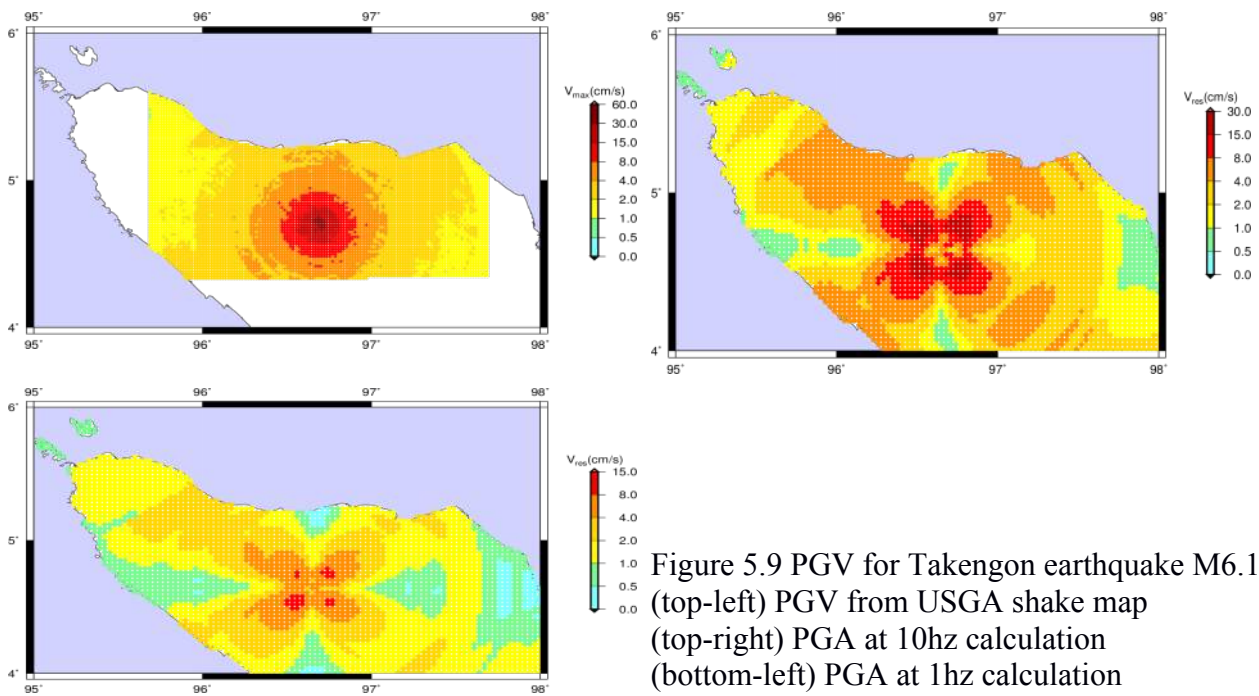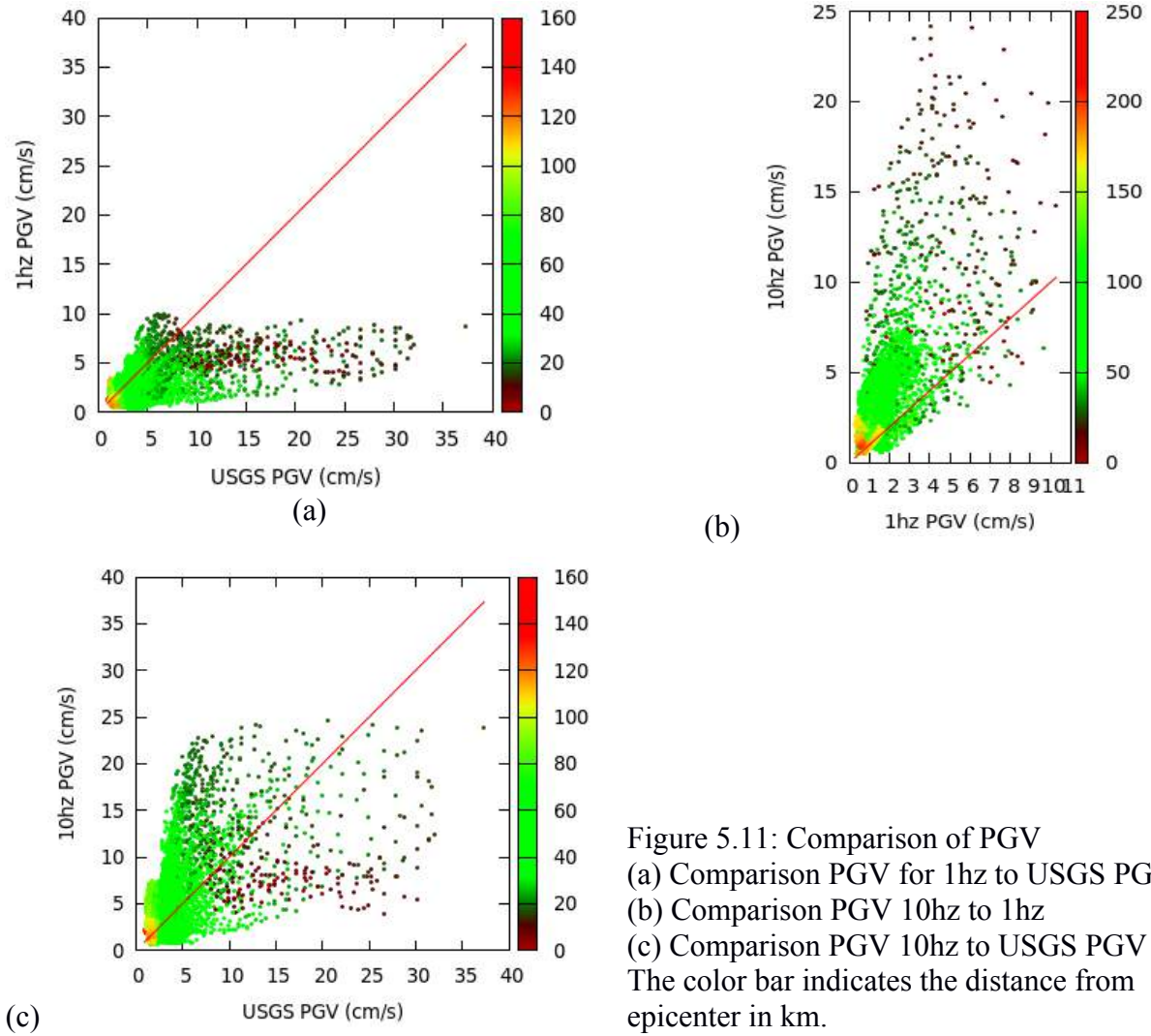
Figure 5.11: Comparison of PGV
(a) Comparison PGV for 1hz to USGS PGV
(b) Comparison PGV 10hz to 1hz
(c) Comparison PGV 10hz to USGS PGV
The color bar indicates the distance from epicenter in km.

The difference between the PGV and PGA values estimated by the modal summation technique and obtained by the USGS shaking map is clearly illustrated in Figures 5.8 and 5.10. Figures 5.11 and 5.12 show the comparative strong ground acceleration obtained by several methods. Figure 5.11a shows the PGV at 1Hz generally has the value lower than the PGV from USGS because the 1Hz calculation might underestimate the PGV value as shown in Figure 5.11b compared with the PGV with 10Hz computation. The PGV computed at the cutoff frequency of 10Hz and the PGV from USGS will have small difference with large scattering as shown in Figure 5.11c.

Figure 5.12 illustrates the difference in the PGA from USGS at the 1Hz and 10Hz computations, and the DGA from the 1hz computation. The PGA at 1Hz computation obviously gives lower value than the PGA from USGS at 10Hz computation does. The DGA compares well with that of from the USGS shake map (Figure 5.12c) and remains lower in value than the PGA at 10Hz computation. Finally, the PGA estimated at 10Hz computation is strongly influenced by the structural model being used, meanwhile the value is quite comparable to the PGA from the USGS shake map as inferred from Figure 5.12e.
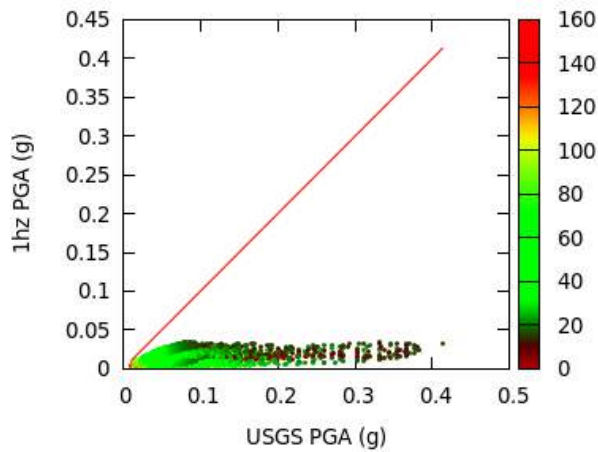
(a)
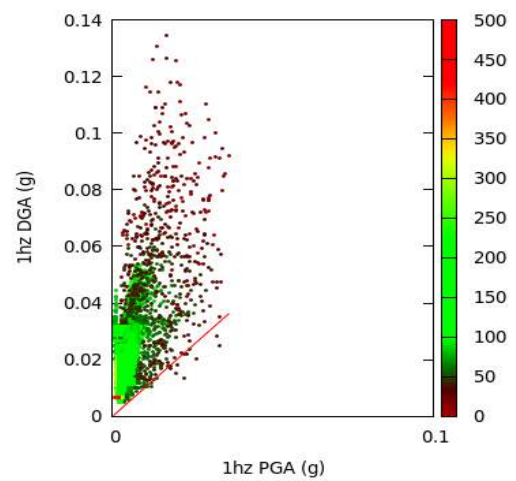
(b)
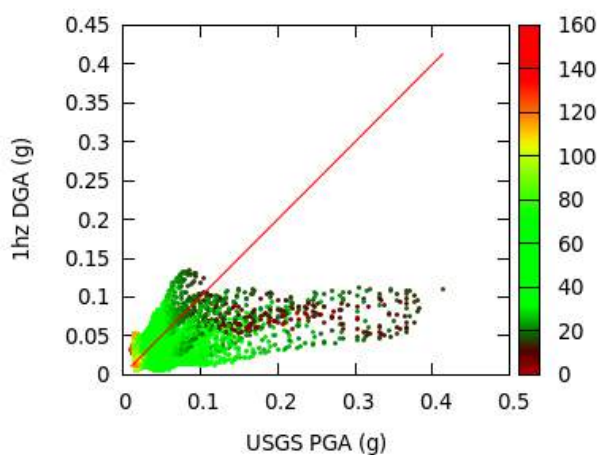
(c)
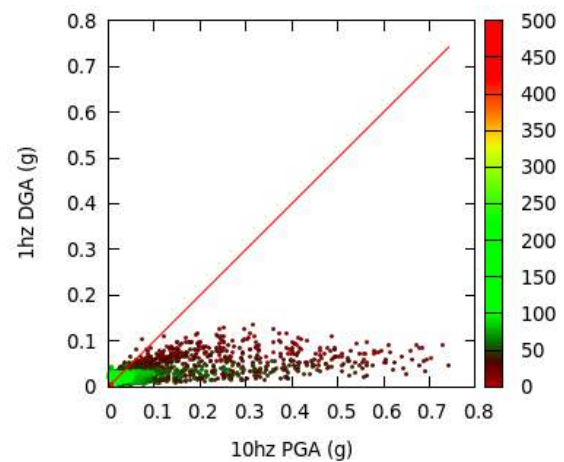
(d)
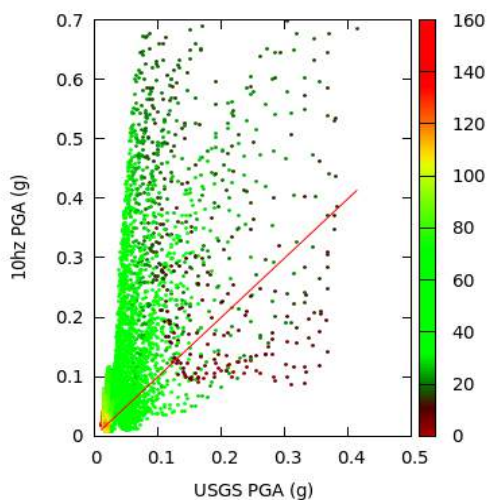
(e)

Figure 5.12: This figure shows the comparative strong ground acceleration from several methods. The color bar indicates the distance from epicenter in km.
(a) PGA for 1hz maximum frequency extremely lower than that of USGS data
(b) Using the DGA method to estimate the expected PGA
(c) DGA getting from 1hz calculation is a better approach to meet the USGS PGA
(d) PGA calculated at 10hz significantly greater than PGA calculated at 1hz
(e) PGA at 10hz has the best approach to the USGS PGA with huge scattered relationship

5.4 Comparison with the Observed Intensity for the Takengon Earthquake

The macroseismic intensity estimation can be done for the areas where the seismic stations are not available so far. The macroseismic intensity has traditionally been used worldwide as a method for quantifying the shaking pattern and the extent of damage for earthquakes. Before the advent of the modern instrumental seismometer, it nonetheless provides a useful mean of describing the complexity of ground motion. The importance of macroseismic intensity data has led to several variants of the original, XII degrees, Mercalli scale (I_{MCS}). So far the most popular are $I_{MSK} \sim I_{EMS-92} \sim I_{MM} \sim (5/6) I_{MCS}$.

The presence and evaluation of the intensity data represent a very significant set of data needed to carry out accurate seismic analysis, in the seismic sources identification and validation of the resultant seismic hazard maps. Seismic intensities will continue to be of value for the earthquake analysis (Wald, 1999). Seismic intensity can cover the area near the source of an earthquake and it can be compared with the peak values of the synthetic strong ground motion and the intensity taken from a field survey.

In the case of the destructive Takengon earthquake on 2 July 2013, several collections of intensity data are available. When the earthquake happened, Prof. Takeo Tabei and I were standing at SGMT (Singah Mata) for a GPS observation. We felt a medium shake with the intensity IV MMI. The second set of intensity data is provided by the USGS website from the instrumental intensity BKNI, GSI, LHMI, PSI, and 3 manual observations, the data of which can cover a distance site. The last intensity data are obtained from Ibnu Rusdy (2016) and involve about 129 intensity data points, concentrated at the near source sites observed by Unsyiah (University of Syiah Kuala), see Figure 5.13. We choose intensity scale in MMI to be consistent with all data given by USGS and Unsyiah team. A selection of destructed buildings during the 2013 earthquake is shown in Figure 5.14, and the considered data are shown in Table 5.2.

The survey was conducted by means of interviews with the local community, if no major damage can be observed. A field investigation was simultaneously performed to check the damage levels at the buildings around the affected area. The classification of the buildings adopted is what has been proposed by Richter (1958) and Musson et al. (2002). Based on the survey, it was found that the highest intensity reached IX MM around Ketol village while VI MM affected the buildings located about 7-8 km from the central destructed building (Rusydy et al., 2015). Most of the survey by Unsyiah team follow the main road and the only focus for the near field with a radius less than 30km and only two the site with the distance 52km and 82km. Whereas, the nearest station from USGS 70km at LHMI and 682km at BKMI. The position of the SGMT team when the earthquake happened is about 34km from the epicenter.
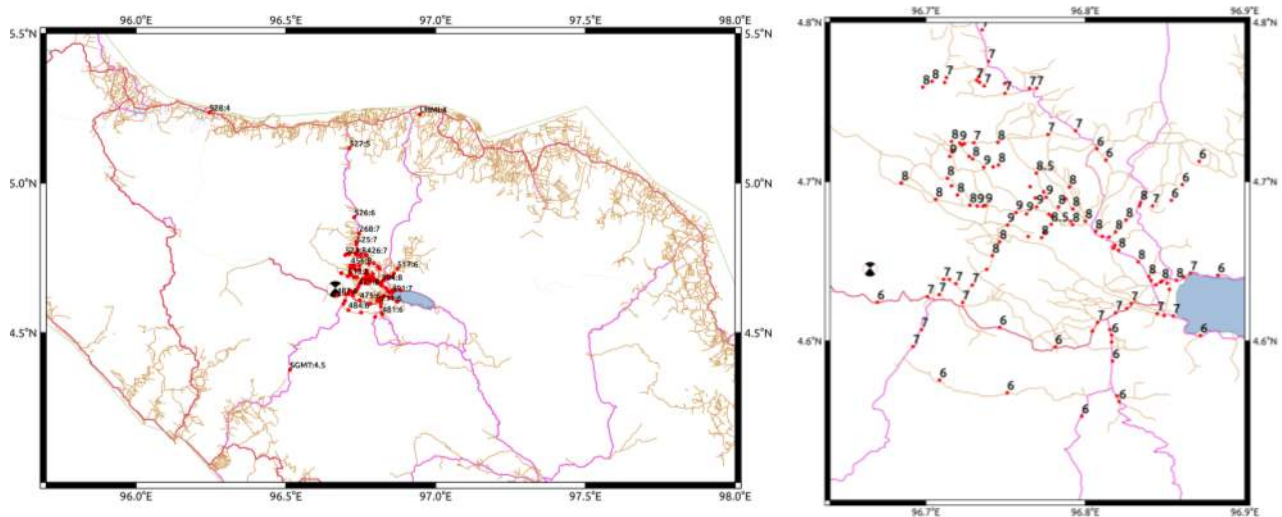
Figure 5.13. Distribution of sites survey for intensity overlay on the road for wide area (left) and for focus area for near field (right)

SD 3 Ketol, IX MMI, (4°41'5.84" N, 96°44'14.61"E), site label: 461

Unsyiah VII MMI, site label unsyia

Mesjid Kute Panang, IX MMI, (4°41'20.91"N, 96°47'16.00"E), site label 438

Private Home, VIII MMI, site label: 457

Figure 5.14 Selected destructive building (Dirhamsyah et. al 2013, Rusydy et. al 2015)

Table 5.2 Selected seismic intensity sites (I in MMI). Intensity values are expressed, coherently with the definition of any macroseismic scale by ordinal numbers, rounding off, when necessary, cardinal values not consistent with the rule.

No	Long.	Lat.	I (MMI)	label	dist (km)	PGA (gal)				PGV (cm/s)			
						USGS	1Hz	DGA	10Hz	USGS	1Hz	10Hz	collector
1	96.7878	4.6891	IX	**438**	14	234.50	17.24	31.56	194.80	18.26	4.48	7.35	Unsyiah
2	96.7754	4.6901	IX	443	13	266.33	18.36	33.51	170.20	21.01	4.67	6.01	Unsyiah
3	96.7739	4.6935	IX	444	13	266.67	19.16	35.26	178.10	21.04	4.88	6.25	Unsyiah
4	96.7789	4.6781	IX	446	13	248.62	15.45	26.88	137.20	18.79	3.95	5.06	Unsyiah
5	96.7359	4.6846	IX	460	9	344.67	17.22	33.91	93.09	28.60	4.36	5.19	Unsyiah
6	96.7374	4.6850	IX	**461**	9	331.78	17.42	34.01	94.96	27.26	4.37	5.17	Unsyiah
7	96.7227	4.7231	VIII	454	11	345.76	22.46	43.55	143.30	28.73	5.64	6.07	Unsyiah
8	96.7161	4.7252	VIII	456	11	354.38	21.75	42.83	133.70	29.64	5.50	5.78	Unsyiah
9	96.7161	4.7193	VIII	**457**	10	358.53	21.18	42.72	123.90	30.11	5.29	5.85	Unsyiah
10	96.7117	5.116	V	527	52	52.19	1.27	3.02	6.94	4.60	0.37	0.60	Unsyiah
11	96.2438	5.2354	IV	528	80	27.63	5.39	15.42	33.91	2.57	1.44	3.61	Unsyiah
12	96.7495	4.7616	VII	unsyia	16	268.45	24.47	46.81	332.90	21.19	6.63	13.35	Unsyiah
13	101.0396	0.3262	1.5	BKNI	682	-	0.67	2.43	0.84	-	0.25	0.28	instrument
14	97.5755	1.3039	1.8	GSI	383	-	0.39	1.46	1.17	-	0.14	0.17	instrument
15	96.9472	5.2288	IV	LHMI	72	30.27	4.71	7.97	31.19	2.43	1.25	2.62	instrument
16	98.9237	2.6938	1.7	PSI	331	-	1.73	5.97	4.52	-	0.59	0.89	instrument
17	100.5	5.48	2.9	T001	435	-	0.39	2.52	0.56	-	0.15	0.15	USGS
18	100.31	5.37	2.7	T002	412	-	0.40	2.65	0.86	-	0.14	0.16	USGS
19	98.67	3.59	3.2	T003	251	10.14	1.32	4.36	3.95	0.85	0.48	0.64	USGS
20	96.5136	4.3758	IV	SGMT	34	54.98	13.39	24.74	151.10	4.04	3.51	5.58	author

However, most of the data distribute in the near field and only a few in the far field. We tried to investigate the correlation between the MM intensity with PGA from USGS shakemap and the intensity against PGA and DGA from 1Hz and 10Hz cutoff frequency computation, as shown in Figure 5.15, and the correlation between the intensity with PGV from USGS shakemap and PGA from 1Hz and 10Hz cutoff simulation as shown in Figure 5.16. In both pictures the PGA/PGV range (the pink vertical segment) is supplied for the ground motion for Modified Mercalli intensities given by Wald et al. (1999), see Table 5.3. There is no fundamental reason to expect a simple relationship between the PGA and the PGV with Intensity; however, following the pioneering work of Cancani (1904) a simple empirical approach with the power law representation is adequate for the range from V to VIII, as determined by Wald et al. (1999):

$$
\begin{aligned}
I_{mm} &= 3.66 \log_{10}(PGA) - 1.66 \\
I_{mm} &= 3.47 \log_{10}(PGV) + 2.35
\end{aligned}
\tag{5.9}
$$

with a unit for PGA(cm/s^2) and PGV(cm/s). We transformed those equations to follow the plotting green line in Figures 5.15 and 5.16, the equations become

$$
\begin{aligned}
PGA &= 10^{\frac{I_{mm}+1.66}{3.66}} \\
PGV &= 10^{\frac{I_{mm}-2.35}{3.47}}
\end{aligned}
\tag{5.10}
$$

Because the PGA in computation (Table 5.2) uses a unit gal (cm/s^2), but we preferred to present it in a unit %g to be more clear, we thus need to multiply it by a factor of 1/9.81 to make it PGA (%g)=PGA (gal)/9.81 as shown in Figure 5.15.

Table 5.3 Range for ground motion for Modified Mercalli intensities (Wald et al., 1999)

Intensity	I	II-III	IV	V	VI	VII	VIII	IX	X+
Peak Accel. (% g)	<0.17	0.17-1.4	1.4-3.9	3.9-9.2	9.2-18	18-34	34-65	65-124	>124
Peak Velocity (cm/s)	<0.1	0.1-1.1	1.1-3.4	3.4-8.1	8.1-16	16-31	31-60	60-116	>116
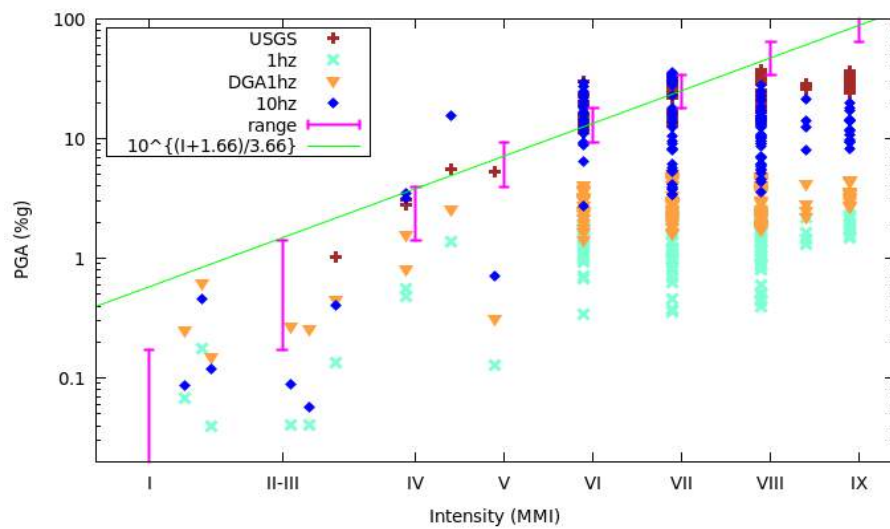
Figure 5.15. Correlation PGA (from USGS, 1Hz, DGA, and 10Hz) with Intensity survey, PGA range for MM (pink lines) and relationship from (Wald et al., 1999) (green line)
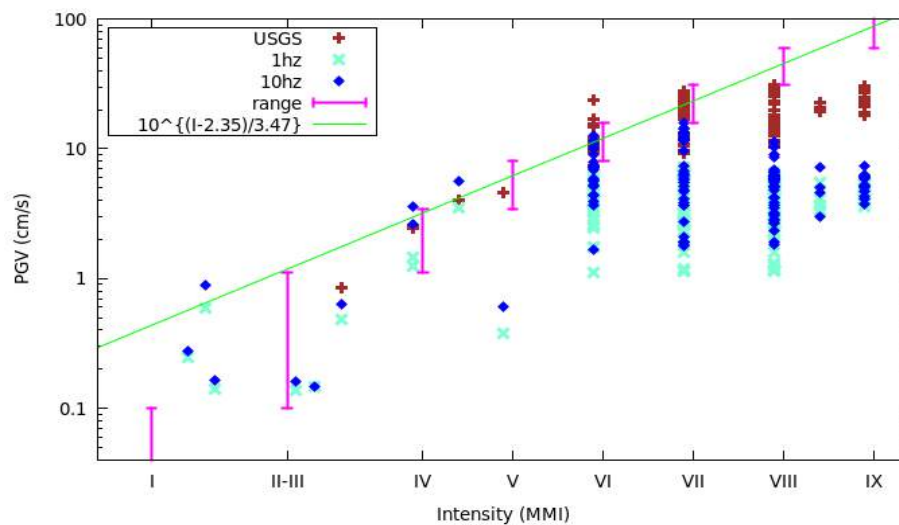
Figure 5.16. Correlation PGV (from USGS, 1Hz, and 10Hz) with Intensity survey, PGV range for MM (pink lines) and relationship from (Wald et al., 1999) (green line)

78

The PGA from the USGS shakemap are relatively higher in comparison with the other obtained results. The simulation with 1Hz cutoff gives a lower value of PGA than it does with 10Hz cutoff, as we could expect. DGA matches the PGA when computed at 10Hz cutoff at the far field sites only. The PGA from the 10Hz cutoff and the USGS shakemap fall within the PGA range obtained from the MM scale for all of the intensity level (in the pink segments range) except the VIII and IX intensity levels. The PGA variation from the simulation at 10Hz cutoff is wider in the variation than the USGS shakemap at the intensity levels VII and VIII. The PGA value from both (USGS and 10Hz computation) has a good agreement with the range of PGA starting from the intensity VI; the lower intensities (V or less) have limited data, and the PGA value from USGS is not always greater than the PGA value obtained from the 10Hz simulation. Although the limited data for intensity lower than V, the PGA value from 10Hz frequency falls within the range of PGA from MM.

As it is natural from earlier discussion, the PGV values from 1Hz and 10Hz simulations are not too different from those of the observed intensity compared with the PGA value from both simulations for all intensities. The PGV from the 10Hz simulation is lower than the PGV from the USGS shakemap as shown in Figure 5.16. The PGV values from the UGSS and the 10Hz simulation are compared with the PGV values from the MMI range. The resulted pattern from those PGV values is then compared with the pattern given out by the PGA values at intensity VII and IX. The two patterns are relatively similar. Although the PGV value from the USGS can reach the value in the range of the intensity VII, the PGV value from the 10Hz simulation cannot. Some PGV values from the 10Hz simulation are in the PGV range of MM at the intensity VI and lower.

The values of PGA and of PGV generated in the simulation are rather lower than the values of PGA and PGV given in Table 5.3 especially for the higher intensity. There are several factors affecting those PGA and PGV low values in the simulation. Firstly, the modal summation technique is valid for the sites at a distance equal 1.5 times the event focal depth. In the case of focal depth 13km, the synthetic PGA and PGV values will underestimate observations at distances less than 18km, as shown in Figure 5.5 for the 10Hz cutoff computation. Most of the sites, with the intensity greater than VIII, have the site-source distance lower than 18km as shown in Figure 5.17. The second factor is the local site condition; most of the sites marked by high-intensity levels lie on the soft sediment of the volcanic alluvium, whereas the sites close to the epicenter are located on the meta-sediments bedrock. Beside these factors, the intensity values are always based on how to carry out the survey, this means the expert's judgment and bias are affecting intensity estimates. Even if in Figure 5.17, few half-integer values are reported (all number should be ordinal and not cardinal), it should be kept in mind that the error affecting intensity estimates, cannot be smaller than one intensity unit, on account of the discrete nature of any macroseismic intensity scale, that for this
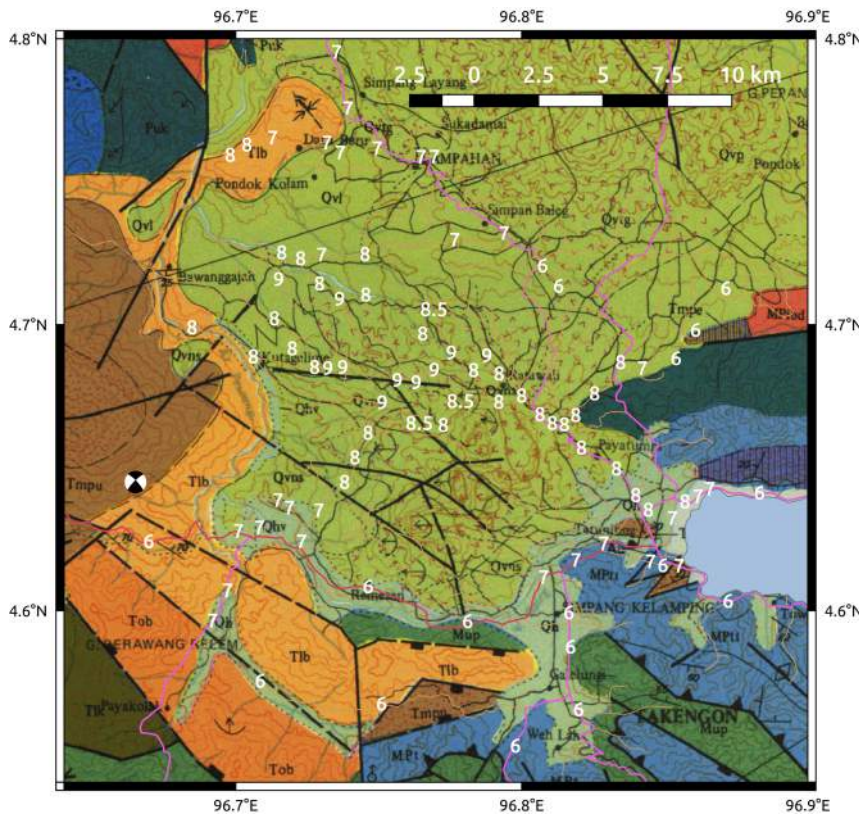
reason is defined in terms of ordinal numbers.

Figure 5.17. The intensity data plotted over the geological map of Takengon. Most of the I≥VIII sites have the distance to epicenter lower than 18km and at sit on soft sediment of Qhv and Qvns volcanic alluvium, whereas the estimated epicenter at AnuBatee fault which located Metasediments Tertiary bedrock Tmpu Peutu Formation (Cameron, et. al 1983). On account of the fact that any macroseismic scale is an integer scale of ordinal numbers, in order to improve the correctness of the intensity data it is needed to re-evaluate the survey documents and seismologist should be involved in a survey after the occurrence of the future earthquake.

5.5 Insights on the Synthetic Seismograms for the Takengon Earthquake.

The seismic hazard assessment was conducted using NDSHA, which relies on the realistic physical simulation for the source, propagation, and site conditions that are capable of generating synthetics seismograms at the sites being observed. The use of the 1D modal summation technique does not take into account the site effect, but it can be appropriately handled using the 2D and 3D approaches. Figure 5.18 (right) shows the surface distribution of different geological rock units (sedimentary and basement rocks) in Northern Sumatra. The effect of the upper most sedimentary layers is discussed in Chapter 7.

The Indonesian governmental institution BMKG (Badan Meteorologi, Klimatologi dan Geofisika) deploys several broadband seismometers and accelerometers in Sumatra. In this part of Indonesia, the Tsunami Early Warning System was designed in 2005 after the 2004 tsunami in Aceh. The data were made available for our research as the courtesy of BMKG in support of research institutes and universities throughout Indonesia including Syiah Kuala University. Due to the high tectonic complexity in Aceh, we hope BMKG could deploy more seismic stations especially in the Takengon area. The information about the location of seismographs and the

seismic network is available at the following link (https://inatews.bmkg.go.id/new/meta_eq.php). The detailed descriptions of the seismic stations being used in this investigation are shown in Table 5.1, the type A (Accelerometer only), S (Seismometer only), and C (Collocated both). Data from the LASI station (Figure 5.23) show that the east-west component of motion is missing in the seed data; whereas, the TPTI station data show several gaps in the recorded data. Consequently, these two stations cannot be used for the comparison.
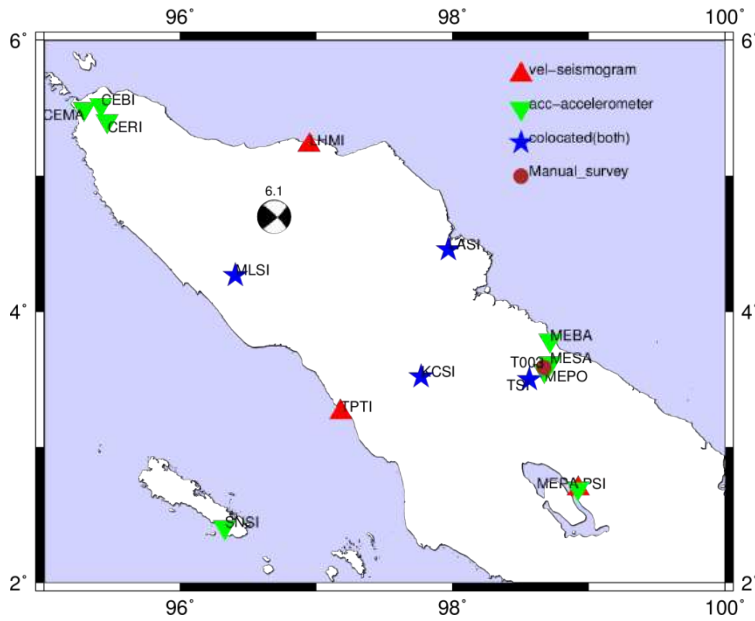
Figure 5.18: (left) Station location of available seismogrphs and accelerometers for the earthquake Takengon M6.1.

Table 5.1 Seismic stations near Takengon Earthquake sorted by the distance between the stations and the earthquake epicenter.

No	Name	Id	Dist. (km)	Lat.	Long.	start	Type	Ground
1	Meulaboh	MLSI	50.874	4.267	96.404	2008	C	Thin sediment
2	Lhokseumawe	LHMI	71.745	5.229	96.947	2007	S	tick sediment
3	Langsa Aceh	LASI	146.341	4.457	97.970	2009	C	tick sediment
4	Sta. Klimatologi Indrapuri Aceh	CERI	157.366	5.404	95.464	2010	A	bedrock
5	Tapaktuan	TPTI	163.203	3.262	97.177	2008	S	bedrock
6	Sta. Met. Blang Bintang Aceh	CEBI	169.023	5.522	95.416	2010	A	Thin sediment
7	Kutacane	KCSI	174.572	3.522	97.772	2008	C	bedrock
8	Sta. Geofisika Matai Aceh	CEMA	178.607	5.496	95.296	2010	A	bedrock
9	Tuntungan	TSI	245.944	3.501	98.565	2005	C	volcanic
10	Sinabang	SNSI	250.106	2.409	96.327	2008	A	volcanic
11	Sta. Klim. Sampali Medan	MESA	254.174	3.620	98.793	2009	A	tick sediment
12	Sta. Geofisika Parapat Medan	MEPA	330.579	2.695	98.923	2009	A	volcanic
		PSI	330.864	2.695	98.924	2009	S	volcanic

81
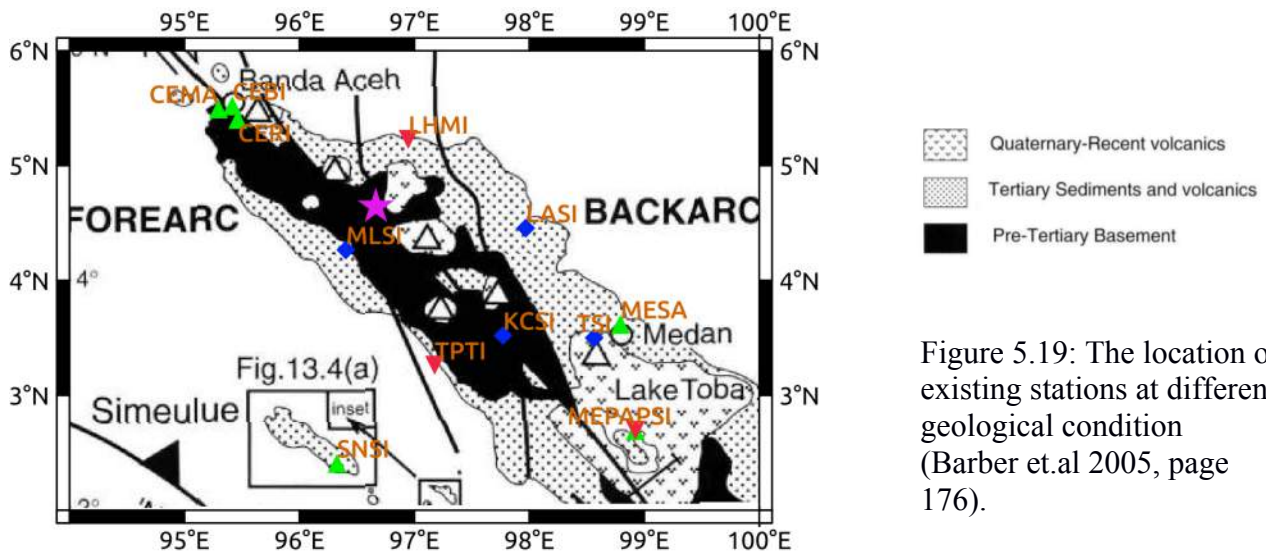
Figure 5.19: The location of existing stations at different geological condition (Barber et.al 2005, page 176).

BMKG has used the seismometers with type Trillium-120 (Nanometrics), BBVS-120 (Geodevices), and STS2. In addition, BMKG has also deployed accelerometers TSA100 and BBAS. Before comparing the computed seismograms with the real recorded seismic data, it is important to know the correct instrumental response for applying the instrument correction and filtering the data at the adopted threshold of frequency used in the seismograms computation. First, we removed the instrument response for the broadband seismometers using the available zeros-poles files in the full seed file format. For the accelerograms, the data is available only in the miniseed format, which does not include the instrument response information. On the other hand, instead of removing the instrument response from the observation data, applying the instrument response to the synthetic data can be an alternative to being comparable. In order to get a proper acceleration value in cm/s/s, it is needed to multiply the accelerograms by a given constant (i.e. KCSI multiply by 0.00000047) as following the standard procedure by BMKG staff (Rudyanto 2015, Happrobo 2015).

The recorded seismograms or accelerograms are plotted with a gray color line while the synthetic seismograms computed at 10Hz and 1Hz cutoff frequency are plotted with green and red lines, respectively.
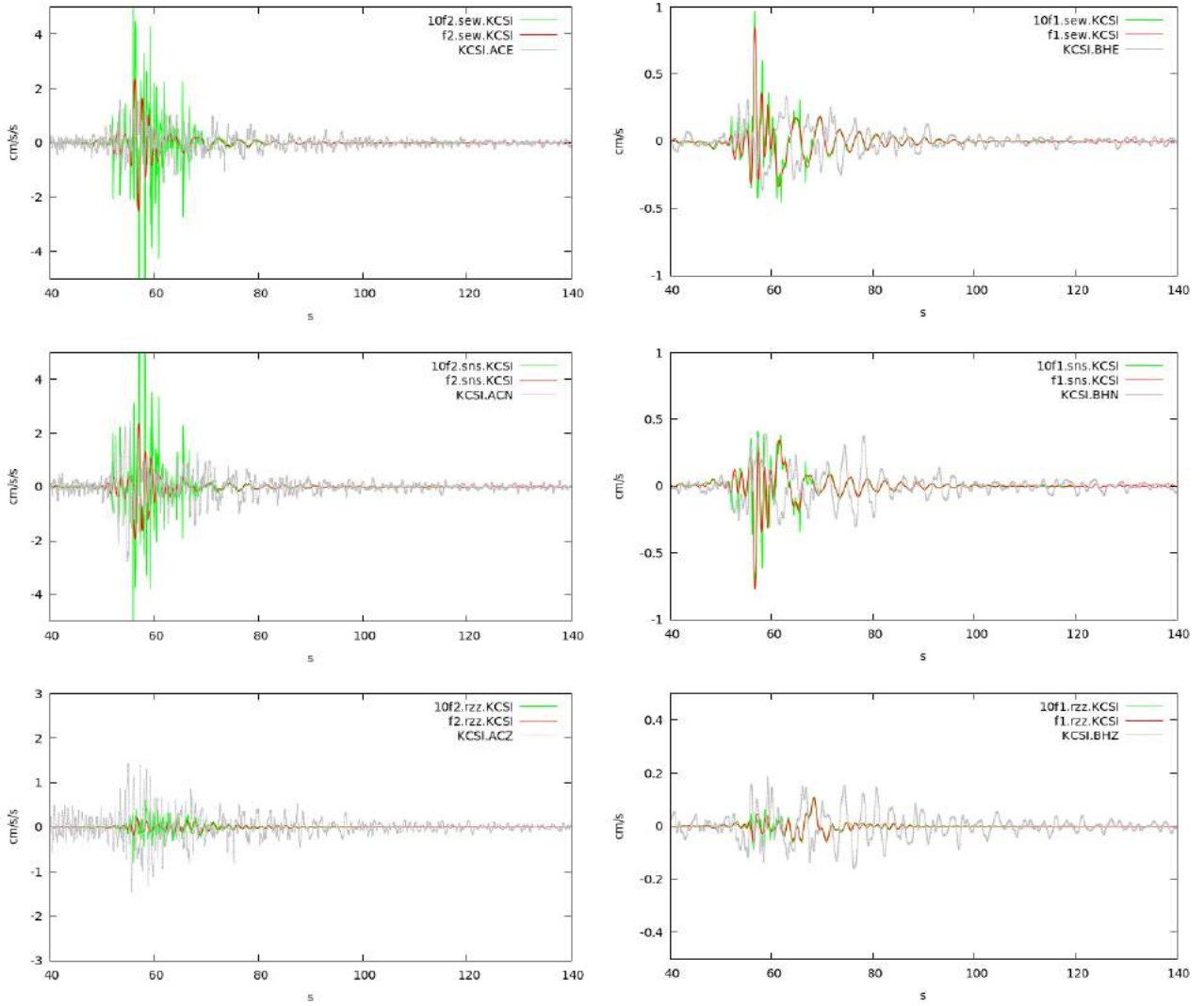
Figure 5.20: Accelerogram (left) and Seismogram (right) for KCSI station at dist=174 km, Kutacane, Aceh. east-west (top), south-north (middle), vertical (bottom)

The KCSI station is located over a thin basin (near the pre-tertiary basement). Most of the plots we used in this discussion are limited to a time window of 100s, and we focused on the surface wave part of the waveform, the damaging ones. The waveforms from the accelerogram and seismograms are more dispersed than the synthetic seismograms because the synthetic seismograms are computed on a 1D rock structure without considering scattering, site effect, and other factors.

83
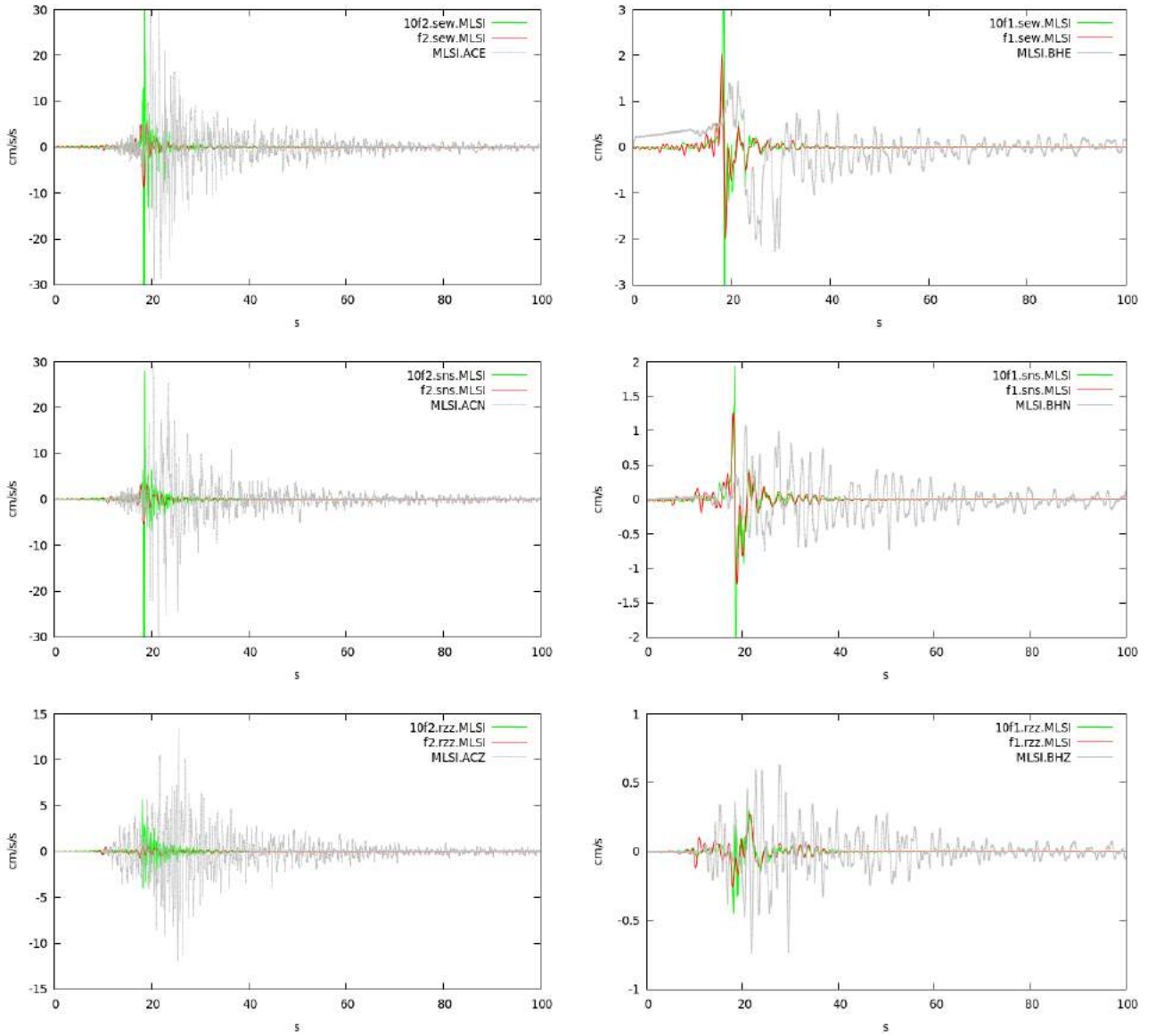
Figure 5.21: MLSI Accelerometer (left) and Seismometer (right) (near Meulaboh) located at dist=50.87km: east-west (top), south-north (middle), vertical (bottom)

The coda duration (wave following the main wave from) is due to the site effect where the seismogram is recorded. The stations located on thick (deep) sediment will have a long coda such as LHMI as shown in Figure 5.21 (left). The seismographs installed on bedrock do not show a long coda and fits well with the theoretically computed seismograms as shown in Figure 5.21 (right). Another site located on the thick sediments is the LASI station (Figure 5.23), which shows a long coda wave. Even if this is a far site and because this site is on the thick sediments, the effect of polarization and amplification remains strong. On the other hand, the TSI station, installed on the volcanic sediments, shows a short coda in comparison with both that of the LASI and of the LHMI.
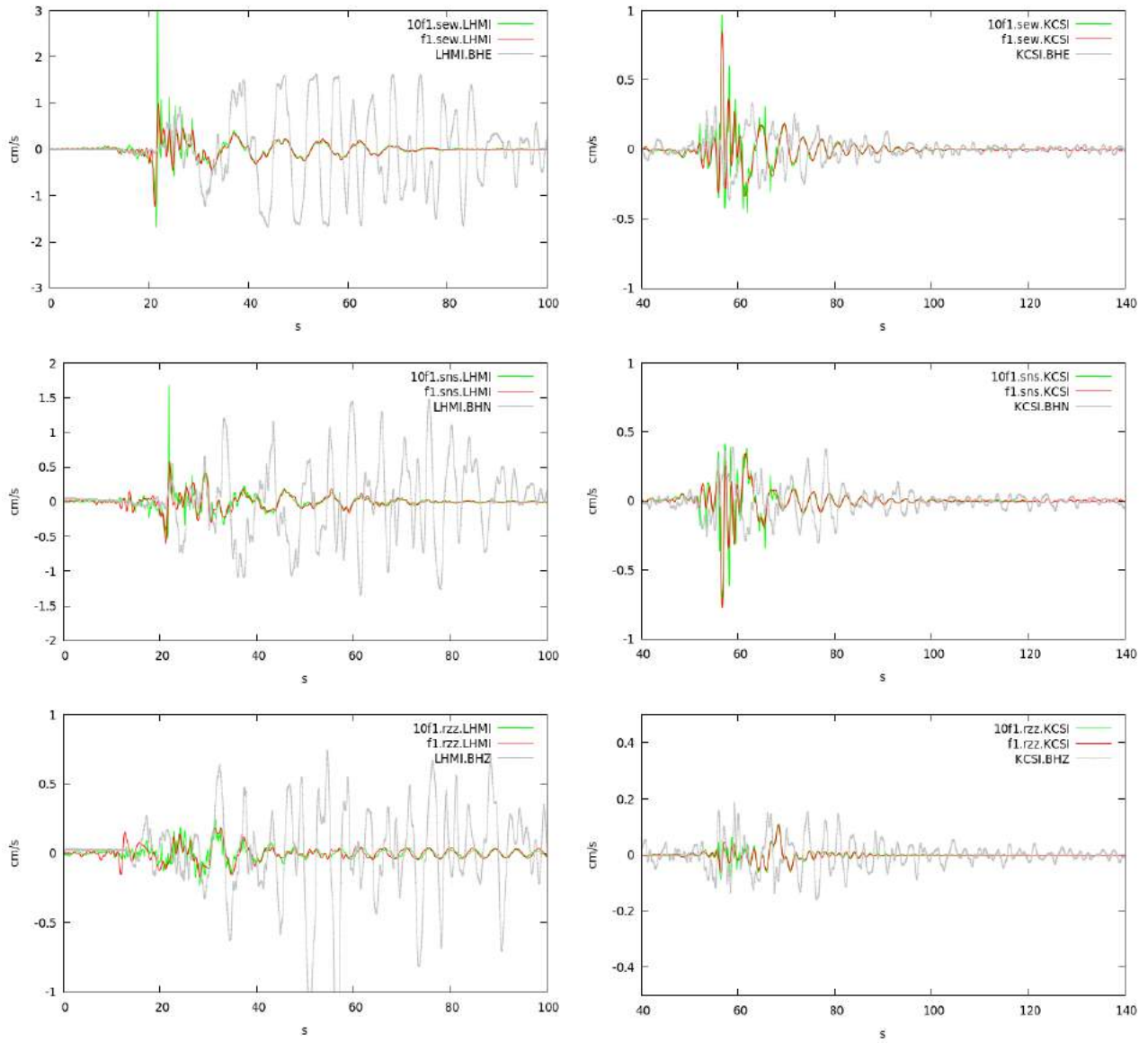
Figure 5.22: Seismometer for LHMI station, located on thick sediments at dist=71.74 (left) and KCSI as station located on bedrock at dist=174 km (right)
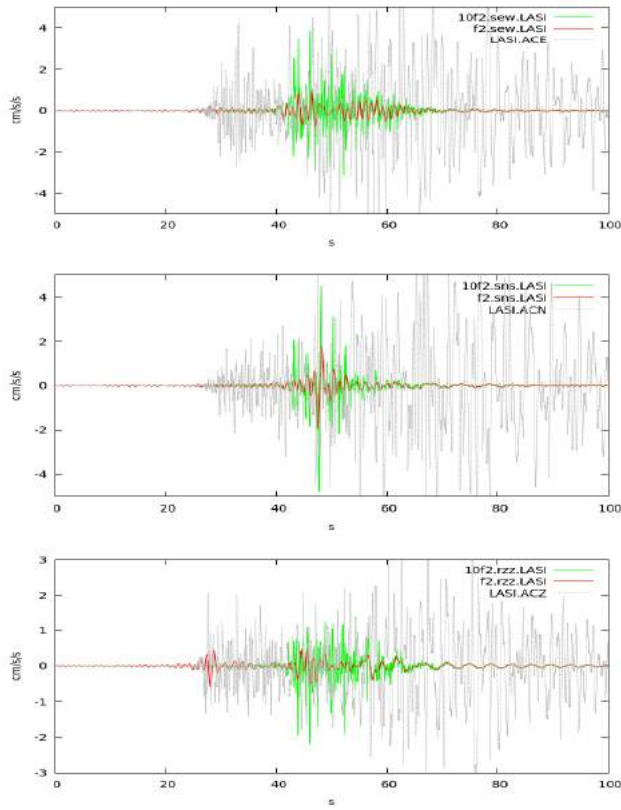
Data from observation for BHE component
not available
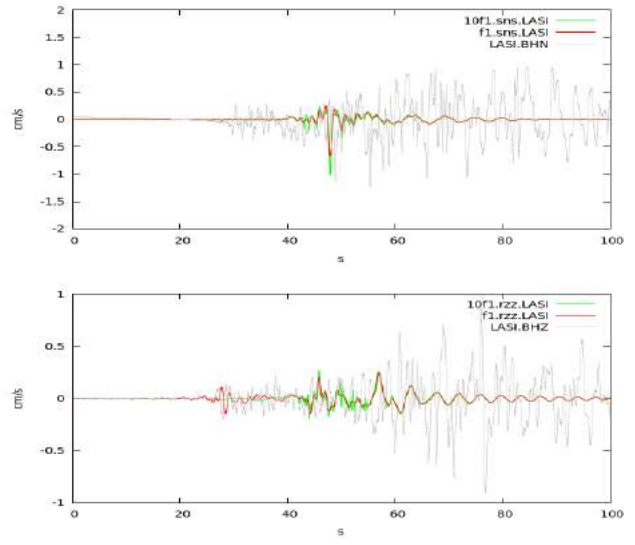
Figure 5.23: Accelerometer (left) and Seismometer (right) of LASI station (in Langsa City), with distance=146.3 km from source and located at tick sediment.
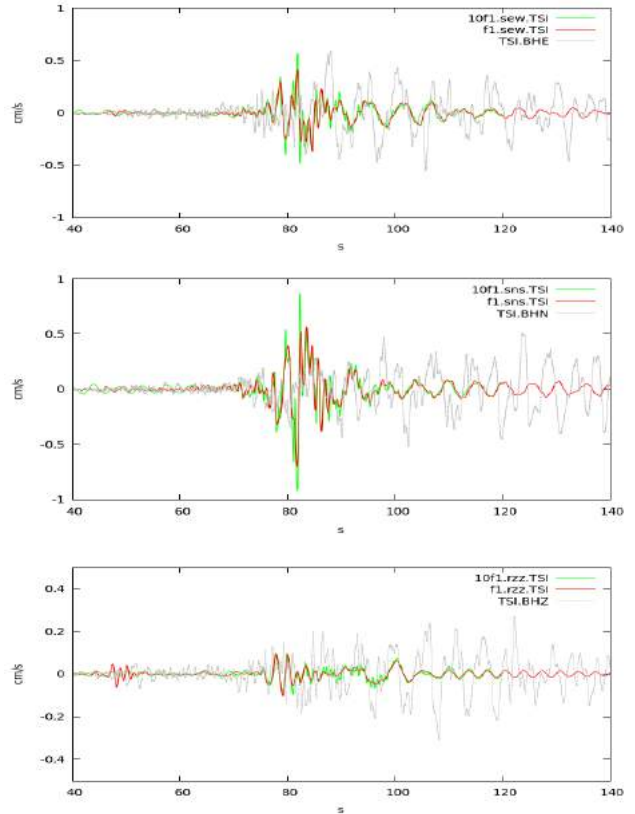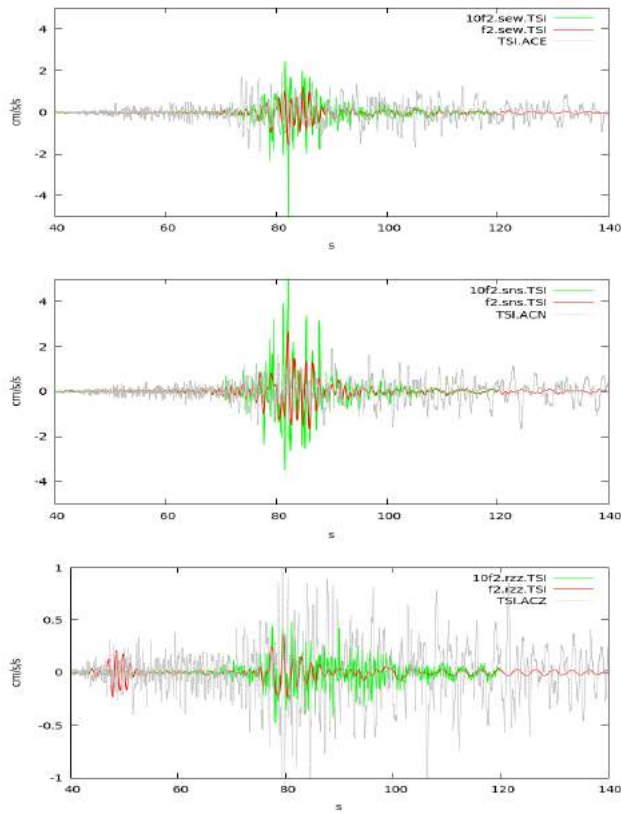
Figure 5.24. Accelerometer (left) and Seismometer (right) TSI (in Tuntungan town), with distance=146.3 km from source and located at tick sediment.
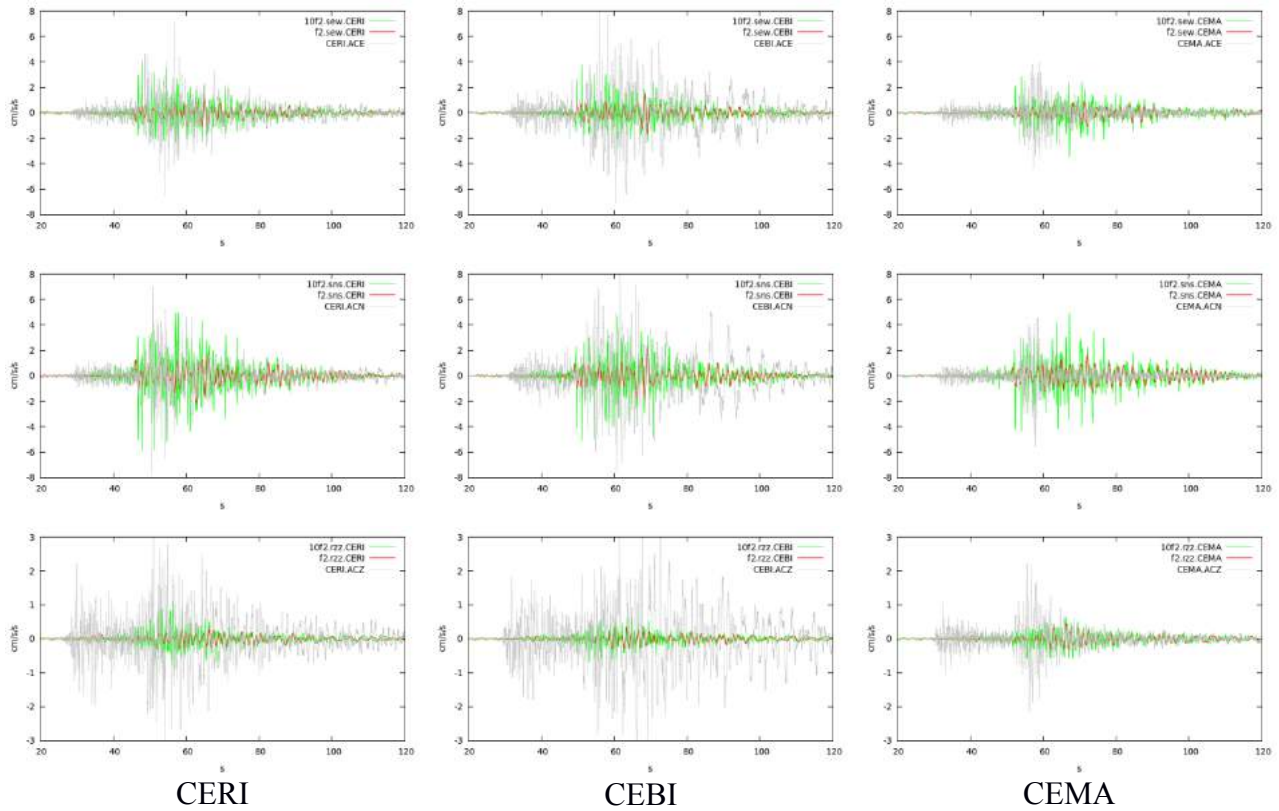
Figure 5.25 The accelerometer clustering near Banda Aceh, CERI (Indrapuri), CEBI (Blang bintang), and CEMA (MataIe), which distance from source 157km, 169km, 178km respectively.

Around the Banda Aceh city, BMKG deployed 3 accelerometers at a distance between 15 and 20km as shown in Figure 5.18. The horizontal components of the CEMA accelerogram, installed on the limestone, is very similar to those of the synthetic seismogram computed using the modal summation technique, but the vertical acceleration is not. A little difference, recognized between the recorded and computed vertical component, may occur due to the fact that the strike-slip fault with rake 170 gives less contribution to the vertical velocity. The CEBI is installed in the International airport Sultan Iskandar Muda on a sedimentary layer; thus, this site shows a strong site effect. The CERI station shows an intermediate "amplification" effect relative to both that of the CEMA and of the CEBI stations.

The MEPA/PSI station is located at 330km distance from the earthquake source, as shown in Figure 5.18. Figure 5.26 shows that the observed seismogram and accelerogram are relatively small compared with the theoretical waveform. One possible reason of the mismatch is that the recorded site is located over the Lake Toba volcanic area, which contains the material that has a strongly damping effect caused by the seismic wave energy.

.
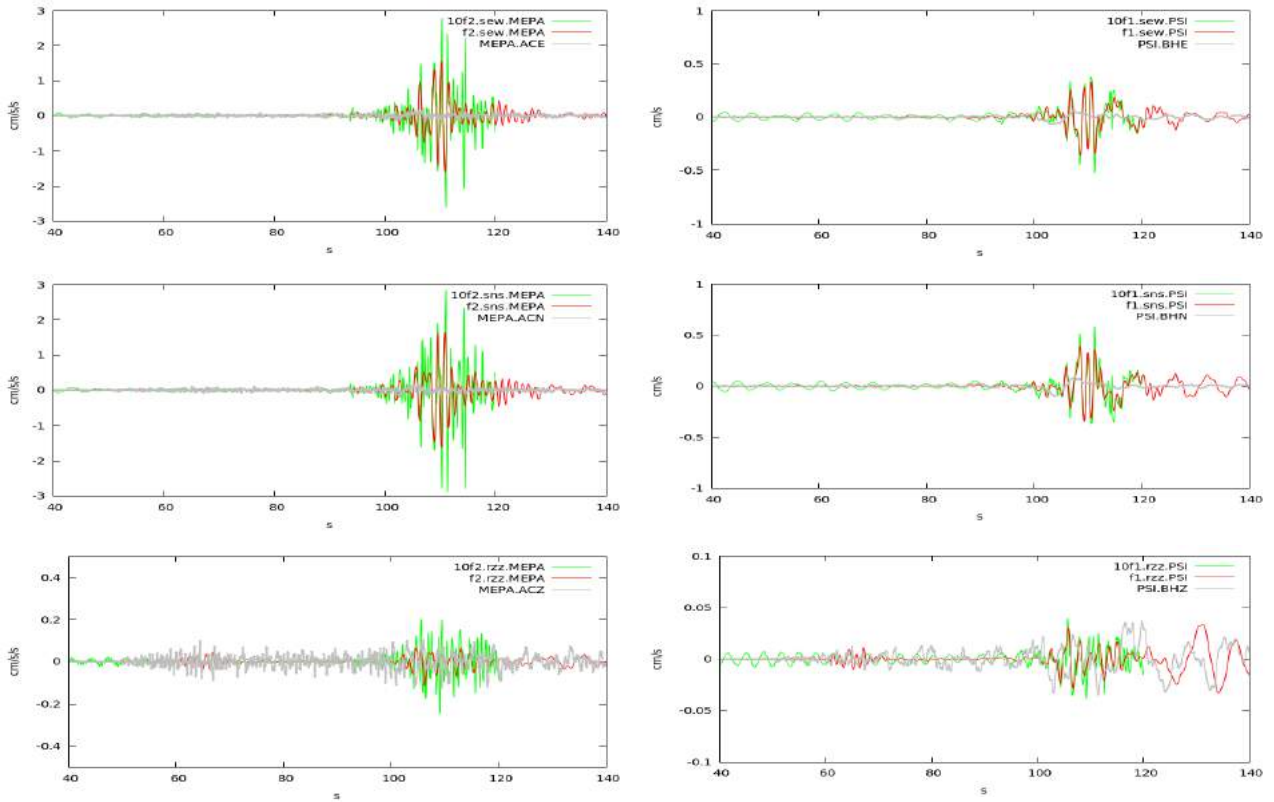
Figure 5.26 Accelerogram MEPA (left) and Seismometer PSI (right) which located at Toba Lake which in the center of volcanic area and the most distance source 330km

.
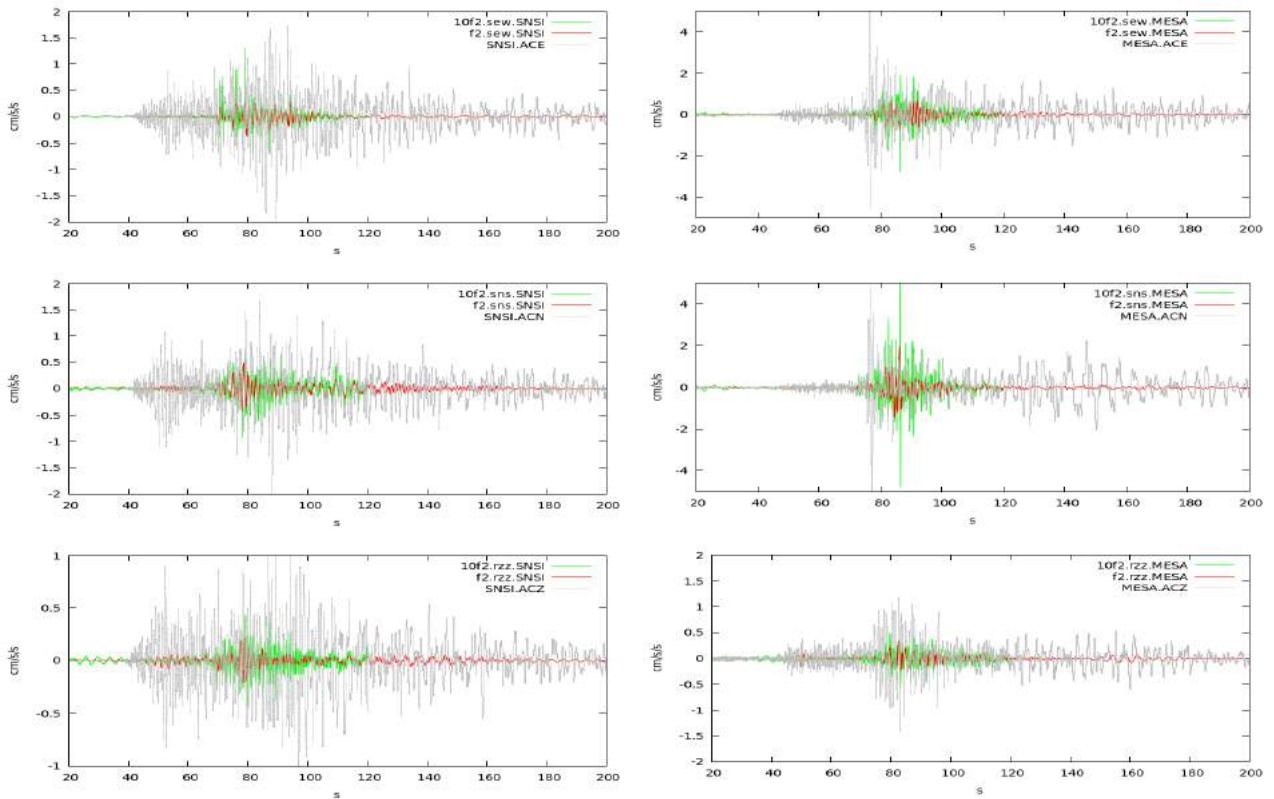
Figure 5.27 The accelerogram from SNSI (left) in Simeulue Island acceleorgram from MESA in Medan city with distance almost same 250km and 254km respectively.

Figure 5.27 shows the comparison between two site stations (i.e. SNSI and MESA) at relatively the same distance from the earthquake (i.e. 250km and 254km, respectively) with two different ray path structures: with and without the oceanic path. The accelerogram from the SNSI (Figure 5.27-left), located on Simeulue Island, shows a very strong dispersion effect compared with that of the accelerogram from MESA (figure 5.27-right), located on the sedimentary basin of the Medan city. This is an interesting topic for the future to verify the strong dispersion from Simeulue Island to investigate the oceanic-continental coupling structural interface (Panza et al., 2010, Bisignano, 2003, Yanovskaya, 2000). From Figure 5.27-right, it is possible to see a shift in the arrival time and large dispersion in the accelerogram from the MESA station; the long coda is due to the scatter of the sedimentary layer.

The computed synthetic seismograms are significantly dependent on the accuracy and amount of details in the structural model being used particularly for the high frequency simulation, and it is difficult to get a good consistency between the observed and computed seismograms because a lot of factors may affect the seismic waves during their propagation. Therefore, comparing the observed and theoretical waveforms at a low frequency might produce a more agreement in the patterns of the waveforms. We performed low pass filtering for the observed waveforms and the synthetic seismograms by using the SAC routine. Figures 5.28, 5.29, and 5.30 show the expected good consistency between the synthetic and observed seismograms.
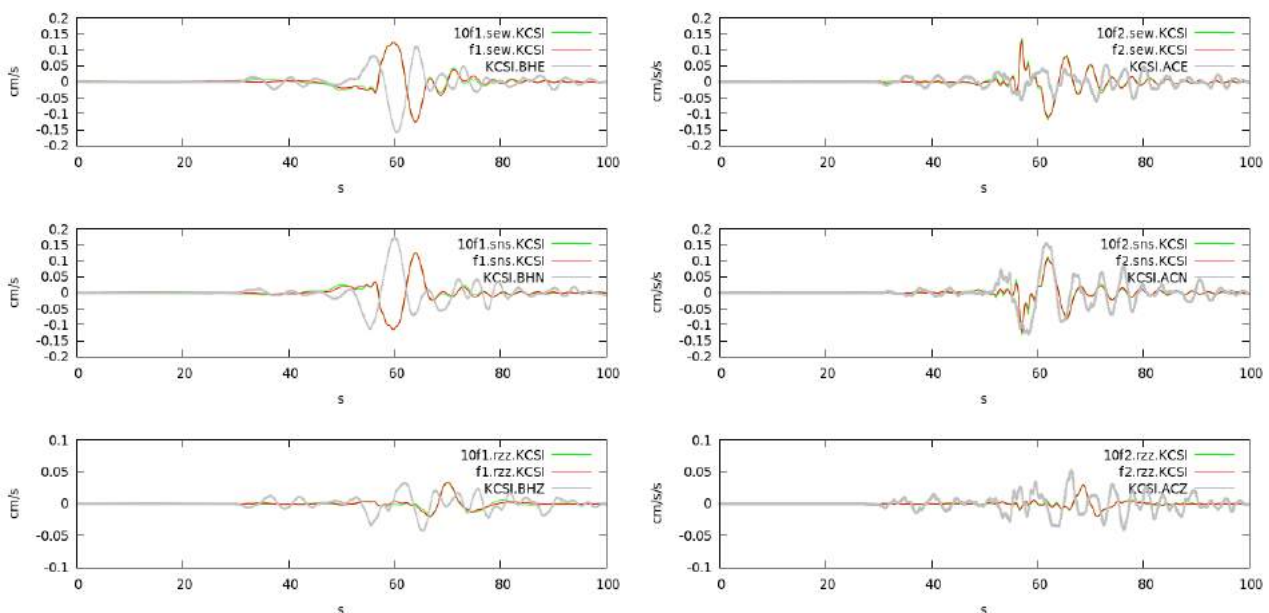
Figure 5.28 Low pass filter accelerogram and seismogram from station KCSI
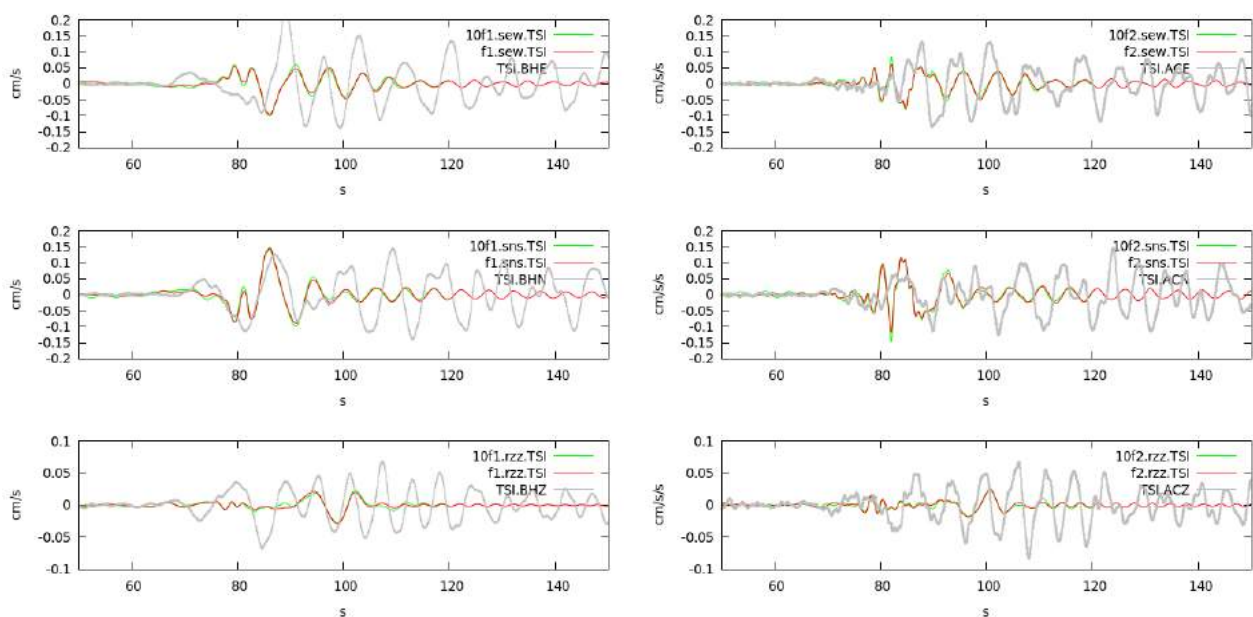
Figure 5.29 Low pass filter accelerogram and seismogram from station TSI
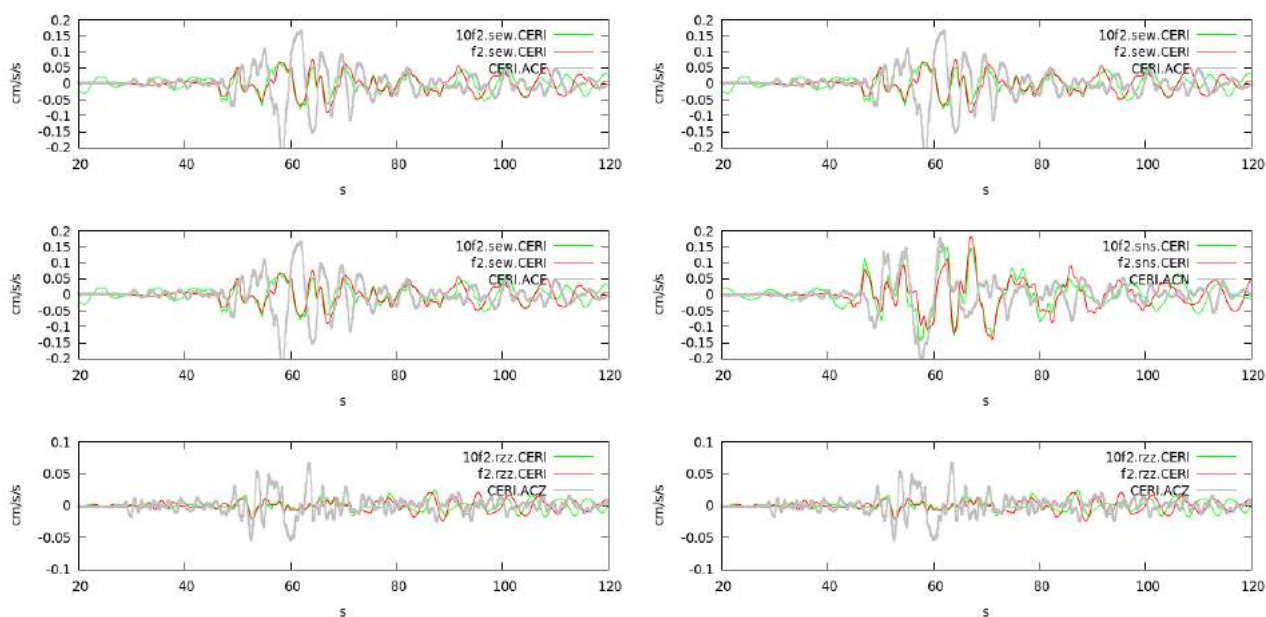
Figure 5.30 Low pass filter accelerogram station CERI (left) and CEMA (right)

90

5.6 Analysis of response spectra for the Takengon Earthquake

In section 5.5 we presented insights on the comparison between the synthetic signals and observed seismograms and accelerograms of the Takengon Earthquake in the time domain. In this section, we investigate the response spectra of the observed and computed signals. The Response Spectral of Acceleration (RSA) and Response Spectral of Velocity (RSV) analysis is very useful for practical engineering purposes.

The use, in the synthetic computations, of the point source approximation give us with a minimal number of free parameters by properly weighting the point source spectrum using the scaling laws of Gusev (1983), as reported in Aki (1987), shown in Figure 5.26. We have chosen these curves for several reasons: as compared to ω^{-2} spectra (e.g., Joyner, 1984; Houston and Kanamori, 1986) Gusev curves, that are based on a solid statistical analysis, in the range from 2s to 0.1s are more conservative for the worst possible scenario; they give often the correct corner frequency in order to fit with the synthetic seismograms the observed amplitudes (e.g. Vaccari, 1995). Less stringent scaling laws can obviously be easily adopted. This is a rough approximation of the physical source process when a large earthquake is considered in the calculation of synthetic seismograms at distances of the same order of the fault dimensions. The synthetic time series are presented only in order to show the spatial variability in the Green's functions scenario when the azimuthal dependence and the effect of the lateral variations are taken into account (Romanelli and Vaccari, 1999).
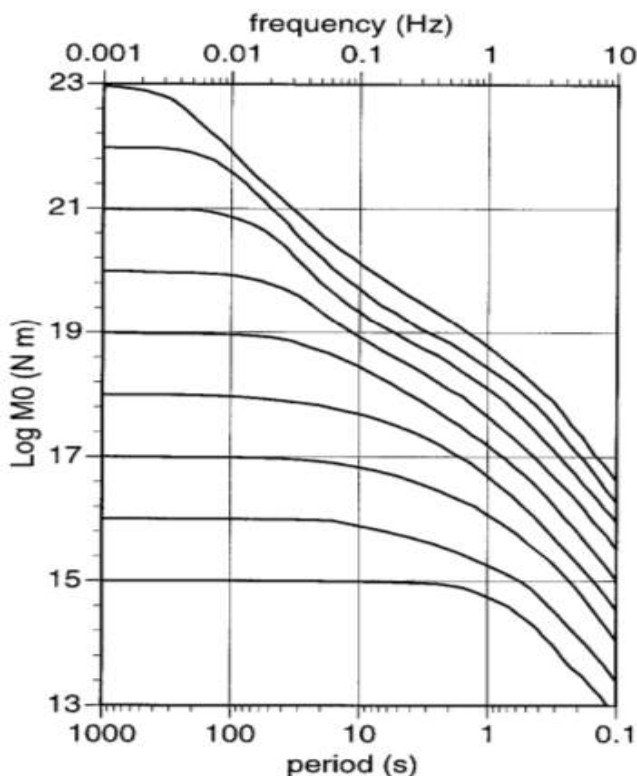
Figure 5.31. Source spectra suggested by Gusev (1983), as reported in Aki (1987), for earthquakes with the range of seismic moment, M_0, from 10^{15} to 10^{23} Nm..
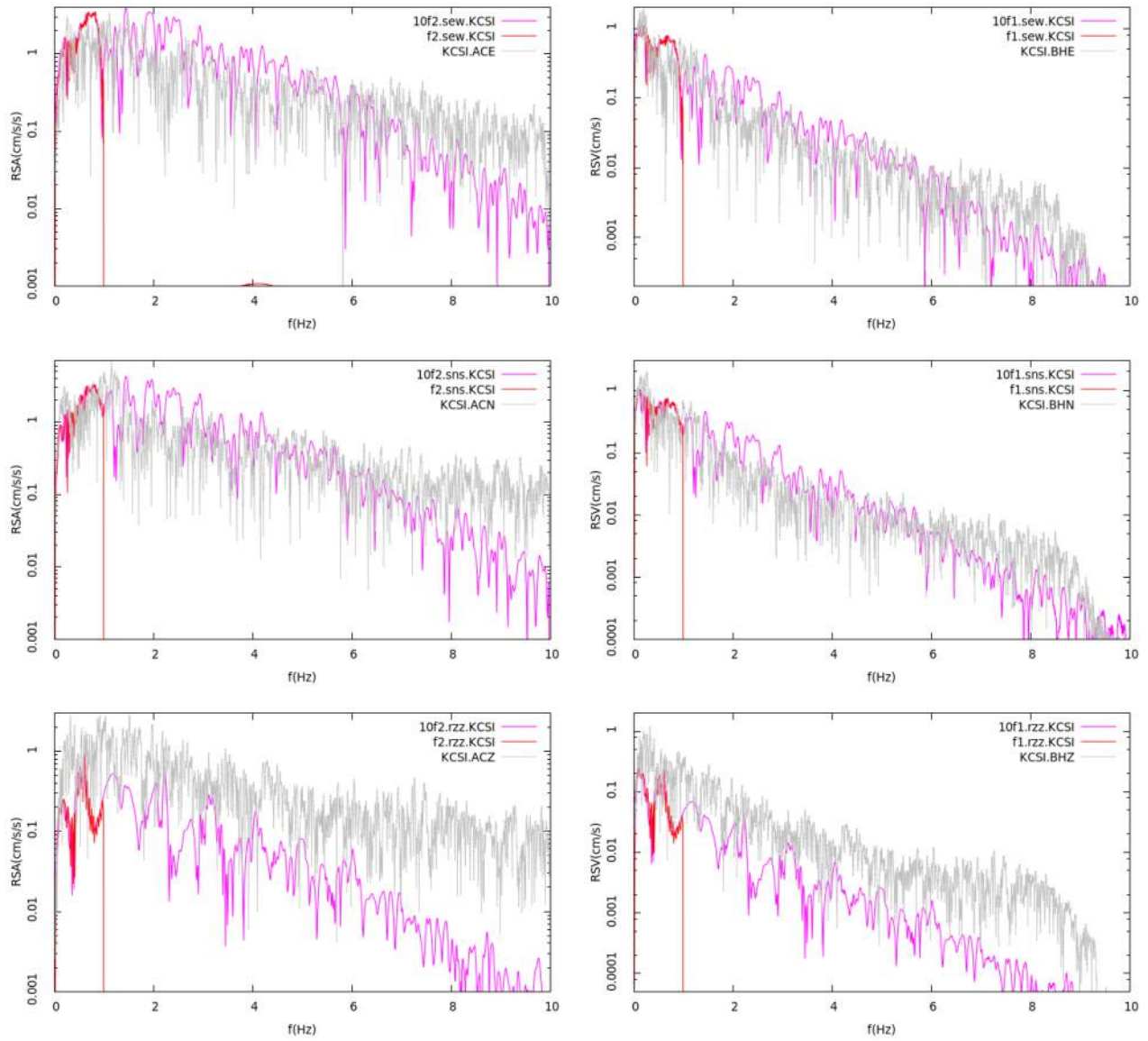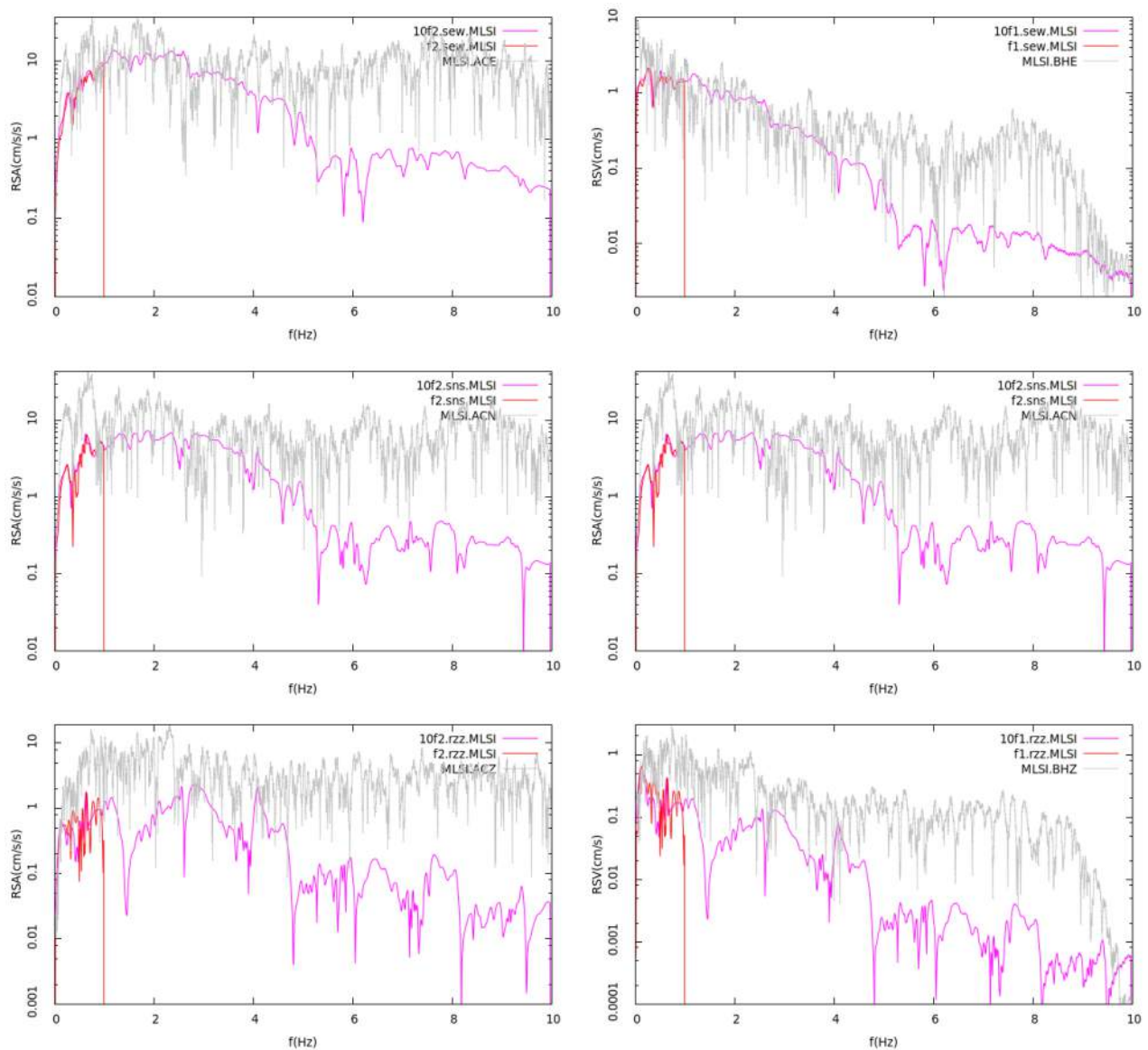
Figure 5.32: Response Spectra for Acceleration (RSA) (left) and Response Spectra for Velocity (RSV) (right) for KCSI station at dist=174 km. Components: east-west (top), south-north (middle), vertical (bottom)

The figures 5.32 to 5.36 show the response spectra as a relation between PSA in logarithmic scale and frequency in linear domain. Each figure contains the response spectra for 1Hz and 10Hz cutoff frequency simulations in red and magenta colored lines, respectively, and overlaid with the spectra from observed data in gray line color. For the analysis of the signals we used SAC software (Goldstein 2005) as shown in listing 5.3.

The figure 5.32 shows the response spectra of horizontal component of 2013 earthquake recorded in KCSI station, which reveal a good consistence with the response from the synthetic seismogram at the same site of the station for both RSA and RSV. The correlation between the response spectra from the vertical component reveals that, the observed seismogram has a higher response spectrum than the vertical of the synthetic seismogram.

```
plt2sac.sh thts610008f1.sew.KCSI.plt      SAC>  r thts610008f1.sew.KCSI.plt.sac
0.29297E-01                               SAC> fft
thts610008f1.sew.KCSI.plt.sac             DC level after DFT is 5.7314e-06
SAC> r thts610008f1.sew.KCSI.plt.sac      SAC> keepam
SAC> p                                    SAC> xlim 0 10
                                          SAC> p
```

Listing 5.3 SAC command to process the synthetics seismogram to spectrum in frequencies domain; the same procedure apply to observation seismogram or accelerogram after removing instrument response.

Figure 5.33: Response Spectral Acceleration (RSA) (left) and Response Spectral Velocity (RSV) (right) for MLSI station at dist=50 km. Components: east-west (top), south-north (middle), vertical (bottom)
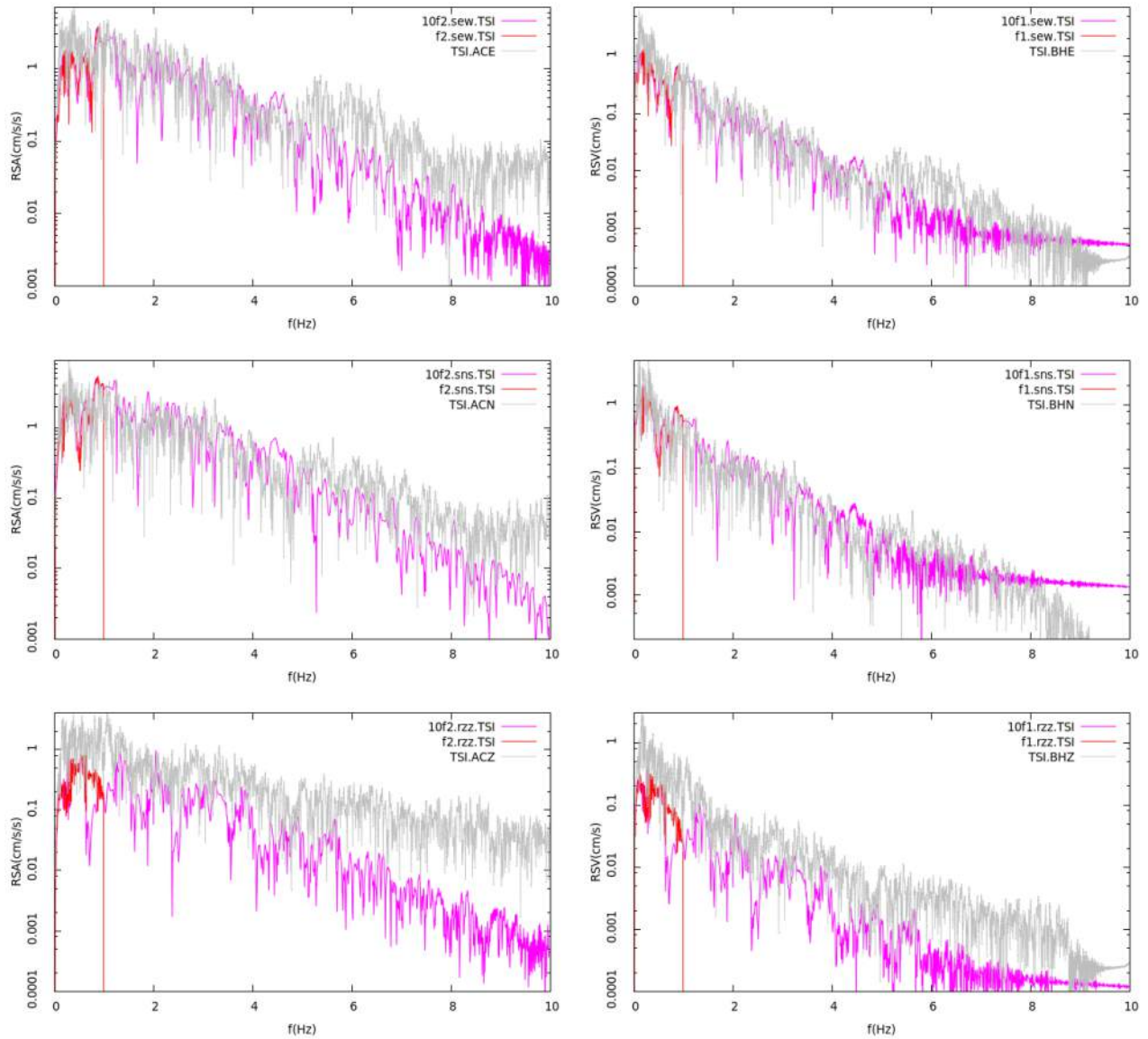
Figure 5.34: Response Spectral Acceleration (RSA) (left) and Response Spectral Velocity (RSV) (right) for TSI station at dist=146 km. Components: east-west (top), south-north (middle), vertical (bottom)

The near receiver, MLSI, as shown in figure 5.33, has relatively flat observational response spectra compared with other stations and the synthetic seismogram response spectra nearly follow the observation response spectra. Response spectra for far field TSI as shown in figure 5.34 has fairly similar pattern with respond spectral for KCSI sites. Figure 5.35 shows the response of RSA station near Banda Aceh which is almost at the same distance from the source and shows similar patterns. Figure 5.36 shown the SNSI site, over oceanic layer, has relatively bigger different between observational and synthetic spectral respond at the high frequency higher compare with site MESA. Generally, the response spectral from synthetic signals is in good agreement with the response spectra from available observations.

CERI   CEBI   CEMA
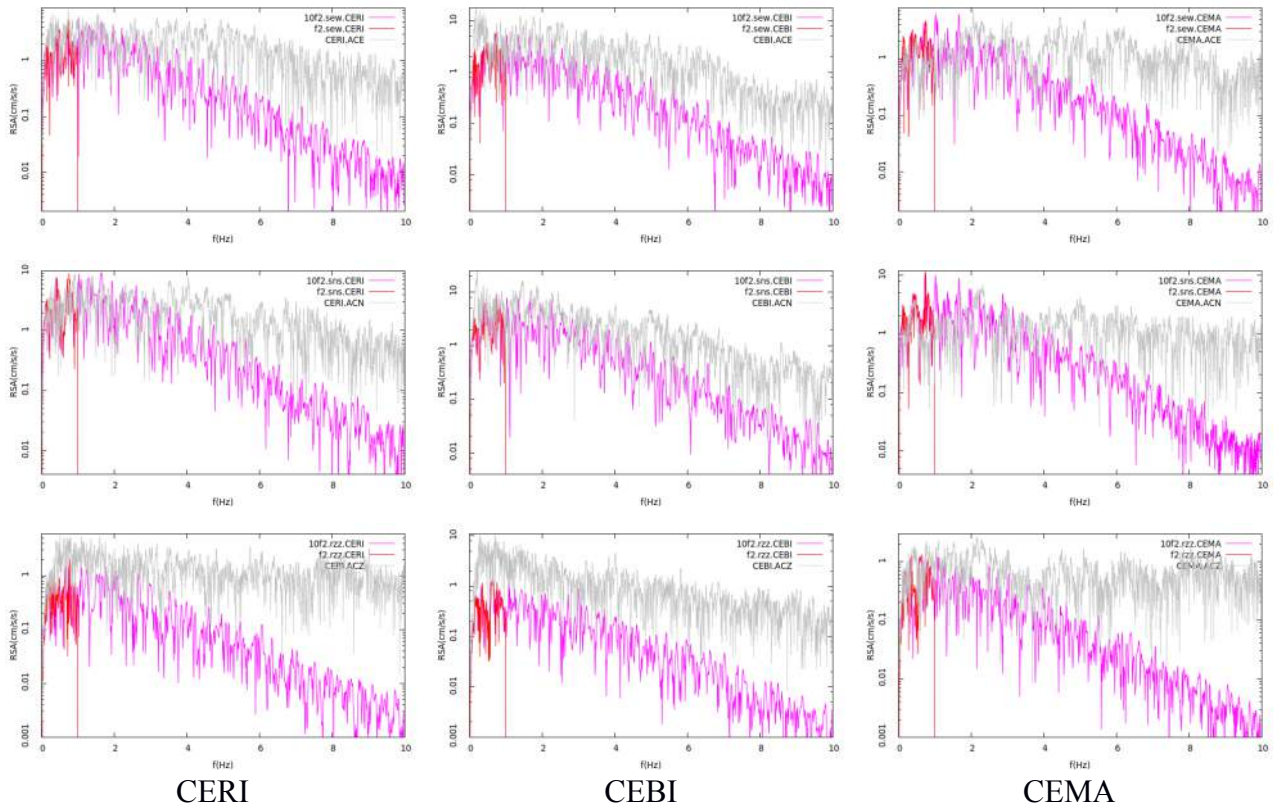
Figure 5.35 Respose Spectra Accelerogram (RSA) near Banda Aceh, CERI (Indrapuri), CEBI (Blang bintang), and CEMA (MataIe), dist=157km, 169km, 178km, respectively.
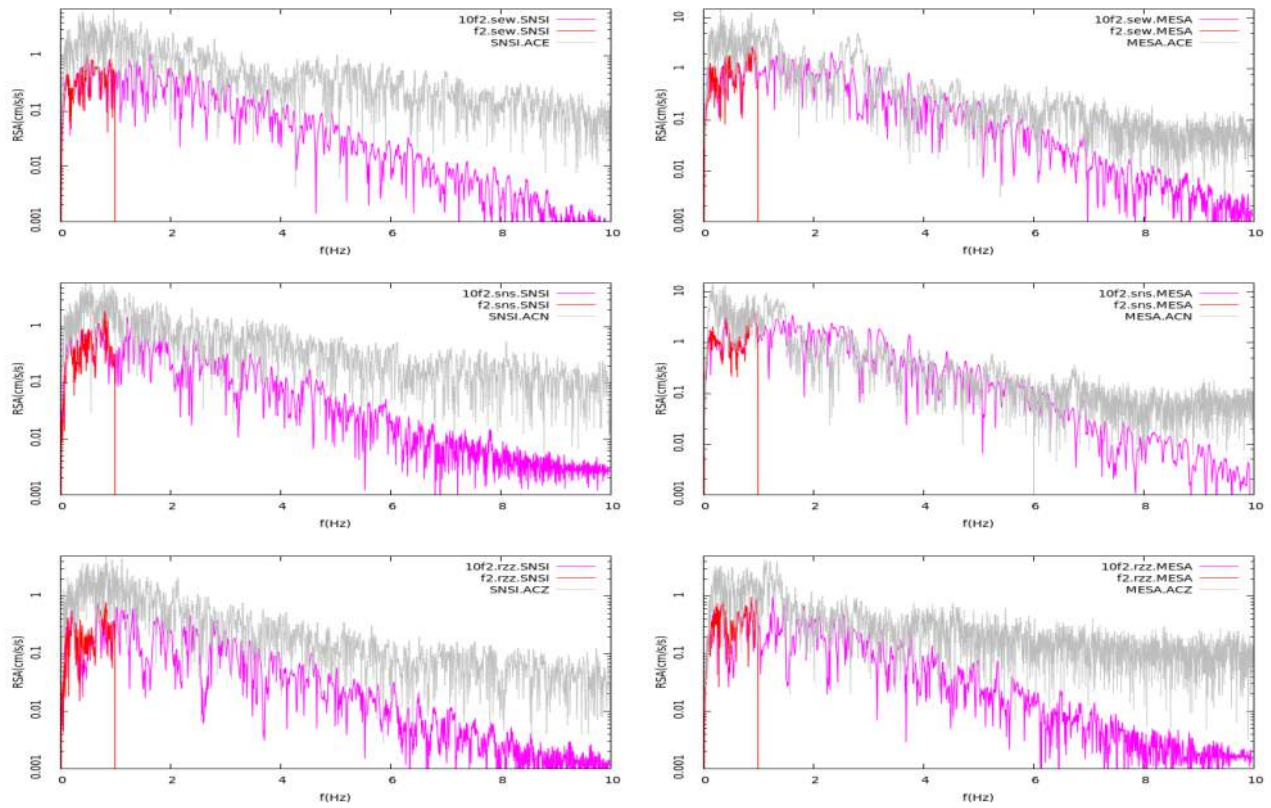
Figure 5.36 RSA for SNSI (left) in Simeulue Island and MESA in Medan city at similar epicentral distance, 250km and 254km, respectively.

6. Regional Scale NDSHA for Sumatra

6.1. The Neo-Deterministic seismic Hazard Assessment at Regional scale

The NDSHA is based on the modeling techniques developed from the knowledge of the seismic source process and from the propagation of the seismic waves, which can realistically simulate the ground motion due to an earthquake by means of the synthetic seismograms (Panza et al., 2001). At the regional scale, a set of sources is defined in the tectonically active areas of the considered region (the tectonic setting and seismotectonic sources for the Sumatra region are discussed in details in Chapter 2 and 3). Once the physical properties of the average structural models have been defined (the structural models given for the Sumatra region are discussed in Chapter 4). The synthetic signals are computed for the upper frequency content of 1 Hz, and the scaled point-source approximation (Gusev, 1983) is still acceptable. The wave propagation is efficiently modeled with the modal summation technique (Florsch et al., 1991; Panza, 1985) and the broadband synthetic seismograms are generated at the free surface on a predefined grid of the points covering the study region (Panza et al., 2012).

In the case where a source–site path crosses one or more boundaries between the structural models, the site structural model is used along the entire path since the station records are usually more sensitive to the local structural conditions as shown by Panza et al. (2001) for the P–SV waves. The horizontal components at each site are first rotated into a reference system common to the whole territory (N–S and E–W directions) and then the vector sum is calculated. The largest amplitude resulting signal, due to any of the surrounding sources, is selected and associated with that particular site. Among the representative parameters of the strong ground motion, we focus on the maximum ground acceleration, velocity, and displacement (PGA, PGV, and PGD) (Parvez et al. 2003). In addition, with respect to Panza et al. (2001), the vertical component of motion has been generated as well, and the vertical peak values are mapped separately from the peak values of the horizontal component as shown in Figure 6.1.1, defined by the vector sum of the radial and transverse components obtained at each site (Panza et al. 2012).

At each site, the horizontal components (P–SV radial and SH transverse) synthetic seismograms are first computed for a seismic moment of 10^{-7} N m and then scaled to the magnitude of the earthquake using the moment–magnitude relation of Kanamori (1977). The finiteness of the source is accounted by scaling the spectrum using the spectral scaling law proposed by Gusev (1983) as reported by Aki (1987). For the period between 1 and 2 s, the Gusev spectral fall-off produces higher spectral values than those in the ω^{-2} spectral fall-off, and thus guarantees a

conservative hazard computation (Vaccari, 1995).

For acceleration, the deterministic modeling can be extended to the frequencies greater than 1 Hz by using the existing standard design response spectra (Panza et al., 1996). The design ground acceleration values are obtained by scaling the chosen normalized design response spectrum (the normalized elastic acceleration spectra of the ground motion for 5 percent critical damping) with the response spectrum computed at the frequencies below 1 Hz. The design ground acceleration (DGA) is obtained through extrapolation using the standard code response spectra following the procedure described by Panza et al. (1996)
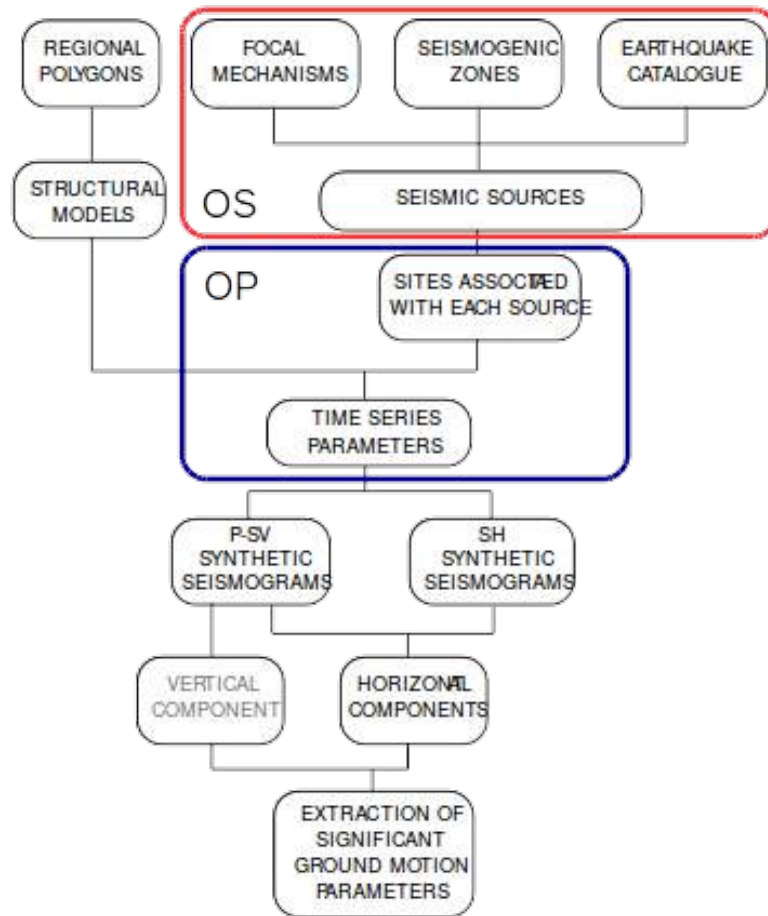
Figure 6.1.1 Flow chart of the standard NDSHA procedure for regional scale with original version source definition (OS) in red box and original paths generator (OP) in blue box

Finally, in the computation of the DGA map, at each site the synthetic response spectrum has been generated for the signals coming from all the sources located within the imposed distance threshold, and the maximum DGA value is mapped, rather than using the shortcut adopted in Panza et al. (2001), where the DGA at each site was computed only for the synthetic accelerogram with the largest amplitude. The modeling has been made with the program package (as original version). The speed optimization 1 has made possible to extend to 150 km for all the events the maximum length considered for the site-source paths (Panza et al., 2012).

The site-source paths and the other input parameter for modeling the time history data are shown in side red box Figure 6.1. The path generator terminology will be used intensively and will be discussed in this chapter. Due to the limitation in the paths generator being used, we suggest several improvements and updates that might be used in the updated new version of the paths generators. The main aim of the update is to optimize the computational time and to apply the flexibility configuration files. The main suggested modification in NDSHA (two paths source definition) is suitable for the Sumatra region due to the structural and tectonic complexities as shown in Figure 6.1.2.
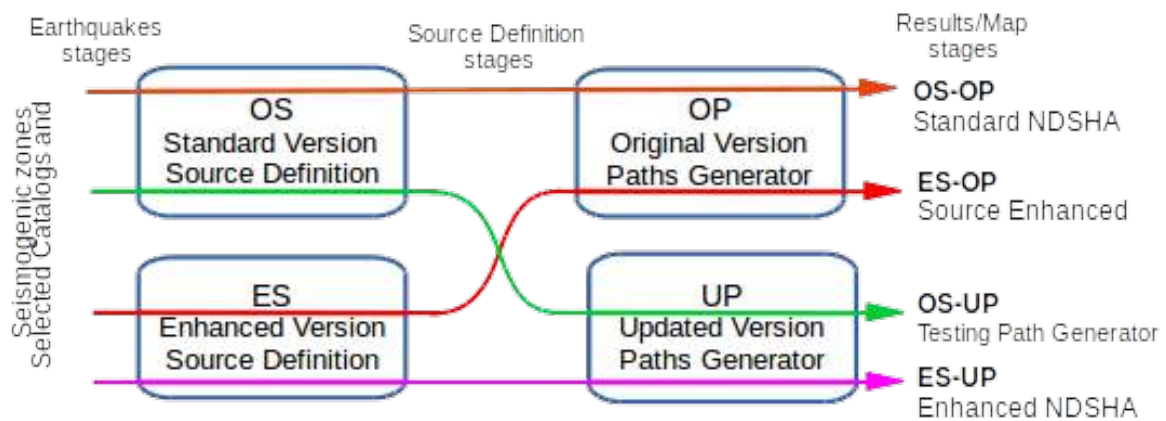
Figure 6.1.2 The flow chart shows the suggested improvements and the comparison to test their performance with NDSHA for Sumatra.

First, we will discuss the procedure that is in use in the standard NDSHA procedure package i.e. the standard source definition and the paths generator (OS-OP, Original Source definition and Original Paths generator), see the brown line flow in Figure 6.2. The enhanced source definition procedure, see Chapter 3, will apply to the original path generator ES-OP (Enhanced Source Definition and Original Path generators), see Figure 6.2. The suggested modifications are not only in the source definition but also in the path generator; and the final result of the enhanced procedures (ES-UP Enhanced Source Definition and Updated Paths generators) is shown in Figure 6.2. In order to test the validation of the updated paths generators (UP), it is better to make a comparison between (OP) and (OS-UP), see Figure 6.2.

6.2. The Performance of Standard Version of NDSHA in Sumatra (OS-OP)

The standard version of the NDSHA approach at a regional scale (Figure 6.1) is illustrated in details by Panza et al. (2001) and in the internal manual in GNDT Deterministic Seismic Zoning Reference Guide (Magrin and Vaccari, 2014). By applying the NDSHA at a regional scale, we have to carry out what is called "a default run". The default parameters are adopted according to the

experience accumulated in running the job for Italy and several other countries (Albania, Algeria, Bulgaria, Croatia, Cuba, Ethiopia, Hungary, Romania, Slovenia). In order to have the homogeneity in the hazard maps for the neighboring Italian countries, they use the default runs. In a default run, the parameter file (`.par`) needed by each program is prepared by some other program done earlier in the sequence.

In the standard package, the preparation of the input data is relatively an easy task, we only have to prepare the parameter files mentioned in the first input file named cells.par. The parameter files for a default run have the name of the program that read them with an extension .par instead of .out (`efft.out` looks for the file `fft.par`, esne.out for sne.par and so on). In the standard version, it is preferred to use the default parameters rather than the modified one. Using the default parameter will be good for the same treatment of the hazard result. However, in some complex cases like Sumatra, there is a need to control these parameters by using the hazard analysis user to handle and accommodate the existing complexity.

To perform the parametric study where the user cannot use the default parameters, the user can run the programs with the non-default parameters. There are two ways suggested to preform the non-default run. We can run a program one at a time, edit the default parameter file generated for the next program, and finally run the next program after editing. Or you may wish to prepare a set of parameter files in advance, one for each program, and modify the hazard job so the default parameter files generated automatically are immediately overwritten by the user-prepared files:

```
ecells.out
mv -f nondefaultsmooth.par smooth.par
smooth.out
mv -f nondefaultinscat.par inscat.par
einscat.out
```

Listing 6.1 The way of user control for each step in standard packaged.

The program ecells.out will generate a default parameter file for the program called *smooth*, but that file will be immediately overwritten by the user-prepared file. The same will happen between *esmooth* and *einscat*, and the same method we can apply for the others stages (Magrin and Vaccari 2014).

Performing the standard NDSHA for Sumatra requires the preparation of input data, i.e. the selected earthquake events, seismogenic zones, and structural models then adopting some parameters in the parameters file named `makehaz.par`. To perform the NDSHA using the improvements, the same starting point will be used as show in Figure 6.2. We start to use the same selected earthquake catalog procedure as that of the eqc4seleted.exe package and the same

seismogenic zones (*.pos and *.fps) as discussed in Chapter 2. All of the enhanced procedure in the flowchart will use the same structural model (*.stp and *.por) as discussed in Chapter 4. In the makehaz.par, we used the default given value as an example.

The entire procedure from the smoothing source definition, paths generators, synthetic seismogram, and extraction of the significant parameters using the original version of NDSHA for the regional scale are used. Also, we will compute the hazard at the two maximum frequencies cutoff, 1Hz and 10Hz. Firstly, we run the standard NDSHA at 1Hz for Sumatra. Secondly, we plot the peak ground displacement (PGD) and peak ground velocity (PGV) as shown in Figures 6.2.1, 6.2.2, 6.2.3, 6.2.4, 6.2.5.

PGD: OS OP 1Hz   PGV: OS OP 1Hz
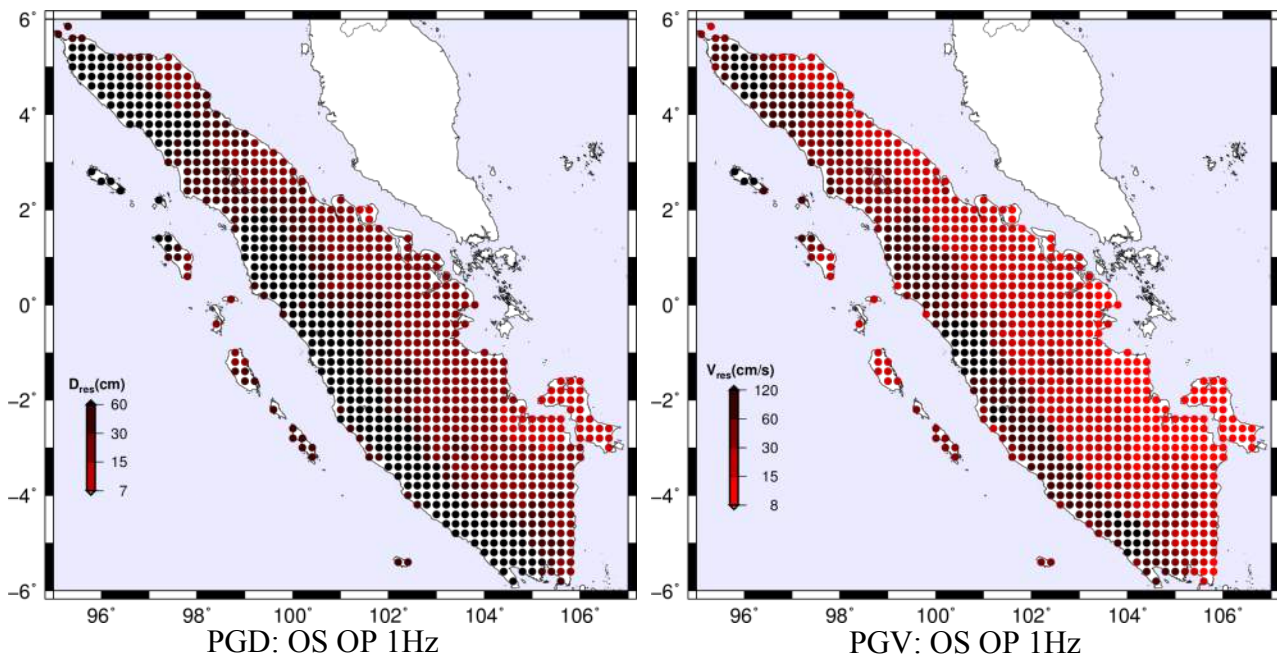
Figure 6.2.1 PGD (left) and PGV (right) produced by standard hazard procedure OS-OP

Computing the synthetic seismograms at 1 Hz as the maximum frequencies will give the results that are relatively little dependent on the structural models but may severely underestimate PGA, see Figure 6.2.2 (left). Therefore, we should estimate the appropriate DGA spectral value from the synthetic seismograms based on the acceleration response spectra and using the procedure developed by Panza, et. al (1999) as shown in Figure 6.2.2 (right). In order to get the realistic PGA, we make a run at the frequencies cutoff 10Hz, see Figure 6.2.3 (left) and the comparison with DGA 1Hz in Figure 6.2.3 (right). For the PGD and PGV results, we could expect from the theoretical considerations and from the results reported by Panza el al. (2012), there is no big difference between adopting 10Hz and 1 Hz as the maximum frequency. The DGA value for the near source zone will give the value lower than that of in PGA, and the reversed condition will happen at the far source zone. The spectral curve used for the DGA calculation is from Eurocode, and in future, we need to apply a more appropriate spectral curve to calculate the DGA for Sumatra.
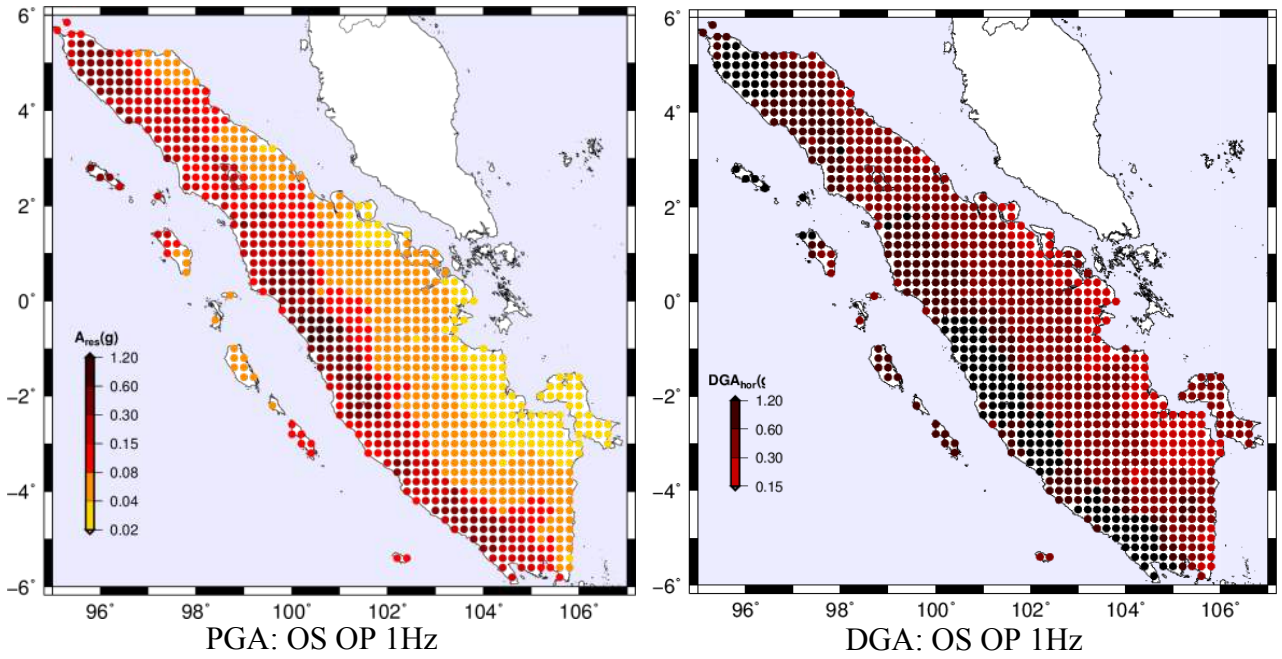
PGA: OS OP 1Hz   DGA: OS OP 1Hz

Figure 6.2.2 PGA at 1Hz (left) and DGA (right) produced by standard hazard procedure OS OP

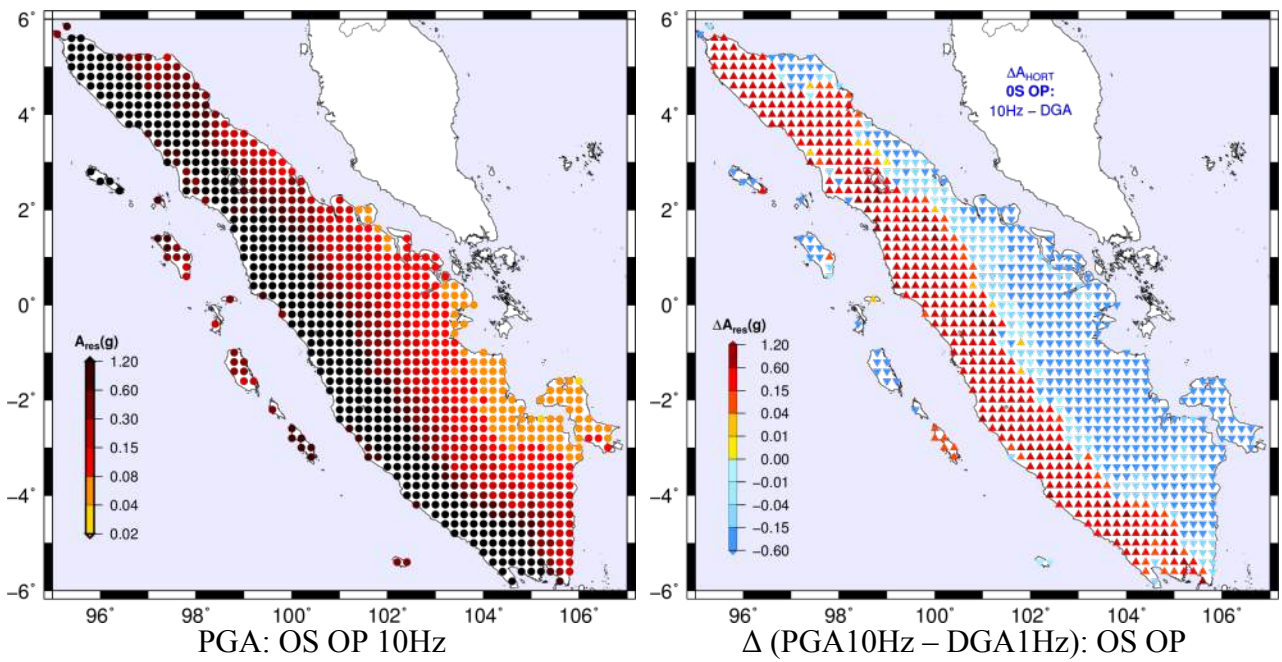PGA: OS OP 10Hz   Δ (PGA10Hz – DGA1Hz): OS OP

Figure 6.2.3 PGA at 10Hz (left) and its different with respect to DGA obtained from computations at 1Hz cutoff(right).

Figure 6.2.4 Difference between 1Hz and 10Hz computation. The picture shows the different degree of sensitivity to the structural models of 10Hz computation (quite sensitive) and 1Hz (little sensitive).
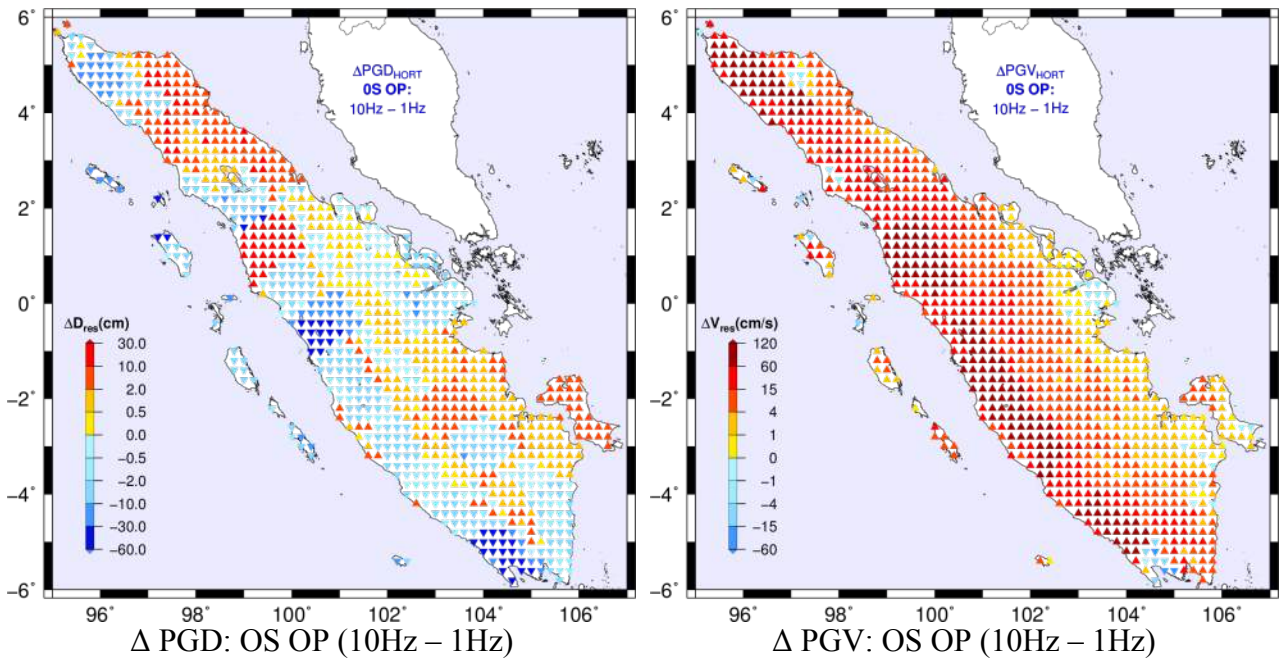
Figure 6.2.4 Different value between runs with maximum frequency 10Hz and 1Hz for PGD (left) and PDV (right)
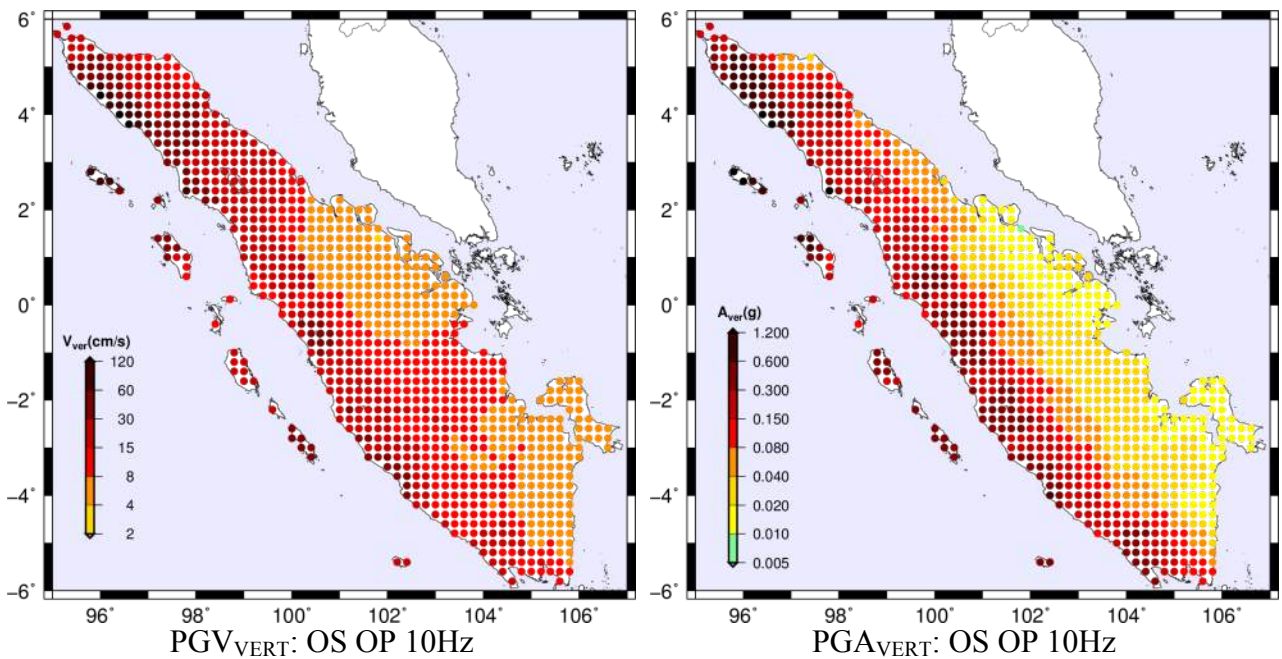
Figure 6.2.5 Vertical component produced by standard NDSHA approach 10Hz for PGD (left) and PDV (right)

The dominant periods maps show that, the dominant period in PGD (Figure 6.2.6) is mainly uniform with a high value meaning that the far field sources is the main contributor to hazard expressed in the PGD. The map of the dominant period in PGV shows that it varies in a wide range at different sites; this could be the effect of both the far field and near field sources to hazard as well as that of the structural models beneath the sites. The PGA (Figure 6.2.7-left) peaks at short periods; this fact is more evident if we plot the frequencies as done in Figure 6.2.7 (right)
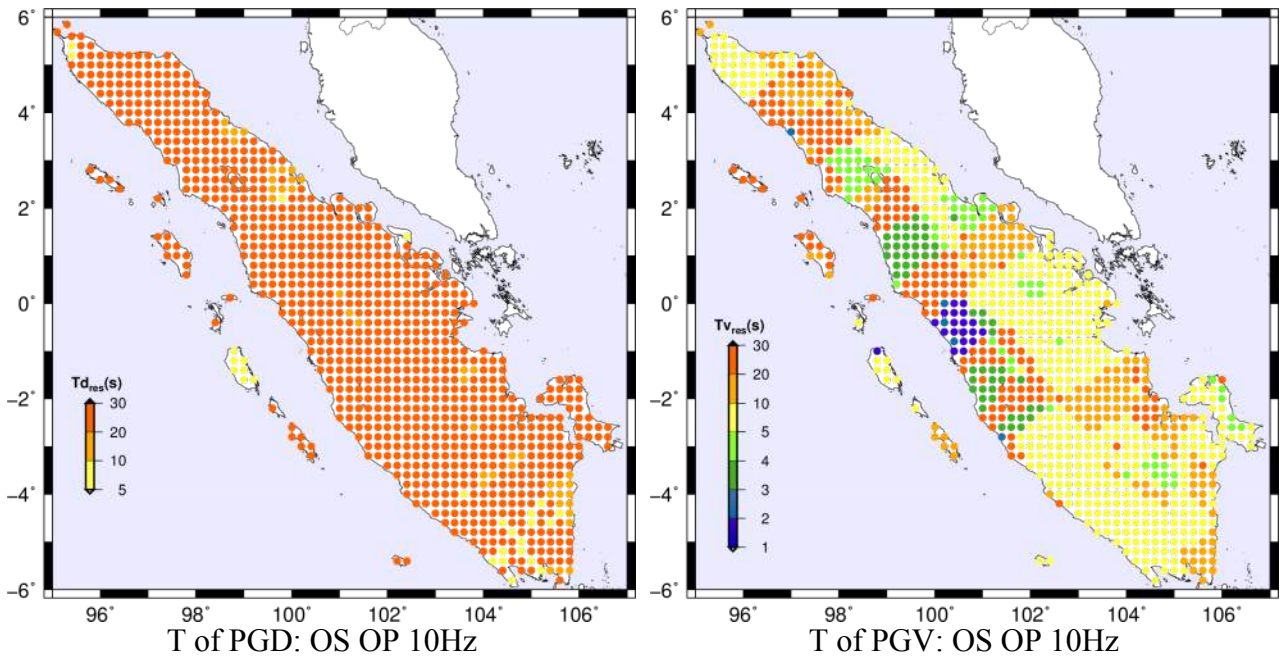
Figure 6.2.6 dominant period for displacement (left) PGD (left) and PDV (right).
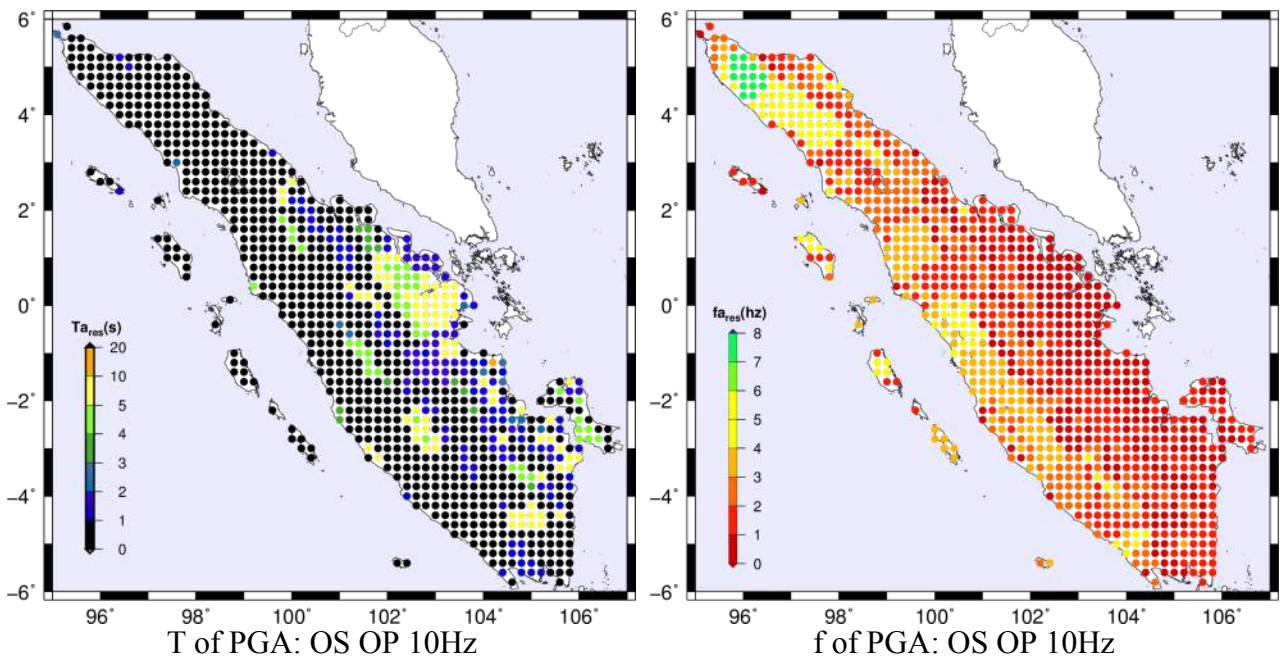
Figure 6.2.7 Dominant frequency (right) and dominant period (left) in PGA.

Figure 6.2.7 shows the dominant frequency in PGA at 10 Hz: the dominant frequency is relatively higher at the eastern part of the Sumatra region due to the proximity of a large magnitude earthquake from the subduction sources, while at the western part the frequency is relatively lower than in the eastern part due to the relatively large distance from the large magnitude earthquake.

Figure 6.2.8 and 6.2.9 show the seismic sources that contribute to the maximum ground motion parameters at different sites and different components. The PGD and PGA values of the horizontal component in Figure 6.2.8 show that the main contributor of the hazard is the lateral Sumatra strike slip. Most of the source contributing to PGA is the near field source compared to

those to PGD. This picture well shows the effect of the attenuation of acceleration at a high frequency. The main source of hazard that contributes to the maximum PGD at vertical component all over the sites is shown in Figure 6.2.9 (left), which is in the subduction zone, meanwhile, the dominant source for the estimated PGV at a vertical component is the near seismic zones as shown in Figure 6.2.9 (right).
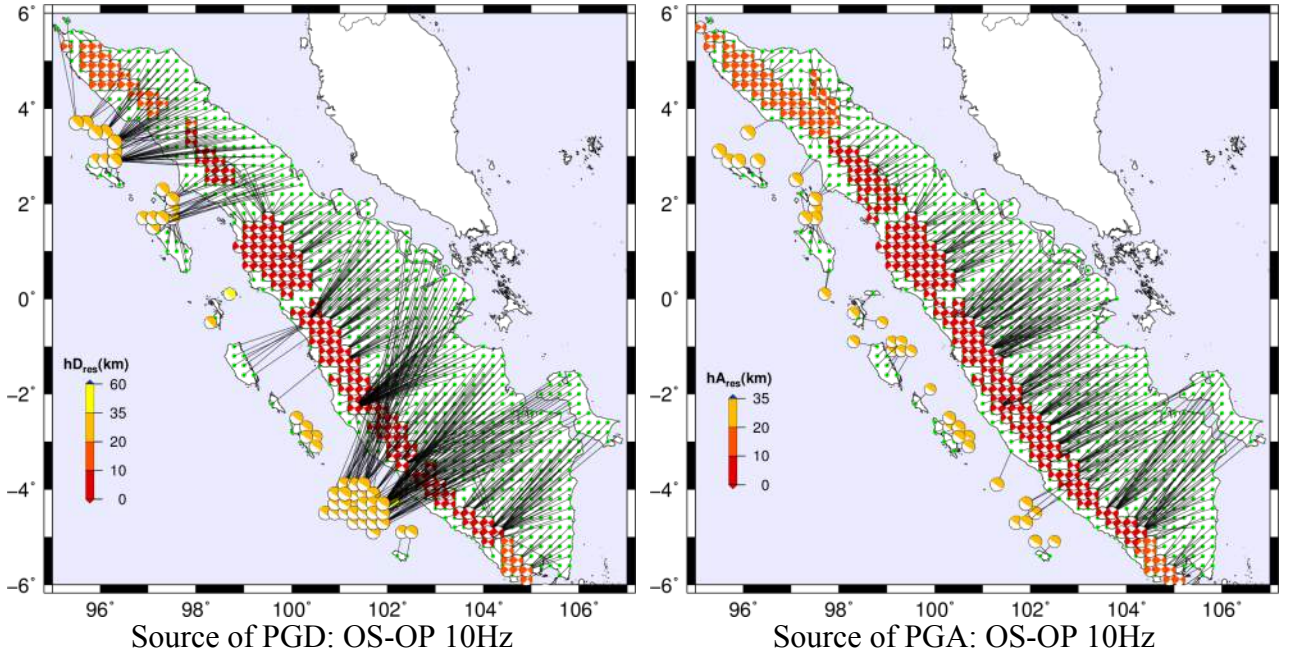

Figure 6.2.8 Plot of sources controlling PGD (left) and PGA (right) for the horizontal component of earthquake ground motion.
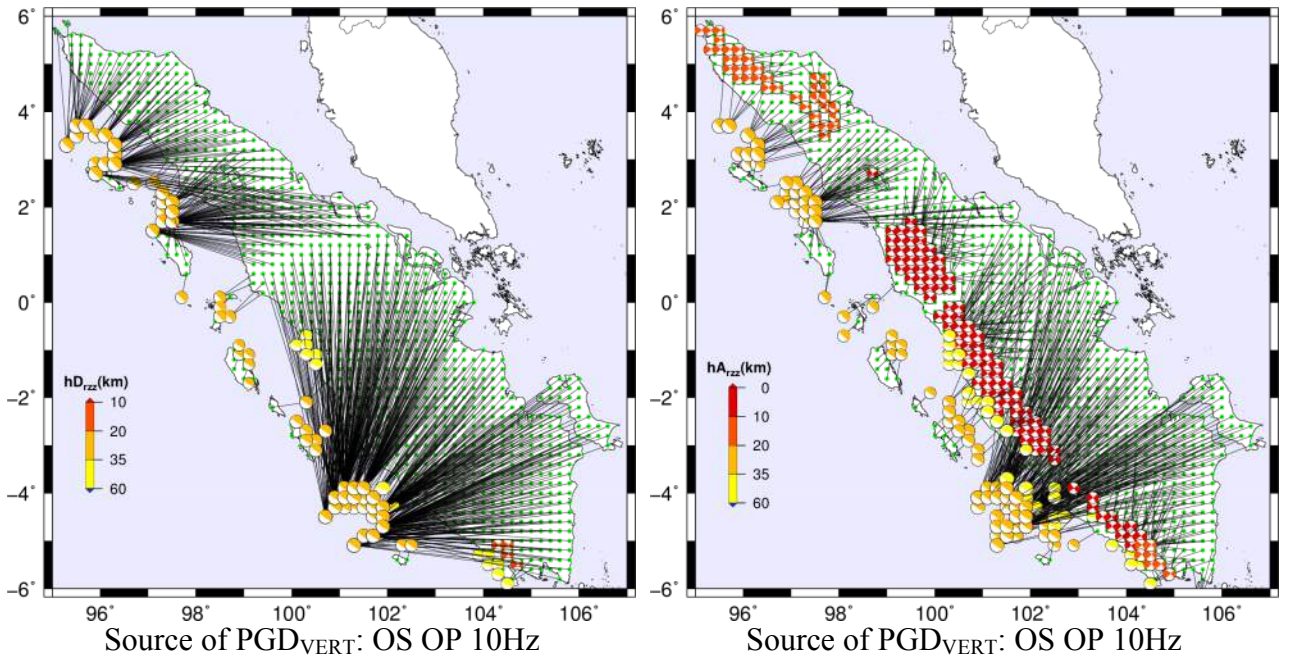
Figure 6.2.9 Plot of sources controlling PGD (left) and PGA (right) for vertical component of earthquake ground motion.

6.3. Enhanced Source Definition and Standard Paths Generator (ES-OP)

The detailed explanation and the reason we introduce the enhanced source definition (ES) procedure are discussed in Chapter 3. In the standard NDSHA procedure, it is preferred the use of the default run, and it depends on the analyst to choose the source definition for the computed hazard. This feature will be discussed in this section by setting the standard NDSHA not to start from the earthquake catalogs but from the enhanced source definition file (*.sut). The figures from 6.3.2 to 6.3.15 show the same runs previously described with the default NDSHA run to provide a proper way for the comparison between the original and enhanced source definition procedures.
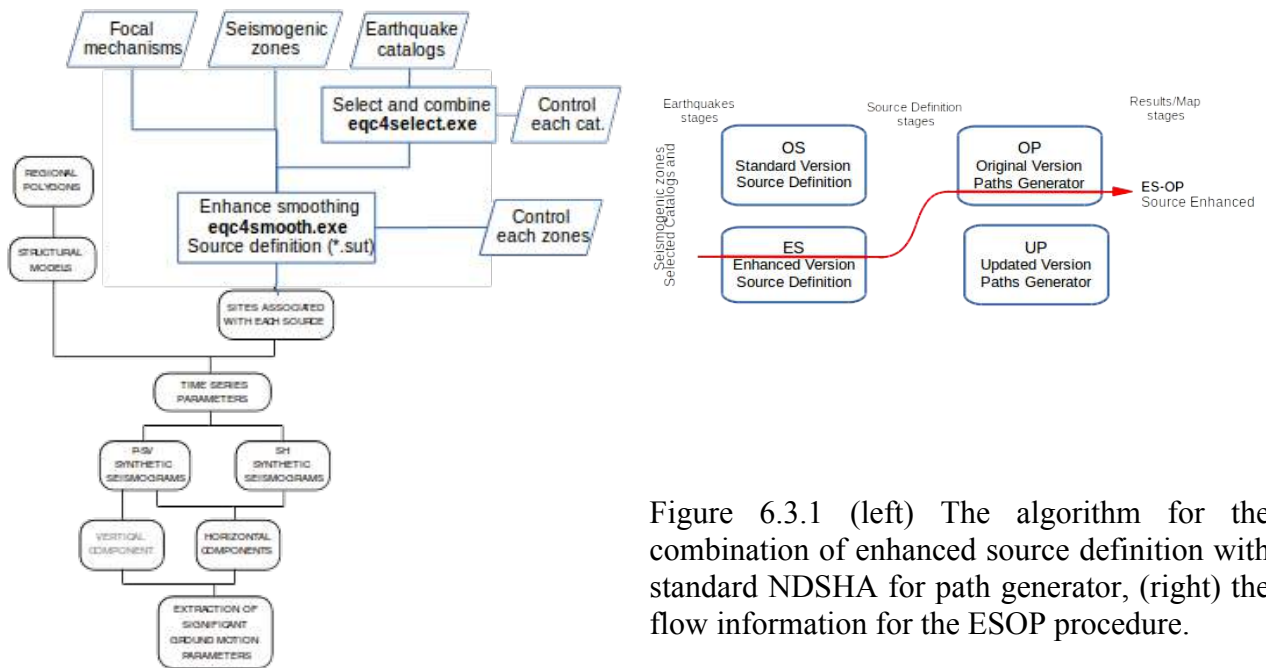
Figure 6.3.1 (left) The algorithm for the combination of enhanced source definition with standard NDSHA for path generator, (right) the flow information for the ESOP procedure.
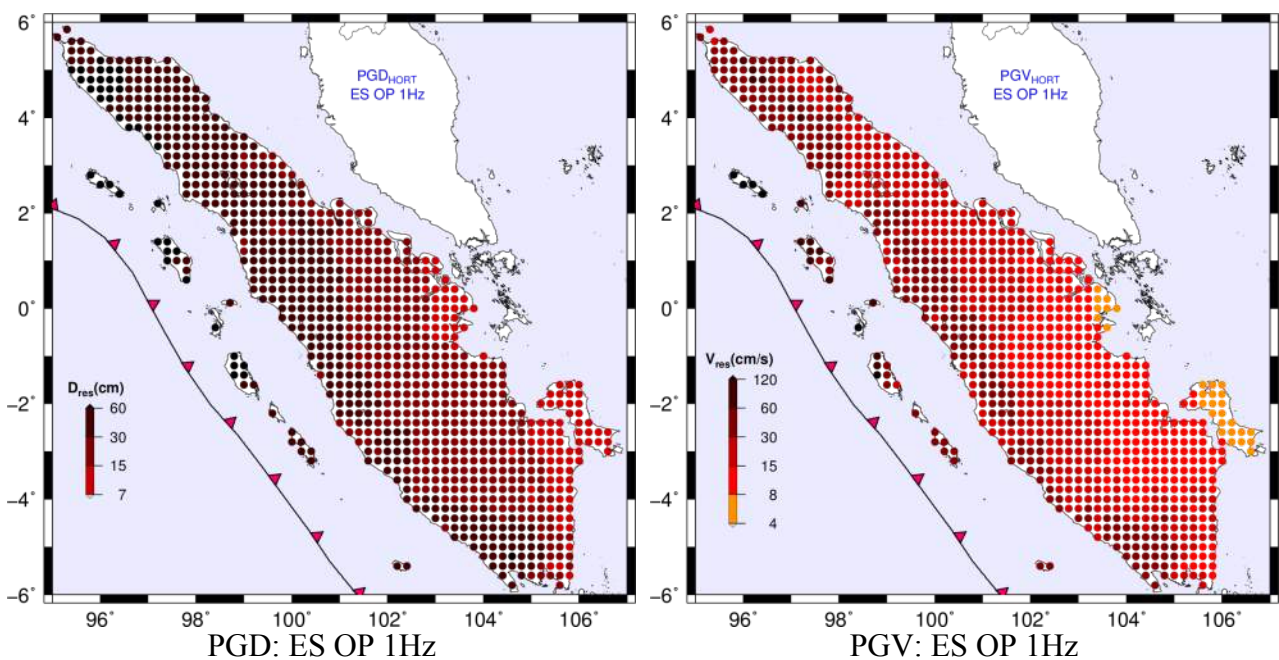

PGD: ES OP 1Hz   PGV: ES OP 1Hz

Figure 6.3.2 PGD (left) and PGV (right) produced by standard hazard procedure ES-OP

PGA: ES OP 1Hz   DGA: ES OP 1Hz
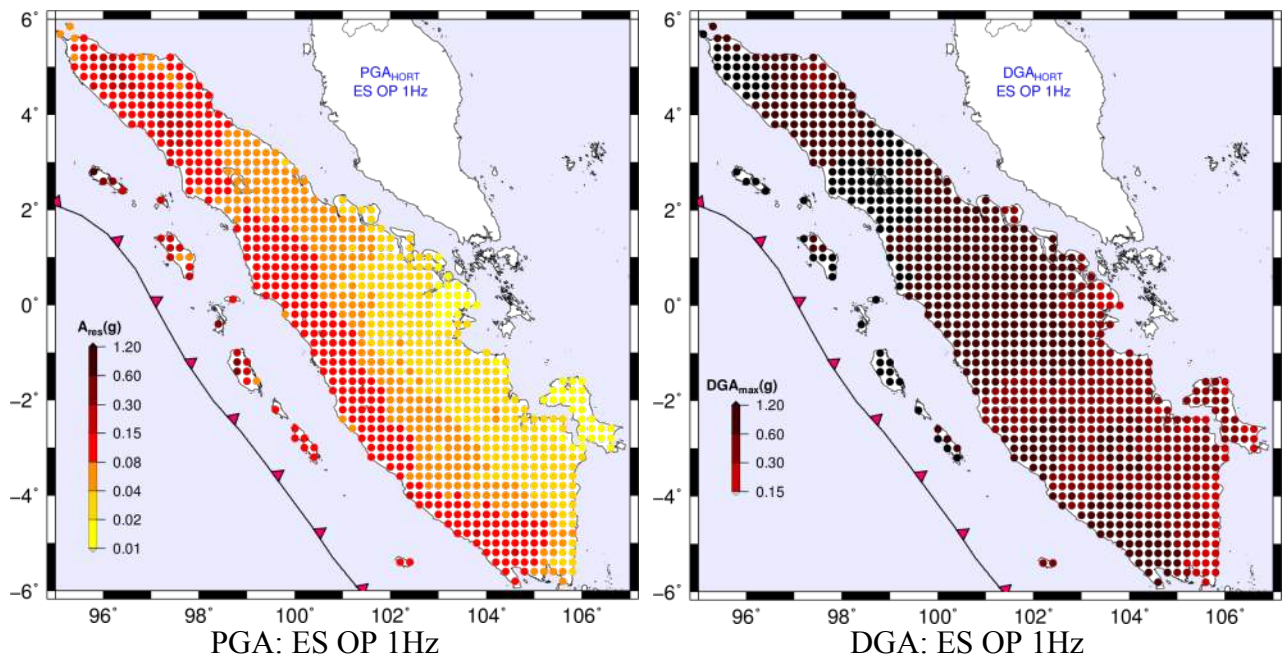
Figure 6.3.3 PGA at 1Hz (left) and DGA (right) produced by standard hazard procedure ES-OP
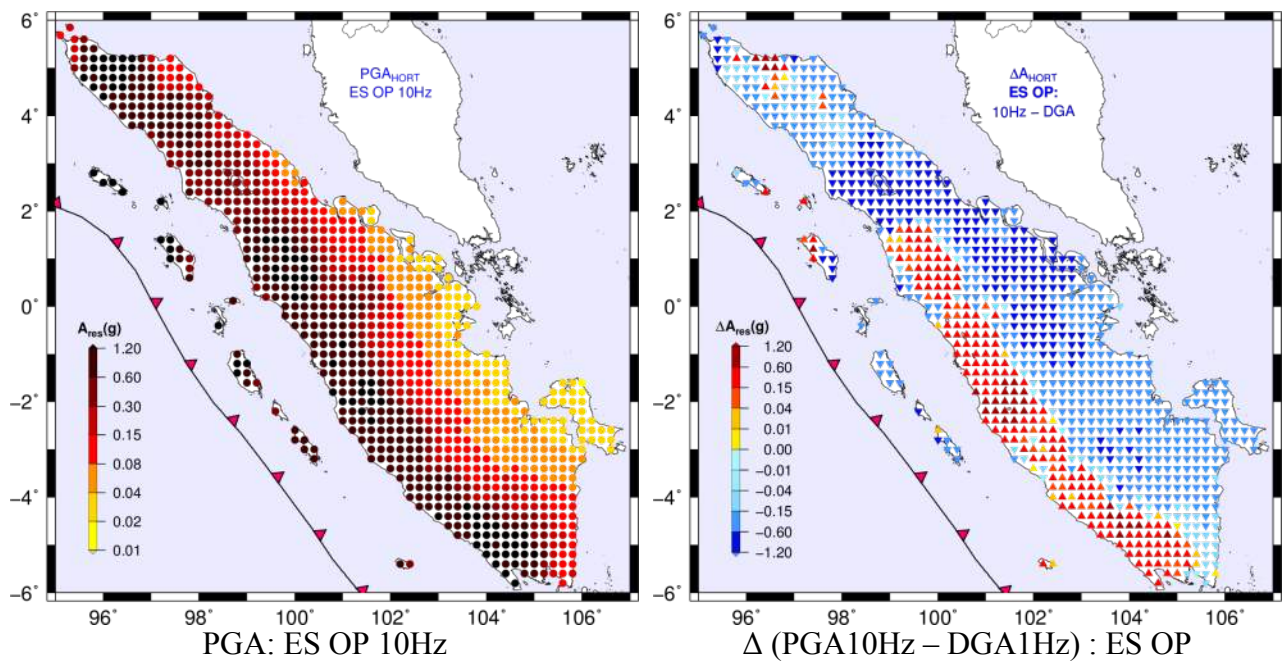

PGA: ES OP 10Hz   Δ (PGA10Hz – DGA1Hz) : ES OP

Figure 6.3.4 PGA at 10Hz (left) and its difference with respect to
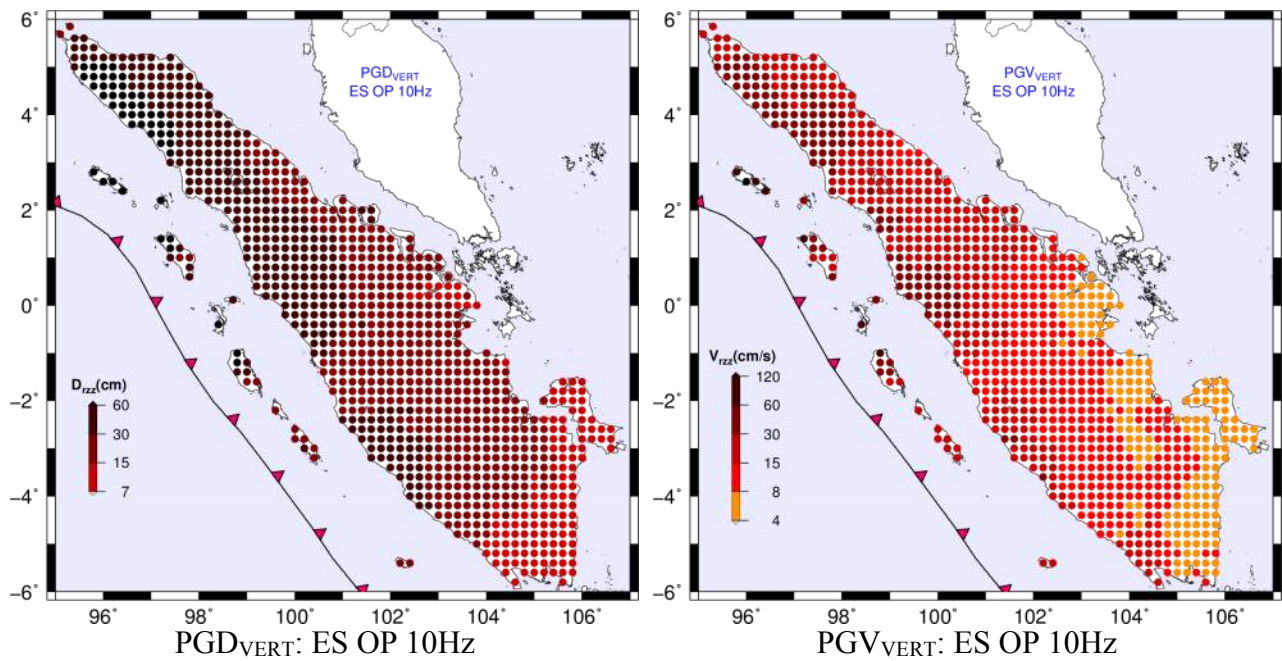DGA from run at 1Hz cutoff (right)

Figure 6.3.5 Estimated PGD (left) and PGV (right) using the
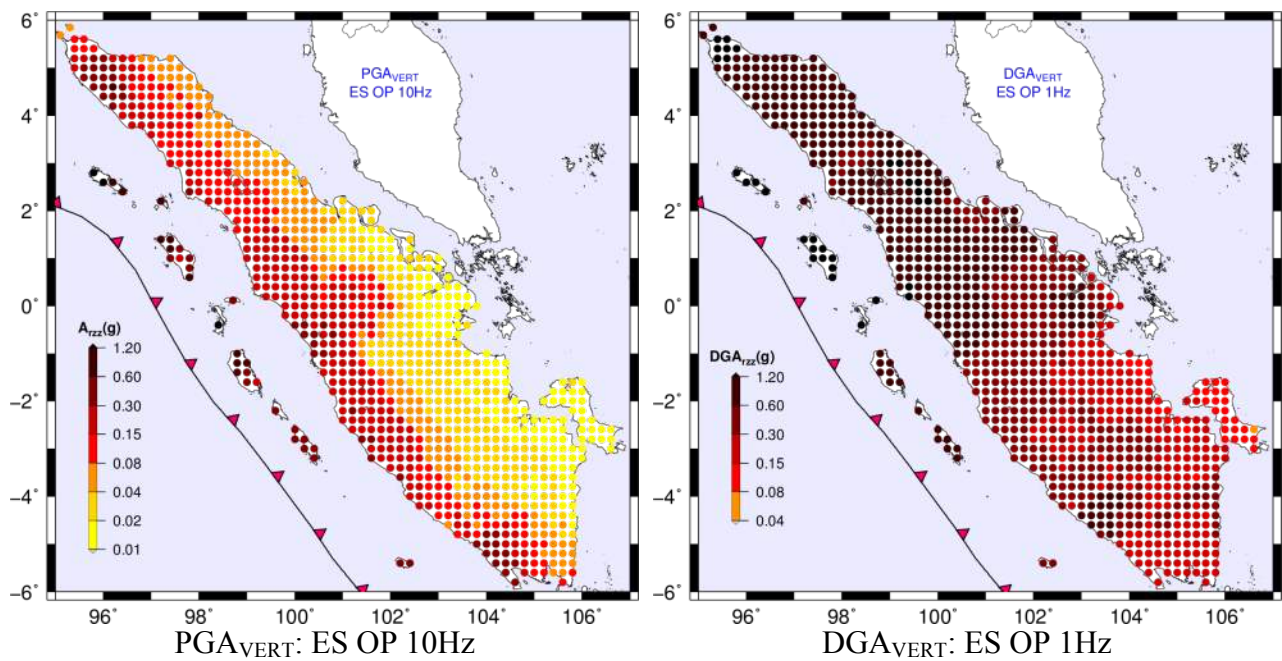possible enhanced version of NDSHA.

Figure 6.3.6 Comparison between the PGA of vertical component (left) computed at 10Hz and
DGA computed from 1 Hz cutoff signals scaled to 10 Hz using building code spectral shape
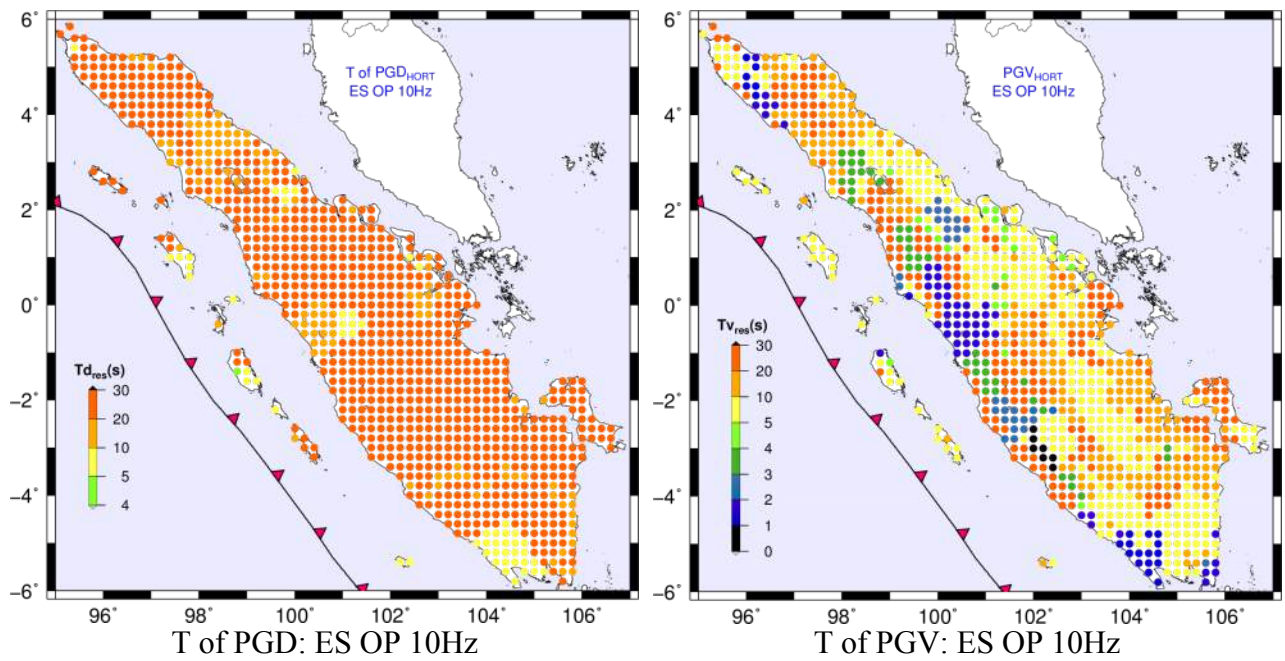(Eurocode) (right).

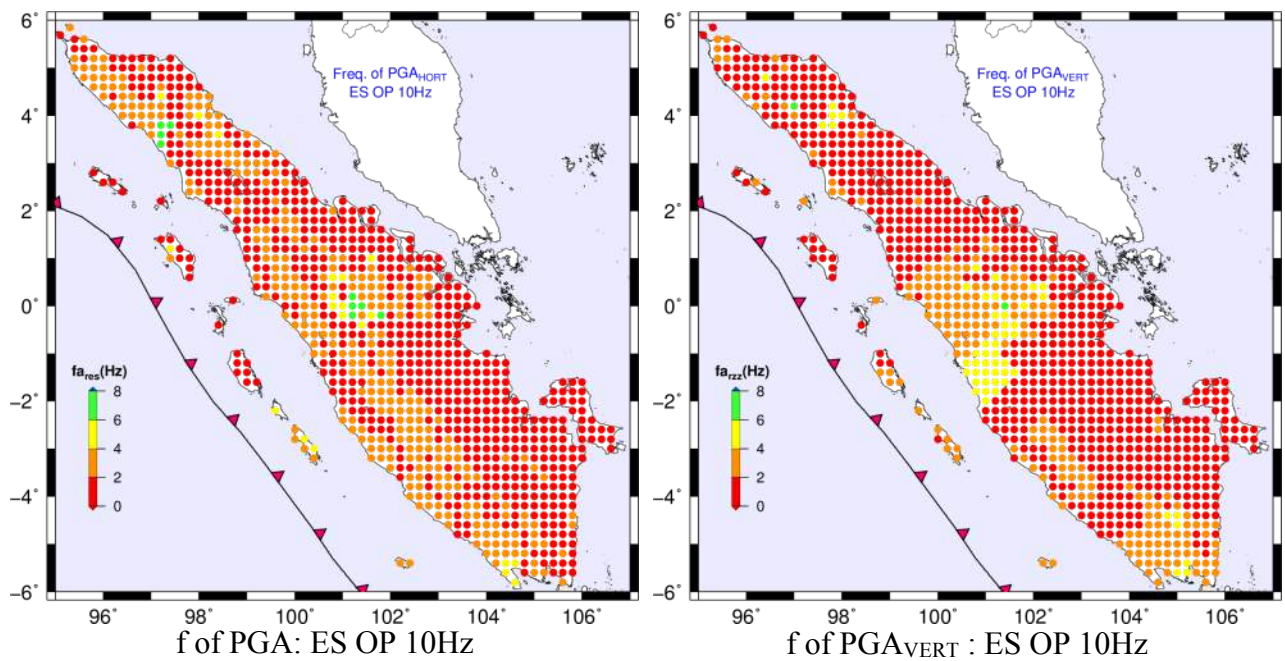Figure 6.3.7 Dominant period of PGD (left) and PGV (right).

Figure 6.3.8 Dominant frequency for PGA computed at 10 Hz for horizontal (right) and vertical components (left)
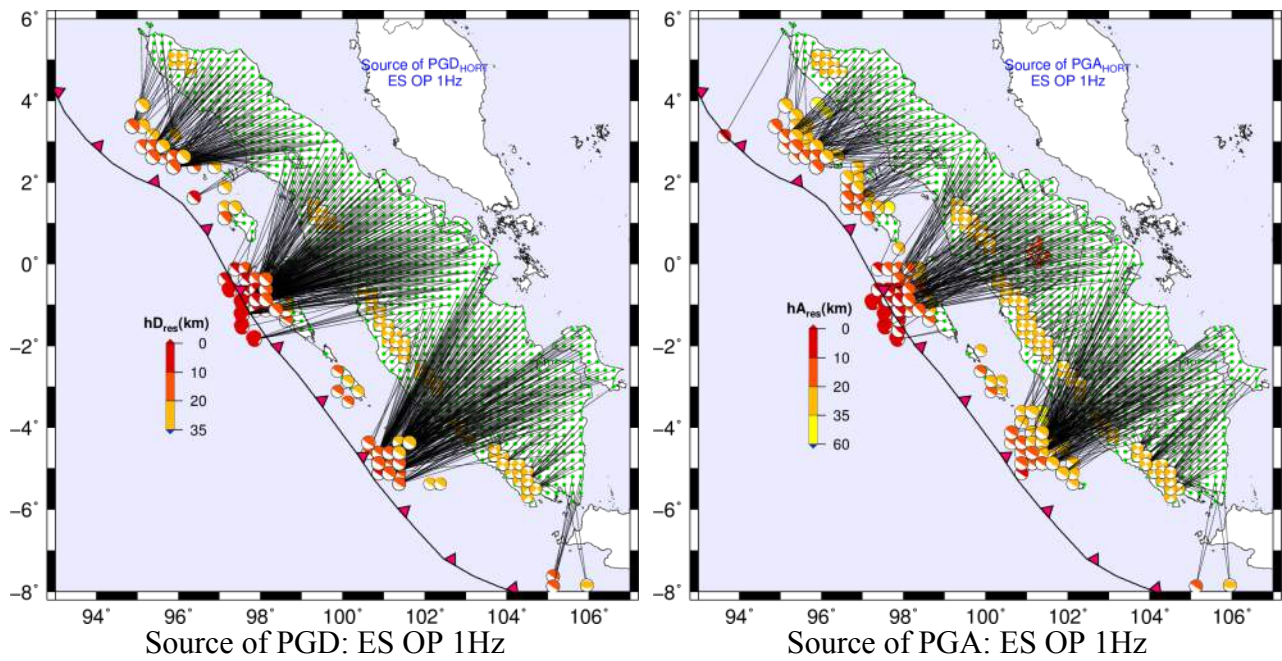
Figure 6.3.9 The sources that control the maximum PGD (left) and PGA (right) computed at 1 Hz cutoff for the horizontal component with the enhanced version of NDSHA.
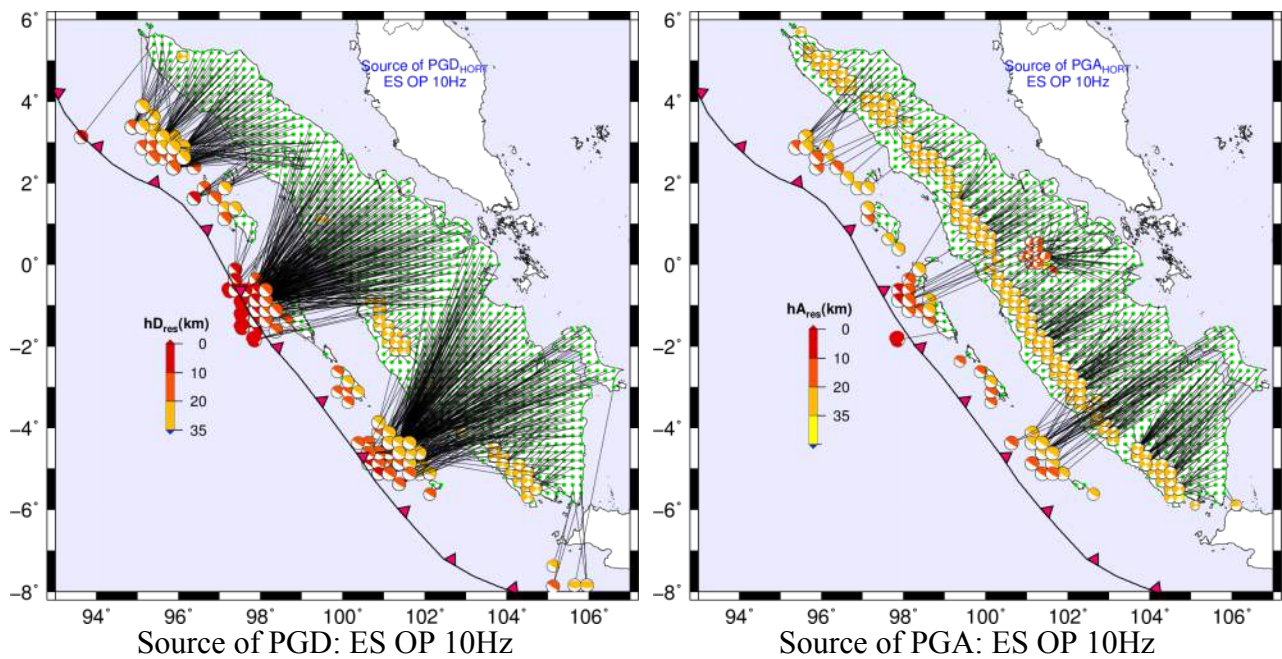

Figure 6.3.10 The sources that contribute the maximum PGD (left) and PGA (right) computed at 10 Hz cutoff for the horizontal component with the enhanced version of NDSHA.
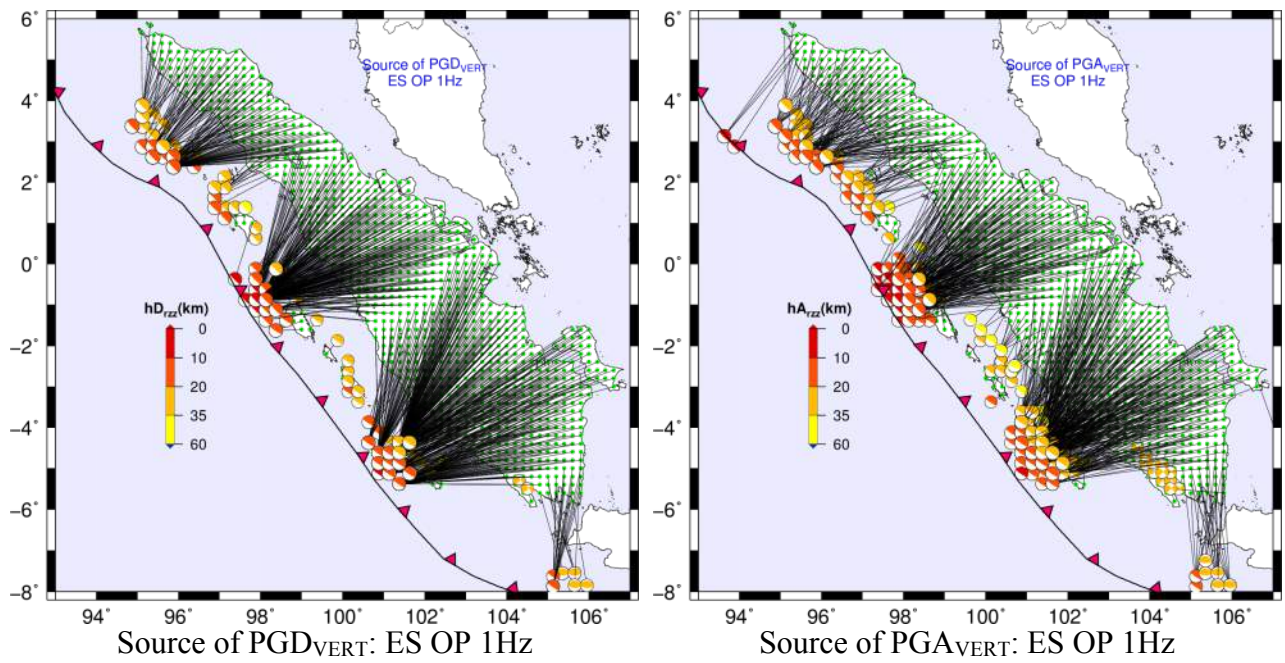
Figure 6.3.11 The sources that control the maximum PGD (left) and PGA (right) computed at 1 Hz cutoff for the vertical component with the enhanced version of NDSHA
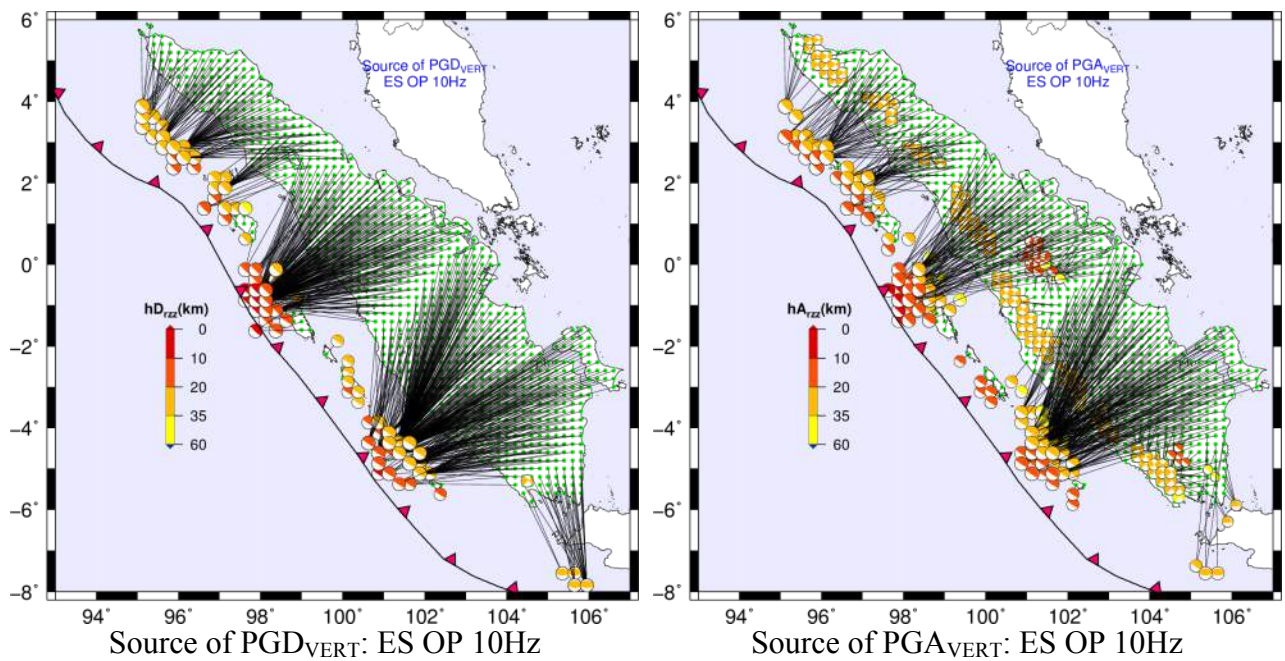

Figure 6.3.12 shows the sources that contribute the maximum PGD (left) and PGA (right) computed at 10 Hz for vertical component using the enhanced version of NDSHA

110

Figure 6.3.13 The difference between horizontal component PGD maps (left) computed at 10 Hz and 1 Hz cutoff frequency and the difference between PGV maps (right) computed at 10 Hz and 1 Hz cutoff using the enhanced version of NDSHA
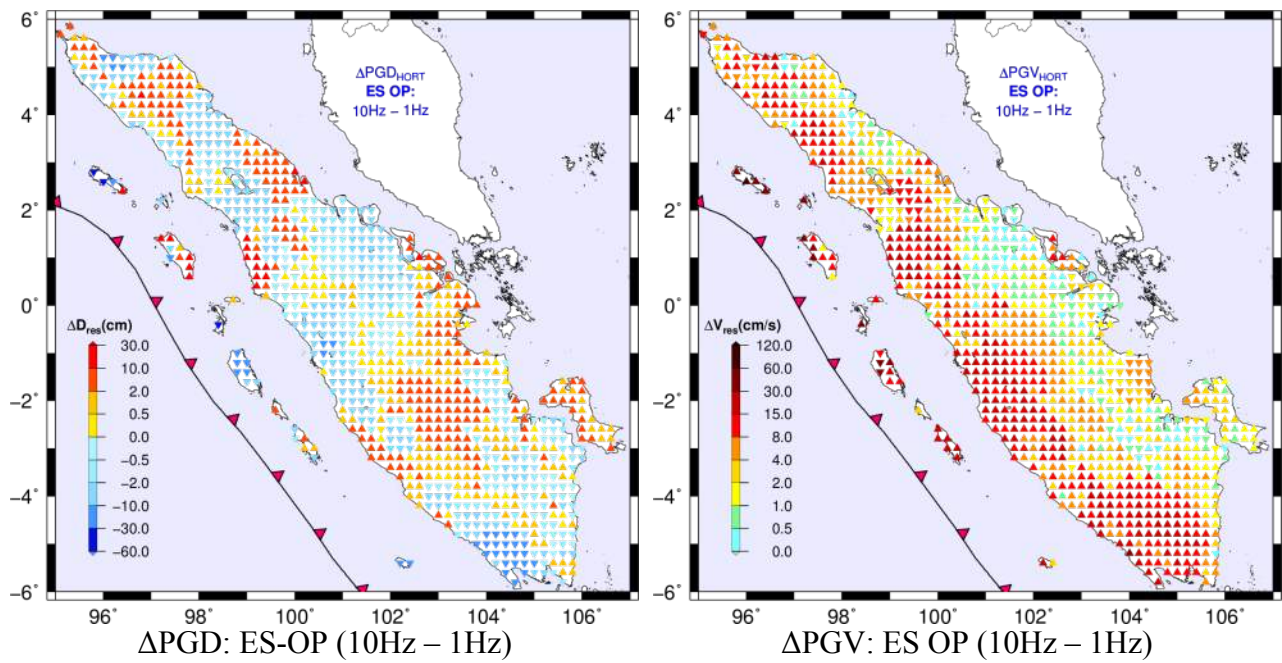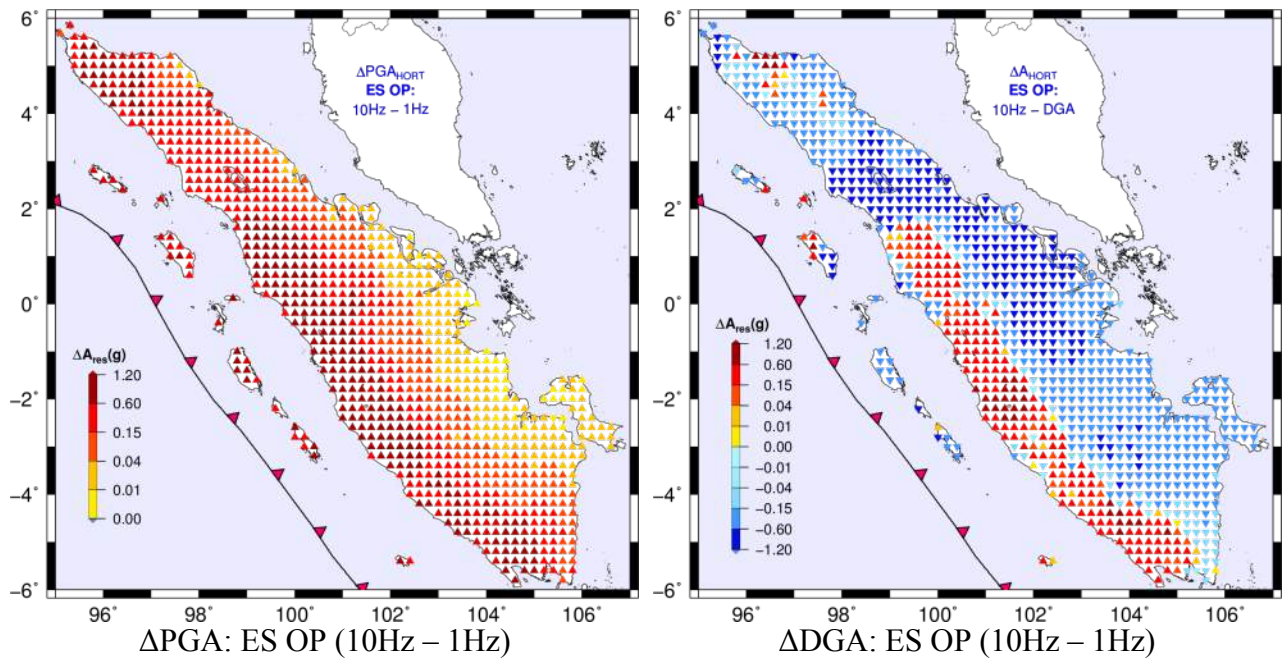

Figure 6.3.14 The difference between horizontal component PGA maps (left) computed at 10 and 1 Hz cutoff frequency and the difference between DGA maps (right) computed at 10 and 1 Hz cutoff using the enhanced version of NDSHA

Figure 6.3.15 The difference between horizontal component PGD maps (left) and PGV maps (right) computed with enhanced (ES) and original source (OS) definition at 1 Hz cutoff frequency.

Figure 6.3.16 The difference between horizontal component PGA maps (left) and DGA maps (right) computed with enhanced (ES) and original source (OS) definition at 1 Hz cutoff frequency.
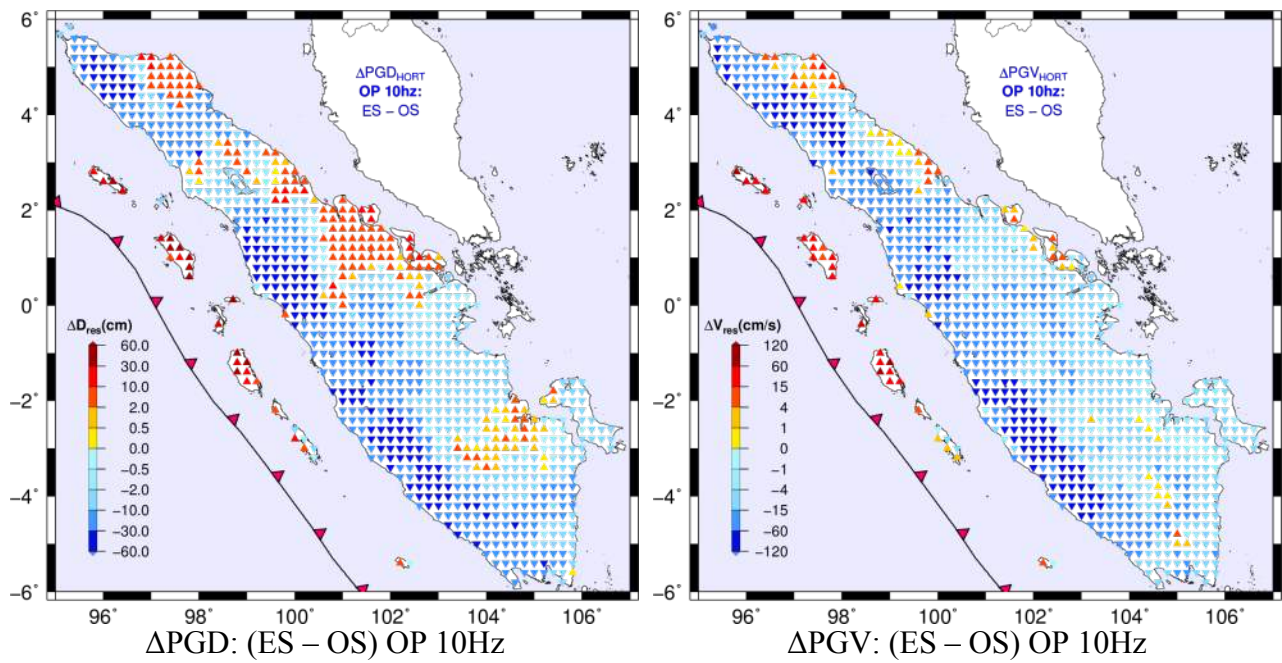
Figure 6.3.17 The difference between horizontal component PGD maps (left) and PGV maps (right) computed with enhanced (ES) and original source (OS) definition at 10 Hz cutoff frequency.
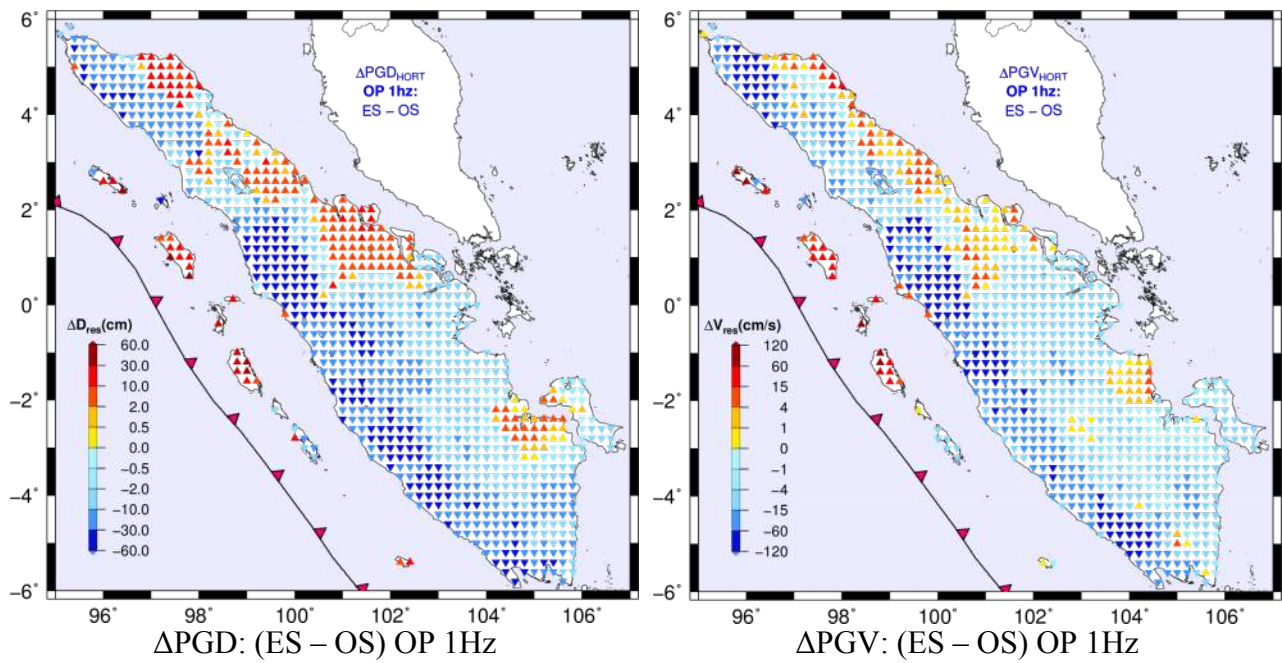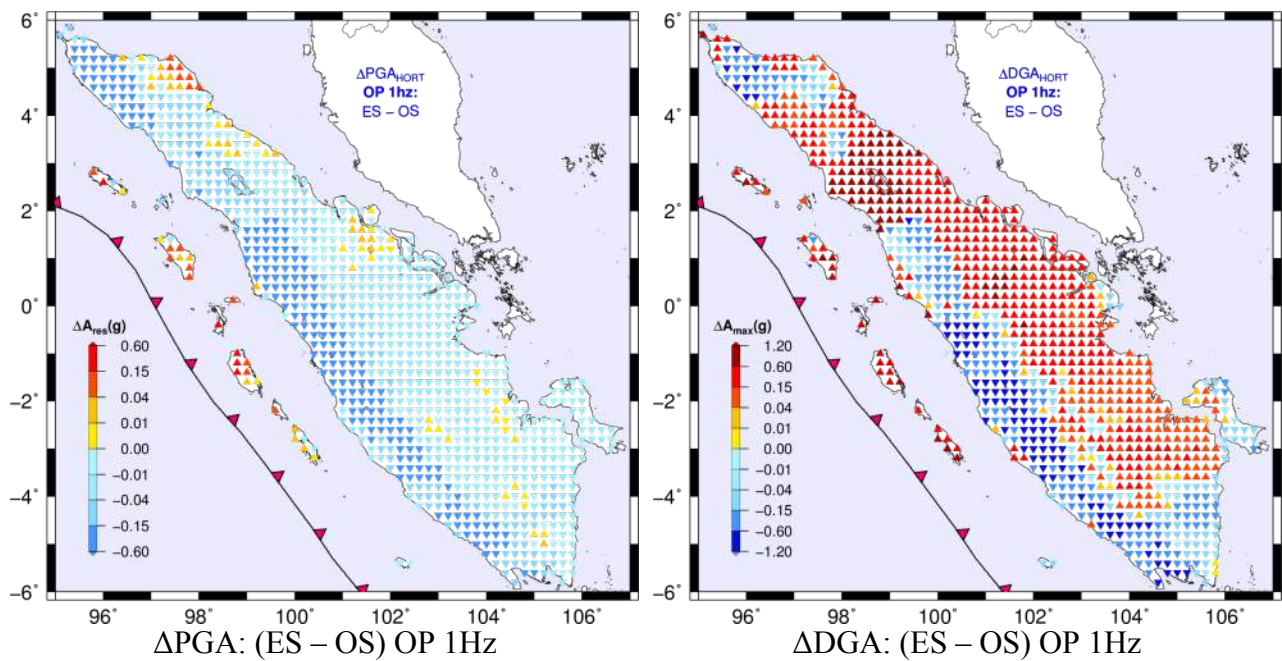

Figure 6.3.18 The difference between horizontal component PGA maps (left) and DGA maps (right) computed with enhanced (ES) and original source (OS) definition at 10 HzHz cutoff frequency.

113

Figure 6.3.19 The difference between Vertical component PGD maps (left) and PGA maps (right) computed with enhanced (ES) and original source (OS) definition at 1 HzHz cutoff frequency.

Figure 6.3.20 The difference between Vertical component PGD maps (left) and PGA maps (right) computed with enhanced (ES) and original source (OS) definition at 10 HzHz cutoff frequency.
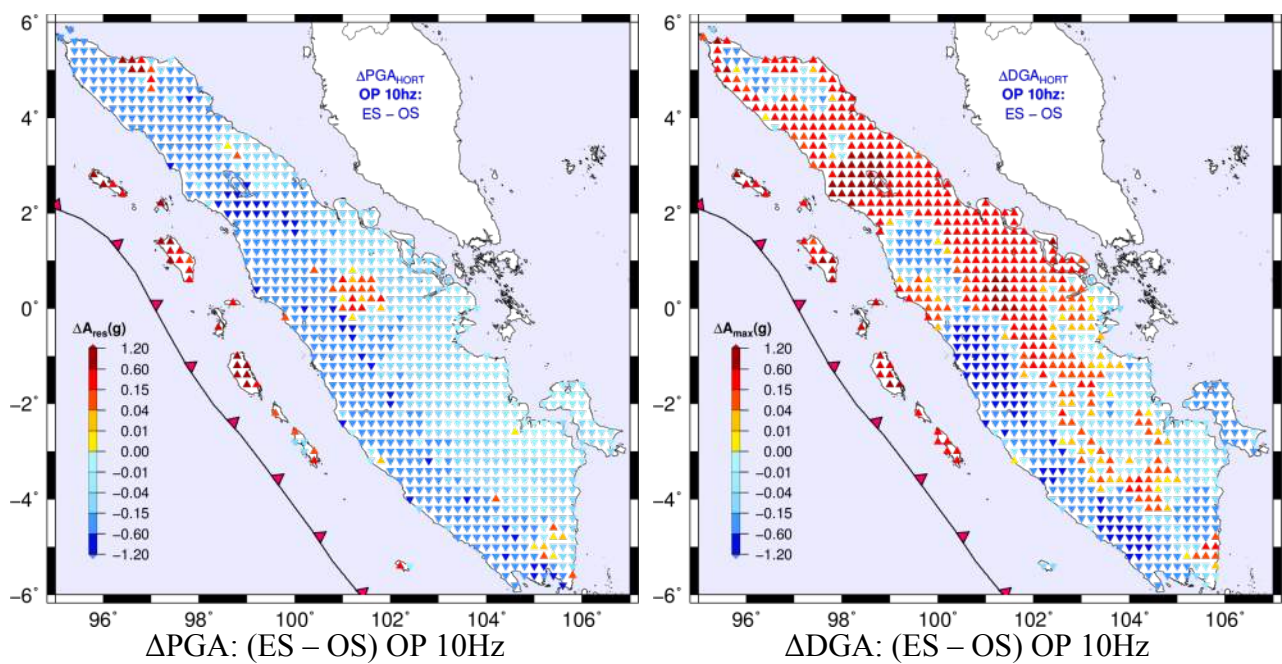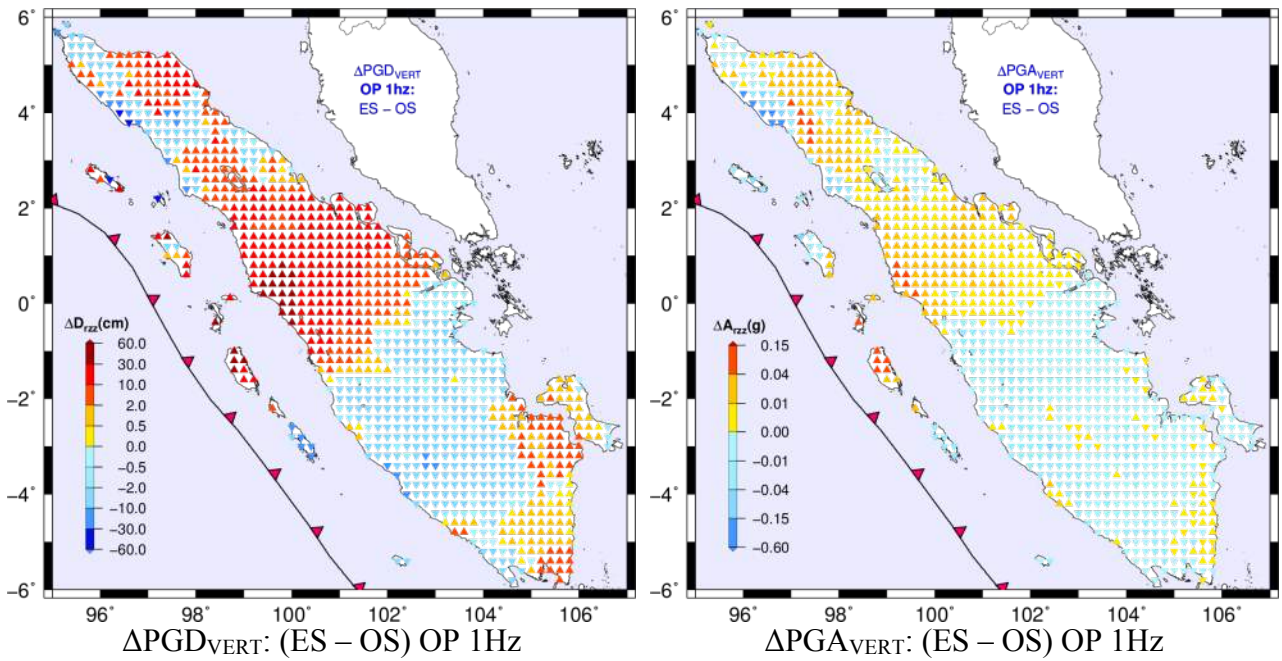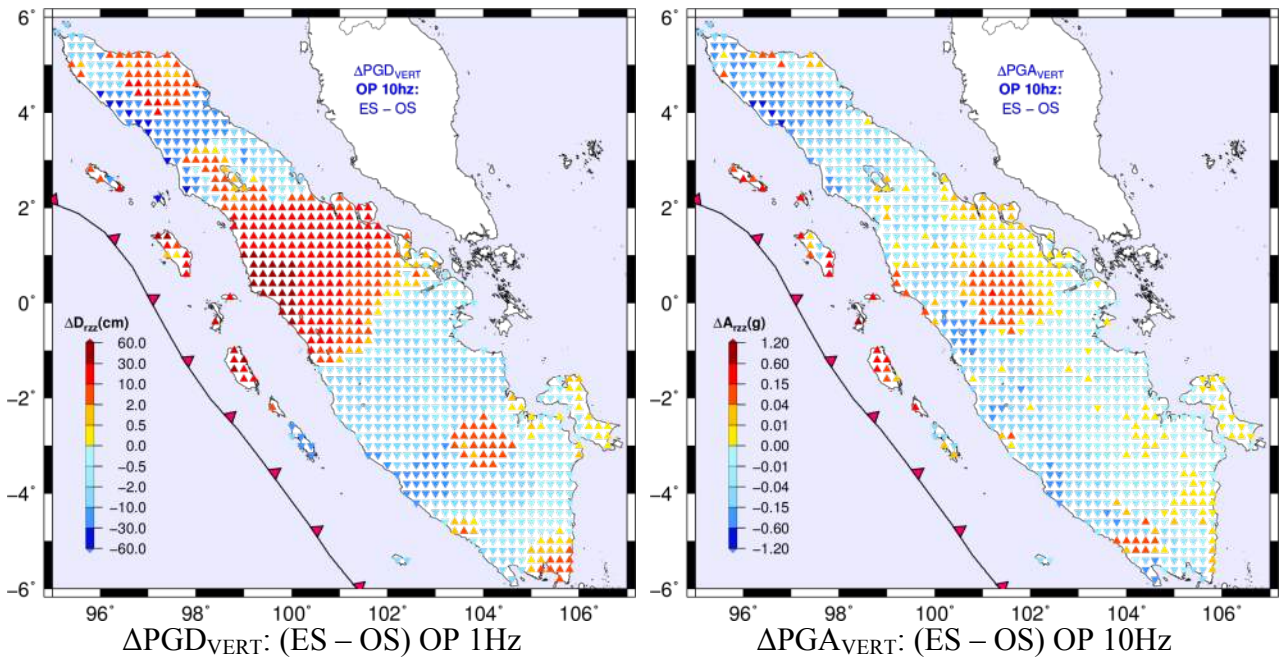
Figures 6.3.3, 6.3.4, 6.3.5, 6.3.6 show that using the enhance source definition produces a PGD, PGV, and PGA very similar to those produced with the standard NDSHA package.

Apparently PGV at 1Hz cutoff based on the ES-OP at the far field source (e.g. Bangka Island) shows a lower value (6.3.2-left) than that of using the standard package OS-OP (6.2.1-left). The PGA produced by ES-OP (Figure 6.3.4) shows a relatively significant decrease at the near and far sites in the Sumatran fault system (e.g. Bangka Island) in comparison with the PGA produced using the standard package OS-OP (Figure 6.2.3). This could be because in the enhanced source definition procedure, we can control the minRun (minimum magnitude run for each site) for each seismogenic zone. We adopted minRun=0 for the seismogenic zones no 13 and 14 and minRun=5.5 for seismogenic zone no 1, 2, and 3. However, in the standard package of NDSHA, a single value of minRun is usually adopted for all of the seismogenic zones. If we set minRun=0, it may cause underestimation for the zones no 1, 2, and 3, but if we set minRun=5, it will lead to overestimation for the zones no 13 and 14.

The computed PGD and PGA by the enhanced procedure ES-OP are more realistic if compared with the standard procedure OS-OP. Figure 6.3.10 (left) shows the estimated PGD using ES-OP at sites far from the sources containing the effects of the distant subduction source, while using OS-OP leads to that of the far sources does not contribute to the computation of PGD at the distant sites (PGD displacement for subduction cannot reach the Bangka Island) and the OS-OP only can get PGD from the near source as shown in Figure 6.2.8 (left). However, the estimated PGA based on ES-OP (Figure 6.3.10-right) and OS-OP (Figure 6.2.8-right) show almost the same result as that of the small source-receiver distance. This is more reasonable because the subduction source can generate a larger magnitude than that of the strike-slip fault (a bigger magnitude even though far can reach a distant field); thus, it can affect Bangka Island with significant impacts while the strike-slip sources cannot.

The enhance source definition produces the different strong motion value when adopting 1Hz and 10 Hz cut off frequency computation (Figures 6.3.13 and 6.3.14) and shows a different behavior similar to that of by the standard source definition procedure OS-OP (Figures 6.2.3-left and 6.2.4-right). The Figures 6.3.15 to 6.3.20 show that the PGD, PGV, and PGA computed using ES-OP are lower in value than those at the same ground motion parameters computed using the standard version. The enhanced ES-OP may produce a greater DGA than the standard procedure OS-EP along northern part of Sumatra. The dominant period in the computed PGV by the ES-OP (Figure 6.3.7-left) is relatively more scattered if compared to the period of PGV produced by OS-OP (Figure 6.2.6-left). One possible reason is that the ES-OP has no fixed source depth (magnitude dependent source depth) if compared to the standard OS-OP. The enhance source definition ES-OP is obviously using the estimated focal depth from the revised earthquake catalogs (as shown by the color of beach balls in Figure 6.3.9-12) while the standard OS-OP using three different magnitude-focal depth threshold values (10km, 15km, 20km) based on Equation (3.1).

6.4. Enhanced Source Definition and Updated Paths Generator (ES-UP)

The NDSHA method is still evolving, and the computer code is being constantly improved since the original implementation, to better fit the need of producing realistic ground shaking maps and ground shaking scenarios, at different scale levels, by incorporating all relevant progresses in the knowledge of geological processes and their numerical modeling (the reduction of the epistemic uncertainty). A complete description of the methodology can be found in Panza et al. (2001). Here we will describe in some detail just the parts of the methodology that has improved over time. Among the most relevant changes recently implemented to the algorithm, as Panza et al. (2012) mentioned, as follows:

- code optimization, which leads to a speedup in the computation by a factor of about 6;
- the possibility to consider the very realistic source models that account for the rupture characteristics at the fault, directivity included;
- the option to consider the sources distributed not only within the seismogenic zones (Meletti, Patacca and Scandone, 2000; Meletti and Valensise, 2004), but also in the nodes identified by the morphostructural zonation (Gorshkov et al., 2002, 2004, 2009);
- the option to compute the synthetic seismograms with a maximum frequency content of 10 Hz;
- the option to compute the ground shaking maps also for the vertical component;
- the option to compute the ground shaking maps associated with the areas alerted by the CN and M8 algorithms (Peresan et al., 2005).

The application of NDSHA for Sumatra, which is characterized by the complex seismogenic zoning, needs some modification to the algorithm being used about the source definition, as discussed before. The proposed updates for NDSHA include the enhanced source definition procedure as discussed in Chapter 3. The new source definition, proposed and tested against the original path definition, successfully produced a hazard map as it was expected. The enhanced source definition is a user-friendly configuration file and gives a lot of flexibility for the user. But when we apply the enhanced source definition, we have to call some *.par files and the standard package with a rigid configuration file. Therefore, we want to update the path generator to adopt the user friendly configuration file. The main goal of making an update for the existing path generator used by the NDSHA approach not only to make it more user friendly but also to handle the problem of the sources unreached in the far receiver in Bangka Island using the medium range (R2) threshold as described before.. The updated path generator (UP) will maintain the efficiency of the computation process to select the significant sources of hazard from the far field zones. Figure 6.4.1

shows the location of the updated path generator (in blue box) and the receiver enhances source definition form (red box).
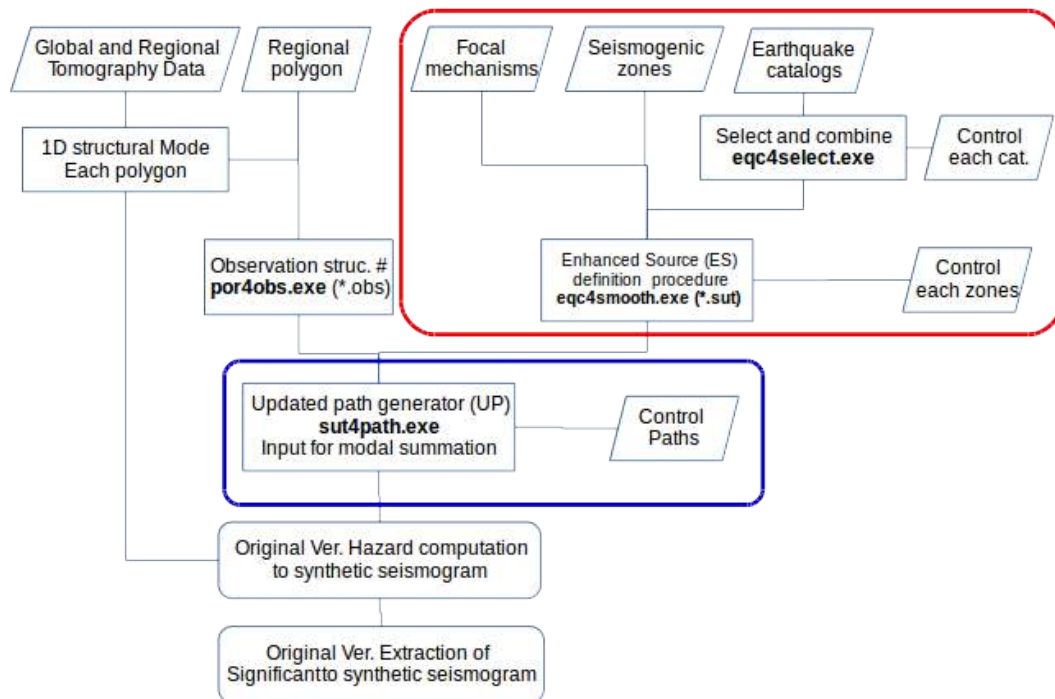
Figure 6.4.1 Flow chart of the standard enhanced NDSHA procedure for a regional scale with the enhanced source definition (OS) in red box and the updated paths generator (OP) in blue box

```
this file for sut4pat.par
-----------------------
shoa9n                           # project name
../base/suman.sut
fmax 1
SPX "s/shof"
sum2.obs
../base/hazdistance.min
../base/hazdistance1.max
INT -5                           # give auto interpolation
MIS 100                          # minimal source per receiver
BIN 1
MOT 2
FUL 1
CLN s f
itacode.cod
SCL 1 90 guphas
```

Listing 6.2. The configuration file for updated path generator

The configuration file starts from the freely typed header in the first line and the second line, and we kept the one traditionally used in the configuration file as line -------------, which will be

ignored by the program if the line starts with the three characters of a strip. The first line following the word will be defined as a project name, in Listing 6.2 project name shoa9n. This configuration file enables the user to set the different parameters. For example, `../base/suman.sut` is very useful when we want to make an experiment with the different source definition because we can control and know very well what file we use. In the standard version, the name should be changed to a project name and be put in the same directory, i.e. sha9n.sut; in our experience, it is easy to make mistakes here because some files are subjecting to the updates and reformatting from time to time, so it is better to fix one source directory for all of the independent files (e.g. the Gusev spectral curves). As an additional example, we perform an experiment using the file name `../base/hazdistance.max,` which is always being used with the same name. The option `SPX "s/shof"` is very helpful to reduce the number of the files in the folder, and subsequently to reduce the used memory in the hard disk space, by referring to the directory of the master spectral files without the need to copy it in the working directory; these features are very useful when we deal with several scenarios.

The main advantage of the updated path generator UP is the transparency of the input file in the computation process. The important motivation for this updated path generator is that not all of the sources have an effect on the site being studied, so it is more useful to define the minimum magnitude at different distances that can affect the site of interest: if we set MIS 100 that means that only 100 path will be used for each receiver. The details about the usefulness of this suggested procedure will be given in the next chapter for increasing the efficiency of the computational process. In the standard package, the interpolation is given by a positive integer number, e.g. 5, and it will set the same interpolation value for all of the computed synthetic seismograms. In the updated version, we give the possibility to change the interpolation value depending on the distance between the source and the receiver with a certain maximum value, e.g. `INT -5` will let the interpolation value to vary from 0, 1 until 5. The application of this method is not an easy task because we also need to define the interpolation parameter based on the source depth in order to reduce the calculation of the eigenfunctions. This feature is a challenging feature to increase the synthetic seismograms efficiently and needs a further investigation in the future.

There are two ways to execute this program: without or with the arguments (i.e. `sut4path.exe and sut4path.exe alternative.par,` respectively). Without the passing parameter, the default configuration file sut4path.par is read, and with the passing parameter, there is the possibility to read another file name, e.g.:

```
sut4path.exe
sut4path.exe alternative.par
```

After the execution, the program will generate several files needed for the computation of the synthetic seismograms. For example, the following file with the project name xxx. The Configuration files are: `makehaz.par`, `sne.par`, `sgv.par`, `sgrz.par`, `sgr.par`, `sgl.par`, `gconv.par`

The input files for generating the synthetic seismograms are : `xxx0001.isg`, `xxx0002.isg`, … number of the polygons.

For the information files : `xxx.pat,`, `rns.lst`, `pat.lst`, `isg.lst`, `xxx.srp`, and the script r file contains :

```bash
#!/bin/bash
nameroot=xxx
fclean.sh s f
START=$(date +%s)
echo estimate    7.8660 hours to run  283177 paths
[[ ! -e accg.cpt ]] && hazcpt.out
esgl0050.out
esgrz0050.out
esne.out
for file0 in $(cat rns.lst);do
find . -maxdepth 1 -name "${file0}.rzz" ! -name "*f[012]".rzz  >> fft.par
done
efft.out
esre.out
find . -maxdepth 1 -name "${nameroot}*f0.rzz" >> cou.par
find . -maxdepth 1 -name "${nameroot}*f1.rzz" >> cou.par
find . -maxdepth 1 -name "${nameroot}*f2.rzz" >> cou.par
ecou.out
efinmax.out
eexmaxsig.out
efinmaxdgav.out
eexmaxsigdga.out
egconv.out
hazgmt.sh xxxf2max.dga
hazgmt.sh xxxf0res.amx
hazgmt.sh  -4 xxxf0res.amx
hazgmt.sh xxxf1res.amx
hazgmt.sh  -4 xxxf1res.amx
hazgmt.sh xxxf2res.amx
hazgmt.sh  -4 xxxf2res.amx
fclean.sh s f
pwd
END=$(date +%s)
DTS=$(echo $END - $START | bc)
DTH=$(echo $DTS | awk '{ print $1/3600}')
echo $DTS | awk '{ print $1/  283177 " second/path"}'
echo estimate    7.8660 hours to run  283177 paths
echo "finish for " $DTH "hours"
```

Listing 6.3. Script r which is generated by sut4path.exe program

Figure 6.4.2 and 6.4.3 show the horizontal PGD and PGV maps computed at 1 hz and 10 hz frequency cutoff using the updated path generator. The source definition is applied using the enhanced source definition, which is used in Section 6.3 as the ES-OP procedure. Therefore, these maps show a slight difference with respect to the picture in Figure 6.3.3.
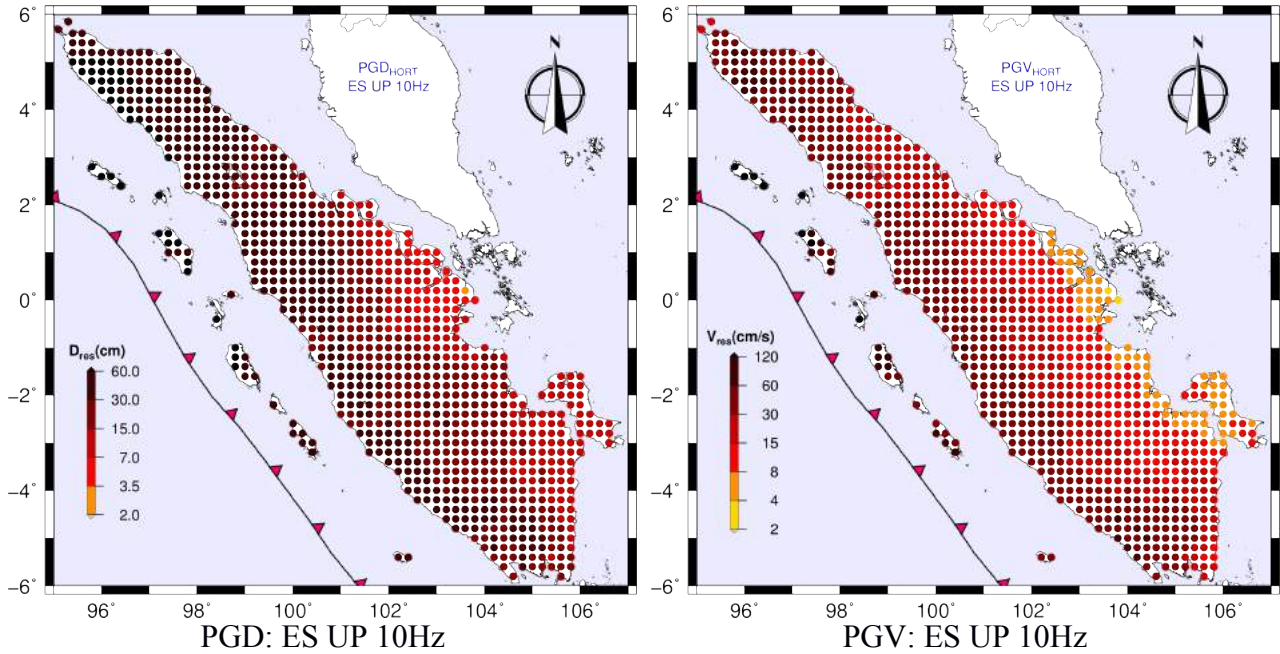
Figure 6.4.2 Horizontal PGD (left) and PGV (right) computed with 10 hz cutoff,
using the ES-UP procedure
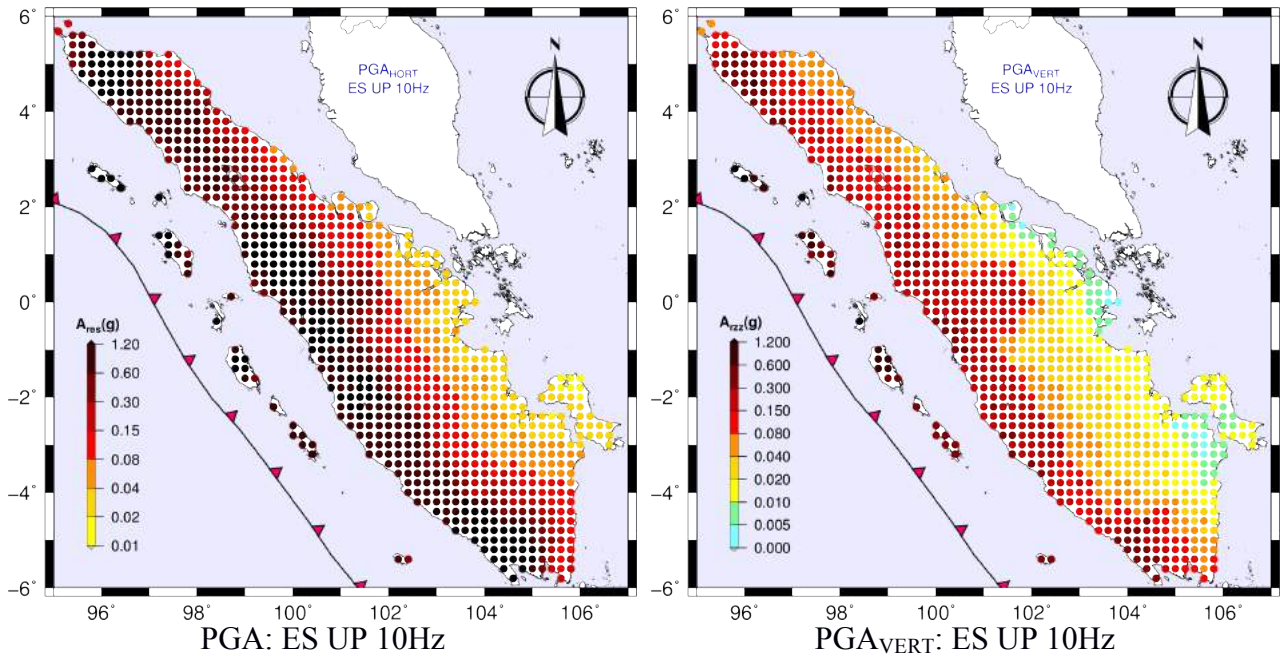
Figure 6.4.3 Horizontal PGA (left) and vertical PGA (right) computed with 10 hz frequency cutoff
based upon the ES-UP procedure

120
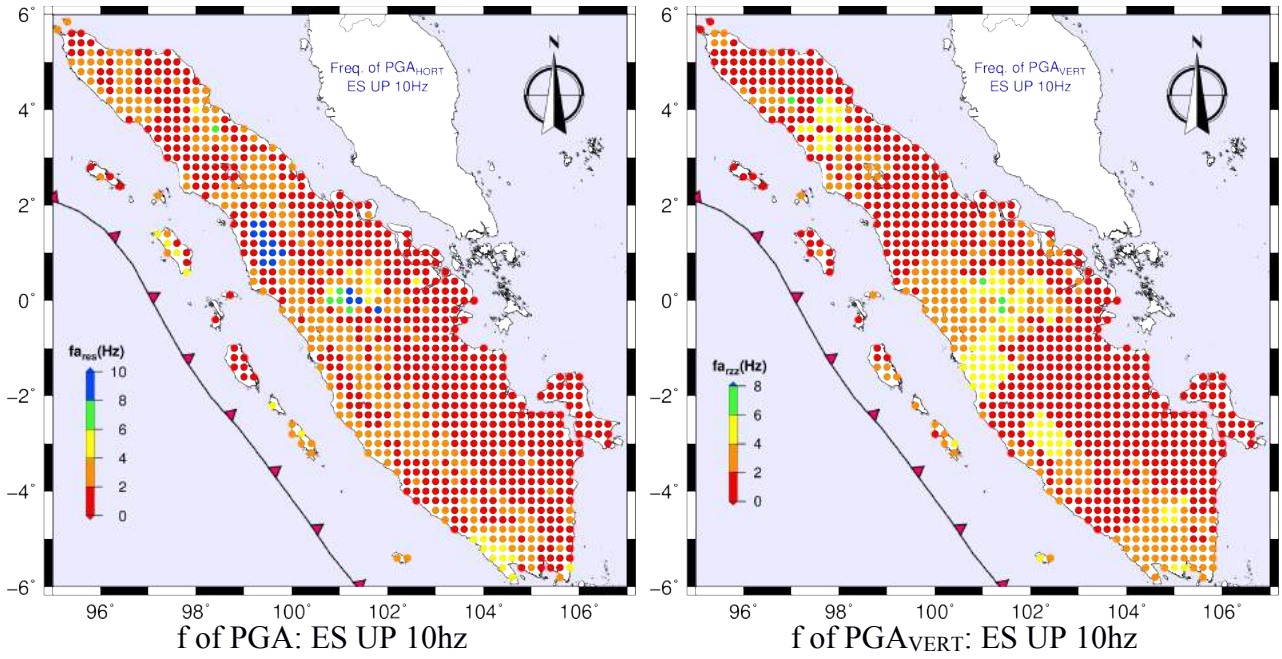
Figure 6.4.4 The dominant frequency of PGA for horizontal (left) and vertical (right) component computed based on the ES-UP procedure.
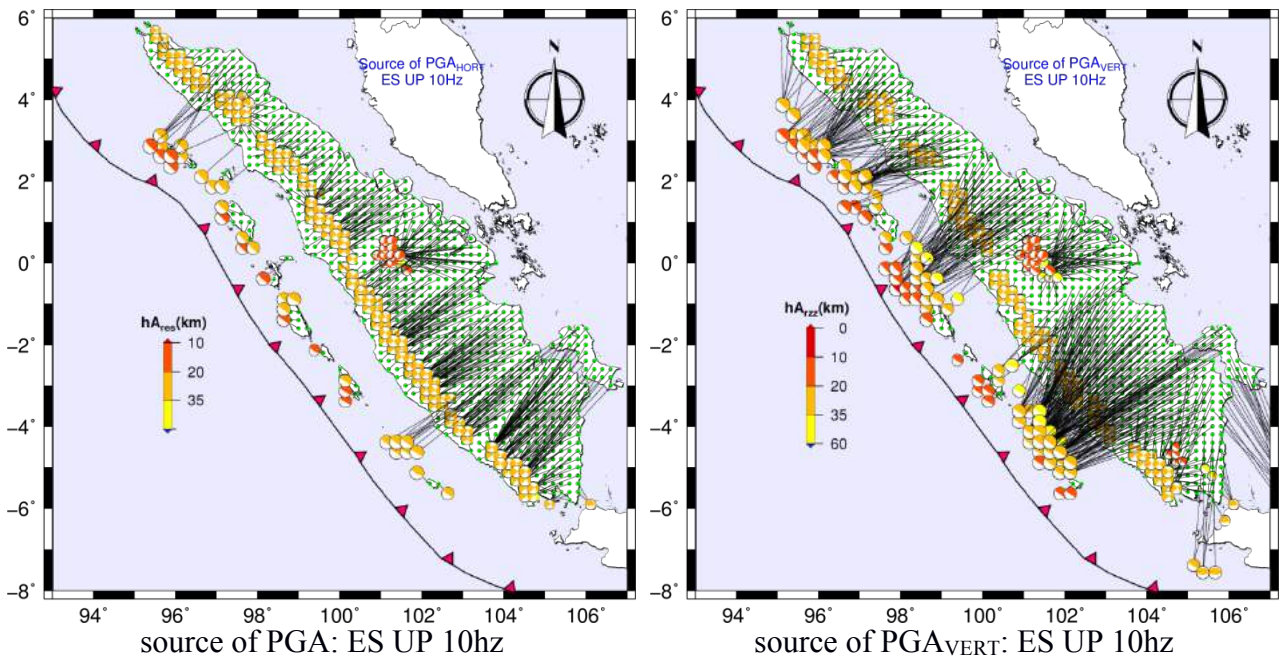
Figure 6.4.5 The sources that contribute the maximum horizontal PGA (left) and vertical PGA (right) computed at 10 Hz cutoff for the horizontal component for the ES-UP version of NDSHA.

The figures from 6.4.2 to 6.4.5 show the capability to produce the hazard maps by using the updated path generator algorithm. The updated software has the capability to produce the results also taken from the standard version. It means that the UP procedure can be embedded in the standard package by replacing OP as shown in Figure 6.4.6 (right). We can verify this fact by using

the same input for the original and the updated version. The original source (OS) definition is used with the updated paths generator: the OS-UP testing path generator. Figure 6.4.7 shows a very small difference between the maps computed using the updated version and the original version of the path definition.
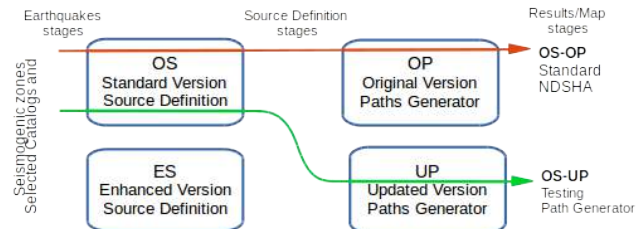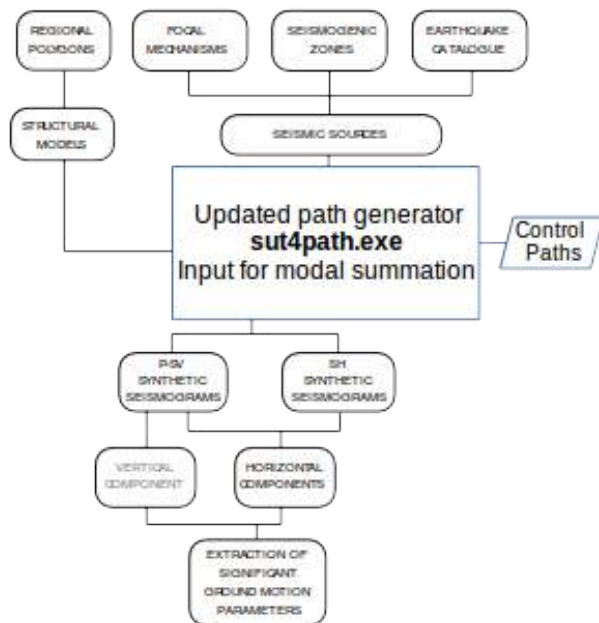
Figure 6.4.6 (right) Standard source definition (OS) send to updated paths generator as result OS-UP with standard setting will be comparable with standard NDSHA OS-OP.
(left) The position of updated path generator UP inside whole standard NDSHA procedure.
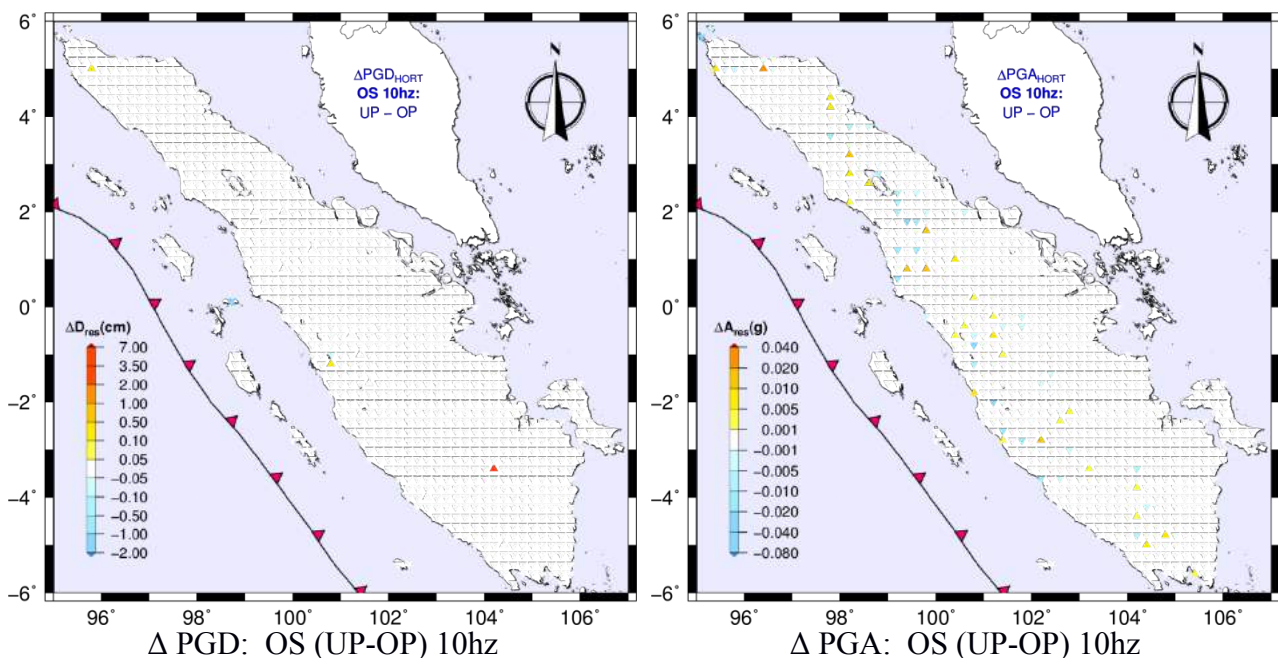
Figure 6.4.7 This picture (left) shows the difference between the computed horizontal PGD using updated and original path generator at 10 hz cutoff; (right) the difference between the computed horizontal PGA using updated and original path generator at 10 hz cutoff. The differences between original and updated versions of travel paths are small and scattered.

6.5. An Efficient Path Generator for reducing Computational Time

The development of the NDSHA software package started from the precise production of the synthetic seismogram by the modal summation (Panza, 1985; Florsch et al.,1991). When applying the modal summation for the calculation of the strong ground motion, they tried to find an efficient way. By definition, the peak ground acceleration (PGA) is equal to the maximum ground acceleration that occurred during the earthquakes shaking at a location. It means that a very conservative approach for the estimate of the most strong ground motion, such as PGA, PGV, and PGA, is obtained by calculating all of the synthetic seismograms from all of the available sources, for both a historical and potential earthquake. In order to build the seismic hazard map, several sites will be investigated, and the total possible paths are given by:

$$
\left(\begin{array}{c} \text{numbers of paths} \\ \text{sources} - \text{receivers} \end{array} \right) = \left(\begin{array}{c} \text{Efficiency} \\ \text{Selected pairs} \end{array} \right) \times \left(\begin{array}{c} \text{numbers of} \\ \text{sources} \end{array} \right) \times \left(\begin{array}{c} \text{numbers of} \\ \text{receivers} \end{array} \right)
\tag{6.1}
$$

Taking the sources directly from the earthquake catalogs to calculate the synthetic seismograms will produce a huge number of the paths, and it is therefore not implemented. Based on Equation (6.1), there are three possibilities to reduce the number of the paths: The first one is to reduce the number of the sources,the second one is to reduce the number of the receivers, and the third one is to reduce the number of the paths that could be used in the computation of the hazard map.

The first application of the NDSHA (Costa et al., 1993; Panza et al., 1996, 2000, 2001) has managed to reduce the number of the sources by grouping them into the homogenous seismogenic areas, and for each group, the representative focal mechanism can be kept constant. The scalar seismic moment associated with each source is determined from the analysis of the maximum magnitude observed in the epicenter area; we call this "source definition". The original version of the source definition algorithm is explained by Panza et al. (1996) as a standard smoothing procedure (OS) and has reduced the number of the sources significantly. Recently, as we discussed in Chapter 3, for the case of Sumatra, the enhanced source definition procedure (ES) takes care of the efficiency of the computation by sorting (divsel) the near source zones from the far source zones. The reduction of the number of the receivers also has been applied in the first application placing the sites at the nodes of a grid with an optimum resolution 0.2°x0.2° that covers the national or regional territory (Panza et al,. 2001). In contrast, the PSHA based on the attenuation equation and the cheap computational cost for each site can be performed at a higher resolution grid (in the case of Indonesia PSHA 0.1°x0.1°) with an apparent relatively high precision, not supported by the quality and quantity of the available data.

In case of Sumatra the number of defined sources are N(ES)=1776 and receiver sites N(sites)=953, this leads to a total of 1776*953= 1692528 paths. In the standard hazard procedures (NDSHA) the choice of source-receiver distances being used is based upon the magnitude of the earthquake source. The maximum source-receiver distance has been set equal to 25, 50, and 90 km, respectively, for M < 6, 6 ≤ M < 7 and M ≥ 7 (Panza, et al., 2001).

In this section, we investigate the effect of using different source-receiver distances (the original file named hazdistance.max is then renamed to hazdistance1.max in this section) on the resultant ground motion distribution over Sumatra. As show in Listing 6.4 in column 1, the maximum source-receiver distance for M<6 is 250 and 600km for M8, the threshold used to produce the maps in Sections 6.2, 6.3, and 6.4. The second modification threshold R2 with the file name hazdistance2.max reduces the distance for the magnitude 8 to 400 km. The last modification is the threshold R3 with the file name hazdistance3.max, which gives a maximum distance of 200 km for magnitude 8. The updated path generator can be performed by changing the setting parameter in sut4path.par with following line.

```
#../base/hazdistance1.max
../base/hazdistance2.max
```

Threshold R1 : file: hazdistance1.max	Threshold R2: file: hazdistance2.max	Threshold R3 : hazdistance3.max
magnitude distance 1 0 250 6 300 7 500 8 600	magnitude distance 2 0 150 6 200 7 300 8 400	magnitude distance 3 0 75 6 100 7 150 8 200

Listing 6.4 The different distance-magnitude scenario thresholds discussed in this section

Figure 6.5.1 (left) shows the original path procedure using the distance-magnitude threshold R2 (filename hazdistance2.max). This choice makes Bangka Island a far field source in which there are no defined paths for the computation of the strong ground motion. Figure 6.5.1 (right) shows the effect on the ground motion of choosing the proper source-receiver distance, and the difference is large at the eastern part of the region.

The simple way to solve this problem is to return back to using the default threshold parameter file. For this case, the problem can be solved but in the future with a large covered area that contains many receivers far from the seismic zone, this method cannot be used anymore. The problem can be handled by increasing the distance-magnitude threshold for the whole area of the Sumatra region in order to place the receivers at a far distance from the sources in Bangka Island. Instead of applying the increasing distance-magnitude threshold for all of the area, we only focus on

the far field seismic sources using other strategies. In the updated path generator, we can control the minimum number of the paths for each receiver from the most significant source that could contribute hazard for the site, namely MIS in the sut4path.par configuration file.
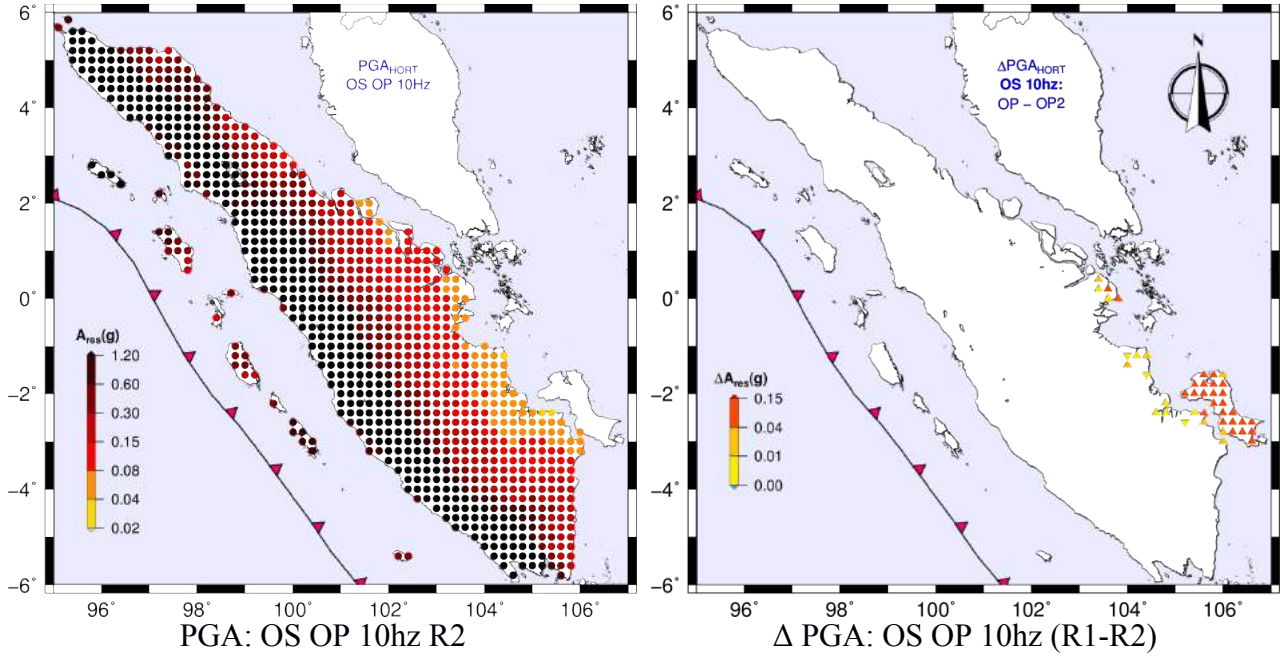

Figure 6.5.1 Horizontal PGA map computed at 10 Hz cutoff based on OSOP procedure with R2 threshold (left) and the difference between R1 and R2 (right)
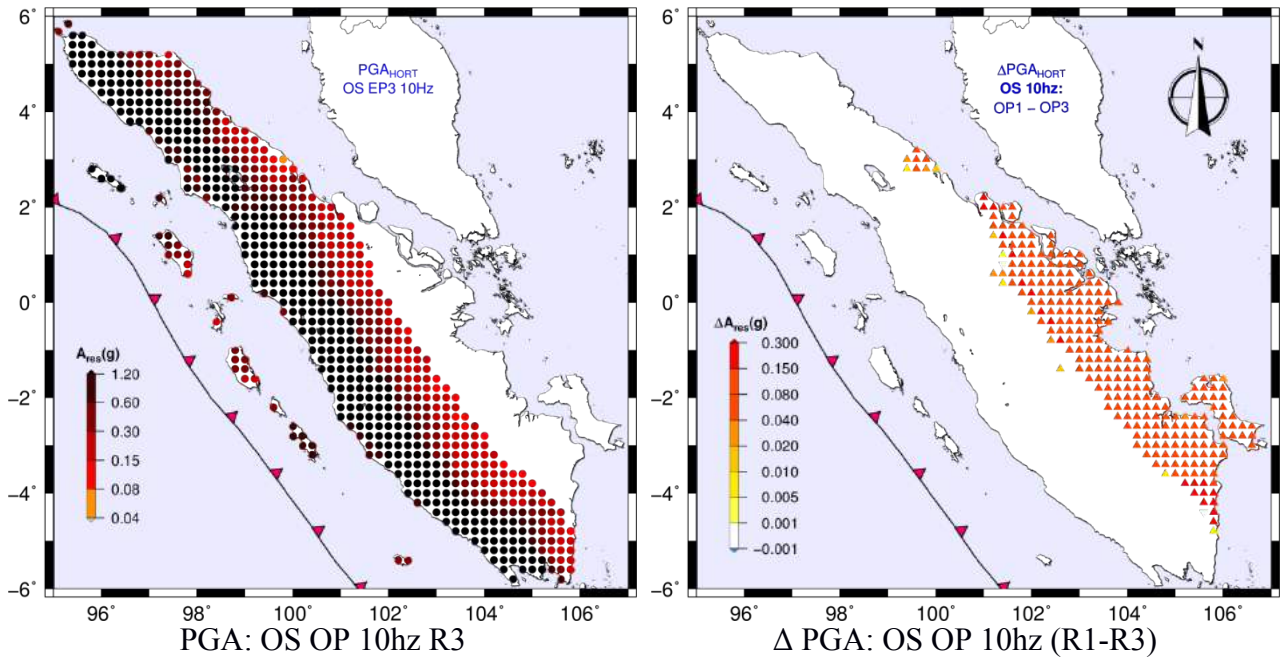

Figure 6.5.2 Horizontal PGA map computed at 10 hz cutoff based on OSOP procedure with R3 threshold (left) and the difference between R1 and R3 thresholds (right)

The determination of the significant seismic sources also brings some problem: we have to calculate the strong ground motion from each source. Using the modal summation method for searching the most significant source is a precise way, but does not meet the solution for reducing the computational time. If no alternative solution is available, we can use the rough approach to search among several significant earthquakes for the site of interest. The rough approach is based on the use of the most popular attenuation laws of the ground motion parameters, like PGA and PGV:

$$\log y = a + b\,M + c\,\log r_f + d\,D_f + e\,S \tag{6.2}$$

where y is the ground motion parameter, a, b, c, d, e coefficients empirically determined, r_f and D_f are the different measures of the distance from the source, and S is a binary variable (0, 1), which depends on the soil type (Panza et al., 2009). Because the equation does not come from a realistic physical simulation, there are a lot of attenuation equations. Douglas (2001) has 212 published attenuation relations for the peak ground acceleration for determining the parameter in Equation 6.2. For example, we choose one of them (Sigbjornsson and Baldvinsson, 1992). By borrowing the parameters from the attenuation formula and by ignoring the soil type, we can rewrite Equation 6.2 in anoother form:

$$\begin{aligned} \log A &= \alpha + \beta M - \log R + bR \\ \text{with: } R &= \sqrt{d^2 + h^2} \end{aligned} \tag{6.3}$$

Because our interest is only to compute the possible hazard from the sources that could generate a large ground motion (effective acceleration) at the sites of interest and to reduce the computational time, we proposed to use the GMPE to get an idea about the value of an effective ground motion, and its relation to the weighting value (W), we then select the first 100 of the significant sources to be computed by the NDSHA approach. Therefore, we can eliminate the parameter α, and the equation will only depend on two parameters, and the weight equation for each path source-receiver becomes:

$$A \propto W = \frac{10^{\beta M + bR}}{R} \tag{6.4}$$

This will be cheap, faster, and easy to implement in FORTRAN as shown in Listing 6.5.

```
beta=0.365; bbb=-0.0039.
R=sqrt(dist2*dist2+depth*depth)
fac_dist=(10**(bbb*R))/R
fac_mag=10**(beta*xmag)
weightrs(iobs,isut)=fac_mag*fac_dist
```

Listing 6.5. The Fortran code describes the weight for each connection path between observation point (`iobs`) and the source definition (`isut`)

In this chapter, we apply the MIS parameter with the 100 sources as shown in Listing 6.2, this means that, the far receiver sites, e.g. Bangka Island, will have the paths from the 100 significant seismic sources only based on Formula 6.4. We do not trust the attenuation equation for the calculating of the strong ground motion parameters; therefore, after selecting the 100 real significant sources, we computed the strong ground motion based on the modal summation method, which relies on the realistic physical simulation.

The MIS feature in the updated path generator allows for reducing the computational time significantly as described in Table 6.1. For the scenario distance-magnitude threshold R1, the OP (original path generator) has 517437 paths less than those produced by the UP (updated path generator) 655490 paths. This is so because even if the site already gets the paths from the threshold process, the UP will force the additional paths until 100 paths are reached. We need about 0.1s computation time per path on the DSTX machine. The real computational time of course also depends on how many programs are running simultaneously on the server. For the distance-magnitude threshold R2, the OP produces fewer paths than the UP does, but the produced map based on the OP does not cover the far sites in Bangka Island. For the distance-magnitude threshold R3, the OP cannot be used anymore (see Figure 6.5.2) even if it produces half of the number of the paths compared with the UP does. The comparison of the computation time based on the UP with the threshold R3 with that of the OP computation time shows a significant decrease of computational time by a factor 4.5768=14.373/3.1404 with no loss in the accuracy of producing a precise strong ground motion map.

Table 6.1. List of number of paths, computational time and hard disk space required for several threshold scenario.

No	Scenario	#paths	Time estimate (hour)	Time reality (hour)	Hardisk space	Condition
1	OS OP R1 10hz	517437	14.373	13.2567	213G	Standard
2	OS OP R2 10hz	240407	6.6780	5.39	113G	No cover Bangka
3	OS OP R3 10hz	62933	1.7481	1.52417	33G	No cover eastern path
4	OS UP R1 10hz	655490	18.208	19.1103	169G	Similar
5	OS UP R2 10hz	322898	8.9694	8.18167	95G	Similar
6	OS UP R1 10hz	113054	3.1404	3.15278	36G	Similar

This MIS feature in the UP algorithm with a short distance-magnitude threshold successfully produces a similar hazard map with a very small difference with respect to the standard version of the OP with a long distance-magnitude threshold R1. There are negligible differences when using a different path generator. Surprisingly, the difference in PGA computed using OP, UP-

R2 and UP-R3 is almost identical (Figure 6.5.3-right is almost identical to Figure 6.5.4-right). Probably, this effect is related to the weight in Equation 6.4 for the PGA purpose.
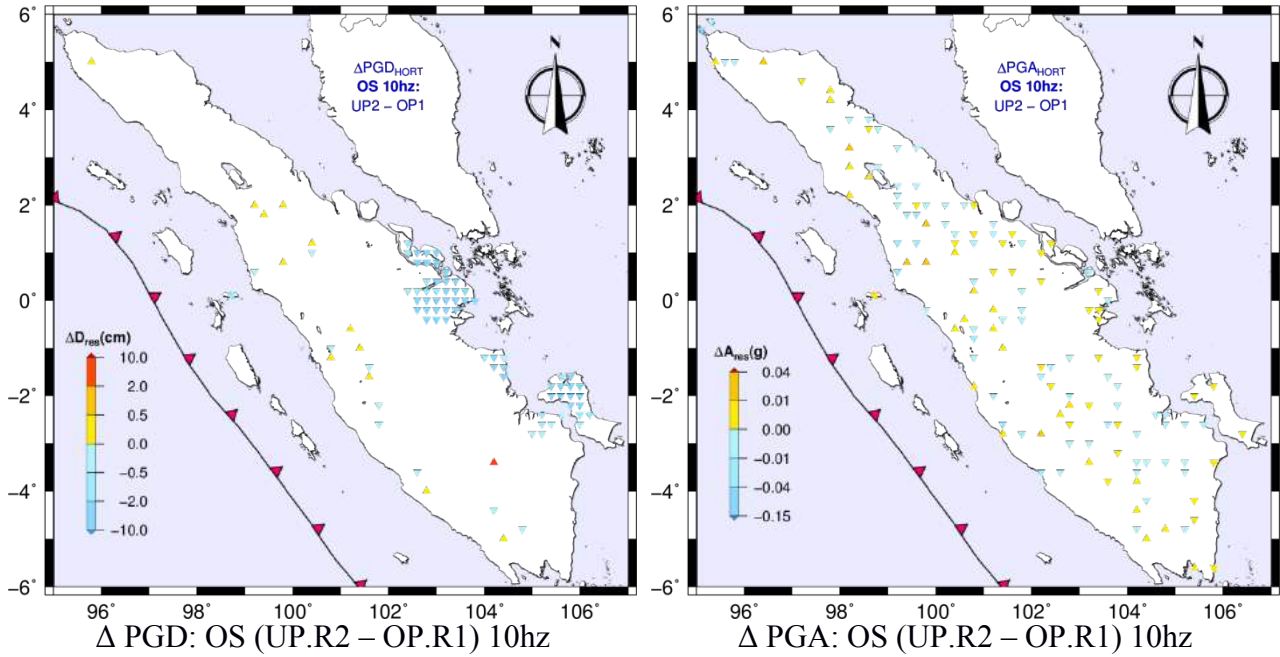
Figure 6.5.3 The updated path generator with threshold R2 has relatively small difference with respect to standard path generator for PGD (left) and PGA (right)
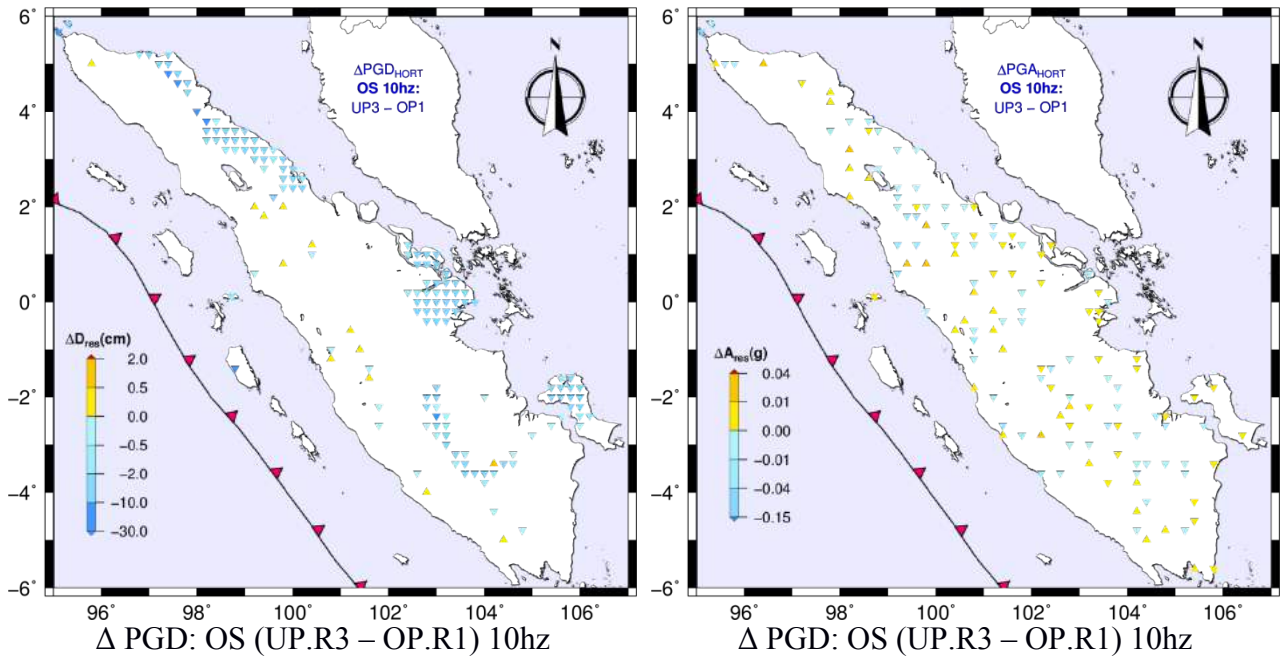

Figure 6.5.4 The difference in PGD (left) and PGA (right) computed using updated path generator at R3 threshold and from the standard path generator at R1 threshold shows relatively a small difference between adopting different magnitude-distance threshold in the resultant ground motion parameters.

6.6. Comparison with Current Official PSHA

The typical seismic hazard problem lies in the determination of the ground motion characteristics associated with future earthquakes, at both the regional and the local scale. The seismic hazard assessment can be performed in various ways, e.g. with a description of the ground shaking severity due to an earthquake of a given distance and magnitude (''ground shaking scenario''), or with the probabilistic maps of the relevant parameters describing the ground motion. The first scientific and technical methods developed for a seismic hazard assessment were deterministic and based on the observation that the damage distribution is often correlated with the spatial distribution and the physical properties of the underlying soil. The 1970s saw the beginning of the development of probabilistic seismic hazard maps on a national, regional and urban (microzoning) scale. In the 1990s, these instruments for the mitigation of seismic hazard came to prevail over a deterministic cartography (Zuccolo et al., 2011).

The probabilistic seismic hazard analysis determines the probability rate of an exceedence, over a specified period of time, therefore it is not scientific (Castanos H. e Lomnitz C., (2002), PSHA: is it Science?, Eng. Geo., 66, 315-317.). PSHA cannot be falsified (parascience): if, in a given location, PSHA declares that in the next 50 years, the probability of an earthquake with a given shaking (hazard) X is 10%, an event with much greater shaking $Y \gg X$ does not falsify the prediction. In fact, by definition, PSHA allows for a probabilty of 10% that the earthquake with shaking Y occurs. On the other side, if the earthquake with shaking $Y \gg X$ does not occur, PSHA is even so "correct". In spite of this various levels of the ground motion are given as in the discussion by Irsyam et al. (2010) and by the digital data from the courtesy of Usamah (2013). The current official PSHA map is available in a PDF map, and there is no official link providing the digital data. Therefore, before we make any comparison analysis with our result, we have to check the data we get from Fauzi (2013) similar to the official PDF version map from Irsyam et al. (2010). The colored map that wet get from the PDF map determines the RGB value in the GIMP Image Editor software, and we use the colored map to make this comparison. Figure 6.5.1 shows the similarity between the PDF version and that of re-plotting from the digital data, thus this data is a representative of the current official PSHA for Sumatra and is reliable for a comparison study. We hope in the future most of the official map produced by the government not only available in a picture map image but also possibly available in a digital format for any potential scientific study.

The digital data resolution for PSHA is 0.1 degree but most of PHSA maps are plotted using a continuous map representation, artificially obtained by interpolation. In PSHA, it is easy to artificially increase the resolution without increasing the computational time because of the use of attenuation equation. On the other side, NDSHA is based on a realistic physical modeling, which

has a cost, in terms of the computational time, for each observation point. Therefore, NDSHA is based on a number observation points with the ideal resolution 0.2 degree for the default value for plotting NDSHA in a regional scale. In some cases, the gridding with 0.2 degrees will miss the small size islands, but we can put an additional point in the center of an island, if the adopted resolution is 0.2 grids as discussed in Chapter 4. By borrowing the observation point coordinates from NDSHA, we interpolated the PGA from a PSHA map in the digital format. Figure 6.5.2 shows the apparent PSHA with the NDSHA based on an observation point.
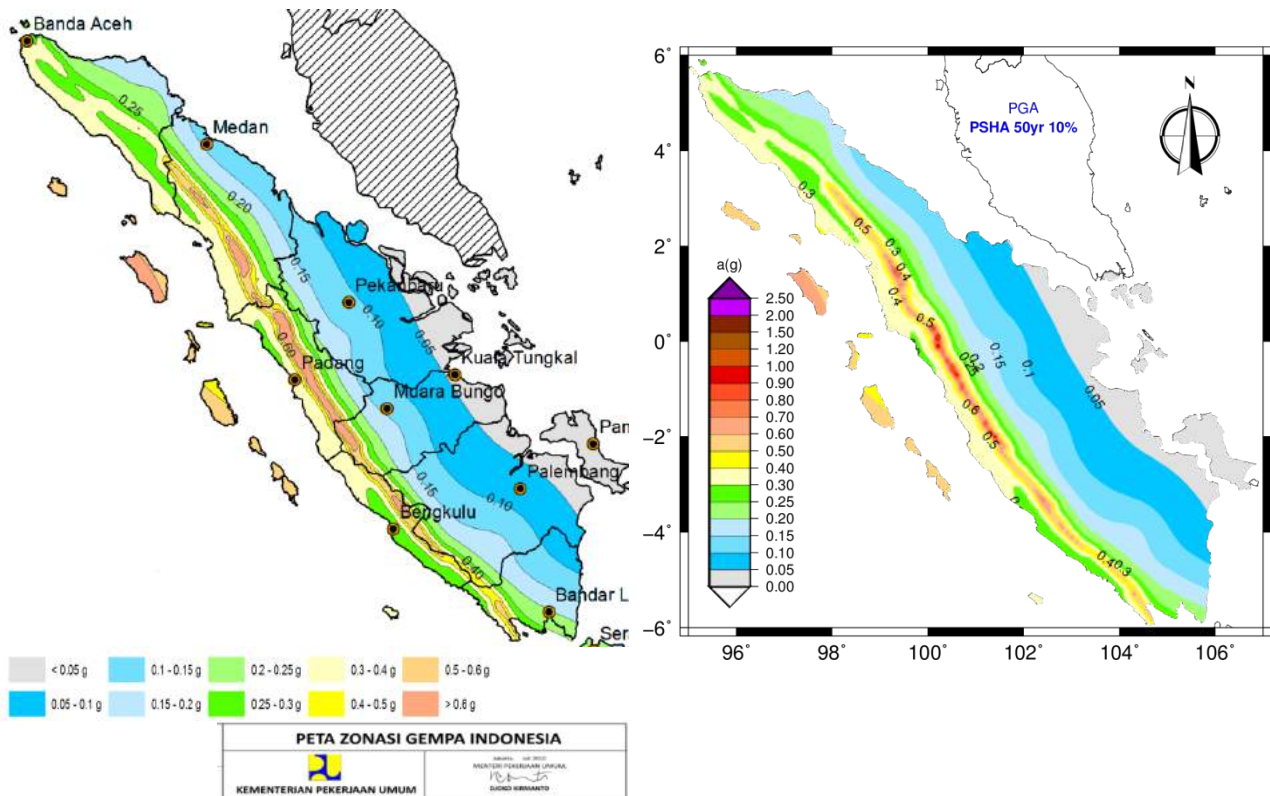

Figure 6.6.1 The official PSHA map for PGA at bedrock with 10% probability of exceedance in 50 years (left). The official map has visual similarity with re-plotted digital data (right) which we will use in this comparison study.

The hazard at a site is given in terms of probability of the exceeding different levels of the ground motion during a specified period of time. This is achieved through the calculation of the frequency of earthquakes with some severity, and the calculation of the conditional probability of exceedance of a given ground motion level for each of these contributing earthquakes (summed over all of the potentially contributing sources). Historically, the most-used parameter in the engineering analysis for the characterization of the seismic hazard is the peak ground acceleration (PGA), which is a single-value indicator commonly used in a seismic hazard assessment (Zuccolo et al., 2011). To check the performance of the PSHA maps against the NDSHA maps, we evaluate all of the available PGA maps based on PSHA estimated at 10% and 2% probability of exceedance in 50 years, which are available in the form of the digital data from Fauzi (2013).
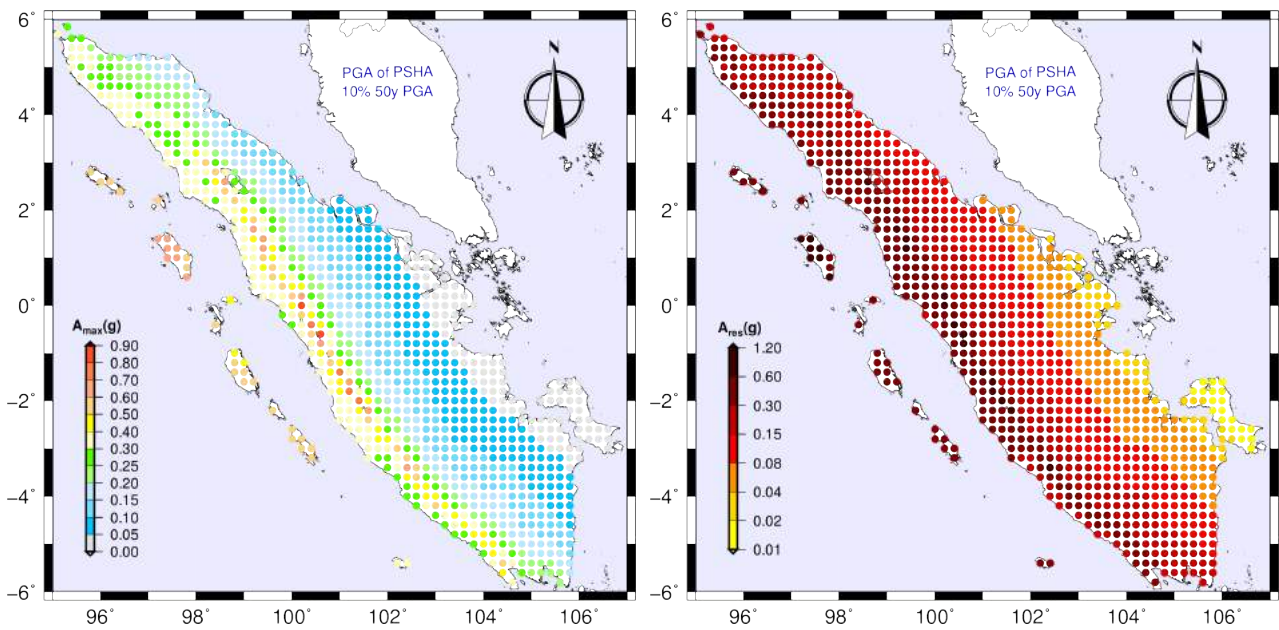
Figure 6.6.2 PSHA data for 10% probability of exceedance during 50 years for observation point from NDSHA study (sum2.obs) is plotting with difference color map: digitization colormap from official map (left) and standard colormap which used for acceleration in NDSHA package (right)
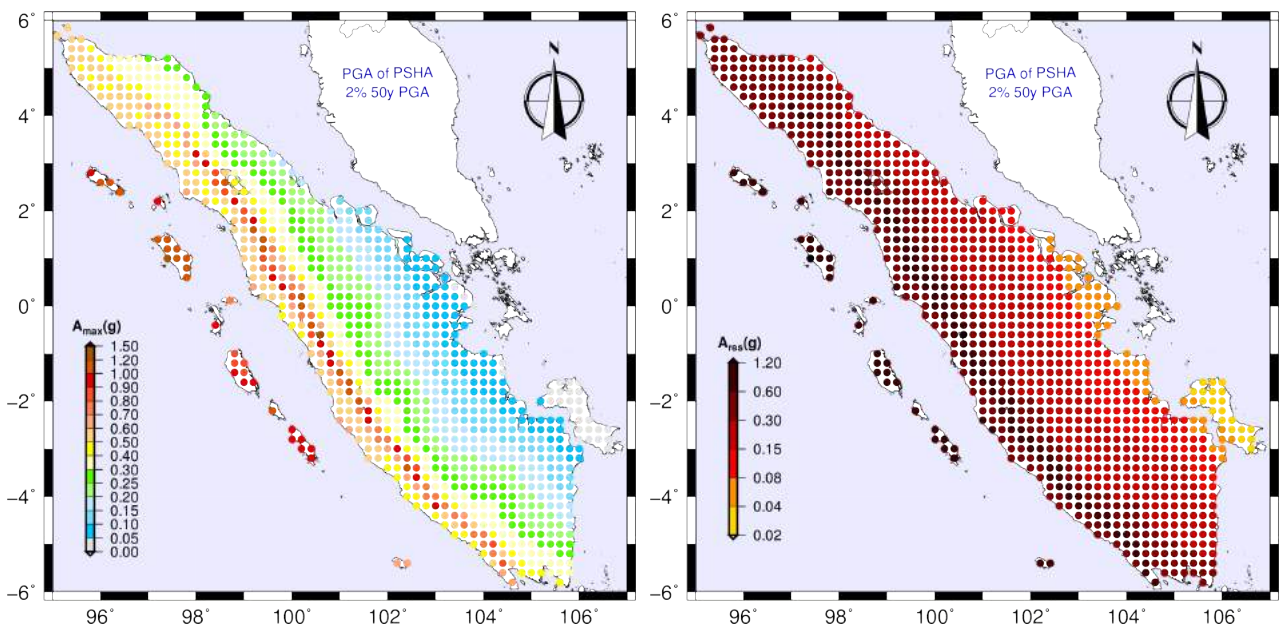
Figure 6.6.3 Similar plotting process with figure 6.6.2 for different 2% probability
of exceedance in 50 years.

The hazard map PSHA as shown in Figures 6.6.2 and 6.6.3 is the revision of the seismic hazard map in the Indonesian Seismic Code SNI 03-1726-2002. Some improvements in the seismic hazard analysis were implemented in the analysis by considering the recent seismic activities around Java and Sumatra. The seismic hazard analysis was carried out using 3-dimension (3-D) seismic source models (the fault source model) using the latest research regarding the tectonic

settings of Sumatra and Java. Two hazard levels were analyzed for representing 10% (Figure 6.6.2) and 2% (Figure 6.6.3) probability of exceedance (PE) in 50 years ground motions for Sumatra (Irsyam et al., 2008; Irsyam et. al., 2010). The PGA given by PSHA 2% probability of exceedance (PE) in 50 years (Figure 6.6.3) obviously has a greater value compared to PGA of PSHA 10% probability of exceedance (PE) in 50 years (Figure 6.6.2).

Δ (DGA OSOP 1hz – PGA PSHA 10%50yr)   Δ (DGA OSOP 1hz – PGA PSHA 2%50yr)

Figure 6.6.4 Difference between DGA (1Hz cutoff) from standard NDSHA and PGA of PSHA 10% (left) and 5% (right) probability of exceedance (PE) in 50 years.

ΔPGA: (OSOP 10hz – PSHA 10%50yr)   ΔPGA: (OSOP 10hz – PSHA 2%50yr)
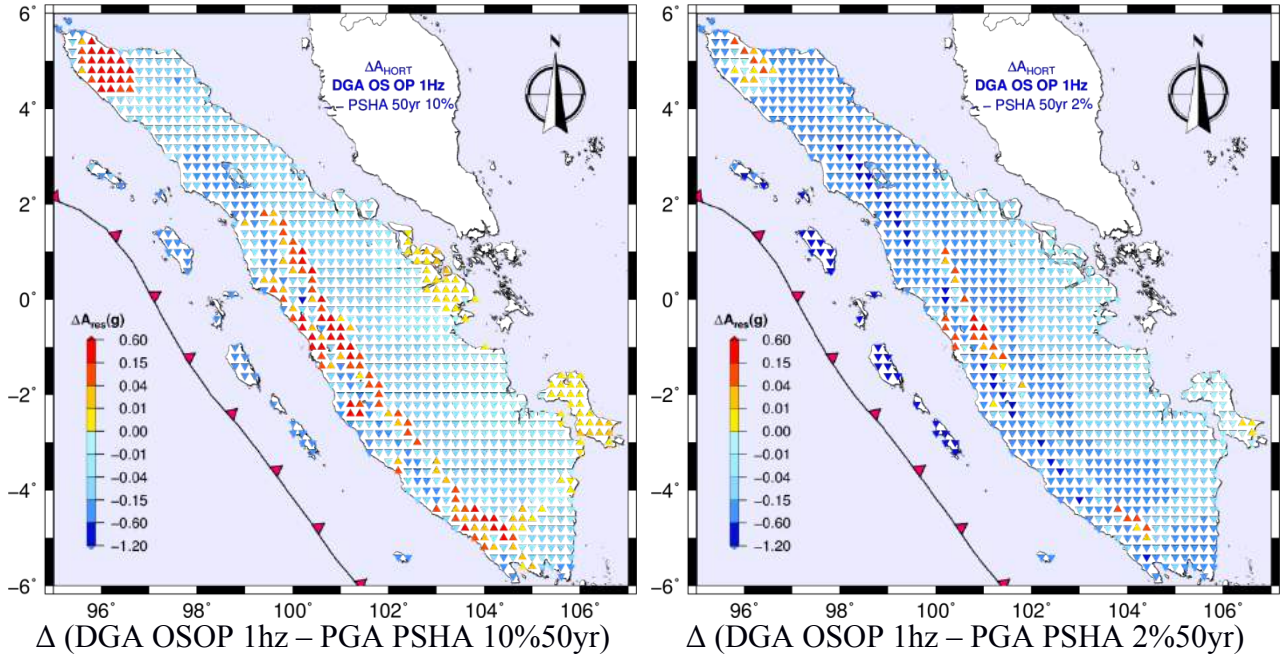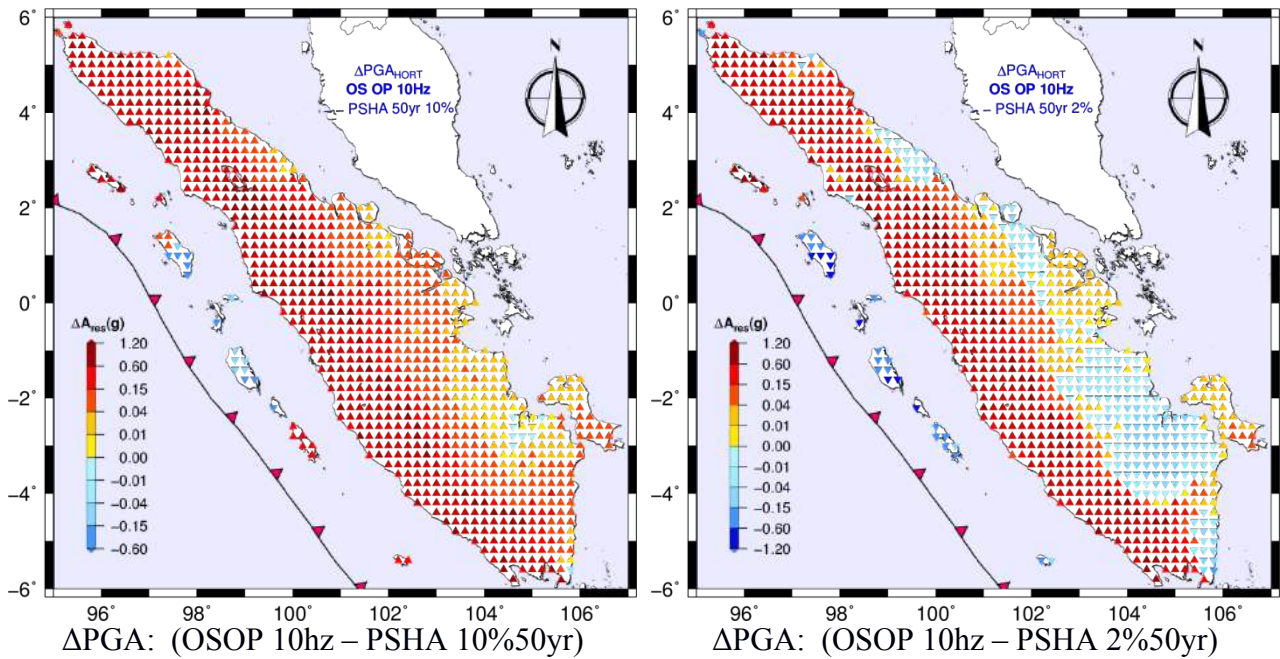
Figure 6.6.5 Difference between PGA (10Hz cutoff) from standard NDSHA and PGA of PSHA 10% (left) and 5% (right) probability of exceedance (PE) in 50 years.

Figure 6.6.4 shows the difference between DGA (NDSHA) and PGA (PSHA) value: the value of DGA is lower than PGA at both probabilities of exceedance (PE) 10% and 2% in 50 years. However, the PGA estimated by the standard NDSHA with 10 hz cutoff is higher than the computed PGA from PSHA at PE 10%. For comparison with PE 2%, the near field NDSHA gives the PGA value greater than that of the PSHA; and for the far field sources, it is the opposite (Figure 6.6.5). This means the NDSHA calculation for Sumatra gives reasonable results based on the adopted magnitude distance threshold. This is due to the fact that the standard NDSHA is based upon the realistic physical simulation of the seismic wave propagation. The comparison between the PGA computed based upon the proposed enhanced version of NDSHA and PSHA shows that the updated version gives the same values at the near sites and lower values at the far sites; whereas, the standard one gives a higher value in NDSHA, which in turn gives a higher PGA value for the near and far field sources.

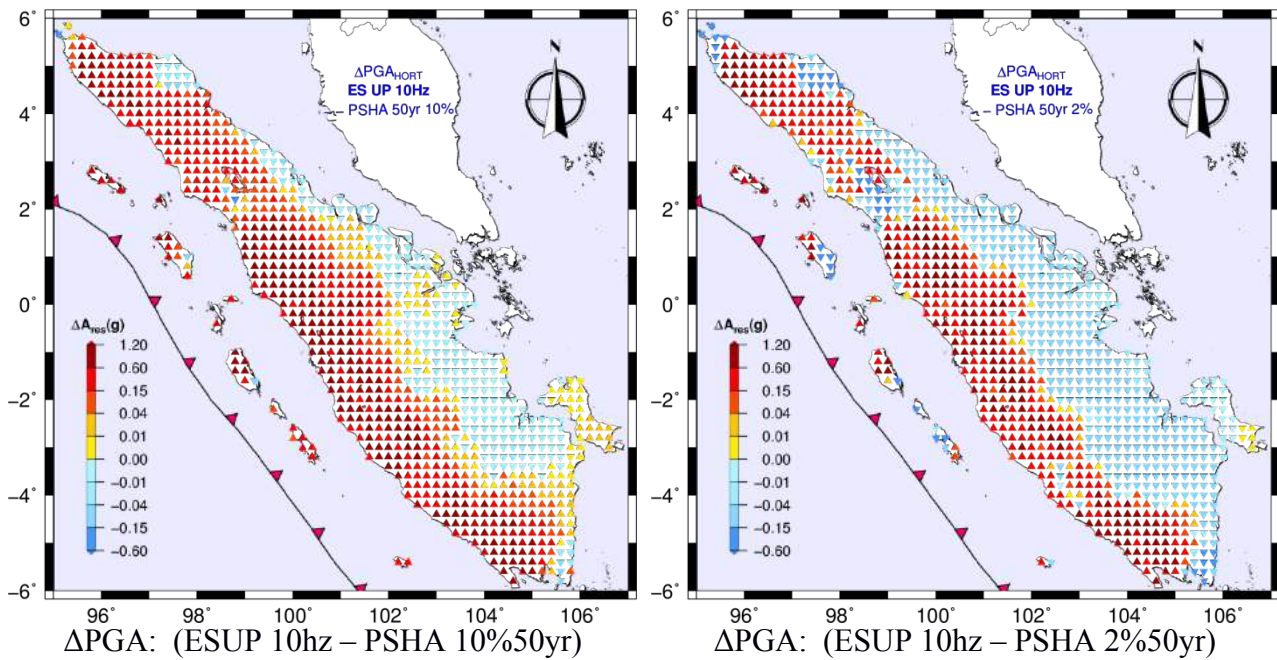ΔPGA: (ESUP 10hz – PSHA 10%50yr)   ΔPGA: (ESUP 10hz – PSHA 2%50yr)

Figure 6.6.6 Difference in PGA (10Hz cutoff) from enhanced NDSHA and PGA of PSHA 10% (left) and 5% (right) probability of exceedance (PE) in 50 years.

7. Local Scale NDSHA (Microzonation) for Banda Aceh City

7.1 NDSHA for Local Scale method with Hybrid Method

The issues pertaining to the urban risks are a pressing concern for people involved in the disaster mitigation. With the progressing urban sprawl and the emergence of many cities around the world, disasters of all kinds become an inevitable consequence of uncontrolled urbanization. Growing environmental and social (purely scientific, practical disaster mitigation, and preparedness) concerns, both on the part of decision-makers and public opinion, have brought a new perspective to the perception of hazard assessment as a valid alternative in the long-term (e.g. urban planning and structural design, retrofitting), and an effective complement in short and medium terms, to traditional design procedure for a resistant and safe environment (Panza et al. 2011).

In the first approximation, which does not account for the local site conditions, the synthetic seismograms are calculated at a regional scale by the modal summation technique (Panza et al., 2001) for the estimation of the strong ground motion at the bedrock, as shown in Chapter 6, with the input based on the enhanced source definition discussed in Chapter 3 and a 1D structural model for each receiver site as discussed in Chapter 4. Most of the urban areas in Sumatra are located in the flat sedimentary basin, for example, the Banda Aceh city. Therefore, for the detailed urban planning of the Banda Aceh city, the regional seismic zoning cannot be used without taking into account the local site condition, which has a great effect on the seismic wave propagation beneath the urban areas, so we have to investigate the detailed structural model for the sedimentary layer in Banda Aceh. Thus, the seismic microzonation is defined as the process of subdividing a potential seismic or earthquake prone area into zones with respect to some geological and geophysical characteristics of the sites and in this chapter, we will use the regional scale seismic input from the modal summation with 2D ground shacking at a local scale to define the site characteristics in the Banda Aceh city.

The proposed methodology for seismic microzoning has been successfully applied to several urban areas worldwide in the framework of the UNESCO/IUGS/IGCP projects "Realistic Modeling of Seismic Input for Megacities and Large Urban Areas" (e.g. Panza et al. , 2001, 2001b, 2002) and "Seismic Hazard in Asia". The methodology has been applied to assessing the

importance of non-synchronous seismic excitation of long structures as well (Panza, et al. 2013). This method has been successfully applied, for the purpose of seismic microzoning, in several urban areas like Mexico City, Rome (Fäh and Panza, 1994), Benevento (Fäh and Suhadolc, 1995; Marrara and Suhadolc, 1998), Naples (Nunziata et al., 1995) and Catania (Romanelli et al., 1998) in the framework of the IUGS-UNESCO-IGCP project (Panza et al., 1999b).

The seismic microzoning computation based on the hybrid method gets advantages by combining the analytical and numerical approaches. Typically, the analytical solution is applied to the regional model by characterizing the path from the source to the local area of interest, and the numerical solution is applied to model the local site conditions. Fäh et al. (1993) developed a hybrid method that combines the modal summation technique, valid for laterally homogeneous anelastic media with the finite difference, and optimized the advantages of both methods. It can take into account the source, path, and local soil effects to calculate the local wave field due to a seismic event. A laterally homogeneous anelastic structural model is adopted, representing the average crustal properties of the region. The generated wavefield is then introduced in the grid that defines the heterogeneous area, and it is propagated according to the finite-differences scheme (Figure 7.1).
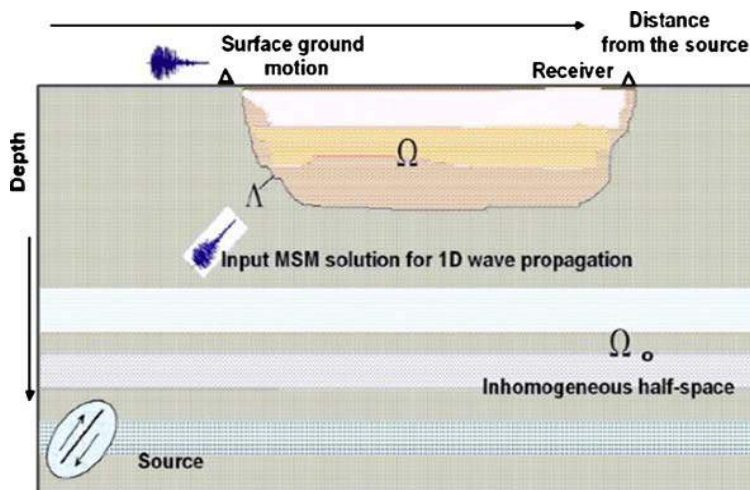
Figure 7.1. Schematic representation of the hybrid technique (Panza, 2009).
Wave propagation is treated by means of the modal summation technique from the source to the vicinity of the local.
Finite different method uses wave propagation in heterogeneous anelastic structure that we may want to model in detail.

Propagation of the waves from the source to the sedimentary basin is computed by the modal summation method for P-SV and SH waves. The detailed description of the hybrid procedure is given by Panza e al. (2001). The explicit finite difference schemes are then used to simulate the propagation of seismic waves in the sedimentary basin. These schemes are based on the formulation of Korn and Stöckl (1982) for SH waves, and on the velocity-stress, finite difference method for P-

SV waves (Virieux, 1986). The schemes are stable for the materials with normal values of Poisson's ratio. The intrinsic attenuation in soft sediments is an important process and is taken into account in the computations to prevent serious errors in the estimation of seismic hazards (Fäh 1992).

In this study the hybrid method will be applied to the investigation of the site-specific microzonation of Banda Aceh, the capital city of Aceh, after applying an improvement in the definition of the structural model. The motivation for choosing the Banda Aceh city as one of the urban areas in Sumatra is because the city is located on a sedimentary layer between two bedrocks, and it is ideal for applying the hybrid model as shown in Figure 7.1. Another reason to choose Banda Aceh for the local scale NDSHA study is the fact that the city is densely populated and is the capital city of Aceh. The method is adopted in order to effectively mitigate (prevention) the earthquake consequences from future strong earthquakes.

7.2 Location and Geology of Banda Aceh City

Banda Aceh is the capital city of Aceh, Indonesia. The city is located in the northern most part of Sumatra Island as shown in Figure 7.2 (left). In addition, the city is the most westerly and early developed city in Indonesia, and on 22 April 2015 it celebrates the 810th anniversary of its existence. The city rose to international prominence in the aftermath of the Indian Ocean earthquake in 2004, which struck off the western coast of Sumatra. Banda Aceh was the closest major city to the 2004 earthquake epicenter and suffered great damage in the earthquake following the devastating damage from tsunami.

Banda Aceh Municipality is a regional autonomy with area 61x36 km^2. The center of Banda Aceh city is well known by its famous historical buildings such as Baiturrahman Grand Mosque at 5°33′13″N 95°19′1.9″E. The population in the administrative Banda Aceh area reaches 249,282 people according to the 2013 census (Illiza and Buchari, 2014). Other administrative areas belong to Aceh Besar district, which is the district capital located at Jantho, see Figure 7.2 (right) location. Syiah Kuala University is the state university of Aceh, located in Banda Aceh and near to the profile of the investigation as shown in Figure 7.2 (right).
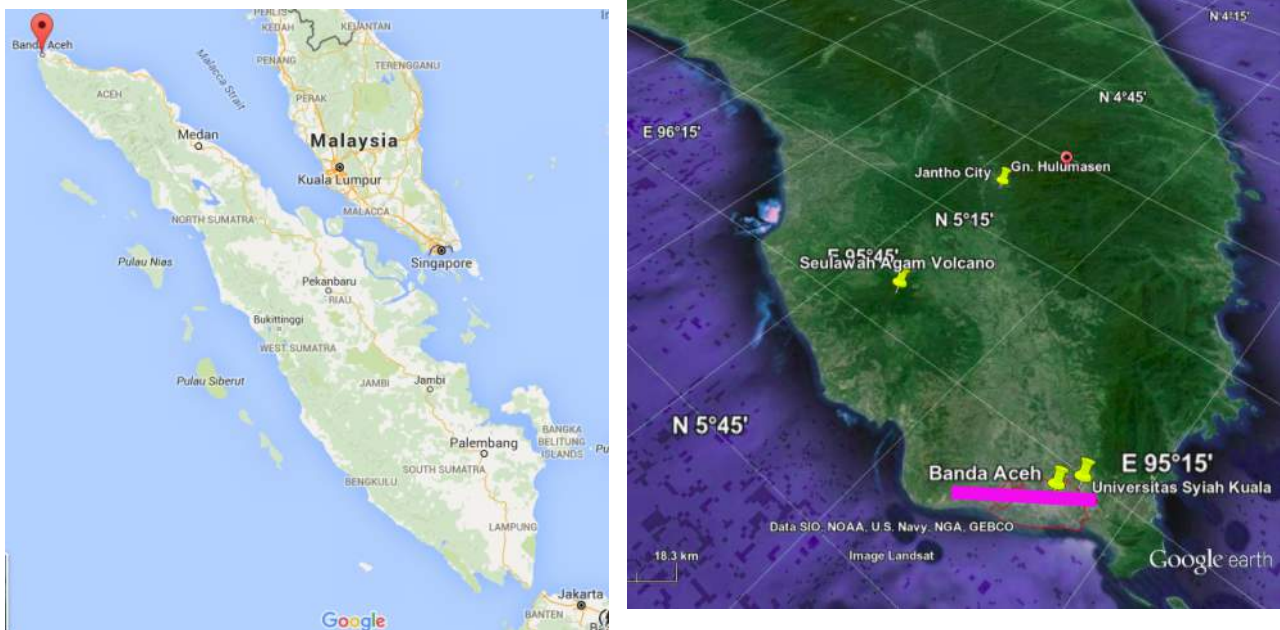
Figure 7.2 (left) The Google Map view of Sumatra and location of Banda Aceh city in the most northwest path of the island. (right) Satellite view of Google Earth: the pink line shows the position of the section considered for the hybrid modeling of earthquake ground motion, and the red line delineates the border of Banda Aceh city in Banda Aceh Basin.

Figure 7.3. Structural map of the North Sumatra Basin and the distribution of tertiary and quaternary sediments in northern Sumatra. (Barber et al., 2005). Banda Aceh city is located in the Northwest Aceh Basin. This map covers Aceh province which is characterized by a complex branching fault system.

Figure 7.4 Geological Map of Banda Aceh city is cropped from map scale 1:250,000 (Bennett et al., 1981). The pink line is the location of the 2D profile used for the hybrid modeling of earthquake ground motion and the blue line is the administrative border of Banda Aceh that sits on quaternary alluvial deposits (Qh).

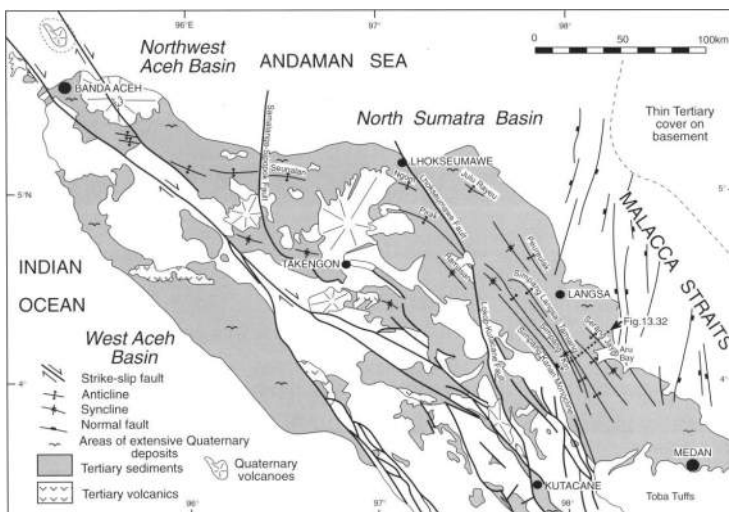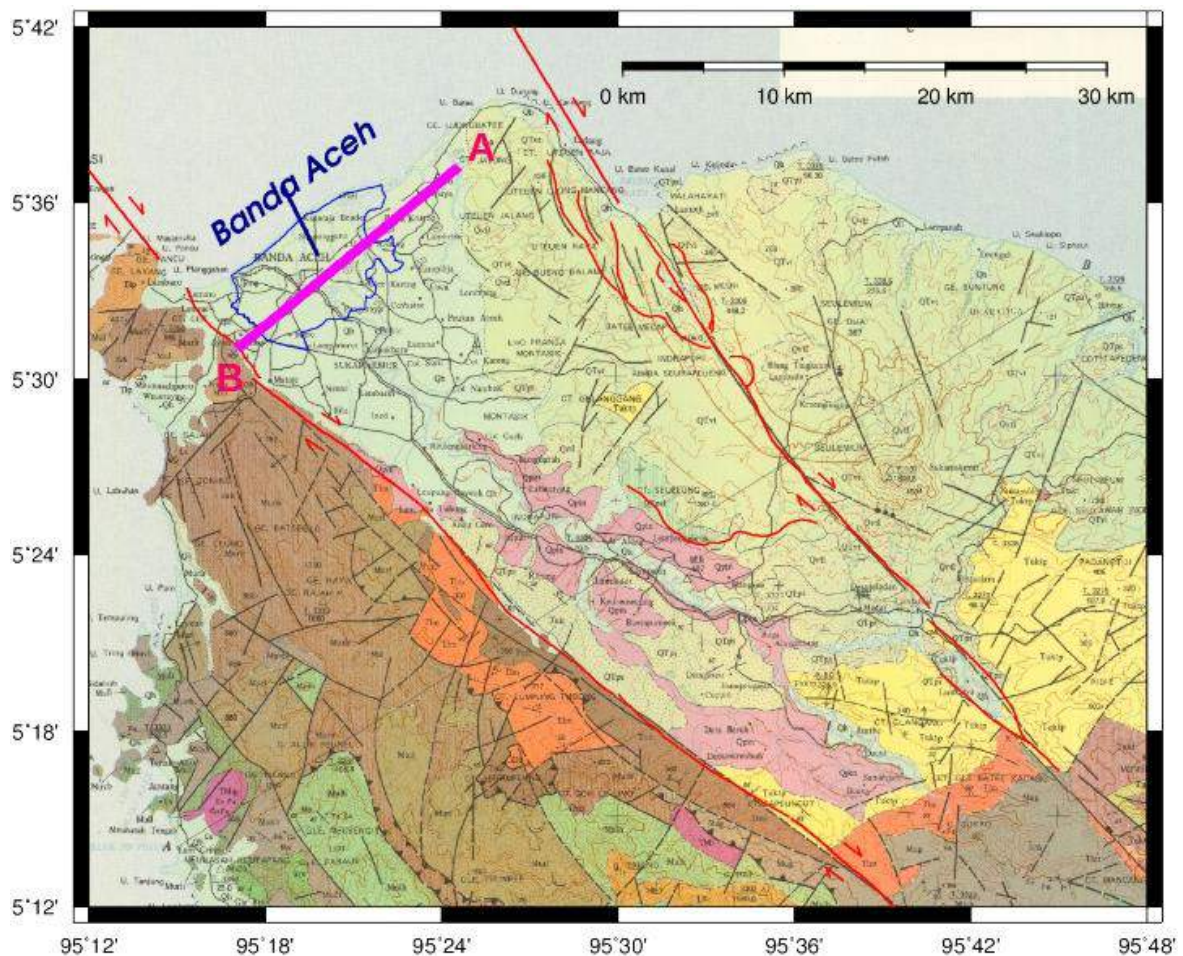The North Sumatra Tertiary sedimentary basin and its westward extension in NW Aceh occupy the northeastern part of Sumatra between Banda Aceh and Medan, extending northwards into the Andaman Sea as shown in Figure 7.3. The earliest sediments in NW Aceh and extending westwards across the Barisan Mountains into the West Aceh Basin, are conglomerates, sandstones, siltstones and shales with interbedded limestones (Meucampli and Agam formations) of Eocene to Early Oligocene age (Bennett et al., 1981; Barber et al., 2005).

The Banda Aceh Basin occupies the northern part of Sumatra Basin which is separated by Quarternary Volcanoes of Seulawah Agam from the North Sumatra Basin. The early published work about the geology of Banda Aceh Basin (Culshaw et al., 1979) shows that the city stands astride the Krueng (River) Aceh which flows in a broad valley between low tertiary and quaternary volcanic hills to the northeast and steeper, cretaceous limestone hills to the southwest. The side B of the profile is terminated by the limestone hills, and the side A of the profile is terminated by the

volcanic hills, as shown in Figure 7.3. The valley itself is filled in with relatively recent alluvial and marine sediments to the depths in excess of 179 meters (Van Es, 1930). These were deposited in a graben structure formed between the main Semangko fault system which marks the northeasterly limit of the Cretaceous limestone and an easterly splay. There is little relief in the lower part of the valley, much of the land being less than 5 meters above sea level. The oldest rocks in the Banda Aceh area are limestones, slates, and phyllites that outcrop at the west side of the Krueng Aceh valley.

The oldest rocks in the Banda Aceh area are the limestones, slates, and phyllites that outcrop on the west side of the Krueng Aceh valley (Bridge, 1976). These outcrops in wedges between the limestones and the quaternary deposits of the valley are thought to be of Paleogene age. However, their relationship to other rocks is confused by their occurrence along the line of the Semangko fault system. The deposits of fossiliferous tuffaceous sandstone from Pliocene or early Pleistocene age are found in the upper valley area near Jantho town. These were probably laid down in a shallow water marine environment that has risen to their present elevation of up to 90 meters above sea level by tectonic uplift. The east side of the valley is flanked by extensive deposits of andesitic tufts and subsidiary flows, some probable water. These deposits and their parent volcano, Seulawah Agam, lie on the line on the east Semangko fault, a splay off the main fault system. The Krueng Aceh valley forms a graben-type structure between these faults. Outcrops of uplifted Pliocene and Pleistocene reef limestones have also been identified along the east coast (Culshaw et al., 1979).

Tertiary sedimentation in the present quadrangle was controlled by the existence of proto Barisan Mountain range, which began to rise from Oligocene. This produced separate basins on its Lamno basin in the west and the Banda Aceh basin in the northeast. The absolute position of the Banda Aceh Basin was originally SE of its present position, later tertiary movements having brought it to present place, but it was always on the west side of the mountain range (Bennett et al., 1981).

We can simplify the geological map and show that Banda Aceh is located on alluvial deposition (Qh) and is not yet consolidated since the Holocene age. Banda Aceh is surrounded by rocks of the Tertiary age-Holocene. Southwest of Banda Aceh is dominated by carbonate rocks and east Banda Aceh is dominated by volcanic rocks. Both rocks are the bedrocks from Banda Aceh alluvial deposition covering Banda Aceh. In the west, Aceh also experiences the Eurasian Plate and the subduction zones of the Indo-Australian Plate. The Great Sumatran Fault runs constantly and causes the movement of the geological structures that affect the Banda Aceh basin, but can be muted with lithological conditions in the form of unconsolidated sediments (Rusdi et al., 2015).

7.3 Basin Structure of Banda Aceh

The construction of the 1D structural model for NDSHA at a regional scale can be built from the global and regional tomography data. Whereas, constructing the 2D structural model for NDSHA at a local scale requires more detailed information about the area being studied. There is no literature about the structure of the basin of Banda Aceh. The earliest geological study was done by Culshaw et al. (1979) until the depth of 30 m. Following earthquake and tsunami, BGR developed the Information System Engineering Geology (ISEG) based on GIS compiling several top soil condition for the reconstruction and rehabilitation of the extended urban area of Banda Aceh that was severely destroyed by the catastrophic 2004 earthquake/tsunami event (Günther, 2007). BGR also made a shallow shear-wave reflection seismic survey for several sites (Polom et al., 2008).

The available information from direct measurement in Banda Aceh is not sufficient information to construct the 2D profile necessary for the hybrid simulation. In order to construct the 2D structure to make the local scale study, we tried to find the other available data near Banda Aceh and make a projection. Fortunately, Project Sumenta-II has sufficient data taken from the seismic expeditions using single channel seismic reflection data acquired in 1991–1992 data along the western margin of Sumatra (Malod and Kamal, 1996). These data were recorded on paper strips, which were scanned, digitized and converted into the SEGY format. In the absence of any velocity information, these data were migrated using a water velocity of 1.5 km/s in order to remove the effect of seafloor scattering. The seismic profile near Banda Aceh basin has become available after that study by Ghosal et al. (2012) later assigned Profile 33.

Profile 33 lies between Weh Island and mainland Sumatra and covers a part of the Breueh Basin and Mergui Basin (Figures 7.6). It is 47 km long and the water depth varies from 375 m in the Breueh Basin to 1275 m in the Mergui Basin. There is a veneer of thin sediments (150 m) over what looks like old deformed sediments in the Breueh Basin. There are no volcanic features observed near the seafloor northeast of this basin, but a small bathymetric depression is observed that might be a near surface expression of the Seulimeum Fault (Figure 7.6-left) (Ghosal et al., 2012).
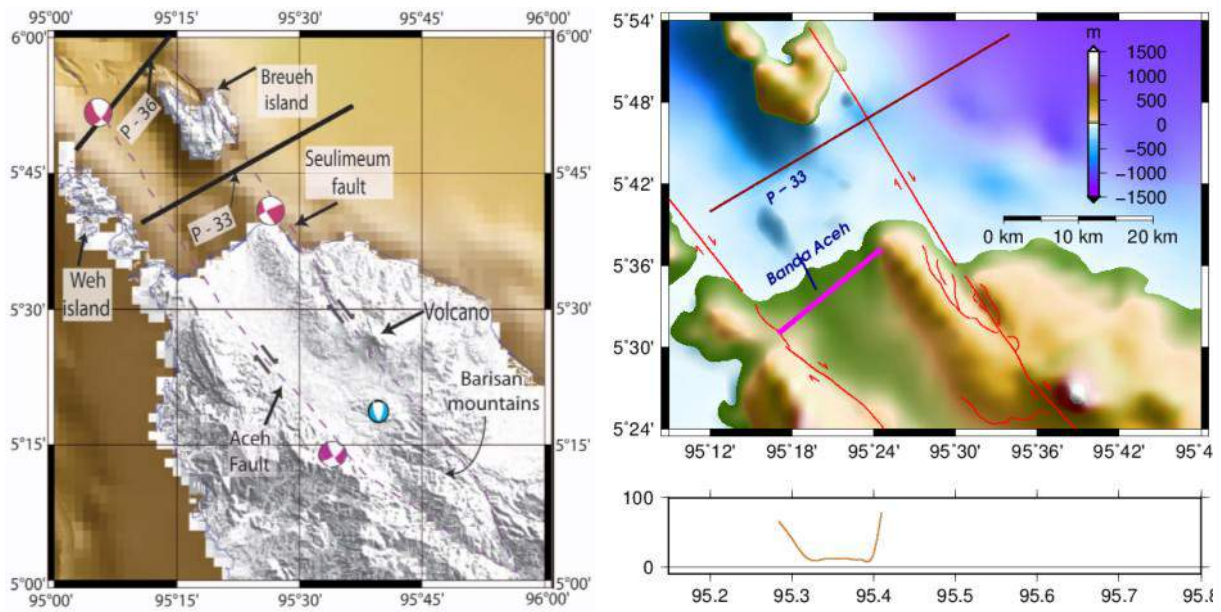
Figure 7.5 (left) Location of the profiles P-33 and P-36 and the valley of Banda Aceh region. The Aceh fault and the Seulimeum fault are marked by the dashed line (Ghosal et al., 2012). (right) Topography map showing the parallel valley for profile P-33 and Banda Aceh basin.
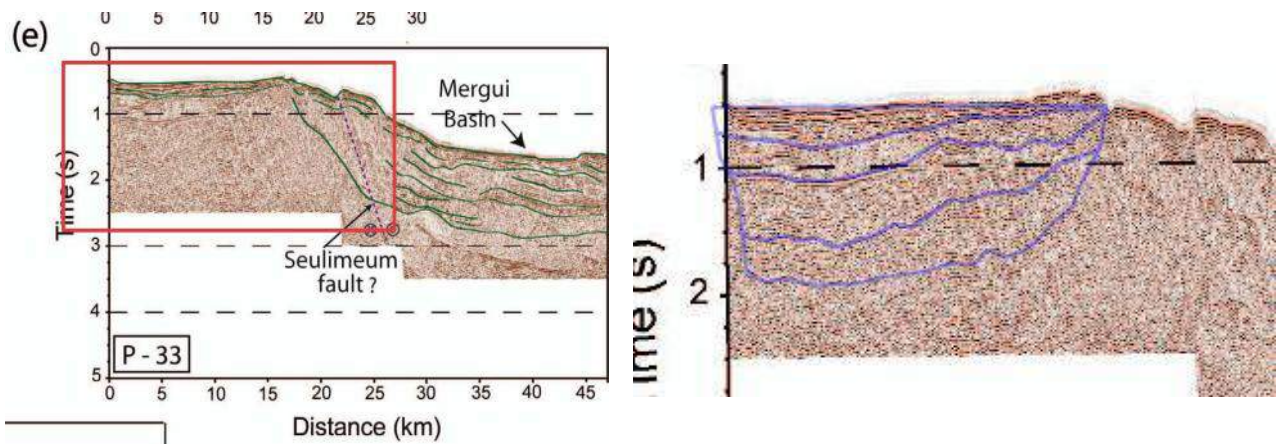
Figure 7.6 (left) Interpreted single channels seismic reflection profiles from the Sumenta-II (Malod and Kamal, 1992) Profile-33 (P-33). (right) Sedimentary layer interpretation based on seismic profiling as the red box of profile P-33 which is near the Banda Aceh Basin using QGIS.

Based on the single channel seismic reflection profile P-33, we interpreted the sedimentary layer which is near the Banda Aceh basin inside the red box Figure 7.6 (left). We use QGIS software (QGIS 2011) to draw the polygon following the pattern of seismic reflection as shown in Figure 7.5 (right). The polygon is saved in .shp format (common standard ESRI format for QGIS). We make a package script, shp2pof.sh, to convert from (*.shp) to a file in a polygon format, which is accepted by hybrid software package (*.pof). The conversion process also reads the table of physical properties of the sedimentary layer as shown in Figure 7.1 in the format Comma Separated

Values (*.csv). The file format is often used to exchange the data between differently similar applications by LibreOffice Calc, Microsoft Excel, or manual text editing.

Because of the coordinate system in QGIS and the size of the picture from a seismic profile in a pixel size, scaling to an appropriate length and depth can be adjusted in the script and plotted as shown in Figure 7.7 (left). The standard procedure to prepare the polygon is using XdigiMac Screen Digitizer (Vacarri 2014d). The polygon produced by QGIS is converted into the 2D hybrid input format and is readable by XdigiMac software package for checking and visualizing the 2D profile before using in the hybrid computation. People familiar with QGIS or other GIS software, e.g. ArcGIS, MapInfo, or other software can produce the *.shp file easily working with their favorite GIS software and has the capability to overlay another data which is difficult if not impossible to apply in XdigiMac.

Table 7.1 is based on the compilation of information from several available studies, such as, ISEG (Günther, 2007) and shallow shear-wave reflection seismic tomography (Polom et al., 2008), and considering geological similarity with previous study using the method (Vaccari et al., 2011; Nunziata et al., 2011; Paskaleva et al., 2007; Mohanty et al., 2009; Alvarez et al., 2005).
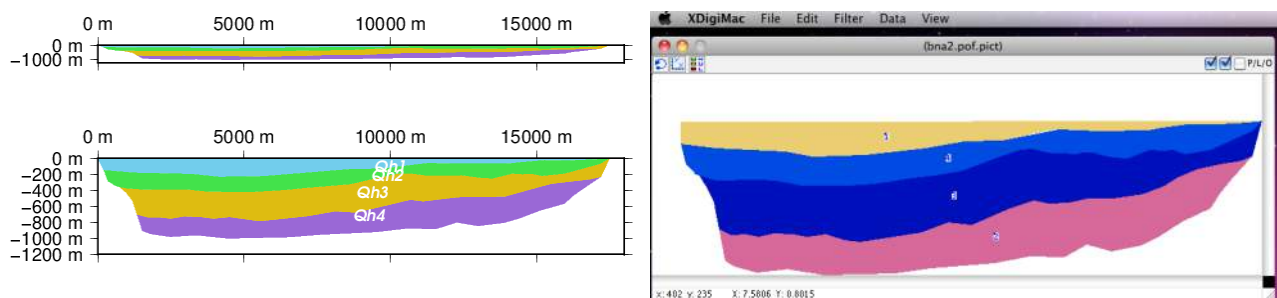
Figure 7.7 The dimension of polygon size after conversion by shp2pof.sh (left) and the program XdigiMac successfully read the bna3.pof produced by the script (right)

Table 7.1 Physical parameters for each layer in spreadsheet (LibreOffice/MSexcel)

Name	rho	Vp	vs	qp	qs	h	epoch	Formation	material
Qh1	1.8	0.6	0.3	60	25	0.25	holocen	Alluvium	gravels,sands,muds
Qh2	1.9	1	0.5	200	100	1	Pleistocene	Alluvium2	Alluvium2
Qh3	2	2	1	300	200	2	meosen	Alluvium3	Alluvium3
Qh4	2.1	2.5	1.4	400	230	2	meosen	Alluvium3	Alluvium3
Bed	2.47	3.5	2.0	1350	600	5.2	egosen	bed	hard

```
thk(km)    rho    Vp(km/s)   Vs(km/s)   Qp       Qs      depth(km)  layer name
  1.1787   1.97   3.500000   2.000000   1350.13  600.00   1.17866   1    SEDS1-BOTTOM
  6.8135   2.47   5.147437   2.904619   1350.13  600.00   7.99216   2    CRUST1-BOTTOM
  8.4092   2.67   6.113295   3.495663   1350.13  600.00   16.4013   3    CRUST2-BOTTOM
 15.1265   2.85   6.686211   3.815870   1350.13  600.00   31.5278   4    CRUST3-BOTTOM
 92.8497   3.30   8.123616   4.628840    450.04  200.00   124.377   5    LID-BOTTOM
100.0000   3.30   7.961142   4.326709    157.52   70.00   224.377   6    ASTHENO-BOTTOM
 55.6224   2.65   8.572799   4.639019    208.83   92.72   280.000   7    M65
 60.0000   2.78   8.753242   4.750742    201.59   89.51   340.000   8    M62
 70.0000   3.47   8.939481   4.861714    156.31   69.40   410.000   9    M69
 80.0000   3.93   9.550887   5.220524    416.59  184.97   490.000   10   M55
 80.0000   3.92   9.810226   5.370601    420.98  186.92   570.000   11   M51
 90.0000   3.92  10.11921    5.566250    425.83  189.07   660.000   12   M48
 90.0000   4.29  10.93294    6.094822   1315.11  583.91   750.000   13   M44
 90.0000   4.40  11.12214    6.236225   1271.93  564.74   840.000   14   M43
 90.0000   4.49  11.28087    6.265922   1255.96  557.65   930.000   15   M41
 90.0000   4.57  11.45185    6.338050   1240.11  550.61  1020.00    16   M39
110.0000   4.63  11.60294    6.432203   1223.39  543.18  1130.00    17   M37
120.0000   4.69  11.77173    6.541500   1204.54  534.82  1250.00    18   M36
150.0000   4.76  11.95084    6.629762   1182.80  525.16  1400.00    19   M33
```


Listing 7.1 1D structural model for 1D hybrid method with the top layer from LITHO1.0 model adjusted to the local conditions expressed in the 2D structural model.

Figure 7.8 (right) Plotting of the 1D structural model from listing 7.1.
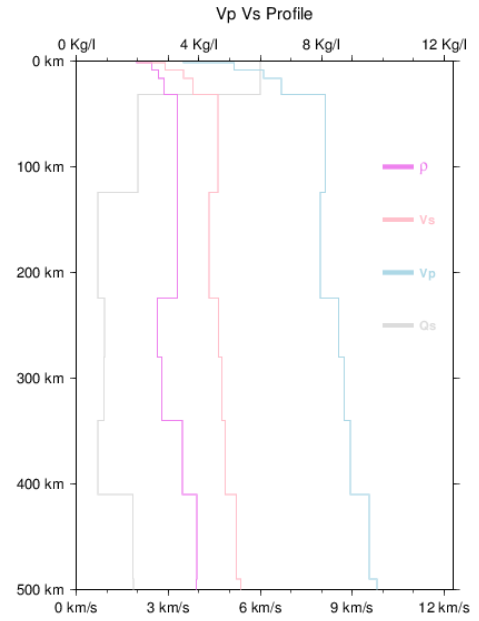
7.4 Source Definition for Local Scale NDSHA

The regional scale NDSHA will compute the synthetic seismogram for many significant sources defined for each area, following source definition as discussed in Chapter 3. For the local scale NDSHA, the computational cost is more expensive because of using the hybrid method to produce synthetic seismogram. Therefore, the only selected scenario sources will be used for the calculation of the most significant contribution to strong ground motion PGD, PGV and PGA. The result, from ES UP 10Hz Figure 6.4.5, shows that the source of PGD and PGV is in the subduction zone and for PGA in the strike-slip fault.

In order to investigate the most significant source of hazard to the Banda Aceh city, we plotted the source related to the most significant ground motion parameter to the sites of interest. Figure 7.9 and 7.10 show the sources for PDG (left) and PGA (right) for the horizontal component (Figure 7.9) and the vertical component (Figure 7.10) at the maximum cutoff frequency of 10Hz and using the enhanced source definition procedure with the updated path generator (ES-UP 10Hz). The picture shows that the PGD in the city is controlled by the big earthquake in the subduction zone as shown in Figure 7.9 (left), and PGA is related to near source as shown in Figure 7.9 (right). However, for the vertical component, almost all vertical PGD is contributed by the subduction zone of the vertical movement from the Sunda megathrust mechanic, see Figure 7.10 (left). The PGA for the vertical component remains controlled by the near field sources from the strike slip seismogenic zones in the land of Sumatra.

PGD: ES UP 10Hz

PGA: ES UP 10Hz

Figure 7.9 Sources that contribute the maximum horizontal component of PGD (left) and PGA (right) computed at 10 Hz cutoff for horizontal component for the ES-UP version of NDSHA.
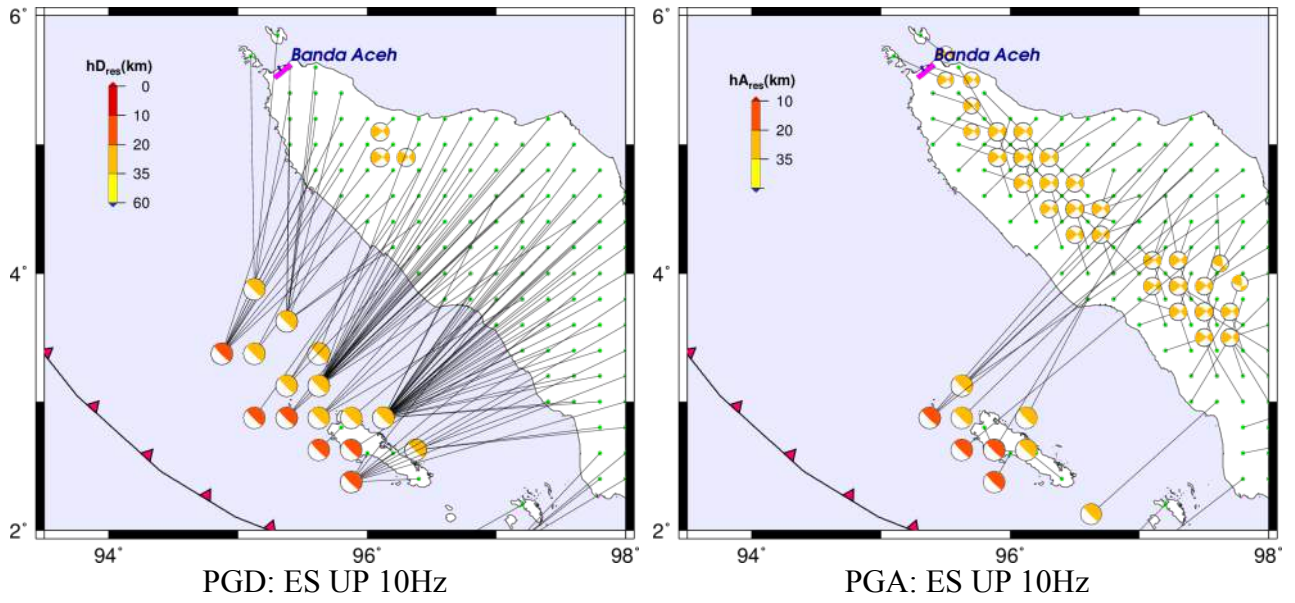

PGD$_{VERT}$: ES UP 10Hz
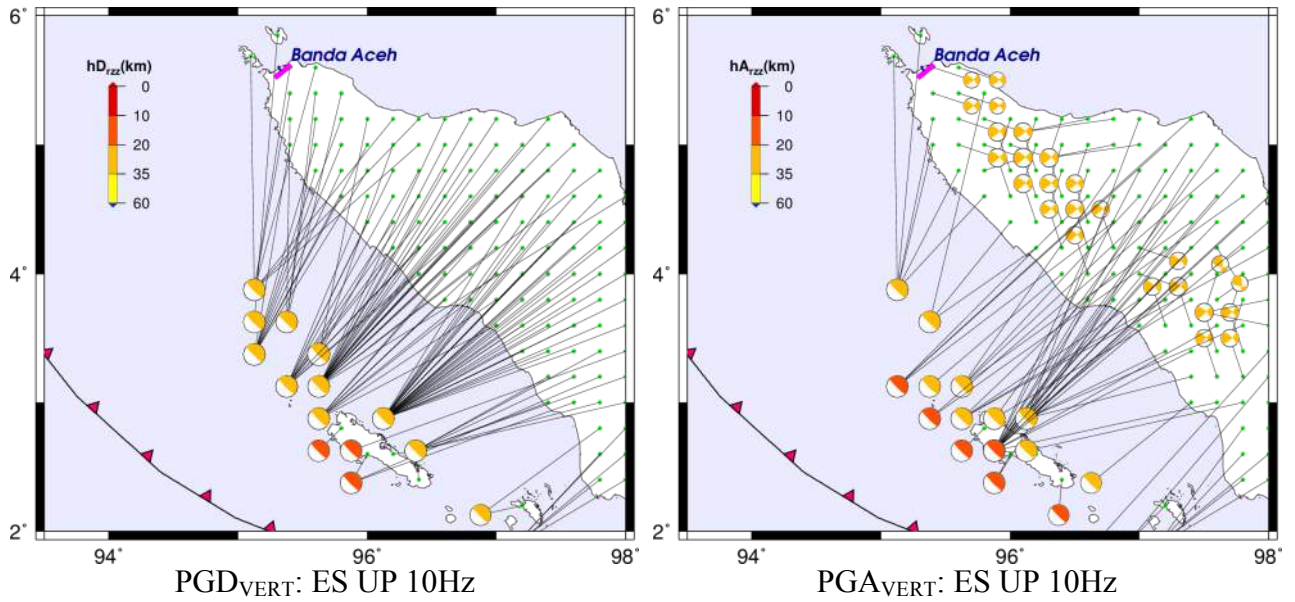
PGA$_{VERT}$: ES UP 10Hz

Figure 7.10 Sources that contribute the maximum vertical component of PGD (left) and PGA (right) computed at 10 Hz cutoff for horizontal component for the ES-UP version of NDSHA.
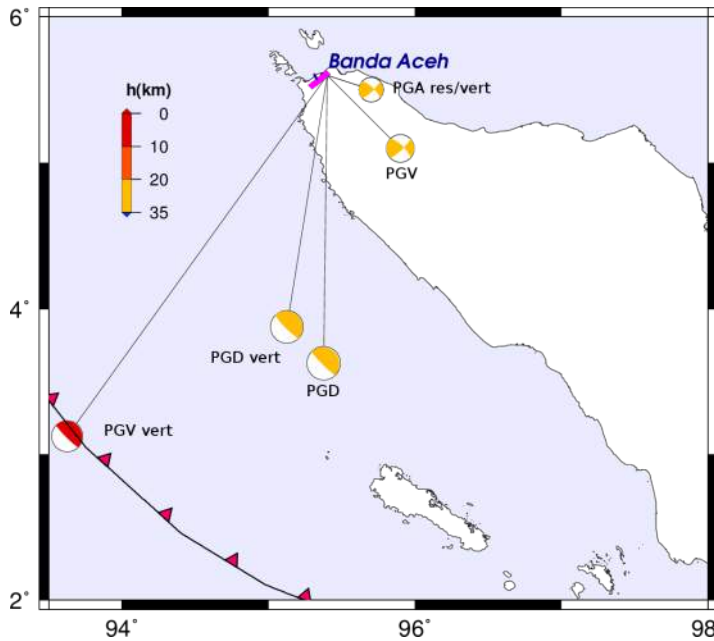
144

Figure 7.11 The source location which contributes to significant strong ground motion PGD, PGV and PGA at cutoff frequency 10Hz. The PGD and PGV for the vertical and horizontal component are from different earthquake sources. Only PGA for the horizontal and vertical component have the same source.

```
comp    slon    slat     dist      az       hs      strike   dip     rake    strrec   mag    amaxa
PGDres  95.3750 3.6250   218.410    0.727  31.306   325.000  7.000  100.000  324.273  8.83  0.4555E+02
PGVres  95.9000 5.1000    78.283  314.956  20.000   313.000 72.000  168.000  358.044  7.41  0.3883E+02
PGAres  95.7000 5.5000    35.031  288.415  20.000   313.000 72.000  168.000   24.585  6.50  0.3081E+03
PGDrzz  95.1250 3.8750   193.173    9.076  28.121   325.000  7.000  100.000  315.924  8.73  0.3833E+02
PGVrzz  93.6250 3.1250   337.214   35.687   5.291   325.000  7.000  100.000  289.313  8.31  0.2186E+02
PGArzz  95.7000 5.5000    35.031  288.415  20.000   313.000 72.000  168.000   24.585  6.50  0.1208E+03
```

Listing 7.2 shows the important parameters selected from a receiver near the Banda Aceh basin, longitude=95.4°, latitude=5.6°.

We chose 2 scenarios for which the source contributes to horizontal PGA and PGD. For subduction, we selected the source, which contributes to significant PGD horizontal with a strike-receiver=325°, dip=7°, rake=100°, magnitude M8.8, and focal depth 31.5 km. The distance from the source to the receiver is in Listing 7.2. For the strike-slip, we inverted the direction of the 2D profile, and the use of strike-receiver=24.585°+180°=204.585°.

```
31.306    Source depth (km)                          20.000    Source depth (km)
324.273   Strike-receiver angle (SH modelling)       204.585   Strike-receiver angle (SH modelling)
7.000     Fault dip          (SH modelling)          72.000    Fault dip          (SH modelling)
100.000   Fault rake         (SH modelling)          168.000   Fault rake         (SH modelling)
324.273   Strike-receiver angle (P-SV modelling)     204.585   Strike-receiver angle (P-SV modelling)
7.000     Fault dip          (P-SV modelling)        72.000    Fault dip          (P-SV modelling)
100.000   Fault rake         (P-SV modelling)        168.000   Fault rake         (P-SV modelling)
208.410   Source-2D model origin distance (km)       35.031    Source-2D model origin distance (km)
8.83      Magnitude                                  6.5       Magnitude 5.3
1         Source (1=point, 2=extended)               1         Source (1=point, 2=extended)
```

Listing 7.3 Part of pfdg13.par configuration file of hybrid 2D for source parameter for subduction zone scenario (left) and for strike slip (right)

145

7.5 Simulation for Subduction Source

The technical procedure for the computation of the seismic microzonation is explained in the Quick Reference Manuals, Ground shaking scenarios along 2D profiles used with the hybrid technique with the point-source approximation (Vaccari, 2015). The computation has two stages: first, it generates a synthetic seismogram with a 1D modal summation. Second, it generates the synthetic seismograms by 2D finite differences. Therefore, we can compare both results in order to get the response spectra ratios.

The complete synthetic seismograms, including all of the main phase reflections, refractions, conversions, and surface waves, have been generated for the profiles of the Banda Aceh city. The seismograms are computed with the cutoff frequency of 1 Hz, as shown in Figure 7.12 (left). The source is taken southeast of the basin at a distance of 208.4 km away from the nearest seismogram computation site. The source represents the subduction zone earthquake with an oblique-slip focal mechanism (stirke=325º, dip=7º, rake=100º, magnitude M8.8, and focal depth 31.5 km. The vertical component reaches the largest peak value as it is a characteristic of the sources for a subduction zone.
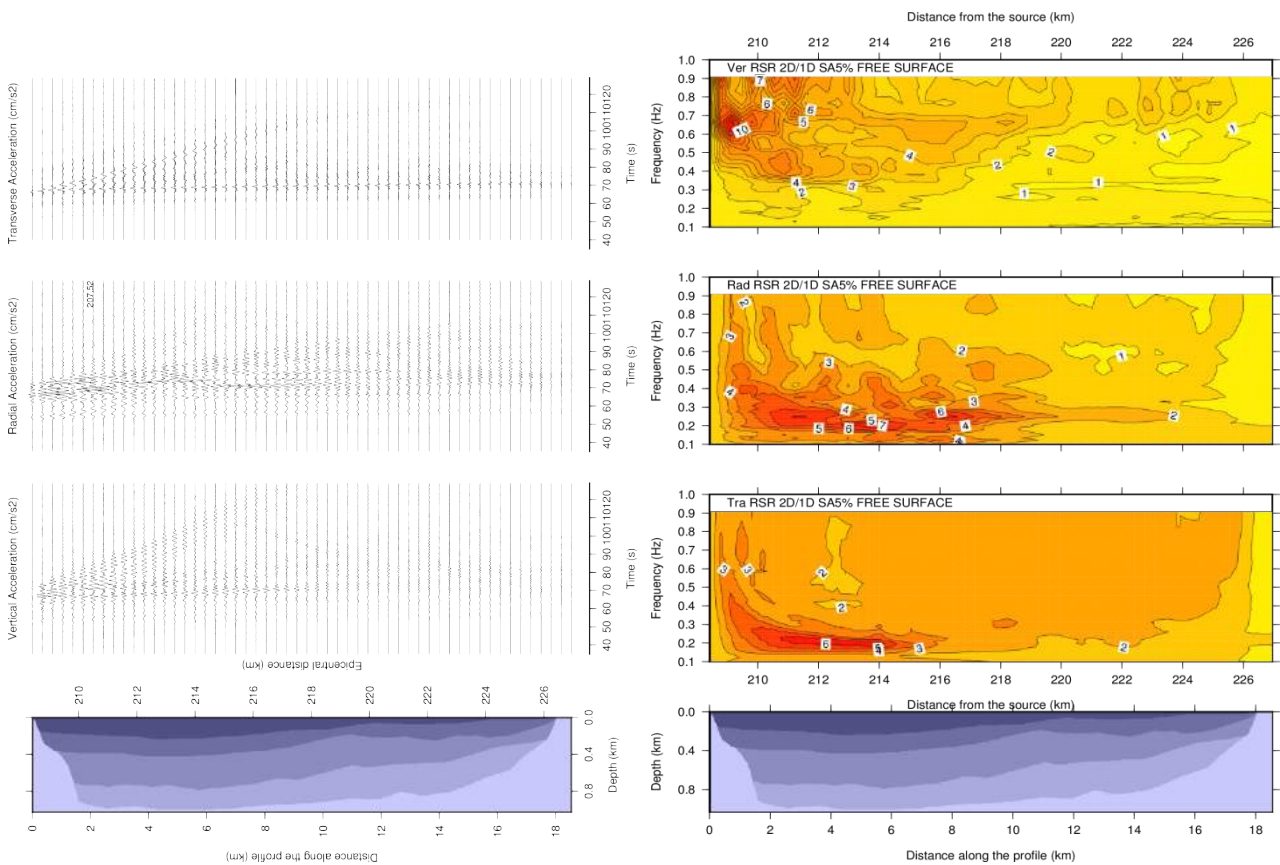

Figure 7.12 (left) The three components accelerograms along the profile. (right) The response spectra ratio (RSR) versus frequency and epicentral distance along the profile.

The local response at a given site is estimated by evaluating the response spectra ratio (RSR). The RSR is expressed as RSR = RS(2D)/RS(1D) where, RS (2D) is the response spectrum (at 5% damping) of the signals in the laterally varying local structure, and RS (1D) is the response spectrum (at 5% damping) of the signals calculated for the bedrock regional reference model. Figure 7.12 (right) shows the RSR for the profile along the Banda Aceh basin with 1 Hz cutoff. The computation is adequate because the high frequencies are not relevant in the far source field at the epicentral distances larger than 200 km.

7.6 Simulation for Strike Slip Source

The strike-slip fault is the controlling earthquake source for PGA on Sumatra. The sources of the dominant PGA for the horizontal and vertical components are from the strike-slip fault in the source as shown in Figure 7.9. The source is taken south of the basin at a distance of 35 km away from the nearest seismogram. Therefore, we need to inverse the geometry of structural sediment geometry as shown in Figure 7.13.
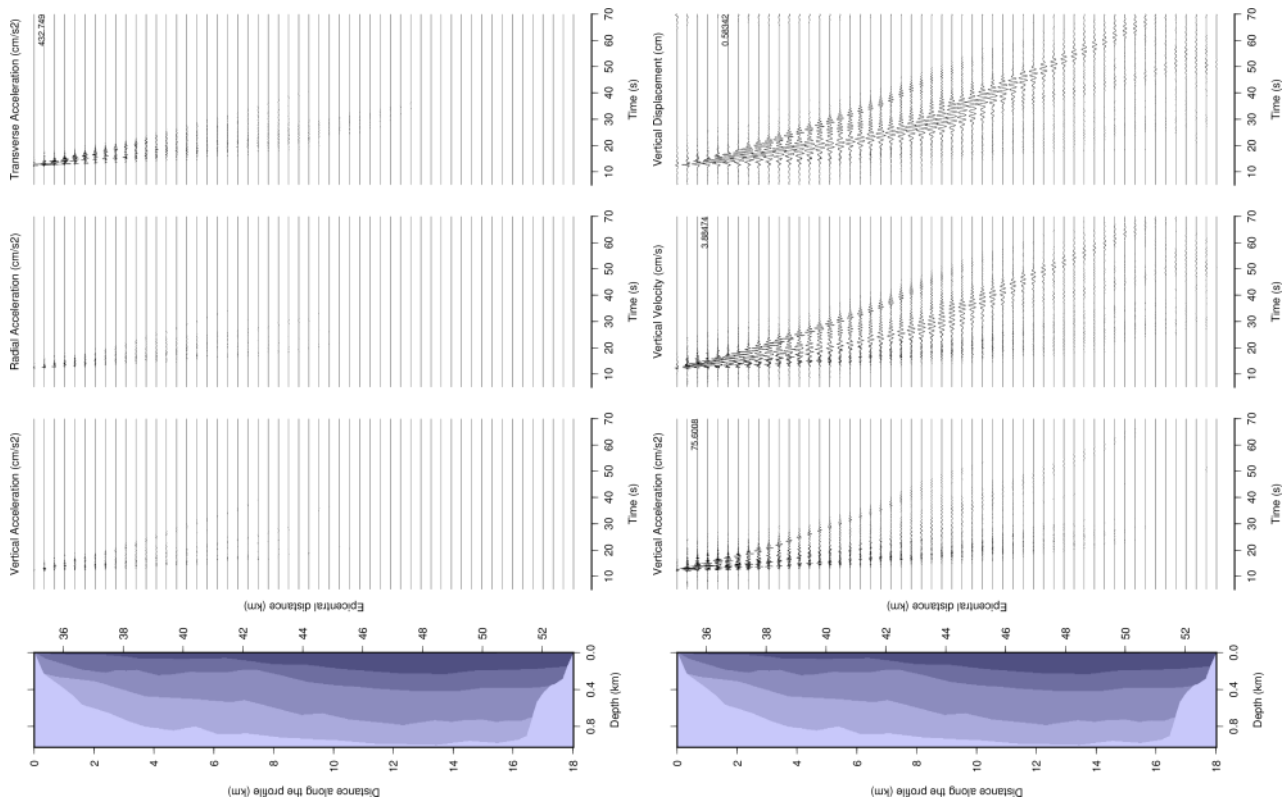

Figure 7.13 (left) The three components accelerograms along the profile (right). The response spectra ratio (RSR) versus frequency and epicentral distance along the profile

147

For the near-field source, the source represents the Sumatra strike-slip fault (strike=313º, dip=72º, rake=168º), magnitude M=6.5, and focal depth = 20.0 km. Because of the short epicental distance, the high frequencies are significant and the simulation of the synthetic seismogram is made with a cutoff frequency of 10Hz. Because of the limitation in the knowledge of the source and the structural models, we trust the result until 5Hz as shown in Figure 7.14. Because the simulation is running with the inverted basin geometry, the resultant response spectra ratio plot is inverted again to its original position, see Figure 7.14 (left). The result shows that the values of RSR depend on the site where the seismic energy enters the basin. This effect is related to the strong amplification (polarization) of the waveform and the strong damping effect of most energy by the sedimentary layer.
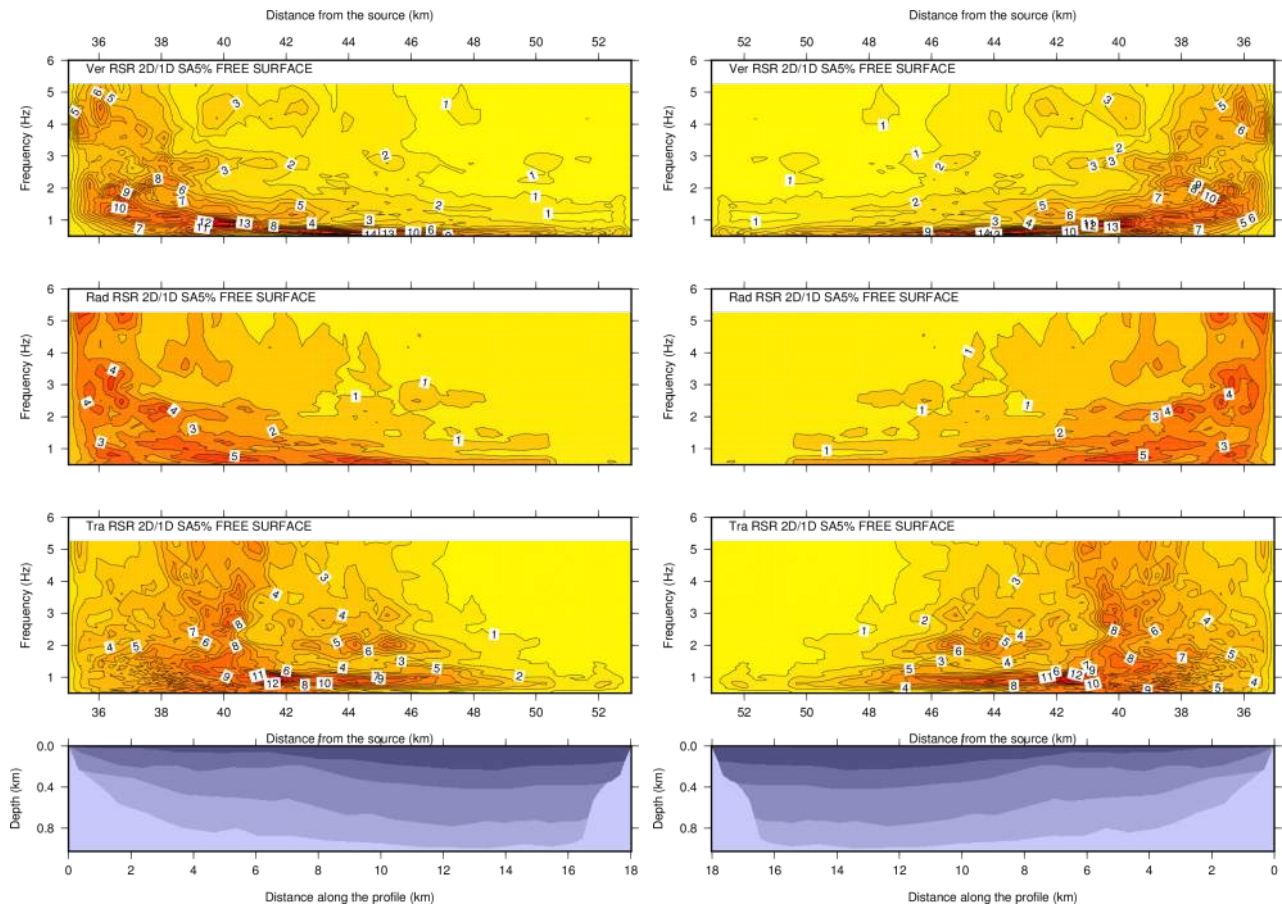

Figure 7.14 (left) shows the response spectra ratio (RSR) versus epicentral distance along the inverted profile; (right) shows the inverted plot of RSR versus epicenteral distance along the inverted profile and it became easy to compare with figure 7.12 (right) because using same geometry of basin.

The RSR are summarized in Figure 7 14. For the vertical component, the largest values (a factor of 14) occur at frequency less than 1 Hz. In some areas, e.g., at the edges of the local model, the frequency of the largest values is higher than 1 Hz. The pattern of the RSR is quite different in the case of radial, but it is similar to transverse component. In the transverse component, the amplification is stronger and occurs within the frequencies between 0.5 and 4 Hz. For the radial component, the largest value (a factor of 5) occurs along a wide range of frequencies relative to the two other components.

The loose soft alluvial sediments underneath the Banda Aceh city are the main factor behind this potential damage because they may not only affect the vertical component but may greatly polarize in the horizontal plane (amplify) the ground motion, as demonstrated by the strong ground motion model. The largest amplification is generally concentrated along the edges of the graben and occurs at frequencies between 0.5 Hz and 2 Hz.

8. Conclusions and Suggestions

8.1 Conclusions

Although widely used, the PSHA method gives a less accurate picture of the physical processes behind an earthquake. The official seismic hazard map for Indonesia (including Sumatra) is produced with the PSHA method by taking into account the updated seismotectonic data, the new fault models, the implemented new GMPE as NGA, and the divided seismic sources based on fault, subduction, and background zones. Due to the absence of GMPE developed using the data observed directly Indonesia as well as the disruption of the tensor nature of earthquake ground motion, predicted by continuum mechanics, in the computed strong motion, caused by the adoption of these relationships, there is a need for a reliable and rigorous definition and characterization of seismic hazard parameters.

A more adequate definition of the seismic ground motion can be given by the NDSHA method, which is based on the possibility of efficiently computing realistic synthetic seismograms by the modal summation technique. NDSHA has been applied in many countries (Panza et al., 2013) for some 20 years and has not yet been contradicted by any observation. NDSHA has been developed to naturally supply realistic time series of ground shaking, including reliable estimates of ground displacement readily applicable to seismic isolation techniques. The NDSHA procedure, which represents a drastic enhancement of DSHA, permits the timely incorporation, as they become available, of new geophysical and geological data, as well as the information from the different Morphostructural Zonation (MZ) developed for the space identification of potential strong earthquake sites in historically seismically quiescent areas. All this leads to the natural definition of a set of scenarios of expected ground shaking at the bedrock. At the local scale, further investigations can be performed taking into account the local soil conditions, in order to compute the seismic input (realistic synthetic seismograms) for engineering analysis of relevant structures, such as historical and strategic buildings (Panza et al., 2013).

Sumatra is among the most active regions in terms of earthquakes, owing to the confluence of multiple plates moving at very high relative speeds. The earthquake activity around Sumatra has multiple sources: thrust earthquakes on the subduction fault, strike-slip earthquakes on the Sumatran fault, deeper earthquakes within the subducting lithosphere, and volcanic earthquakes. The first step of any seismic hazard assessment is the identification of seismic sources that can affect the area of study. This step needs an accurate earthquake catalog as complete as possible.

One of the important advantages of NDSHA is that it is not necessary to involve the earthquake recurrences nor the "return period", which, due to the sporadic occurrence of large earthquakes, are subject to large uncertainties, the former, and is physically rootless, the latter.

The USGS catalog, in this study, is combined with the catalogs from Engdahl et al. (1998), ISC, BMKG and Pesicek et al. (2010). In order to improve the poor earthquake catalog for the Sumatra fault, the earthquake information from geological investigations (Natawidjaja and Triyoso, 2007) is used. In order to combine several earthquake catalogs compiled by different authors with different details and completeness, we developed an updated selection procedure routine, namely eqc4select.exe. This selection procedure is very useful to deal with huge data sets with different formats, and it is useful to remove any error from the data if they are not in the proper range. The selection procedure reduced significantly (about 50%) the number of events from 25910 records to 13317 records.

Sumatra is surrounded by several kinds of faults: subduction, strike-slip, spreading, inter-plate from the Ninety East Ridge and the Investigator Ridge. Based on the tectonic setting, seismicity, and the similarity in the spatial distribution of focal mechanisms, we defined 15 seismogenic zones for Sumatra: each zone has a different level of complexity. The zones that contribute high hazard are Aceh, Semangko, Krakatau, Meulaboh, Padang, Nias, Mentawai. The zones that contribute moderate hazard are Lokop, Inter-plate, Medan, and Palembang. Finally, the zones that contribute low hazard are Java Sea, NSR, Sunda Trench, and Jakarta.

NDSHA can provide strong ground motion synthetic seismograms based on a realistic physical simulation for each source-receiver path. In order to reduce the number of computation and uncertainties of the earthquake catalogs, a smoothing procedure is needed (Panza et al., 1990). By applying the standard smoothing procedure (OS) to the selected earthquakes (13317) reduces the required source definitions to 2612.

Due to the complexity and variety of the seismogenic zones in Sumatra, the options and features provided by OS are not sufficient to handle the complexity of Sumatra seismogenic zones. Therefore, we developed an enhanced source definition procedure (ES) by using a flexible user-friendly configuration file, the setting parameters per polygon, a smoothing radius unit in degree or cell, the partitioning or transparent effect by grouping zones, the geometrical magnitude smoothing, the magnitude range limitation, and the ellipsoid geometrical smoothing algorithm. Besides the smoothing of the earthquake magnitude, we also enhanced the procedure to determine the focal depth from the depth distribution file or from the depth of the maximum magnitude in the cell. Having the new features and the more control on the individual seismotectonic zone gives us the details needed for controlling the smoothing process. The challenge to use the enhanced source definition procedure (ES) does not only come from the increase of the number of parameters for

each zone but also from the very large number of parameters in the case where many zones are used. After exploring the hypocenter distribution and slab distribution, finally, we defined 15 seismotectonic zones needed for the next step in the hazard computation, which is handled in our study using the ES procedure. The ES algorithm can reduce the number of the source from the standard smoothing of 2612 records to only 1776 records.

The realistic estimation of seismic hazard needs earthquake source model and medium structural model accuracy as much as possible. NDSHA can provide the strong ground motion parameters based on the realistic physical simulation of the seismic wave propagation within the structural model i.e. density, V_P, V_S, Q_P, and Qs. The information of P-wave and S-wave is taken from Pesicek et al. (2010) and Widiyantor (2008), respectively. And for the upper part of the structural model, we take the information from LITHO1.0. In order to have an optimum number of structural models, we rotated the cellular grid by 54º with respect to the north; thus, the number of the polygons is 49: 14 polygons for the small islands and 35 polygons for Sumatra.

The NDSHA computation is run using synthetic seismograms, and a new version of the parametric testing program was developed with several features with a user-friendly configuration file and with a support for handling an extended source parameter. The program succeeded to provide an input for the modal summation computation and to produce the strong ground motion by taking into account the angular radiation pattern.

We validated the results against the shaking map and the observed time series taken from the Takengon earthquake (occurred on 2 July 2013) with a magnitude of 6.1. The comparison showed a satisfactory agreement with the estimated value from NDSHA, the shaking map from USGS, and the observed intensity. The waveforms from the observed accelerograms and seismograms are more dispersed than those from the synthetic seismograms. Such disperse difference took place because the synthetic seismograms were computed on a 1-dimensional rock structure without taking into account the factors in scattering and site effect. The length of the coda duration was controlled by the site effect at a location station. The station located on a bedrock is in good agreement with the theoretical synthetic seismogram.

The enhanced source definition (ES) was applied with the original version of the standard path generator (OP). The use of the enhanced source definition produces PGD, PGV and PGA is very similar to what is produced by the standard NDSHA package. The PGA produced by ES-OP shows a relatively significant decrease at near and far sites within the Sumatran fault system (e.g. Bangka Island) in comparison with the PGA produced using the standard package OS-OP. This could be because in the enhanced source definition procedure we controlled the minRun (a minimum magnitude run for each site) for each seismogenic zone individually.

The PGD and PGA computed by the enhanced procedure ES-OP are more realistic if compared with the values obtained with the standard procedure OS-OP. The result shows that the estimated PGD using the ES-OP at far sites, relative to the earthquake sources, is dominated by the distant subduction source, while using the OS-OP leads to that, the far seismic sources-receivers are not considered in the computed PGD at distant sites (PGD from near sources is only registered). This is due to the magnitude distance threshold being used by the original version of NDSHA. However, the estimated PGA based on ES-OP and OS-OP shows almost the same result in a small source-receiver distance. This result is more reasonable because the subduction source can generate a larger magnitude than the strike-slip fault; thus, it can affect Bangka Island with significant impacts, whereas the strike-slip sources cannot.

The dominant period in the computed PGV by the ES-OP is relatively more scattered if compared with the dominant period of PGV produced by OS-OP. One possible reason is that the ES-OP has no fixed source of depth (the magnitude depth-dependent source) if compared to the standard OS-OP. The enhanced source definition ES-OP obviously uses the estimated focal depth from the enhanced smoothing procedure while the standard OS-OP uses three different magnitude-focal depth with varied threshold values (10km, 15km, 20km).

We succeeded in updating the path generator (UP) to adopt the user-friendly configuration file and to handle the problem where the sources are not registered in the far receivers in Bangka Island when using the medium range of the magnitude distance threshold R2 (M7.0 and M8.0 have a range of 300km and of 400km, respectively). We can verify this fact by using the same input for the original and the updated version. The result shows a very small difference between the map computed using the updated version of OS-UP and the original version of OS-OP with a path definition. The MIS feature in the updated path generator allows the reduction of the computational time significantly. For the distance-magnitude threshold R3, the result from OP cannot be used anymore even if it produces the number of paths half compared to the number of the paths the UP produces. The comparison of the computation time for UP with threshold R3 and the OP with the standard threshold shows a significant decrease of the computational time (by a factor 4.5) with no loss in the accuracy of the produced PGA.

The PGA estimated by the standard NDSHA with 10 Hz cutoff is higher than the PGA computed from PSHA at PE 10%. The comparison between the PSHA map computed at 2% probability of exceedance and the NDSHA map shows that the PGA computed by NDSHA is greater in value than the PGA estimated by PSHA at the nearest sites, whereas the opposite is true in the case of the distant sites, relative to the epicentral distance. Accordingly, the NDSHA calculation for Sumatra gives a reasonable result in respect to the adopted magnitude distance threshold. The result is reasonable because the standard NDSHA is produced by using a realistic

physical simulation of the seismic wave propagation.

In this study, we applied the hybrid method to investigate the site-specific microzonation of Banda Aceh, the capital city of Aceh Province, after we improved the definition of the structural model. Additionally, we defined the mechanical properties of the sedimentary layer of the Banda Aceh basin in reference to the nearest available seismic profile. We performed two earthquake scenarios, which are significant to PGD and PGA with the city of Banda Aceh. In some areas, e.g., at the edges of the local model, the frequency of the largest values is higher than 1 Hz. The loose soft alluvial sediments underneath the city of Banda Aceh are the main factor behind this potential damage because the sediment may not only affect the vertical component but also greatly polarize the horizontal plane, which in turn amplifies the ground motion, as demonstrated by a strong ground motion model. The largest amplification is generally concentrated along the edges of the graben and occurs at frequencies between 0.5 Hz and 2 Hz.

The entire research process of this study can be summarized as shown in Figure 8.1 as the NDSHA method was done in two different scales. The regional scale, covering Sumatra, uses the seismogenic zones taken from the earthquake catalogs and the smoothing source definition enhanced procedure, the regional data structural models in 1D. Then we tested and verified the modal summation method using a single source, which was run with an updated path definition based on many sources. The result was the NDSHA map of Sumatra. On the other hand, the local scale, covering Banda Aceh city, uses a specific site taken from one of the many sources that was done the updated path definition of the regional scale. Additionally, we also used the local data structural models in 2D by running the local scale hybrid 2D method across several selected sources. The result of the local scale computation is the microzonation map of Banda Aceh City.

8.2 Suggestions

The NDSHA method is still evolving, and the computer code is being improved constantly since its conception, to accommodate the demand for the realistic ground shaking maps and the ground shaking scenarios, at different scales, by incorporating all relevant progresses in the knowledge of geological processes and their numerical modeling (Panza et al., 2012).

Adding the feature of the updated path generator makes it possible to combine 10Hz and 1Hz computation in a single program run by adopting different cutoffs: 10Hz for a near source and 1Hz for a distant source. Moreover, the standard process for calculating the synthetic seismogram in hazard computation can take a lot of space in data storage (hard disk) and consume a considerable amount of time for an I/O process. If the server is using an I/O network, it will take more time for sending the data via the network. The updated procedure for hazard computation should be

modified by completing the process of modal summation, rotation, and scaling and by selecting a significant seismogram in a single process per receiver. Such an improvement will reduce the use of data storage and computational time significantly.

Future studies could be devoted to better characterize the structural models, e.g. by modeling the regional surface wave tomography in Sumatra to improve the computed synthetic seismograms by including the oceanic-continent paths and implementing more realistic extended source models to deal with mega earthquakes.
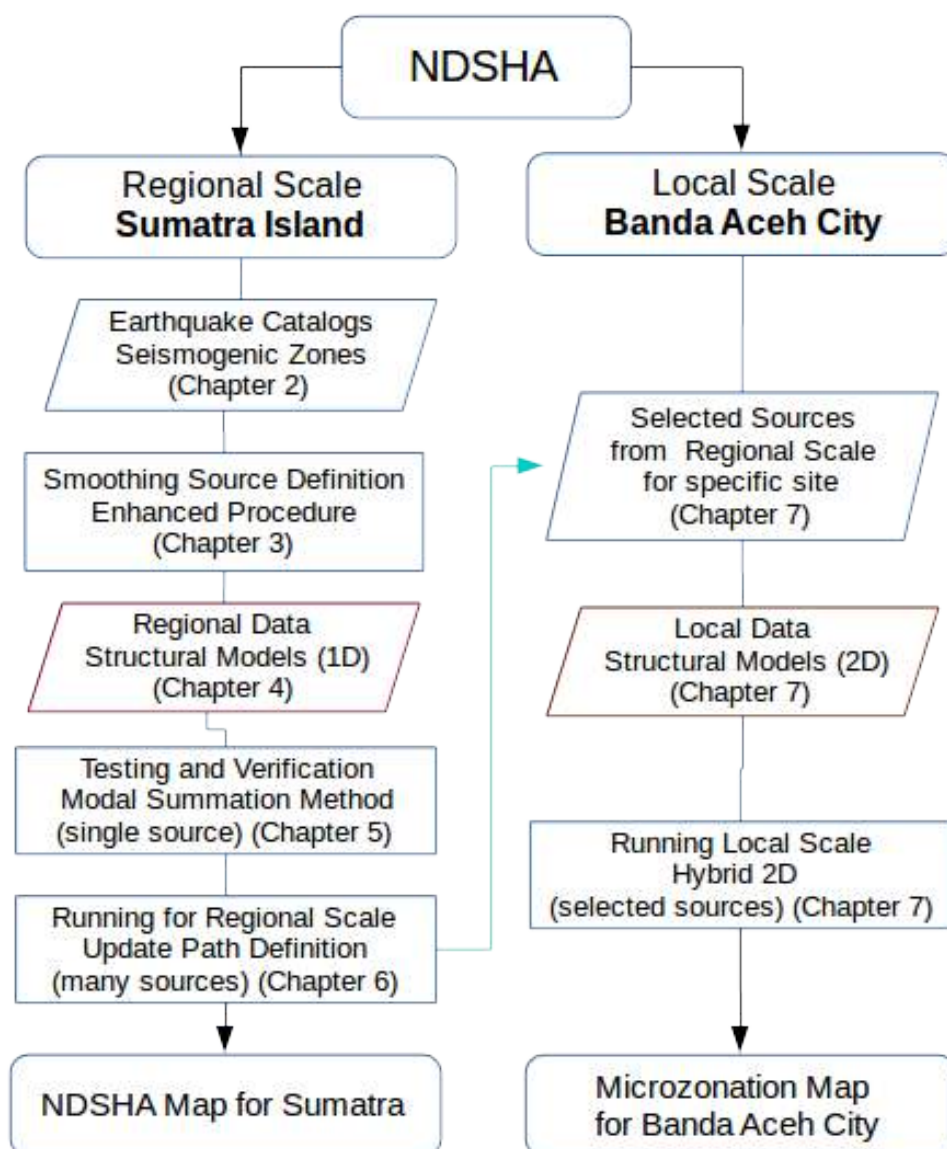
Figure 8.1 Summary diagram work flow for NDSHA: regional scale for Sumatra Island and local Scale for Banda Aceh City

Acknowledgments

References

Aki, K. (1987). Strong Motion Seismology. In Strong Ground Motion Seismology (pp. 3-39). Springer Netherlands.

Aki, K. dan Richards, P.G. (2002). Quantitative Seismology. University Science Books, Sausalito, CA, USA. ISBN 978-0935702965.

Alvarez, L., Vaccari, F., Panza, G.F., and Pico, R. (2005). Seismic Microzoning From Synthetic Ground Motion Parameters: Case Study, Santiago de Cuba. Soil Dynamics and Earthquake Engineering, 25(5), pp.383-401.

American Society of Civil Engineers (ASCE) (2010). Minimum Design Loads for Buildings and Other Structures, American Society of Civil Engineers, No.7, ISBN 978-0-7844-1115-5.

Anderson, Don L. (1989). Theory of the Earth. Blackwell Scientific Publications, Boston, MA. ISBN 0865423350. p. 301.

Artemieva, I.M. and Mooney, W.D. (2001). Thermal Thickness And Evolution Of Precambrian Lithosphere: A Global Study, J. Geophys. Res., 106, 16,387-16,414, 2001. http://www.lithosphere.info.

Badan Standarisasi Nasional (2002). Tata Cara Perencanaan Ketahanan Gempa untuk Bangunan Gedung SNI 03-1726-2002, Standar Nasional Indonesia.

Barber, A.J., Crow, M.J., and Milsom, J. (2005). Sumatra: Geology, Resources and Tectonic Evolution. Geological Society of London.

Bassin, C., Laske, G., and Masters, G. (2000). The Current Limits of Resolution for Surface Wave Tomography in North America, EOS Trans AGU, 81, F897, 2000. http://igppweb.ucsd.edu/~gabi/rem.html.

Beca, Carter, Hollings, and Ferner (1978). Indonesian Earthquake Study (6 volumes), Wellington, New Zealand (unpublished).

Bellier, O., et al. (1997). "Paleoseismicity and Seismic Hazard along the Great Sumatran Fault (Indonesia)." Journal of Geodynamics 24.1 (1997): 169-183.

Ben-Menahem, A. and Harkrider, D.G. (1964). Radiation Patterns of Seismic Surface Waves from Buried Dipolar Point Sources in a Flat Stratified Earth. Journal of Geophysical Research, 69(12), 2605-2620.

Bennett, J.D., Bridge, D.McC., Cameron, N.R., Djunuddin, A., Ghazali, S.A., Jeffrey, D.H., Kartawa, W., Keats, W., Rock, N.M.S., Thomson, S.J., and Whandoyo, R. (1981). 1:250,000 Geologic Map of the Banda Aceh Quadrangle, Sumatra, Geological Research and Development Centre, Jalan Diponegoro 57, Cable P3G, Bandung, Indonesia, 1981.

Brandmayr, E., Marson, I., Romanelli, F., and Panza, G.F. (2011). Lithosphere Density Model in Italy: No Hint for Slab Pull. Terra Nova, 23(5), 292-299.

Bridge, D.Mc. (1976): Geological Report, Sheet NB 46-12-C (Banda Aceh). Integrated Geological Survey of Northern Sumatra. Report No. 17 (unpublished).

Burridge, R. and Knopoff, L. (1964). Body Force Equivalents for Seismic Dislocations. Bulletin of the Seismological Society of America, 54(6A), 1875-1888.

Cameron, N.R., Bennett, J.D., Bridge, D.Mc.C., Clarke, M.C.G., Djunuddin, A., Ghazali, S.A.,Harahap, H., Jeffery, D.H., Kartawa, W., Keats, W., Ngabito, H., Rocks, N.M.S., and Thompson, S.J. (1983). Geologic Map of the Takengon Quadrangle, Sumatra, Geological Research and Development Centre, Scale 1:250.000,Pusat Penelitian dan Pengembangan Geologi.

Cancani, A. (1904). Sur L'emploi D'une Double Echelle Seismique Des Intesites, Empirique Et Absolue, G. Beitr. 2, 281-283.

Castaños, H. and Lomnitz, C. (2002). PSHA: Is It Science? Engineering Geology, 66(3), 315-317.

Costa, G., Panza, G.F., Suhadolc, P., and Vaccari, F. (1993). Zoning of The Italian Territory in Terms of Expected Peak Ground Acceleration Derived from Complete Synthetic Seismograms. Journal of Applied Geophysics, 30, 149–160.

Culshaw, M.G., Duncan, S.V., and Sutarto, N.R. (1979). Engineering Geological Mapping of the Banda Aceh Alluvial Basin, Northern Sumatra, Indonesia. Bulletin of the International Association of Engineering Geology-Bulletin de l'Association Internationale de Géologie de l'Ingénieur, 19(1), 40-47.

Curray, J.R. (1989). The Sunda Arc: a Model for Oblique Plate Convergence. Netherlands Journal of Sea Research, 24, 131 – 140.

Curray, J.R. and Munasinghe, T. (1991). Origin of the Rajmahal Traps and the 85 E Ridge: Preliminary Reconstructions of the Trace of the Crozet Hotspot. Geology, 19(12), 1237-1240.

Curray, J.R. (2005). Tectonics and History of the Andaman Sea Region. Journal of Asian Earth Sciences, 25(1), 187-232.

Dalton, C.A., Ekström, G., and Dziewonski, A.M. (2008). The Global Attenuation Structure of The Upper Mantle. Journal of Geophysical Research 113. DOI:10.1029/2007JB005429.

Dirhamsyah, M. Syamsidik, Ibnu Rusydy, Putra Pagihariadi, and Teuku M. Rasyif (2013). Paparan Hasil Kajian Dampak Gempa Bumi Bener Meriah-Aceh Tengah. Presentation at Universitas Syiah Kuala (unpublished).

Djamal, Illiza.S. and Budiman, B. (2014). Statistics of Banda Aceh, 2014.

Doglioni, C. and Panza, G. (2015). Chapter One-Polarized Plate Tectonics. Advances in Geophysics, 56, 1-167.

Douglas, J. (2001). A Comprehensive Worldwide Summary of Strong-Motion Attenuation Relationships for Peak Ground Acceleration and Spectral Ordinates (1969 to 2000). Imperial College of Science, Technology and Medicine, Civil Engineering Department.

Dziewonski, A.M., Chou, T.-A., and Woodhouse, J.H. (1981). Determination of Earthquake Source Parameters from Waveform Data for Studies of Global and Regional Seismicity. J. Geophys. Res., 86, 2825 – 2852.

Eaton, J.W. (2002). GNU Octave Manual. Network Theory Limited.

ElGabry, M.N., Panza, G.F., Badawy, A.A., and Korrat, I.M. (2013). Imaging a Relic of Complex Tectonics: The Lithosphere and Asthenosphere Structure. In The Eastern Mediterranean. Terra Nova, 25(2), 102-109.

Ekstrom, G., Tromp, J., and Larson, E.W.F. (1997). Measurements and Global Models of Surface Wave Propagation. J. Geophys. Res., 102, 8137 – 8157.

Engdahl, E.R., van der Hilst, R.D., and Buland, R. (1998). Global Teleseismic Earthquake Relocation with Improved Travel Times and Procedures for Depth Determination. Bulletin of the Seismological Society of America, 88, 722–743.

Fäh, D. (1992). A hybrid technique for the estimation of strong ground motion in sedimentary basins. Ph.D. Thesis. Swiss Federal Institute of Technology, Zurich.

Fäh, D., Suhadolc, P., and Panza, G.F. (1993). Variability of Seismic Ground Motion in Complex Media: The Case of a Sedimentary Basin in the Friuli (Italy) Area. Journal of Applied Geophysics, 30(1-2), 131-148.

Fäh, D. and Panza, G.F. (1994). Realistic Modelling of Observed Seismic Motion in Complex Sedimentary Basins. Annali di Geofisica, 3, 1771–1797.

Fäh, D., Suhadolc, P., and Panza, G.F. (1994). A Hybrid Method for the Estimation of Ground Motion in Sedimentary Basins: Quantitative Modeling for Mexico City. Bulletin of the Seismological Society of America, 84(2), 383-399.

Fäh D., Iodice C., Suhadolc P., and Panza G.F. (1995). Application of Numerical Simulations for a Tentative Seismic Microzonation of the City of Rome, Ann. Geofis., 38, 607–616.

Fauzi, U.J., Fauzi, A., Irsyam, M., and Toha, F.X. (2011). Proposed Long Period Transition Map for New Indonesia Earthquake Resistant Building Code Based on Indonesia Seismic Hazard Map 2010. In Proceedings of the Annual International Conference, Syiah Kuala University-Life Sciences & Engineering Chapter (Vol. 1, No. 2).

Fauzi, U.J. (2013). (Personal Communication about PSHA Digital Data).

Fitch, T.J. (1972). Plate Convergence, Transcurrent Faults, and Internal Deformation adjacent to Southeast Asia and the Western Pacific. Journal of Geophysical Research, 77(23), 4432-4460.

Flory and Denis (2012). One Year after Fukushima: Lessons for a Safer Nuclear Energy - Keynote Iaea Deputy Director General, Plenary Session, Monday, 19 March 2012. One Year after Fukushima: Lessons for a Safer Nuclear Energy.

Florsch, N., Fah, D., Suhadolc, P., and Panza, G.F. (1991). Complete Synthetic Seismograms for High-Frequency Multimode SH-Waves. Pure and Applied Geophysics, 136, 529–560.

Fukushima and Tanaka (1990). A New Attenuation Relation for Peak Horizontal Acceleration of Strong Earthquake Ground Motion in Japan. Bull. Seismol. Soc. Am., 80 (1990), pp. 757–783.

Ghosal, D., Singh, S.C., Chauhan, A.P.S., and Hananto, N.D. (2012). New Insights on the Offshore Extension of the Great Sumatran Fault, NW Sumatra, from Marine Geophysical Studies. Geochemistry, Geophysics, Geosystems, 13(11).

Goldstein, P. and Snoke, A. (2005), "SAC Availability for the IRIS Community", Incorporated Institutions for Seismology Data Management Center Electronic Newsletter.

Gorbatov, A., Limaye, A., and Sambridge, M. (2004). Tomoeye: A Matlab Package for Visualization of Three-Dimensional Tomographic Models. Geo- chem. Geophys. Geosyst., 5, Q04003. DOI:10.1029/2003GC000653.

Gorshkov, A.I., Panza, G.F., Soloviev, A.A., and Aoudia, A. (2004). Identification of Seismogenic Nodes in the Alps and Dinarides. Bollettino Della Società Geologica Italiana, 123(1), 3-18.

Gorshkov, A.I., Panza, G.F., Soloviev, A.A., and Aoudia, A. (2002). Morphostructural Zonation and Preliminary Recognition of Seismogenic Nodes around the Adria Margin in Peninsular Italy and Sicily. Journal of Seismology and Earthquake Engineering, 4(1), 1.

Gorshkov, A.I., Panza, G.F., Soloviev, A.A., Aoudia, A., and Peresan, A. (2009). Delineation of the Geometry of Nodes in the Alps–Dinarides Hinge Zone and Recognition of Seismogenic Nodes (M>= 6). Terra Nova, 21(4), 257-264.

GSHAP (1999). The Global Seismic Hazard Assessment Program (GSHAP) 1992–1999. Ann. Geofis. (1999).

Gunawan, Endra, Sagiya, T., Ito, T., Kimata, F., Tabei, T., Ohta, Y., Meilano, I., Abidin, H.Z., Nurdin, I., and Sugiyanto, D. (2014). A Comprehensive Model of Postseismic Deformation of the 2004 Sumatra–Andaman Earthquake Deduced from GPS Observations in Northern Sumatra. Journal of Asian Earth Sciences 88 (2014): 218-229.

Günther, A. (2007). An Information System Engineering Geology (ISEG) for Urban Spatial Planning. In Geophysical Research Abstracts (Vol. 9, p. 06099).

Gusev, A.A. (1983). Descriptive Statistical Model of Earthquake Source Radiation and Its Application to an Estimation of Short-Period Strong Motion. Geophysical Journal International, 74(3), 787-808.

Gusev, A.A. (2011). Broadband Kinematic Stochastic Simulation of an Earthquake Source: A Refined Procedure for Application in Seismic Hazard Studies. Pure Appl. Geophys., 168(1–2). DOI:10.1007/s00024-010-0156-3.

Hanks, T.C., and Kanamori, H. (1978). Moment Magnitude Scale. In Transactions-American Geophysical Union (Vol. 59, No. 12, pp. 1128-1128). 2000 Florida Ave Nw, Washington, DC, 2009: Amer. Geophysical Union.

Hamilton, W. (1979). Tectonics of the Indonesian Region. United States. Geological Survey Professional Paper, 1078.

Happrobo and Satrio (2015). (Personal Communication with BMKG staff in Banda Aceh).

Haskell, N.A. (1964). Total Energy and Energy Spectral Density of Elastic Wave Radiation from Propagating Faults. Bull. Seismol. Soc. Am., 54, 1811–1841.

Houston, H. and Kanamori, H. (1986). Source Spectra of Great Earthquakes: Teleseismic Constraints on Rupture Process and Strong Motion. Bulletin of the Seismological Society of America, 76(1), 19-42.

IAEA (2010). Seismic Hazards in Site Evaluation for Nuclear Installations. Specific Safety Guide, No. SSG-9.

International Building Code（IBC）(2000). International Code Council. International Conference of Building Officials. Whittier, CA, and others.

International Council of Building Officials (1997). Uniform Building Code. Whittier, CA.

International Building Code (IBC) (2009). International Code Council, Inc.

International Seismological Centre (ISC) (2013). Online Bulletin, http://www.isc.ac.uk, Internatl. Seis. Cent., Thatcham, United Kingdom, 2013.

Irsyam, M., Dangkua, D. T., Hendriyawan, Hoedajanto, D., Hutapea, B.M., Kertapati, E.K., and Petersen, M.D. (2008). Proposed Seismic Hazard Maps of Sumatra and Java Island and Microzonation Study of Jakarta City, Indonesia. Journal Earth System Science, 865-878.

Irsyam, M., Sengara, W., Aldimar, F., Widiyantoro, S., Triyoso, W., Natawidjaja, D.H., Kertapati, E., Meilano, I., Asrurifak, M., Suhardjono, and Ridwan, M. (2010). Summary of Study: Development of Seismic Hazard Maps of Indonesia for Revision of Hazard Map in SNI 03-1726-2002. Indonesia Seismic Hazard Map Revision Team.

Irsyam, M., Asrurifak, M., Ridwan, M., Aldiamar, F., Sengara, I.W., Widiyantoro, S., and Firmanti, A. (2013). Past Earthquakes in Indonesia and New Seismic Hazard Maps for Earthquake Design of Buildings and Infrastructures. In Geotechnical Predictions and Practice in Dealing with Geohazards (pp. 33-46). Springer Netherlands.

Irwandi, I. ... T., Meilano, Ito, T., Gunawan, E., Kimata, F., Tabei, (2010). Aceh Geodynamics and

GPS Observation: Investigate Post-Seismic Deformation in Aceh after 2004 Sumatra Earthquake (Presentation). Advanced Conference on Seismic Risk Mitigation and Sustainable Development, ICTP, Trieste 10-14 May 2010.

Ito, T., Gunawan, E., Kimata, F., Tabei, T., Meilano, I., Sugiyanto, D., Nurdin, I., and Agustan, A. (2008). Crustal Deformation in North Sumatra Island Detected by Continuous GPS Network (AGNeSS). AGU Fall Meeting Abstracts.

Ito, T., Gunawan, E., Kimata, F., Tabei, T., Simons, M., Meilano, I., Agustan, Ohta, Y., Nurdin, I., and Sugiyanto, D. (2012). Isolating along-strike Variations in the Depth Extent of Shallow Creep and Fault Locking on the Northern Great Sumatran Fault. J. Geophys. Res.: Solid Earth 117 (B6), 1978–2012.

Ito, Takeo, Endra Gunawan, Fumiaki Kimata, Takao Tabei, Irwan Meilano, Yusaku Ohta, Nazli Ismail, Irwandi Nurdin, and Didik Sugiyanto. (2016). Co-seismic offsets due to two earthquakes (M w 6.1) along the Sumatran fault system derived from GNSS measurements. Earth, Planets and Space, 68(1), 1-8.

Ivanka, P., Silvia, D., Giuliano, G.P., and Franco, V., (2007). An Earthquake Scenario for the Microzonation of Sofia and the Vulnerability of Structures Designed by Use of the Eurocodes. Soil Dynamics and Earthquake Engineering, 27(11), pp.1028-1041.

Jansen, P.J. (1903). Verslag Eener Geologisch-Mijnbouwkundige Verkenning Der Atjeh-vallei. Jaarboek van het Mijnwezen in Nederlandsch Oost-lndie 1903.

Jeffery, D.It., Cameron, N.R., and Suharsono (1976). Geological Report. Sheet NB 46-12-B&D (Banda Aceh). Integrated Geological Survey of Northern Sumatra. Report No. 16 (unpublished).

Joyner, W.B. (1984). A Scaling Law for the Spectra of Large Earthquakes. Bulletin of the Seismological Society of America, 74(4), 1167-1188.

Kanamori, H. (1977). The Energy Release in Great Earthquakes. Journal of Geophysical Research 82.20: 2981-2987.

Karig, D.E., Lawrence, M.B., Moore, G.F., and Curray, J.R. (1980). Structural Framework of the Fore-arc Basin, NW Sumatra. Journal of the Geological Society, London, 137, 77-91.

Kausel, E. and Schwab, F. (1973). Contributions to Love-Wave Transformation Theory: Earth-Flattening Transformation for Love Waves from a Point Source in a Sphere. Bulletin of the Seismological Society of America, 63(3), 983-993.

Macpherson, K.A., Hidayat, D., and Goh, S.H. (2012). Receiver Function Structure Beneath Four Seismic Stations in the Sumatra Region. Journal of Asian Earth Sciences, Volume 46, 2 March 2012, Pages 161-176.

Kennett, B.L.N., Engdahl, E.R., and Buland, R. (1995). Constraints on Seismic Velocities in the Earth from Travel Times. Geophys. J. Int., 122, 108-124.

Klugel, J.U. (2007). Comment on ''Why Do Modern Probabilistic Seismic-Hazard Analyses Often Lead to Increased Hazard Estimates?'' by Julian J. Bommer and Norman A. Abrahamson, Bull Seism. Soc. Am., 97, 2198–2207.

Knopoff, L. (1964). A Matrix Method for Elastic Wave Problems. Bulletin of the Seismological Society of America, 54(1), 431-438.

Korn, M. and H. Stöckl. (1982). Reflection and Transmission of Love Channel Waves at Coal Seam Discontinuities Computed with a Finite Difference Method. J. Geophys.,50,171-176.

Kossobokov, V.G. and Nekrasova, A.K. (2012). Global Seismic Hazard Assessment Program Maps Are Erroneous. Seismic Instruments, 48(2), 162-170.

La Mura, C., Yanovskaya, T.B., Romanelli, F., and Panza, G.F. (2011). Three-Dimensional Seismic Wave Propagation by Modal Summation: Method and Validation. Pure and Applied Geophysics, 168(1-2), 201-216. Special Issue: Advanced Seismic Hazard Assessment. Part I: Seismic Hazard Assessment.

Lasitha, S., Radhakrishna, M., and Sanu, T.D. (2006). Seismically Active Deformation in the Sumatra-Java Trench-Arc Region: Geodynamic Implications. Current Science, Vol.90, No.5, 690-696.

Laske, G. and Masters, G. (1997). A Global Digital Map of Sediment Thickness, EOS Trans. AGU, 78, F483, 1997. http://igppweb.ucsd.edu/#sediment.html.

Laske, G., Masters., G., Ma, Z., and Pasyanos, M. (2013). Update on CRUST1.0-A1-degree Global Model of Earth's Crust, Geophys. Res. Abstracts, 15, Abstract EGU2013-2658, 2013.

Leyendecker, E.V., Hunt, R.J., Frankel, A.D. and Rukstales, K.S. (2000). Development of Maximum Considered Earthquake Ground Motion Maps. Earthquake Spectra, 16, 21–40.

Levshin, A.L. (1973). Surface and Channel Seismic Waves. Nauka, Moscow.

Magrin, A., Mura, C.L., Vaccari, F., Panza, G.F., and Gusev, A.A. (2011). Seismic Hazard Assesment: Parametric Studies on Grid Infrastructures.

Magrin, A. (2013). Multi-Scale Seismic Hazard Scenarios. Dissertation, University of Trieste.

Magrin, Andrea, and Vaccari, F. (2014). GNDT Deterministic Seismic Zoning Reference Guide: The DSTX Manuals. Department of Geosciences, University of Trieste.

Magrin, A., Parvez, I.A., Vaccari, F., Peresan, A., Rastogi, B.K., Cozzini, S., Bisignano D., Romanelli, F., Choudhury, P., Roy., K.S., Mir, R.R., and Panza, G.F. (2016). Neo-deterministic Definition of Seismic and Tsunami Hazard Scenarios for the Territory of Gujarat (India). In Earthquakes and Their Impact on Society (pp. 193-212). Springer International Publishing.

Malod, J.A. and Kamal, B.M. (1996). The Sumatra Margin: Oblique Subduction And Lateral Displacement of the Accretionary Prism. Geol. Soc. Spec. Publ., 106(1), 19–28. DOI:10.1144/GSL.SP.1996.106.01.03.

McCaffrey, R. (1992). Oblique Plate Convergence, Slip Vectors, and Forearc Deformation. J. Geophys. Res., 97, 8905–8915.

McCaffrey, R. (2009). The Tectonic Framework of the Sumatran Subduction Zone. Annu. Rev. Earth Planet. Sci. 2009.37:345-366.

Marrara F. and Suhadolc P. (1998a). Observation and Modelling of Site Effects in the Volvi Basin, Greece. In The Effects of Surface Geology on Seismic Motion, pp.973–980, eds Irikura, K., Kudo, K., Okada, H., Sasatani, T., Balkema, Rotterdam.

Maruyama, T. (1963). On the Force Equivalents of Dynamical Elastic Dislocations with Reference to the Earthquake Mechanism. Bull. Earthquake Res. Inst., Tokyo Univ., 41,467-486.

Masterlark, T. and Hughes, K.L. (2008). Next Generation of Deformation Models for the 2004 M9 Sumatra‐Andaman Earthquake. Geophysical Research Letters, 35(19).

Meletti, C., Patacca, E., and Scandone, P. (2000). Construction of a Seismotectonic Model: the Case of Italy. Pure and Applied Geophysics, 157(1-2), 11-35.

Meletti, C. and Valensise, G. (2004). Zonazione Sismogenetica ZS9–App. 2 Al Rapporto Conclusivo. Gruppo di Lavoro MPS (2004). Redazione Della Mappa Di Pericolosità Sismica Prevista Dall'ordinanza PCM, 3274.

Mohanty, W.K., Walling, M.Y., Vaccari, F., Tripathy, T., and Panza, G.F. (2009). Modeling of SH-

and P-SV-Wave Fields and Seismic Microzonation based on Response Spectra for Talchir Basin, India. Engineering Geology, 104(1), pp.80-97.

Morita and Shin (2009). IAEA Involvement in Seismic Safety. IAEA Statute, Safety Standards on Hazard Assessment and Design, Siting, and Site Selection. Joint ICTP/IAEA Advanced Workshop on Earthquake Engineering for Nuclear Facilities, 30 November - 4 December 2009.

Musson, R.M. and Cecić, I. (2002). Chapter 12, Intensity and Intensity Scales. IASPEI New Manual of Seismological Observatory Practice, GeoForschungsZentrum, Potsdam.

Natawidjaja, Hilman, D., and Triyoso, W. (2007). The Sumatran Fault Zone-From Source To Hazard. Journal Of Earthquake and Tsunami, Vol. 1, No. 1 (2007) 21–47.

Nunziata, C., Fah, D., and Panza, G.F. (1995). Mitigation of Seismic Hazard of a Megacity: the Case of Naples.

Nunziata, C., Costa, G., Mararra, F., and Panza, G.F. (2000). Calibrated Estimation of the Response Spectra for the 1980 Irpinia Earthquake in the Eastern Area of Naples, Earthq. Spectra.

Nunziata, C., Sacco, C. and Panza, G.F. (2011). Modeling of Ground Motion at Napoli for the 1688 Scenario Earthquake. Pure and Applied Geophysics, 168(3-4), pp.495-508.

Panza, G.F. (1985). Synthetic Seismograms: the Rayleigh Waves Modal Summation, J. Geophys., 58, 125-145.

Panza, G.F. and Suhadolc, P. (1987). Complete Strong Motion Synthetics. Seismic Strong Motion Synthetics 4: 153-204.

Panza, G.F., Vaccari, F., Costa, G., Suhadolc, P. and Faeh, D. (1996). Seismic Input Modelling for Zoning and Microzoning. Earthq. Spectra, 12, 529±566.

Panza, G.F., Vaccari, F., and Romanelli, F., (1999). The IUGS-UNESCO IGCP Project 414: Realistic modelling of Seismic Input for Megacities and Large Urban Areas, Episodes, 22, 26–32.

Panza, G.F., Romanelli, F., and Vaccari, F. (2001). Seismic Wave Propagation. In Laterally Heterogeneous Anelastic Media: Theory and Applications to Seismic Zonation. Advances in Geophysics, Volume 43, 2001, Pages 1–95.

Panza, G.F., Romanelli, F., and Vaccari, F. (2001b). Realistic Modeling of Seismic Input in Urban Areas: a UNESCO-IUGS-IGCP Project. Pure and Applied Geophysics 158(12), 2389-2406.

Panza, G.F., Alvarez, L., Aoudia, A., Ayadi, A., Benhallou, H., Benouar, D., Bus, Z., Chen, Y.-T., Cioflan, C., Ding, Z., El-Sayed, A., Garcia, J., Garofalo, B., Gorshkov, A., Gribovszki, K., Harbi, A., Hatzidimitriou, P., Herak, M., Kouteva, M., Kuznetzov, I., Lokmer, I., Maouche, S., Marmureanu, G., Matova, M., Natale, M., Nunziata, C., Imtiyaz A. Parvez, Paskaleva, I., Pico, R., Radulian, M., Romanelli, F., Soloviev, A., Suhadolc, P., Szeidovitz, G., Triantafyllidis, P., and Vaccari, F. (2002). Realistic Modeling of Seismic Input for Megacities and Large Urban Areas: the UNESCO/IUGS/IGCP Project 414. Episodes, 25(3), 160-184.

Panza, G.F. (2009). Neo-deterministic (NDSHA) and Probabilistic Seismic Hazard (PSHA) Assessments: a Comparison over the Italian Territory. Joint ICTP/IAEA Advanced Workshop on Earthquake Engineering for Nuclear Facilities.

Panza, G.F., Paskaleva, P., Dineva, P., and Mura, C.L. (2009). Earthquakes Site Effects Modeling by Hybrid MS-BIEM: the Case Study of Sofia, Bulgaria. Earth and Environmental Science Volume 20, Number 2 (2009), 91-116. DOI: 10.1007/s12210-009-0049-5.

Panza, G.F., Irikura, K., Kouteva, M., Peresan, A. , Wang, Z., and Saragoni, R. (2011). Advanced Seismic Hazard Assessment. Pure and Applied Geophysics, Vol. 168, Issue 1, pp. 1-9.

Panza, G.F., Mura, C.L., Peresan, A., Romanelli, F., and Vaccari, F. (2012). Seismic Hazard Scenarios as Preventive Tools for a Disaster Resilient Society. Chapter Three. Advances in Geophysics. Vol. 53, 2012, pp. 93–165.

Panza, G.F., Irikura, K., Kouteva, M., Peresan, A., and Wang, Z. (2012a). Advanced Seismic Hazard Assessment. Pure and Applied Geophysics,Vol. 1/1939- Vol. 169/2012. Special Issue: Advanced Seismic Hazard Assessment. Part I: Seismic Hazard Assessment.

Panza, G.F., Peresan, A., and Mura, C.L. (2013). Seismic Hazard and Strong Ground Motion: an Operational Neo-Deterministic Approach from National to Local Scale. In UNESCO-EOLSS Joint Commitee (Ed.), Encyclopedia of Life Support Systems (EOLSS), Geophysics and Geochemistry. Developed under the Auspices of the UNESCO, Eolss Publishers, Oxford ,UK, pp. 1E49.

Parvez, I.A., Vaccari, F., and Panza, G.F. (2003). A Deterministic Seismic Hazard Map of India and Adjacent Areas. Geophysical Journal International, 155(2), 489-508.

Parvez, I.A., Romanelli, F., and Panza, G.F. (2010). Long Period Ground Motion at Bedrock Level in Delhi City from Himalayan Earthquake Scenarios. Pure and Applied Geophysics.

Paskaleva, I., Dimova, S., Panza, G.F., and Vaccari, F. (2007). An Earthquake Scenario for the Microzonation of Sofia and the Vulnerability of Structures Designed by Use of the Eurocodes. Soil Dynamics and Earthquake Engineering, 27, 1028-1041.

Paskaleva, I., Kouteva, M., Vaccari, F., and Panza, G.F. (2010). Some Contributions of the Neo-Deterministic Seismic Hazard Assessment Approach to the Earthquake Risk Assessment for the City of Sofia. Pure and Applied Geophysics.

Pasyanos, M.E., Masters, T.G., Laske, G., and Ma, Z. (2014). LITHO1.0: An Updated Crust and Lithospheric Model of the Earth. J. Geophys. Res., 119 (3), 2153-2173. DOI: 10.1002/2013JB010626. http://igppweb.ucsd.edu/~gabi/litho1.0.html

Pavlov, V.M. (2002). A Convenient Technique for Calculating Synthetic Seismograms in a Layered Half-Space. In Proceedings of the International Conference Problems of Geocosmos, St. Peteburg, pages 03–08, 2002.

Pavlov, V.M. (2009). Matrix Impedance in the Problem of the Calculation of Synthetic Seismograms for a Layered-Homogeneous Isotropic Elastic Medium. Izvestiya Physics of the Solid Earth, 45(10):850–860, 2009.

Peresan, A., Kossobokov, V., Romashkova, L., and Panza, G. F. (2005). Intermediate-Term Middle-Range Earthquake Predictions in Italy: a Review. Earth-Science Reviews, 69(1), 97-132.

Peresan, A., Zuccolo, E., Vaccari, F., Gorshkov, A., and Panza, G.F. (2012). Neo-Deterministic Seismic Hazard and Pattern Recognition Techniques: Time-Dependent Scenarios for North-Eastern Italy.Volume 169 / 2012. Special Issue: Advanced Seismic Hazard Assessment. Part II: Regional Seismic Hazard and Seismic Microzonation Case Studies.

Pesicek, J.D. (2009). Structure of the Sumatra-Andaman Subduction Zone. Dissertation, University of Wisconsin-Madison.

Pesicek, J.D., Thurber, C.H., Zhang, H., DeShon, H.R., Engdahl, E.R., and Widiyantoro, S. (2010d). Teleseismic Double Difference Relocation of Earthquakes along the Sumatra Andaman Subduction Zone Using a 3-D Model. Journal of Geophysical Research: Solid Earth 115 (B10)

Pesicek, J.D., Thurber, C.H., Widiyantoro, S., Zhang, H., DeShon, H.R., and Engdahl, E.R. (2010). Sharpening the Tomographic Image of the Subducting Slab Below Sumatra, the Andaman Islands and Burma. Geophys. J. Int. (2010) 182, 433–453.

Petersen, M.D., Dewey, J., Hartzell, S., Mueller, C., Harmsen, S., Frankel, A., and Rukstales, K.

(2004). Probabilistic Seismic Hazard Analysis for Sumatra, Indonesia and across the Southern Malaysian Peninsula. Tectonophysics, 390(1), 141-158.

Polom, U., Arsyad, I., and Kümpel, H.J. (2008). Shallow Shear-Wave Reflection Seismics in the Tsunami Struck Krueng Aceh River Basin, Sumatra. Advances in Geosciences, 14, pp.135-140.

Prawirodirdjo, L., Bock, Y., Genrich, J.F., Puntodewo, S., Rais, J., Subarya, C., and Sutisna, S. (2000). One Century of Tectonic Deformation Along the Sumatran Fault from Triangulation and Global Positioning System Surveys. Journal of Geophysical Research 105(B12).

PU (Departemen Pekerjaan Umum), Ditjen Cipta Karya, Direktorat Masalah Bangunan. (1983). Peraturan Perencanaan Tahan Gempa Indonesia untuk Gedung.

QGIS, D.T. (2011). Quantum GIS Geographic Information System. Open Source Geospatial Foundation Project.

Richard, Xu, C., and Stewart, R. (2006). Estimating Seismic Attenuation (Q) from VSP Data. CSEG Recorder, 31, pp.57-61.

Romanelli, F., Vaccari, F., and Panza, G.F. (1998). Realistic Modelling of Ground Motion: Techniques for Site Response Estimation. In Proc. 6th U.S. National Conf. on Earthquake Engineering, CD-ROM: Paper 433, EERI, Seattle.

Romanelli, F. and Vaccari, F. (1999). Site Response Estimation And Ground Motion Spectrum Scenario In The Catania Area. Journal of Seismology, 3(3), 311-326.

Romanelli, F., Panza, G.F., and Vaccari, F. (2004). Realistic Modeling of the Effects of Asynchronous Motion at the Base of Bridge Piers. Journal of Seismology and Earthquake Engineering, 6(2), 19-28.

Rudyanto, A. (2015). (Personal Communication with BMKG staff, Jakarta).

Rusdi, M., Roosli, R., and Ahamad, M.S.S. (2015). Land Suitability Evaluation for Settlement based on Soil Bearing Capacity in Banda Aceh, Indonesia. Advances in Environmental Biology, 53-57.

Rusydy, I., Syamsidik, S., and Pagihariyadi, P. (2015). Pemetaan Makroseismik Untuk Pendugaan Sumber Gempa Bumi, Studi Kasus: Gempa Bumi Aceh Tengah 2 Juli 2013. Proseding Konferensi Nasional FPT PRB.

Rusydy, I. (2016). (Personal communication for Intensity Data)

Saraò, A., Das, S., and Suhadolc, P. (1998). Effect of Non-Uniform Station Coverage on the Inversion for Earthquake Rupture History for a Haskell-Type Source Model. Journal of Seismology, 2(1), 1-25.

Sieh, K. and Natawidjaja, D. (2000). Neotectonics of the Sumatran Fault, Indonesia. J. Geophys. Res. 105 28,295–28,326.

Sigbjornsson, R. and Baldvinsson, G.I. (1992). Seismic Hazard and Recordings of Strong Ground Motion in Iceland. Pages 419–424 of: Proceedings of Tenth World Conference on Earthquake Engineering, vol. 1.

Standar Nasional Indonesia (SNI) (2002). Tata Cara Perencanaan Ketahanan Gempa untuk Bangunan Gedung (SNI 03-1726-2002), Badan Standardisasi Nasional.

Stein, S. and Wysession, M. (2003). An Introduction to Seismology, Earthquakes, and Earth Structure. Blackwell Publishing, 2003, pp.192.

Syukri, M., Fauzi, A., Fashbir, and Irwandi (2012). Numerical Simulation for Scenario-Based Volcanic Hazard Assessment (VHA) at Seulawah Agam Volcano, Aceh, Sumatra. Proceedings

of The Annual International Conference Syiah Kuala Univeristy. Life Sciences & Engineering Chapter. Banda Aceh.

Tabei, T., Kimata, F., Ito, T., Gunawan, E., Tsutsumi, H., Ohta, Y., Yamashina, T., Soeda, Y., Ismail, N., Nurdin, I. and Sugiyanto, D. (2015). Geodetic and Geomorphic Evaluations of Earthquake Generation Potential of the Northern Sumatran Fault, Indonesia.

Tapley, B. et al. (2005). GGM02 - An improved Earth Gravity Field Model from GRACE, Journal of Geodesy, 79, 467-478.

Uniform Building Code (UBC) (1997). Volume 2, International Conference of Building Official.

USGS, NEIC (2008). Seismic Hazard of Western Indonesia, Map prepare by United State of Geology Survey. http://earthquake.usgs.gov/research/hazmap/product_data.

USGS (2009). Poster of the Southern Sumatra, Indonesia Earthquake of 30 September 2009 - Magnitude 7.6.

USGA (2013). http://earthquake.usgs.gov/earthquakes/eventpage/usb000i4re#scientific_summary.

Vaccari, F. (1995). LP-Displacement Hazard Evaluation in Italy. Proc. 24th General Assembly of the European Seismological Commission (1995): 1489-1498.

Vaccari, F., Walling, M.Y., Mohanty, W.K., Nath, S.K., Verma, A.K., Sengupta, A., and Panza, G.F. (2011). Site-Specific Modeling of SH and P-SV Waves for Microzonation Study of Kolkata Metropolitan City, India. Pure and applied geophysics, 168(3-4), pp.479-493.

Vaccari, F. (2015m). Quick Reference Manuals: 1D Modal Summation Technique Computation of Modes, Eigenfunctions, Synthetic Seismograms. Document Version 1.2. Department of Mathematic and Geosciences, Group of Seismology. Trieste University.

Vaccari, F. (2014d). The DSTX Quick Reference Manuals, XdigiMac Screen Digitizer. Document version 1.3. Department of Mathematic and Geosciences, Group of Seismology. Trieste University.

Vaccari, F. (2015h). Quick Reference Manuals Ground Shaking Scenarios along 2D Profiles Hybrid Technique, Point-Source Approximation. Document version 1.3. Department of Mathematic and Geosciences, Group of Seismology. Trieste University.

Van, E.S.L.J.C. (1930). Onderzoek Naar De Watervooziening Van Oelee Lheu. Goot Atjeh en Onderh. Direktorat Geologi, Sub Direktorat Geologi Teknik ttydrogeologi, Seksi Geologi Teknik, Laporan No. 191 (unpublished).

Virieux, J. (1986). P-SV Wave Propagation in Heterogeneous Media: Velocity-Stress Finite-Difference Method. Geophysics, 51, 889-901.

Yao, H., Shearer, P. M., & Gerstoft, P. (2013). Compressive sensing of frequency-dependent seismic radiation from subduction zone megathrust ruptures. Proceedings of the National Academy of Sciences, 110(12), 4512-4517.

Youngs, R.R., Chiou, S.J., Silva, W.J., and Humphrey, J.R. (1997). Strong Ground Motion Attenuation Relationships for Subduction Zone Earthquakes. Seismological Research Letters, 68(1), 58-73.

Wang, Z. (2008). Understanding Seismic Hazard And Risk: A Gap Between Engineers and Seismologists. The 14th World Conference On Earthquake Engineering, October 12–17, 2008, Beijing, China, Paper No. S27-001.

Wang, Z. (2011). Seismic Hazard Assessment: Issues and Alternatives. Pure and Applied Geophysics 168,11-25

Widiyantoro, S., Gorbatov, A., Kennett, B.L.N. and Fukao, Y. (2000). Improving Global Shear Wave Traveltime Tomography Using Three-Dimensional Ray Tracing and Iterative Inversion. Geophys. J. Int., 141, 747–758.

Widiyantoro, S. (2008). (Personal Communication about Vs Tomography Data).

Widiyantoro, S., Pesicek, J.D., and Thurber, C.H. (2011). Subducting Slab Structure Below The Eastern Sunda Arc Inferred from Non-Linear Seismic Tomographic Imaging. Geological Society, London, Special Publications, 355(1), 139-155.

Wald, D.J., Quitoriano, V., Heaton, T.H., and Kanamori, H. (1999). Relationships between Peak Ground Acceleration, Peak Ground Velocity, and Modified Mercalli Intensity in California. Earthquake Spectra: August 1999, Vol. 15, No. 3, pp. 557-564

Wald , D. J., Quitoriano, V., Heaton, T.H., Kanamori, H., Scrivner, C.W., and Worden, C.B. (1999). TriNet "ShakeMaps": Rapid Generation of Peak Ground Motion and Intensity Maps for Earthquakes in Southern California. Earthquake Spectra: August 1999, Vol. 15, No. 3, pp. 537-555.

Wessel, P. and Smith, W.H. (1998). New, Improved Version of Generic Mapping Tools Released. Eos, Transactions American Geophysical Union, 79(47), 579-579.

Wessel, P., Smith, W. H., Scharroo, R., Luis, J., & Wobbe, F. (2013). Generic mapping tools: improved version released. Eos, Transactions American Geophysical Union, 94(45), 409-410.

Wyss, M., Nekrasova, A., and Kossobokov, V. (2012). Errors in Expected Human Losses due to Incorrect Seismic Hazard Estimates. Natural hazards, 62(3), 927-935.

Zuccolo, E., Vaccari, F., Peresan, A., and Panza, G.F. (2011). Neo-Deterministic and Probabilistic Seismic Hazard Assessments: a Comparison over the Italian Territory. Volume 168, Numbers 1-2 / January 2011.